

CARBIDE COMPOSITION CHANGES IN
POWER PLANT STEELS
AS A METHOD OF
REMANENT CREEP LIFE PREDICTION

By
Rachel Clare Thomson
Newnham College, Cambridge

Department of Materials Science and Metallurgy
Pembroke Street
Cambridge
CB2 3QZ

*A dissertation submitted for the
degree of Doctor of Philosophy*

September 1992

Declare the past, diagnose the present, foretell the future.

Epidemics, Book I, Section 11

Hippocrates of Cos, *ca* 460–*ca* 357 BC

PREFACE

This dissertation is submitted for the degree of Doctor of Philosophy at the University of Cambridge. It contains an account of research carried out between October 1989 and September 1992 in the Department of Materials Science and Metallurgy, Cambridge, under the supervision of Dr. H.K.D.H. Bhadeshia. Unless appropriately referenced, the work is original and is not the result of collaboration. No part of this dissertation has been, or is currently being, submitted for any degree or diploma at this, or any other, university. This dissertation contains less than 60,000 words.

Rachel Thomson
September 1992

ACKNOWLEDGEMENTS

I wish to thank Professor C. Humphreys for the provision of laboratory facilities in the Department of Materials Science and Metallurgy at the University of Cambridge. I am indebted to Dr H.K.D.H. Bhadeshia for his encouragement and enthusiasm during the course of this work.

I would like to thank both National Power and the Science and Engineering Research Council for providing financial support for this project, and especially Dr D. Gooch of the National Power Technology and Environment Centre (NPTEC), Leatherhead, for the helpful discussions and interest he has shown in this work. I must also thank Mrs P. Dolbear at NPTEC for her assistance with X-ray diffraction studies.

I am also grateful to the staff at the National Physical Laboratory, Teddington, particularly Mr H. Davies and Dr A. Dinsdale, for the provision of MTDATA, a program for the calculation of chemical equilibria in multicomponent systems, and their advice on its use.

Thanks are also extended to the technical staff of the department who have contributed to this project; in particular, Mr D. Nicol for valuable advice on electron microscopy and carbon replica preparation, Mr J. Leader for his general ability to get equipment working, the photographic department – Mr B. Barber and Mrs C. Best for their generous help, and Mr G. Morgan and his staff in the workshop for making some of my specimens.

I must also thank my friends and colleagues in the department, especially Dr R. Reed (now of Imperial College) for his early help with transmission electron microscopy, Dr C. Boothroyd for his help with scanning transmission electron microscopy, G. Rees, M. Gregg and J. Race. My thanks also go to the other members of the Phase Transformations group, with whom it has been very enjoyable to work. I am also grateful to I. Redfern for his assistance with computing matters. Helpful discussions with Drs S. Babu, H. Harada, M. Miller, J. Whiteman and Professors C. Atkinson and G. Olson are acknowledged with pleasure.

Finally, I wish to thank my family for their unfailing support and encouragement.

ABSTRACT

The prediction of the remanent creep [†] life of a component requires a knowledge of both the service stresses and temperatures. Temperature data are subject to considerable scatter due to spatial variations around the components, and irregular fluctuations with time as a result of changes in the mode of plant operation. It has been shown that a change of about 10°C can lead to a corresponding change in the remanent life estimate by a factor of two. It is therefore desirable to be able to estimate the average thermal history of each component in order to accurately assess its remaining creep life, thereby avoiding premature replacement whilst maintaining safety standards. In this work, changes in the steel microstructure are related to the thermal history, thereby enabling the microstructure to be used as an in situ **time-temperature recorder**.

When many of the conventional power plant steels entered service, their microstructures contained relatively fine particles of cementite whose substitutional solute concentration was initially similar to the solute content of the steel as a whole. These carbides were far from their equilibrium chemical composition, size and shape. During service at high temperatures the cementite tends to approach its equilibrium composition with respect to the substitutional elements, which can, in principle, be used to estimate the thermal history of the component. The purpose of this work is to determine the fundamental factors controlling the rate at which carbide compositions change, so that the extrapolation of experimental data can be made with greater confidence.

Experimental studies have been made using energy-dispersive X-ray analysis in a transmission electron microscope of the kinetics of cementite enrichment in steels which have pearlitic, bainitic or martensitic microstructures. Simultaneous measurement of particle size and composition over a wide range of tempering times at various temperatures have established the fact that smaller particles enrich more quickly than larger ones.

Power plant components can be very large, with the microstructure varying considerably within a given component. Since the formation of allotriomorphic ferrite causes an increase in the carbon concentration of the residual austenite, which subsequently transforms to bainite, the distribution and scale of cementite precipitation is also expected to vary significantly with the volume fraction of bainite. Theory indicates that the rate at which the cementite particles change composition will also differ as a consequence. For example, the cementite in regions

[†] Creep deformation is the time-dependent plastic extension which a material undergoes when subject to a load at elevated temperature for a long period of time.

containing less bainite is expected to enrich at a lower rate compared with those particles in regions with a large amount of bainite. The effect of typical variations in the microstructure on cementite enrichment kinetics is studied for different volume fractions of allotriomorphic ferrite and bainite in $2\frac{1}{4}\text{Cr1Mo}$ steel.

A theoretical model has been developed of the diffusion of substitutional solute elements to cementite particles in microstructures typical of power plant steels, subject to the thermodynamic constraints which determine the equilibrium composition of the two phases. The theoretical predictions have been compared with experimental observations in $\frac{1}{2}\text{Cr}\frac{1}{2}\text{Mo}\frac{1}{4}\text{V}$ and $2\frac{1}{4}\text{Cr1Mo}$ steels. The theoretical modelling of the diffusion fields around enriching particles has highlighted the need for the compositions of the substitutional solute elements at the ferrite/cementite interface to be known accurately. The composition–distance profiles of alloying elements through a particle have therefore been studied using atom probe field ion microscopy and scanning transmission electron microscopy to establish whether in fact local equilibrium exists at the carbide/matrix interface.

Extension of the model to treat enrichment and coarsening simultaneously has been considered. In reality, both these processes contribute significantly in the approach towards equilibrium, especially at the later stages of service. It has been shown that the driving forces for the processes of enrichment and coarsening in fact compete against one another and that the coarsening process is defeated by enrichment process until the particles are close to their equilibrium composition.

At long service times, all of the common power plant steels are expected to precipitate more stable alloy carbides, at the expense of cementite. Alloy carbide precipitation has been investigated in a 12Cr1Mo1V steel in which the enrichment kinetics are much faster than in a low alloy steel. However, it has been found that the equilibrium alloy carbide precipitates during the commercial stress–relief heat treatment and does not change in composition during further tempering. This is an important result; indications are that once the cementite transforms to alloy carbides, any changes in their composition are not large enough for this method to be used as a quantitative estimation of remanent life. Low alloy steels, however, contain cementite for a considerable fraction of their useful service life.

CONTENTS

Preface	ii
Acknowledgements	iii
Abstract	iv
Contents	vi
Nomenclature and Abbreviations	viii
Chapter 1: Introduction to Remanent Life Prediction	1
1.1 Introduction	2
1.2 Methods of remanent life prediction	9
1.3 Possible future indicators of thermal history	20
1.4 Conclusions	20
Chapter 2: Physical Metallurgy Of Alloyed Steels	22
2.1 Introduction	23
2.2 Bainite	26
2.3 Martensite	30
2.4 Summary of transformation mechanisms	36
2.5 Carbide precipitation	37
2.6 Interphase precipitation	41
Chapter 3: Theoretical Studies – An Introduction	43
3.1 Introduction	44
3.2 Partitioning in pearlitic and bainitic cementite	44
3.3 Equilibrium compositions of cementite and ferrite	46
3.4 Diffusion coefficients	48
3.5 One dimensional modelling	49
3.6 Consideration of the effect of particle size	57
Chapter 4: Experimental Procedure	60
4.1 Introduction	61
4.2 Materials	62
4.3 Heat treatments	62
4.4 Hardness measurements	63
4.5 Optical microscopy	63
4.6 Transmission electron microscopy	64
4.7 Energy dispersive X–ray analysis	67
4.8 Particle size measurements	70
4.9 Bulk extraction of carbides and X–ray diffraction	71
Chapter 5: $2\frac{1}{4}$ Cr1Mo Steel	73
5.1 Introduction	74
5.2 Materials	75
5.3 Initial heat treatments	76
5.4 Tempering heat treatments	92
5.5 Results and discussion from bainitic microstructures	94
5.6 Results and discussion from mixed microstructures	131
5.7 Comparison of experimental results and theoretical predictions	141
5.8 Conclusions	142

Chapter 6: $\frac{1}{2}\text{Cr}\frac{1}{2}\text{Mo}\frac{1}{4}\text{V}$ Steel	146
6.1 Introduction	147
6.2 Materials and heat treatment	147
6.3 Experimental results	148
6.4 Modelling of the diffusion process	152
6.5 Conclusions	160
Chapter 7: 12Cr1MoV Steel	161
7.1 Introduction	162
7.2 Materials and heat treatment	162
7.3 Results	163
7.4 Discussion	177
7.5 Conclusions	177
Chapter 8: Atom Probe and STEM Investigations	179
8.1 Introduction	180
8.2 Atom probe field ion microscopy	182
8.3 Scanning transmission electron microscope studies	190
8.4 Conclusions	192
Chapter 9: Further Theoretical Studies	193
9.1 Introduction	194
9.2 Experimental studies of particle coarsening	194
9.3 Particle size and solubility	196
9.4 Approximations	199
9.5 Application to simultaneous coarsening and enrichment of cementite	200
9.6 Conclusions	202
Chapter 10: Conclusions and Suggestions for Future Work	204
APPENDIX I	207
APPENDIX II	209
APPENDIX III	214
REFERENCES	219

NOMENCLATURE AND ABBREVIATIONS

a	Lattice parameter
at.%	Concentrations in atomic percent
A	Constant
A	Number of cavitating grain boundaries
A_{e_1}	Temperature of the eutectoid reaction
A_{e_3}	Temperature separating the $\alpha + \gamma$ and γ phase fields for a specific alloy
b.c.c.	Body-centred cubic
B	Constant
B_s	Bainite start temperature
c	Speed of light in vacuo
c	Thickness of a plate
c'	Dimensionless concentration in the finite difference method
$c^{\alpha\theta}$	Concentration in ferrite in equilibrium with cementite
$c^{\theta\alpha}$	Concentration in cementite in equilibrium with ferrite
c_{∞}^{α}	Equilibrium concentration in ferrite
c_{∞}^{θ}	Equilibrium concentration in cementite
c_r^{α}	Equilibrium concentration in ferrite at the ferrite/cementite interface
c_r^{θ}	Equilibrium concentration in cementite at the ferrite/cementite interface
\bar{c}	Average concentration in the alloy
C	Constant
C_A	Weight fraction of element A
d	Interatomic spacing along a specific crystallographic orientation
D	Diffusion coefficient
D_0	Pre-exponential factor for the diffusion coefficient
D_{α}	Diffusivity in ferrite
D_{θ}	Diffusivity in cementite
e	Electronic charge
eV	Electron volt
E	Strain energy
EDX	Energy-dispersive X-ray analysis
f	Volume fraction of martensite
f.c.c.	Face-centered cubic
g	Chemical potential
g_0	Chemical potential of pure substance
G_m	Molar Gibbs free energy
h	Planck's constant
HP	High pressure
HV	Vickers Hardness units
I	Integrated intensity per unit length of diffraction line
I_A	Characteristic intensity of element A
ILS	Invariant line strain
ISO	International Standards Organisation
IP	Intermediate pressure
IPS	Invariant plane strain
k	Boltzmann constant
k_{AB}	Experimental constant
k_z	Partition coefficient with respect to element z
L	Camera length
LP	Low pressure

m	Electronic mass
M_s	Martensite start temperature
MLI	Mean Linear Intercept
MTDATA	Metallurgical and Thermodynamic Data Service
n	Number of atoms
n_α	Number of slices of ferrite
n_θ	Number of slices of cementite
N	$\sqrt{h^2 + k^2 + l^2}$ where h , k and l are plane indices
N_A	Avagadros number
NDT	Non-destructive testing
NP-LE	Negligible partitioning local equilibrium
NPL	National Physical Laboratory
O	Surface area
P-LE	Partitioning local equilibrium
q	Half thickness
Q	Activation free energy per mole for diffusion
r	Grid parameter in the finite difference method
r	Radius of a spherical particle
r	Length of a plate
R	Universal gas constant
R	Distance between transmitted and diffracted electron beams
s	Shear component of a shape deformation strain
ss	Supersaturated
S_v	Grain surface area per unit volume
STEM	Scanning Transmission Electron Microscopy
t'	Dimensionless time in the finite difference method
t	Time
t_c	Time to reach a specific concentration
t_i	Time
t_{if}	Failure time
T	Temperature
T_i	Temperature
T_o	Temperature at which austenite and ferrite of the same composition have the same free energy
T'_o	As T_o but accounting for the stored energy of ferrite
TEM	Transmission Electron Microscopy
TTT	Time-Temperature-Transformation
us	Unsaturated
V	Volts
V_b	Volume fraction of bainite
V_m	Molar volume
V^α	Volume fraction of ferrite
V^θ	Volume fraction of cementite
W_s	Widmanstätten ferrite reaction start temperature
wt.%	Concentrations in weight percent
\bar{x}	Mean concentration in bulk alloy
x_z	Mole fraction of element z
x_s	Thickness of slice in finite difference method
x_{T_o}	Carbon concentration in austenite at end of bainite reaction
x'	Dimensionless distance in the finite difference method
x_α	Concentration in ferrite

x_α	Half-thickness of ferrite in diffusion couple
x_θ	Thickness of cementite in diffusion couple
$x^{\gamma\alpha}$	Concentration (of carbon) in austenite in equilibrium with ferrite
$x^{\alpha\gamma}$	Concentration (of carbon) in ferrite in equilibrium with austenite
y_z	Concentration of element z
α	Ferrite
α_1	One-dimensional parabolic thickening rate constant
α'	Martensite
α_{1b}	Lower bainite
α_{ub}	Upper bainite
α_w	Widmanstätten ferrite
γ	Austenite
γ	Interfacial free energy per unit area
γ_{en}	Enriched austenite
Γ	Activity coefficient
δ	Dilational component of a shape deformation strain
ΔT	Metal-to-steam temperature differential
ϵ	Epsilon carbide
ζ	Volume fraction of allotriomorphic ferrite
θ	Bragg angle
θ	Cementite
λ	Wavelength
λ	Absolute activity
λ_o	Absolute activity of pure substance
μ	Shear modulus
σ_i	Stress
σ_{ref}	Reference stress
ϕ	Equilibrium volume fraction of ferrite

CHAPTER 1

INTRODUCTION TO REMANENT LIFE PREDICTION

This chapter provides a general introduction to my research and contains a review of remanent life prediction procedures.

CHAPTER 1

INTRODUCTION TO REMANENT LIFE PREDICTION

1.1 Introduction

High temperature power and process plant components are designed to codes which define a conservative useful life. Therefore, it could be supposed that the plant will give satisfactory service up to, but not much beyond the design life. However, experience has shown that many power plant can operate safely for times significantly longer than their design lives. Therefore two distinct parts of service can be defined:

- (a) the original design life, and
- (b) the safe economic life (which is outside the influence of the design codes but may be a significant fraction of the total service life).

Materials operating at high temperatures under creep conditions have a finite operating life and so consideration must be given to a 'beyond design' end-of-life criterion.

The assessment of the remanent creep life [†] in carbon and low-alloy steel components operating at elevated temperatures has, in recent years, received increased attention from power generation authorities, petrochemical companies and government inspection and certification agencies throughout the world.

In England and Wales there are at least 54,000 MW of electricity generating capacity, including 12 power stations which between them contain a total of 41 highly efficient 500 MW coal fired units. These stations have comparatively low operating costs and are therefore used for every day (base-load) generation. However, these stations were built in the 1960s and 1970s, individual units having now reached total operating times in the range 90,000–120,000 hours. It has been established that it is economically desirable and technically possible to extend the lives of these stations to periods in excess of 250,000 hours.

1.1.1 Replacement strategy

In order to implement this policy, the criteria which determine whether or not a component should be replaced need to be considered. Two possible options have been investigated:

- (a) After 150,000 hours service to replace all major components which can be shown to survive 150,000 hours, but which cannot be guaranteed to survive beyond 250,000 hours, and

[†] The remanent creep life is the service time remaining for a partially creep damaged component before creep-induced failure occurs, and relates to components operating under high temperature conditions where creep is the main mode of failure.

- (b) to replace each major component only when remanent life assessment techniques indicate that this is necessary.

The first criterion is certainly the simplest and would ease the problem of planning for refurbishment programmes since several years notification of the need for replacement could be given. This would, however, in many cases lead to the premature or completely unnecessary replacement of components which would not have been established to have an 'end-of-life' condition in terms of degradation and damage. It may also increase the periods during which the plant is not operational which would result in substantial cost penalties. The second possibility is the one adopted by the generating companies as it avoids these disadvantages and is financially beneficial. Components are not generally replaced prior to need and hence refurbishment work can be spread over the complete operating life of the units, thereby reducing the time for which the plant is not operational. However, for this strategy to be implemented it is clearly necessary to develop an accurate and reliable procedure for remanent creep life assessment, a procedure based on sound physical principles so that extrapolation over long periods of time can be carried out with confidence.

1.1.2 The need for life assessment

The reasons why remanent life appraisal is necessary can be summarised as follows:

- Safety: To meet safety regulations specified by legislative bodies and the utility insurers, and therefore to preserve the safety of personnel and plant integrity.
- Operation: To avoid costly, unscheduled plant shutdowns by preventing high temperature failures.
- Strategy: To plan for component replacement and to allow time for the manufacture of replacements and therefore to allow operation of high temperature plant beyond the original design life.

1.1.3 Procedure documents

In order to develop a life assessment procedure for a particular component, it is necessary to consider the operating regimes, the type of component and the materials from which it is manufactured, the potential failure mechanisms and the available failure statistics, and also the difficulties in repairing the component and the cost of any shutdowns. Formal procedure documents have been or are being written to assess the safe and economic life of each component and the need for replacement. The procedures are based on a system of regular monitoring of operating parameters, systematic inspection, the procurement of samples for post-service testing and the calculation of remaining life by using relevant materials data in an established

relationship describing the degradation and life-limiting failure mechanisms. An important aspect of these formal procedure documents is that they link the ‘science’ of life prediction established within the laboratory with the ‘engineering requirements’ associated with continued operation, the need for repair, or in some cases replacement, and the requirements for non-destructive testing (NDT) inspection.

1.1.4 Power plant

In a power station heat is produced by burning coal or oil (or from a nuclear pile) within a furnace. Water is supplied to the boiler from a common feed main by feed pumps. The feedwater first passes through the economiser and into the steam drum. (The economiser is situated next to the tubes containing the exit steam from the furnace walls and so it is used to preheat the feedwater before it enters the boiler.) The water is then drawn from the steam drum into the tubes lining the furnace walls, subsequently returning to the drum as a mixture of water and steam.

Water and steam are separated within the steam drum, the water being returned to the furnace wall tubes by boiler circulating pumps. Hot gases from the combustion chamber flow across the boiler horizontally to heat the superheaters, reheaters and economiser elements, before flowing to the gas airheater (to heat the incoming air to the combustion chamber). Steam from the drum then passes through the superheater pendants to the high pressure (HP) cylinder where it is directed through nozzles on to the turbine blades to rotate the turbine. Exhaust steam from the HP cylinder returns to the boiler to pass through the reheater pendants so that its temperature is restored. The reheated steam is then passed to the intermediate pressure (IP) cylinder, the exhaust from which is then passed directly into the low pressure (LP) cylinder. The HP, IP and LP cylinders are coupled together to drive the rotor of the generator. The route for water and steam circulation is illustrated schematically in Figure 1.1.

A diagram of a power station boiler and the associated steam plant (Littlebrook Power Station Guide, National Power Technical Publications) is given in Figure 1.2.

Consideration must be given to the types of component and materials likely to require accurate life prediction. In general, these will depend on plant design and operational practice. However, other criteria include the severity of the operating regime, known failure statistics, the difficulty of repair and the cost of associated outages, the cause of failure and the potential benefits to be gained by developing an accurate life predictive capability.

On the first of these criteria it is evident that boiler components offer a more pressing need than turbine components. This is because turbine components, although operating under extremely onerous conditions, nevertheless generally operate within the design parameters for

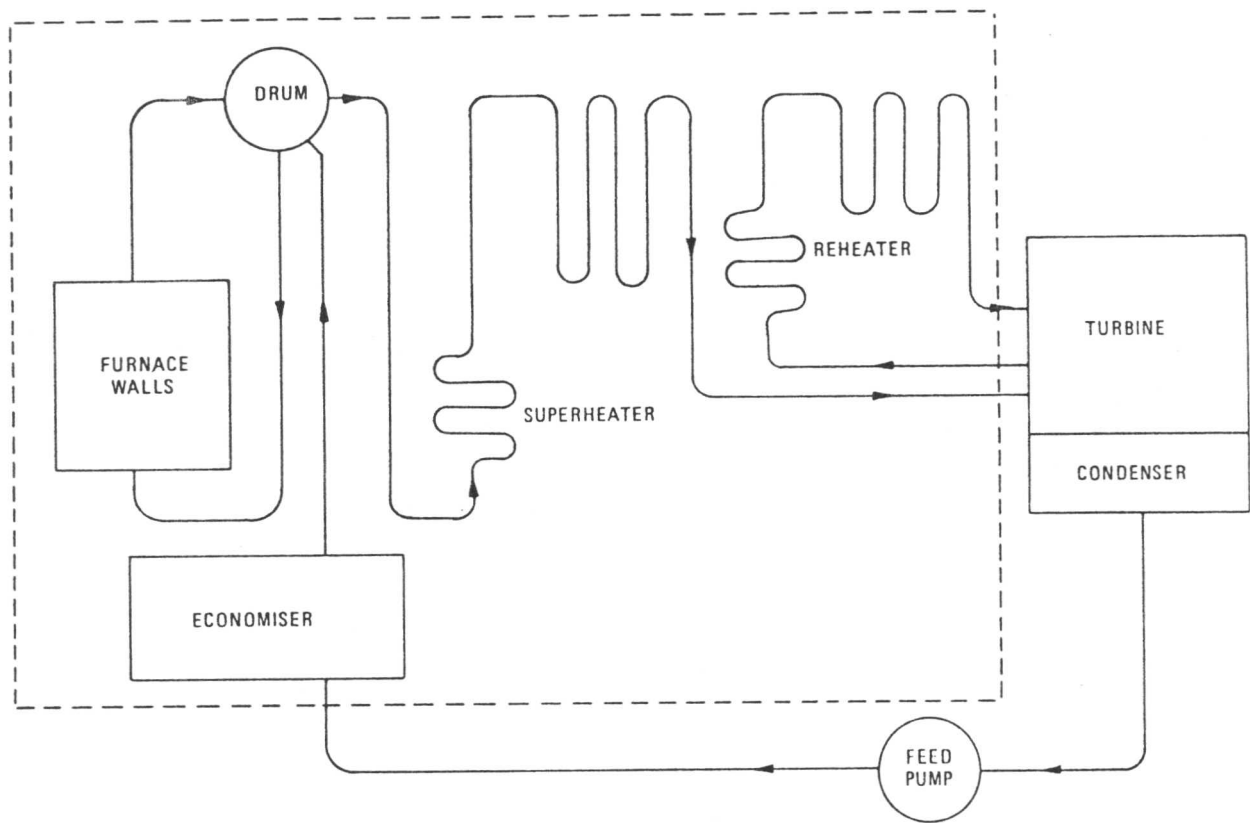


Figure 1.1: Water and steam circulation in power plant (Davison and Yeldham, 1975).

temperature, pressure and cyclic loading. Boiler components such as tubing and steam headers, however, frequently operate outside the parameters used in their design, particularly with respect to temperature and corrosive environment.

The main components which are critical are steam headers, superheater and reheater tubing in boilers, turbine valve chests, rotors and casings, main steam and reheat pipework, generator rotors and bolts used for high temperature applications. A summary of the components for which it would be possible to draw up a procedural document and their typical life limiting factor is shown in Table 1.1. The typical areas of attention for plant life extension on coal-fired power stations are illustrated in Figure 1.3.

Table 1.1: Typical life limiting factors for power station components.

Component	Typical Life Limiting Factor
<i>Boilers</i>	
Headers–superheater, reheater	Creep, thermal fatigue
Tubes–furnace wall	Fireside corrosion
Superheater, reheater	Creep, fireside corrosion
<i>Pipework</i>	
HP and RH pipework	Weld cracking, creep
Boiler and turbine valves	Weld cracking, creep, bolt failures
	Thermal fatigue
<i>Turbines and generators</i>	
Turbine valve chests	Thermal fatigue, creep, bolt failures
Turbine HP and IP casing	Thermal fatigue, creep
Turbine HP and IP rotors	Creep, fatigue
High temperature bolting	Creep, stress erosion, thermal fatigue
Generator rotors	Fatigue

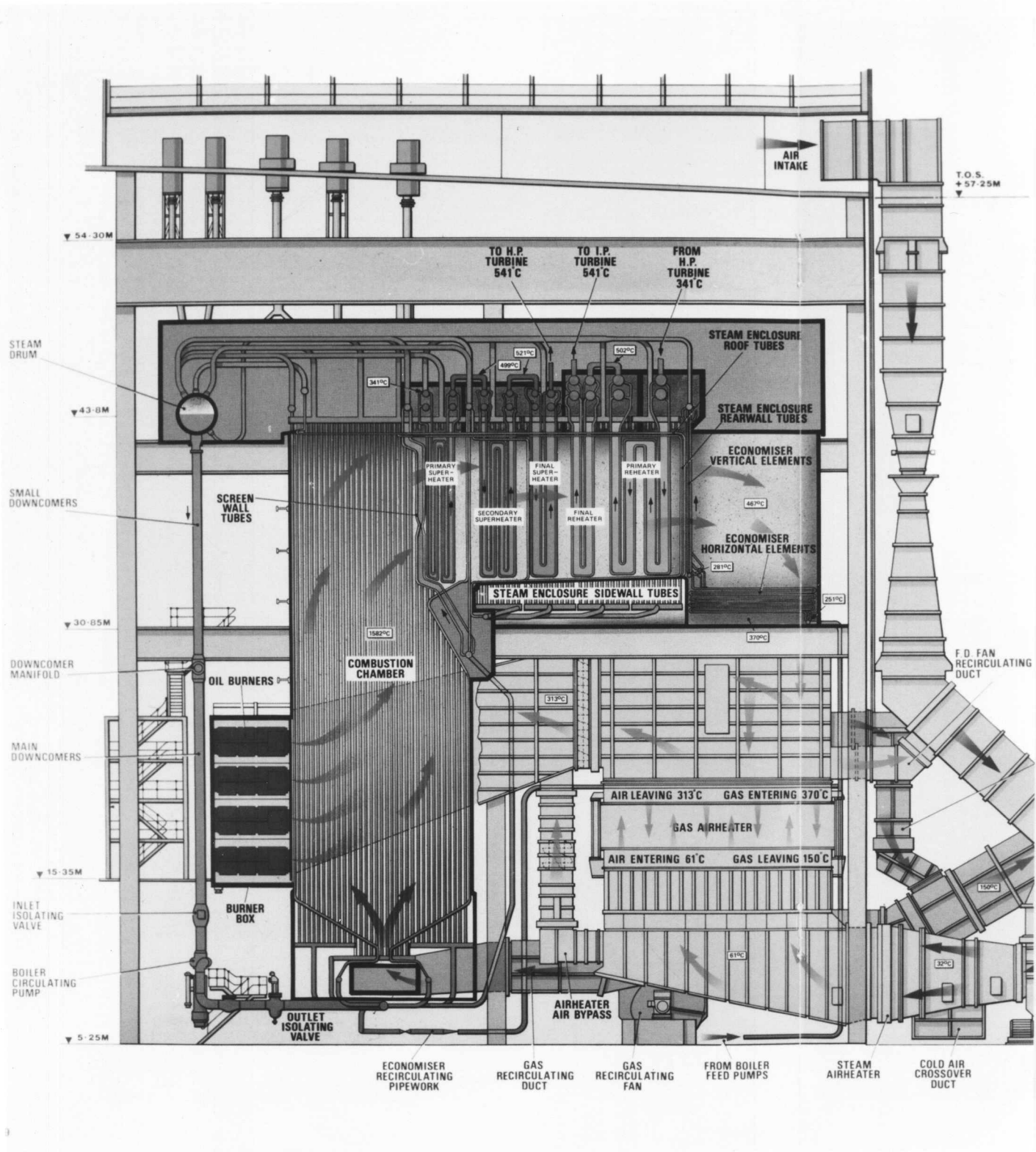


Figure 1.2

typical areas of attention for plant life extension on coal

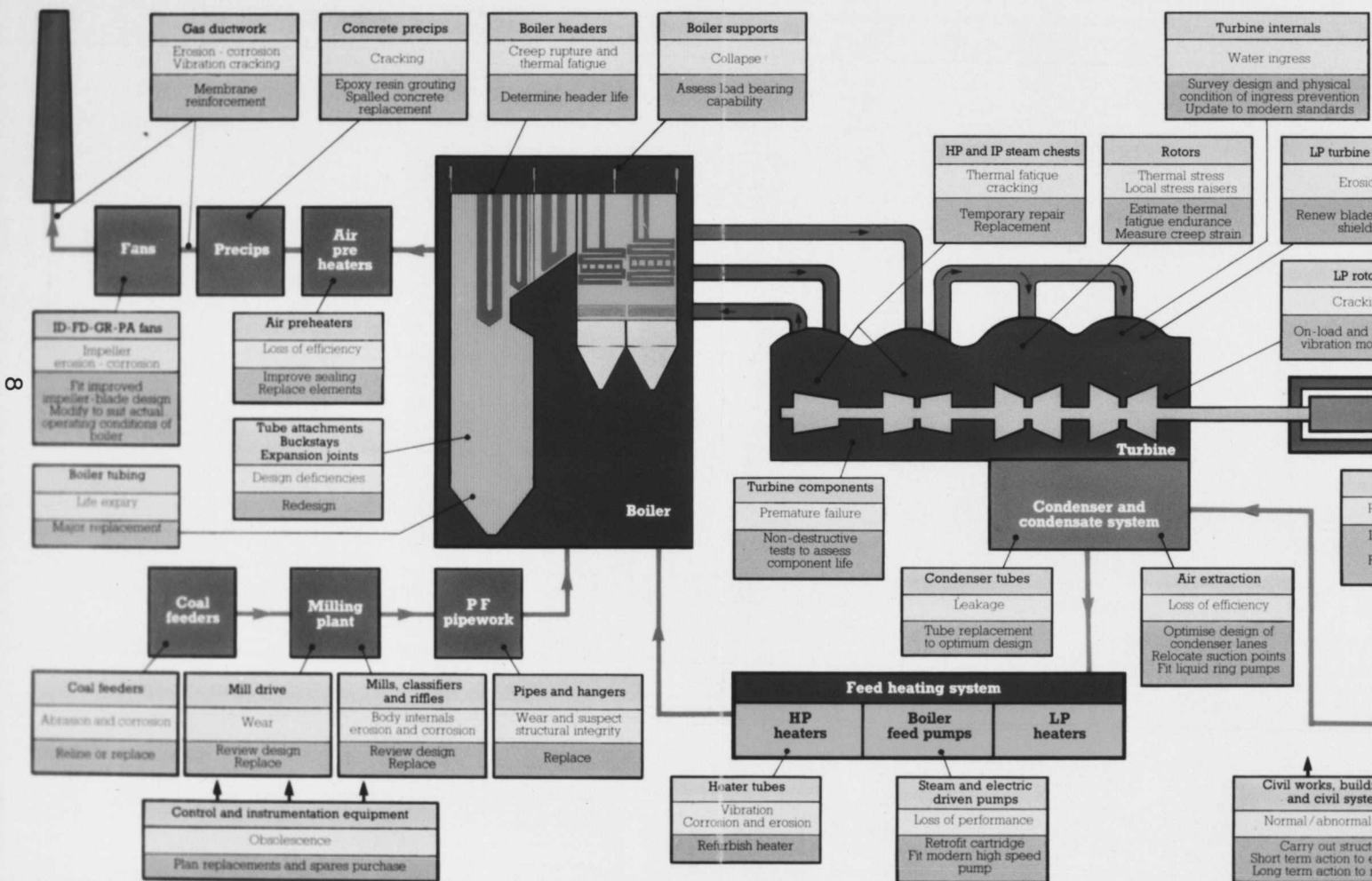


Figure 1.3

1.2 Methods of remanent life prediction

The useful life of power plant components can be limited by various damage mechanisms including creep, fatigue, wear and corrosion. This work focusses on the prediction of remanent life by estimation of the thermal history of low alloy ferritic and bainitic steels, $\frac{1}{2}\text{Cr}\frac{1}{2}\text{Mo}\frac{1}{4}\text{V}$ and $2\frac{1}{4}\text{Cr1Mo}$, and martensitic 12Cr1Mo1V steels, which ultimately fail under creep conditions. Creep strength arises from the addition of substitutional alloying elements, (Mo, Cr, V and Mn), to the base steel composition. There are two contributions to the creep strength. The first arises from solid solution strengthening, the added alloying elements making cross slip and dislocation climb more difficult (Argent *et al.*, 1970) by distorting the solvent lattice. Molybdenum, the largest of the substitutional alloying elements, is the most effective addition in solid solution strengthening. The second contribution to creep strength, which is particularly important in the later stages of service, is the ability of the alloying elements to form a stable dispersion of precipitates which hinder dislocation motion and prevent the migration of boundaries and sub-boundaries during creep. Creep resistance is attenuated as the more stable carbides coarsen, spheroidise and agglomerate (Sellars, 1974).

Creep damage itself can be said to occur by two different methods; the development of intergranular cavities leading to cracking, and secondly an acceleration of the creep rate directly related to microstructural changes such as the coarsening of initially creep resistant precipitate dispersions, changes in precipitate identity, increasing grain size or a change in the number density of dislocations. These two processes occur simultaneously and will depend on the initial heat treatment conditions, the applied stress and the temperature.

For high temperature plant investigations a wide variety of complementary techniques to estimate the remaining life of components are employed, several of which are being used under service conditions. These have been reviewed extensively (Cane and Townsend, 1984; Wilson, 1986; Cane, 1986; Cane and Williams, 1987) and the various techniques are summarised below:

- (1) Post-exposure creep testing of components.
- (2) Metallography to assess the extent of microstructural degradation, with particular emphasis on cavity nucleation and cracking.
- (3) Examination of plant operational records, e.g. temperature and pressure records taken daily, the use of standard materials data and the life fraction rule.
- (4) Estimation of the average thermal history of a component by detailed investigation of carbide composition, identity and size within the microstructure.

1.2.1 Post exposure creep testing

Creep life has most commonly been estimated using parametric relationships to extrapolate short term creep data obtained at elevated stresses and/or temperatures. Post-service evaluation techniques can clearly be classed as mostly destructive methods of assessment, to the extent that a weld repair may be needed due to the volume of material required. To obtain results in a reasonable time, the tests have to be performed under accelerated conditions by increasing stress or temperature or both. If tests are performed by accelerating the temperature at constant stress care must be taken to avoid excessive oxidation of the test piece. Tests may have to be performed under a non-oxidising environment, either in a vacuum or argon. Both creep and rupture testing have been well documented (Hart, 1976; Woodford, 1974) therefore only a brief example of the use of creep testing is presented here.

Samples were cut from a $\frac{1}{2}\text{Cr}\frac{1}{2}\text{Mo}\frac{1}{4}\text{V}$ reheater drum after 70,000 hours service and machined into specimens for creep testing (Cane and Townsend, 1984). The drum was known to be overheating and thermocouple measurements revealed a maximum operating temperature of 592°C. Creep rupture tests were performed at the operational stress, 43 MPa, and at temperatures between 640 and 680°C. The data were extrapolated linearly at a slope parallel to that of the mean data for unused material to predict the remanent life at the service temperature, and an estimation of the life which would be gained by a reduction in the operating temperature. This is illustrated in Figure 1.4. It should be noted that such extrapolation will not take fully into account the microstructural changes during service and therefore the results should be treated with caution.

1.2.2 Metallographic examination of damage

Increasing effort has been put into the assessment of remanent life by direct observation of the steel microstructure. It is therefore necessary to identify what features in the microstructure indicate a departure from the steady strain rate and the onset of tertiary creep. If creep cavitation can be identified as a failure mechanism in a particular component, then quantification of the number density of cavities can be a useful indicator of the remanent life. Some low alloy steels are susceptible to low ductility creep failures in certain microstructural conditions, particularly the coarse grained structures which occur in weld heat affected zones. Others have low ductility in their standard condition. Eventual failure results from the nucleation, growth, and coalescence of cavities on grain boundaries (especially prior austenite grain boundaries). Cavities are often associated with the larger grain boundary alloy carbides, and oxide and sulphide particles. The cavities provide nuclei for microcrack initiation, can locally alter the

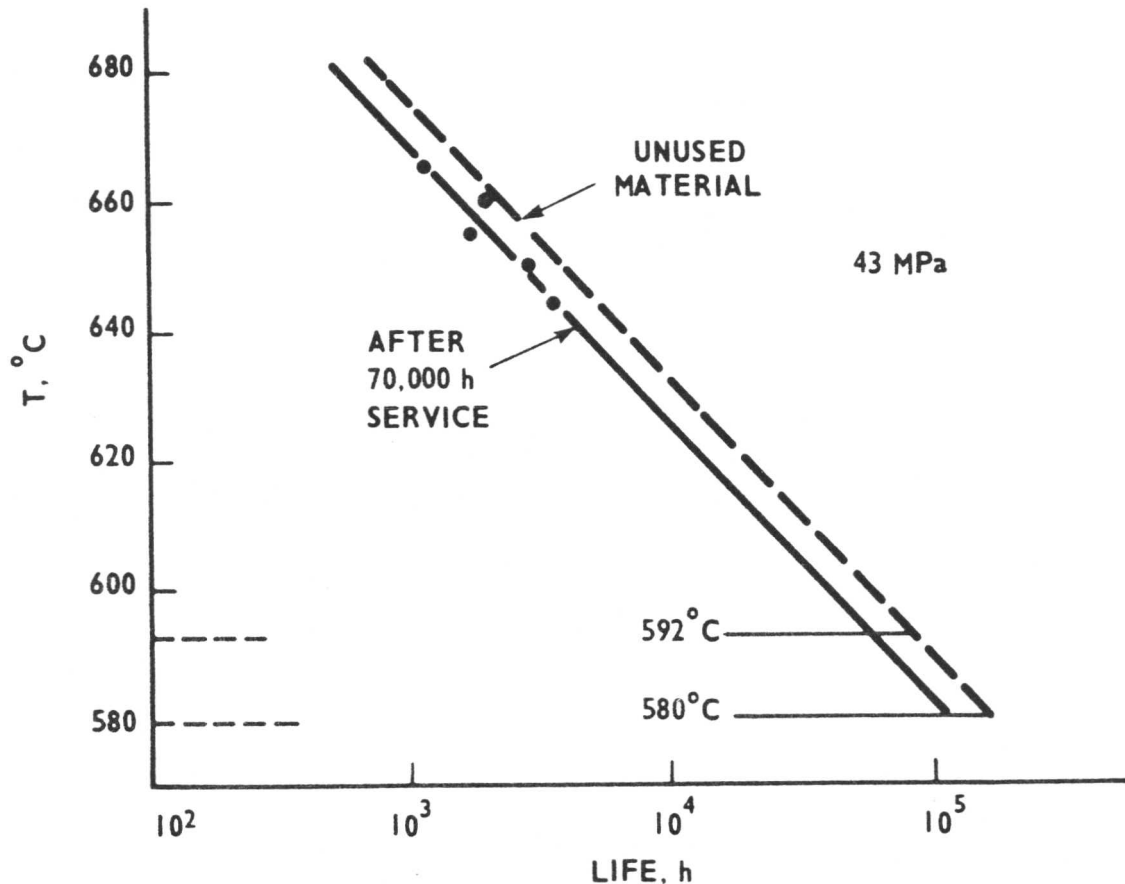


Figure 1.4: Remanent life assessment of $\frac{1}{2}\text{Cr} \frac{1}{2}\text{Mo} \frac{1}{4}\text{V}$ steel reheater drum material by iso-stress post-exposure testing (Cane and Townsend, 1984).

nature of the fracture path and may change the balance of the elements in the solid solution.

Experimental studies have been made (Shammas, 1987) in which the number fraction of cavitated grain boundaries has been measured at various stages throughout a creep test. This fraction is usually termed the 'A' parameter. Assessment of the 'A' parameter is made by taking plastic replicas from a metallographically prepared surface which is subsequently examined with an optical microscope. A sequence of micrographs illustrating the accumulation of creep damage in a $1\text{Cr} \frac{1}{2}\text{Mo}$ steel is shown in Figure 1.5. Initially isolated cavities ($A=0.102$) gradually orientate parallel to the stress axis ($A=0.204$), and then develop into microcracks ($A=0.289$). Macrocracks correspond to a value of $A \approx 0.5$ at which point the component should clearly be removed from service.

In steels of high creep ductility, from which most high temperature components are constructed, significant cavitation does not occur until late in life and is not therefore a useful indicator of remaining life. Effective use of this method of cavitation damage quantification is therefore restricted to weld heat affected zones rather than bulk material.

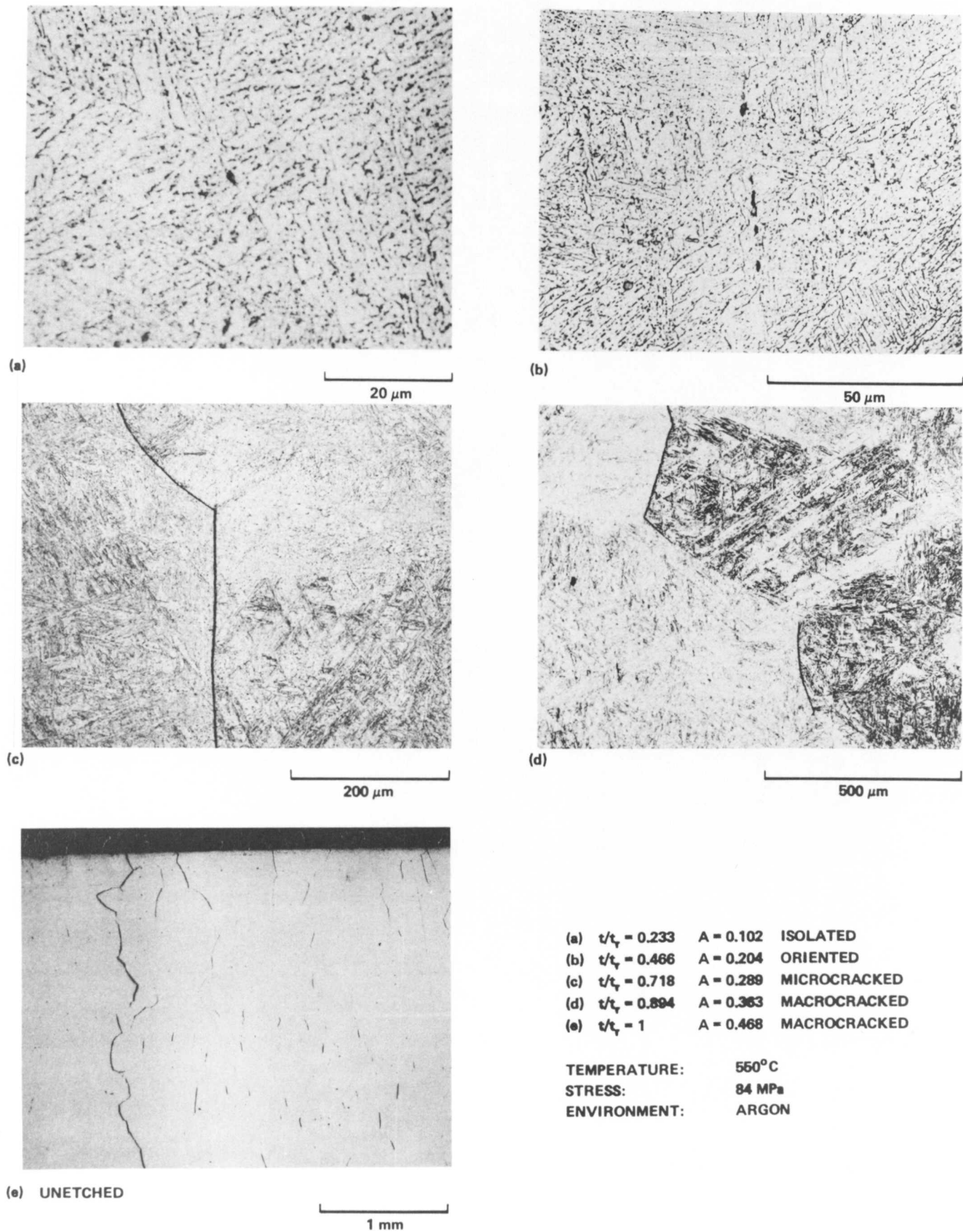


Figure 1.5: Accumulation of creep damage through life of a $1\text{Cr}\frac{1}{2}\text{Mo}$ steel specimen (Shammas, 1987).

1.2.3 Assessment based on plant operational records

An analysis of the past operating history of a component is one of the most important steps in any remanent life assessment procedure. In practice, data taken during plant operation include pressure and temperature measurements, these being logged continuously or taken at fixed times during the day. To calculate a preliminary assessment of the exhausted creep life fraction, the life fraction rule (Robinson, 1938) is used. This states that

$$\sum_i \frac{t_i(\sigma_i, T_i)}{t_{if}(\sigma_i, T_i)} = 1 \quad (1.1)$$

where t_i is the time spent at stress σ_i and temperature T_i , and t_{if} is the failure time at stress σ_i and temperature T_i . It was proposed that for any series of stress and temperature conditions, the life fractions could be linearly summed with final failure denoted by unity. This is a very simple procedure and thus can be used as a first stage of remanent life assessments to establish components requiring further monitoring. For many years the life fraction rule has been used without much consideration of the potential errors.

The failure time, t_{if} , at a particular stress, σ_i , is taken from the International Standards Organisation (ISO) stress rupture data. For any class of material upper and lower bounds have to be placed on the rupture life due to the range of variables such as specimen size and composition variations involved in collecting ISO data. This immediately introduces pessimism into remanent life estimates because it is usually necessary to use the lower bound of the data because it is not possible to identify the actual position of the material within the band without additional creep testing and/or knowledge of virgin material properties. If archive material is no longer available it would be necessary to reheat-treat the service exposed material to recreate the starting microstructure, although it should be noted that for some materials simply repeating the original heat treatment may not restore the material to its original condition. This bandwidth is illustrated for $2\frac{1}{4}\text{Cr1Mo}$ steel at 560°C (based on the stress to give failure in 100,000 hours), the bandwidths being given as a percentage change in the applied stress, in Table 1.2.

Table 1.2: The variation in failure time as a function of the percentage change in the applied stress.

% Change in stress	-20%	-10%	-5%	0	5%	10%	20%
Failure time, hours	38 000	62 000	78 000	100 000	110 000	130 000	200 000

Another problem with the use of standard data is that often they only exist for times of approximately 80,000 hours and so extrapolation to times approaching 150,000 hours is uncertain. This is because during tests the load carrying area is reduced as the specimen extends and by oxidation. Current extrapolation procedures do not take this into account and therefore errors in life estimates occur. The life fraction rule is often used in conjunction with post-exposure testing to determine the failure times at specific stresses, rather than using standard materials data.

The earliest difficulty to be recognised was that when smaller specimens were machined from failed uniaxial creep samples, they had a finite life on retesting, inferring that the life fraction rule is conservative. Alternatively, such results could be interpreted to mean that creep damage is not distributed uniformly within a specimen, being primarily at the point of failure, and thus sampling errors are always present.

To be able to apply the life fraction rule it is necessary to know the representative rupture stress for the component concerned. The key point is that the majority of creep-rupture data are generated under simple uniaxial conditions, whereas in reality components are subject to much more complex loading. It is necessary, therefore, to be able to define a representative stress which, when applied to uniaxial data, adequately characterises the component deformation and failure. The idea of using a reference stress, σ_{ref} , has received much attention in recent years. σ_{ref} for a particular component is defined as that stress which would fail a simple tensile specimen at the same temperature in the same time as the component. When the temperature also varies with time, a reference temperature can be similarly defined at which the comparative specimen test should be performed. Determination of reference stresses and temperatures for irregularly shaped components can now be accomplished by theoretical and experimental work involving computer techniques such as finite element stress analysis together with model and full size component testing. A typical finite element mesh used to calculate the reference stress for a complex pipe geometry is shown in Figure 1.6.

It has been shown that operational stresses and times can be determined accurately and therefore the only unknown for input into the life fraction rule is the exact operating temperature of a particular component. The accuracy of remanent creep life estimates using the life fraction rule depends critically upon the sensitivity of the component material to variations in temperatures. Therefore, careful attention is required when establishing component metal temperatures from operating records. Depending on the direction of heat flow, the metal temperatures may be higher or lower than the steam and may vary significantly with plant operation. The importance of accurate service temperature assessments was emphasized by Cane

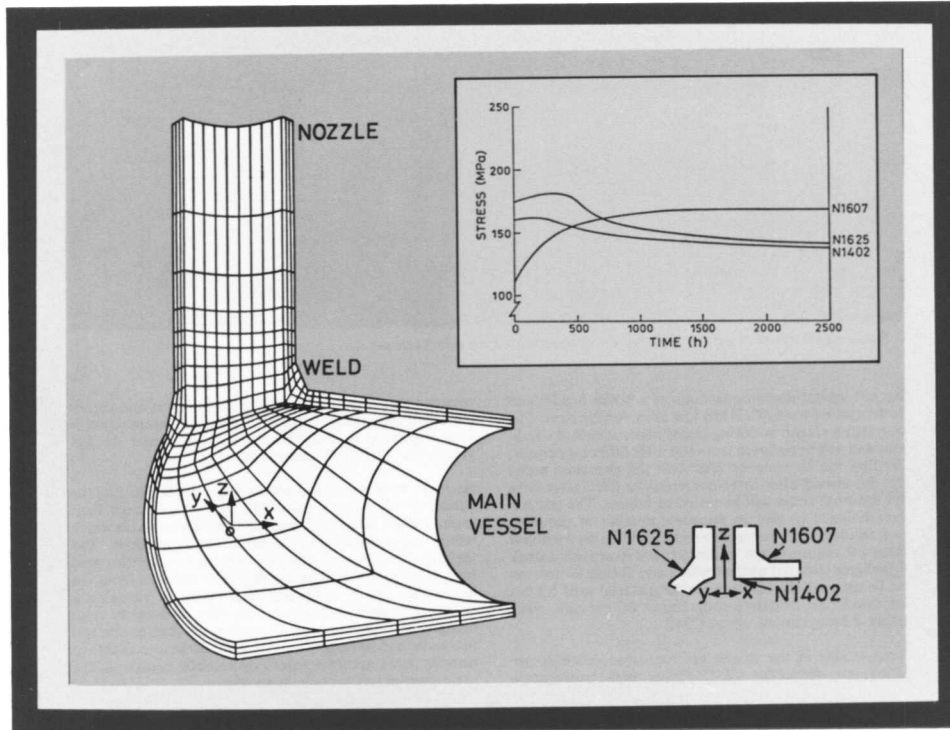


Figure 1.6: A typical finite element mesh used to calculate the reference stress for a complex pipe geometry (Gooch, 1988). The inset shows typical results of a finite element analysis plotted as stress as a function of time at certain critical locations.

and Townsend (1984). They considered in particular the measurement of the temperature of steam headers, and found that errors in the measurement of operating temperature and of the accumulated time-temperature behaviour arose from:

- (1) instrumentation errors,
- (2) spatial variations in the temperature along the header,
- (3) and irregular temperature fluctuations with time as a result of changes in the mode of boiler operation.

The inlet stub tube variation around an 18 tube element on a 500 MW reheater drum is shown in Figure 1.7. It is clear that determination of the metal temperature by measurement of the steam temperature can lead to large errors. For conservatism in the life estimate calculation it is necessary to assume a large ΔT for the metal-to-steam temperature differential, and consequently considerable pessimism is observed in the creep life estimate. The uncertainty may be as high as $\pm 5^\circ\text{C}$.

The effect of temperature on rupture life is illustrated in Table 1.3. This is based on the

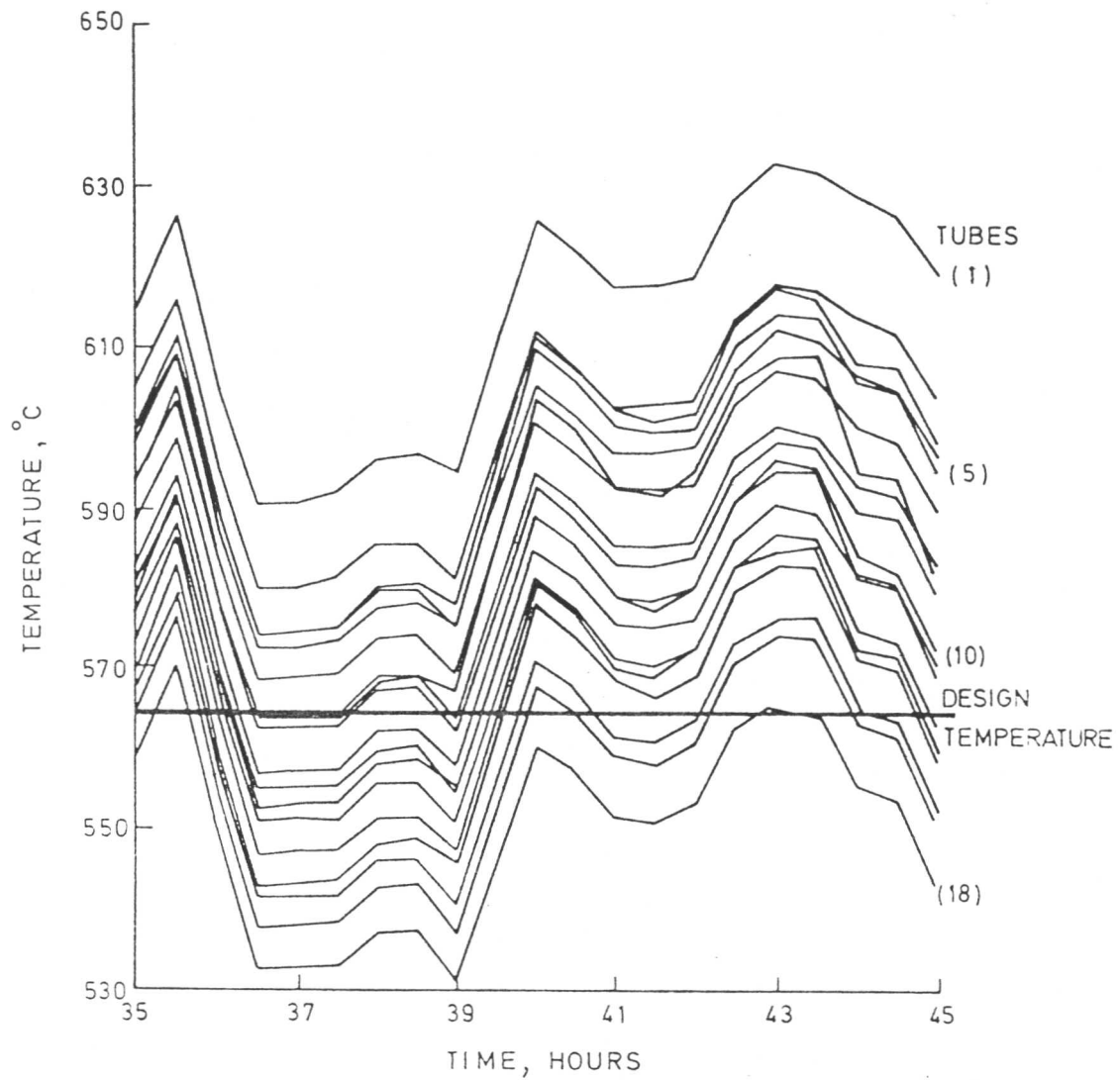


Figure 1.7: Inlet stub tube temperature variation around an eighteen tube element on a 500 MW reheater drum (Cane and Townsend, 1984).

mean stress to give failure in $2\frac{1}{4}\text{Cr1Mo}$ at 560°C in 10^5 hours, and indicates that an error in temperature evaluation of 10°C can lead to variations in the life estimate by a factor of 2.

Table 1.3: The effect of temperature on rupture life.

Temperature / $^{\circ}\text{C}$	540	550	560	570	580
Failure time /Hours	2.5×10^5	1.7×10^5	1×10^5	56 000	32 000

1.2.4 Estimation of the average thermal history of a component

If it is assumed that fluctuations in temperature and time will produce the same effect as an average temperature over the same total time then it is possible to obtain a better estimate of the remanent creep life by establishing an effective temperature experienced by a component. Detailed microstructural studies can therefore be used to independently support and improve upon the service temperature estimates based on operating records.

The first attempts to relate microstructural changes to the creep life of components were made by Toft and Marsden (1961). They focussed on the spheroidization of carbides in pearlitic and ferritic microstructures of $1\text{Cr}\frac{1}{2}\text{Mo}$ steels. Tubes from a number of power stations which had experienced service for up to 100,000 hours and at temperatures in the range 454–518°C were examined optically. There were a number of difficulties in this work, primarily because all the materials had slightly different base compositions and because the metal temperature histories were not known. Stress rupture tests were carried out at 565 and 510°C for up to 10,000 hours. It was found that there was a clear trend for a decrease in the rupture strength with increasing carbide spheroidization and precipitation of carbides other than cementite. The strength properties were found to be the poorest when the carbide M_6C was present in the microstructure. The detailed microstructural results of this work are presented in Table 1.4.

Toft and Marsden also made the interesting observation that during a large part of the life of the pipes examined there appeared to have been very little creep. Creep only began to occur at a significant rate when the strength properties had decreased as a result of prolonged heating or the wall thickness had been reduced by an appreciable amount. In order to relate the results of the microstructural investigations with operational parameters, the temperature measurement available nearest the pipe removed from service was combined with the operating time of the plant using a conventional time–temperature parameter of the form $t(C + \log T)$, where t is the service time, T the temperature and C a constant, and plotted against the degree of spheroidization observed. A reasonable correlation was found, and it was proposed that an estimate of service temperature could be obtained by classifying the microstructure into one of a number of distinct bands with respect to the degree of spheroidization. This could then be related to the time–temperature parameter, from which the service temperature could be determined. This method is, however, limited by the resolution of light microscopes and the large extrapolation involved.

A number of other attempts have been made to relate precipitate spacing with creep life (Carruthers and Day, 1968; Hale, 1975; Battaini *et al.*, 1990) but these have been met with limited success due to difficulties in characterising complex precipitate distributions. A potentially

Table 1.4: Stages in carbide spheroidization and precipitation in $1\text{Cr}\frac{1}{2}\text{Mo}$ steel superheater tubes (Toft and Marsden, 1961).

Stage	Spheroidization	Precipitation
A	Typical of the structure of a new tube consisting of ferrite and a very fine pearlite.	The carbide present in the pearlite areas is Fe_3C . Evidence of Mo_2C particles beginning to precipitate in the ferrite grains (up to $0.1\ \mu\text{m}$).
B	The first stages of carbide spheroidization usually coinciding with the appearance of small particles of carbides at the grain boundaries.	Small particles of both Cr_7C_3 and Mo_2C (up to $0.2\ \mu\text{m}$) present in the ferrite, (particles of Cr_7C_3 probably also present on the grain boundaries but not yet identified).
C	An intermediate stage of spheroidization, showing more distinct signs of carbide spheroidization in the pearlite areas, but some carbide plates still evident. Increased carbide precipitation within the ferrite grains and at the grain boundaries.	Medium sized particles of Cr_7C_3 and Mo_2C (up to $0.5\ \mu\text{m}$) present in the ferrite.
D	Spheroidization of the carbides is virtually complete, but they are still grouped in the original pearlitic pattern.	Some cementite particles have transformed to Cr_7C_3 . The particles of Mo_2C and Cr_7C_3 in the ferrite have further increased in size (Mo_2C up to $1.5\ \mu\text{m}$).
E	Spheroidization is complete and the carbides are dispersed, leaving little trace of the original pearlite areas.	The pearlite areas have dispersed and the Fe_3C particles have completely transformed to Cr_7C_3 and Mo_2C particles. The Mo_2C and Cr_7C_3 precipitates are large in size (Mo_2C up to $1.5\ \mu\text{m}$).
F	There is a marked increase in the size of some carbide particles, partly due to coalescence.	The pearlite areas are completely dispersed. The amount of Mo_2C present throughout the structure has decreased to form areas of the complex metal carbide M_6C . This metal carbide is Mo rich, but contains both Cr and Fe. Some new grains of ferrite may have been formed.

more powerful method is to investigate the microstructure of the steel in detail with particular reference to carbide composition and type. Carbide composition measurements can now be made routinely using energy dispersive X-ray analysis techniques facilities on transmission electron microscopes. Titchmarsh (1978) demonstrated this method by studying alloy carbides in $2\frac{1}{4}\text{Cr}1\text{Mo}$ steel. He found that each carbide type had a distinct composition with respect to the substitutional alloying elements in the steel. Carbides can be extracted from the bulk material using carbon replication techniques (Smith and Nutting, 1956) which ensures there is no interference from the matrix in measuring the composition of each individual carbide.

Carruthers and Collins (1981) monitored changes in the composition of pearlitic cementite in $\frac{1}{2}\text{Cr}\frac{1}{2}\text{Mo}\frac{1}{4}\text{V}$ and $1\text{Cr}\frac{1}{2}\text{Mo}$ steels using scanning transmission electron microscopy (STEM) and energy-dispersive X-ray analysis as a function of service conditions. They found that the concentration of the substitutional alloying elements Cr, Mo and Mn in the cementite gradually increased with service time at the expense of the Fe content. They therefore proposed that changes in substitutional solute concentration of carbides with time was a viable method for the estimation of the effective temperature experienced by a component. Afrouz *et al.* (1983) then investigated changes in bainitic cementite composition in reheat-treated and service-exposed material in a $1\text{Cr}\frac{1}{2}\text{Mo}$ steel. Afrouz *et al.* confirmed the results of Carruthers and Collins, observing an approximately linear relationship between the changes in concentration of the substitutional solute elements in the cementite and $\text{time}^{\frac{1}{3}}$, which they justified on the basis of diffusion controlled coarsening theory (Christian, 1975). Further work by Du (1986) has provided a large amount of experimental data on composition changes in pearlitic and bainitic cementite; however, no physical explanation of the composition changes was put forward.

A firm theoretical basis is needed in order to model the diffusion processes resulting in the composition changes in the cementite. Bhadeshia (1989) has developed a model to predict the rate at which the alloying elements redistribute between ferrite and cementite, subject to the thermodynamic constraints which determine the equilibrium amount of alloy in the two phases. The model uses a finite difference method to find numerical solutions to the diffusion equation. (Due to the irregular distribution and varying sizes of the cementite particles it would be very difficult, if not impossible, to obtain analytic solutions to the diffusion equation.) The model so far has highlighted the factors controlling the approach to equilibrium. In particular, particle size has been found to have a strong influence on the rate at which cementite composition changes. Reasonable agreement has been found with experimental data to date. However, the model contains a number of simplifications. It assumes that diffusion occurs only in one dimension, that particle size does not change during enrichment, that the diffusion coefficient of the substitutional alloying elements in ferrite is the same as in cementite, that local equilibrium is maintained at the interface during diffusion and interaction between the diffusing elements is neglected. The aim of this work is to test the assumptions of this model, and develop it further to overcome some of its limitations. Experiments are performed on a variety of steels using many different techniques to verify and assist with the development of the model.

1.3 Possible future indicators of thermal history

It has recently been suggested that small amounts of additional material, 'plugs', could be attached to power plant in order to estimate the average thermal history of critical components. These plugs have specific advantages over thermocouples in that they are fixed directly to the metal, eliminating any metal-steam temperature differentials, and that they can be manufactured into convenient shapes such as bolts or clips for ease of attachment to the components being assessed. Peak temperature indicators have also been tested. These consist of a material of a suitable known melting point which melt when the temperature exceeds the working limits. Peak temperature indicators are not suited to situations where there are periodic small excursions above and below the service temperature in power plant.

The first commercial 'plug' was developed by Shell Research Ltd. and made use of hardness changes in metals and alloys as a function of high temperature heat treatment. However, the questionable reliability of portable hardness testers has led to the introduction of a new device. The newest indicator of thermal history developed by Lai *et al.* (1990), subject to Patent Application 8918774.4, is made from a duplex stainless steel which contains austenite and ferrite. The device relies on the fact that austenite gradually decomposes to ferrite, carbides and intermetallics on annealing at high temperatures. A simple on-site measurement of the magnetic permeability of the 'plug' can be used to determine its ferrite content, ferrite being ferromagnetic and austenite not. The measured ferrite content can then be used, in conjunction with the initial ferrite content and the operating time, to determine the average thermal history of the material to which the 'plug' is attached. The effect of thermal excursions about the operating temperature on the transformation characteristics of the duplex stainless steel are currently being investigated.

1.4 Conclusions

Over recent years much work has been done within the power generation industry on developing a reliable and accurate methodology for estimating the remaining creep life of high temperature components. It has been shown that techniques based on the measurement of operational parameters and the use of the life fraction rule give poor accuracy and are generally pessimistic due to conservatism in assessing the input data. Much greater accuracy can be achieved by direct access to the component for post and during service measurements and sampling.

Continuing research and development is needed to improve remanent life estimates, particularly on more sensitive post service inspection methods. The focus of this work therefore not

to study the factors conferring creep resistance on power plant steels, but to model theoretically and verify experimentally changes in carbide composition, size and identity, so that the steel microstructure can be used as a **time-temperature recorder**. A more accurate assessment of the thermal history experienced by a component can then be used, together with stress measurements, to predict the remaining life of a particular component ensuring the safe and economic extension of high temperature plant service beyond present, generally conservative, design limits.

CHAPTER 2

PHYSICAL METALLURGY OF ALLOYED STEELS

This chapter contains a review of the physical metallurgy of alloyed steels. This is important in that changes occurring in carbide composition, identity, size and shape are put into the context of the different matrix microstructures in which they occur.

CHAPTER 2

PHYSICAL METALLURGY OF ALLOYED STEELS

2.1 Introduction

When the high temperature face-centred cubic (f.c.c.) phase, austenite, in steel decomposes to the less dense body-centred cubic (b.c.c.) phase, ferrite, a number of different microstructures and morphologies can form which depend on the cooling rate, the presence of alloying elements, and the conditions and availability of lower energy nucleation sites for heterogeneous nucleation.

2.1.1 The distribution of alloying elements in steels

In steels in which the austenite transforms to ferrite and carbides on slow cooling, the role of the alloying elements can be split into three categories. Firstly, there are elements which are normally found mostly in the ferrite phase such as Ni, P and Si, their solubility in cementite or in alloy carbides being quite low. Secondly, there are elements which can both form stable carbides and can be found in solid solution within the ferrite. Typical elements which exhibit this type of behaviour are Mn, Mo, Cr, V, W, Ti and Nb. The amount of each needed in its carbide depends on the carbon content of the steel; however, they are usually present in excess of this amount, with the remainder going into solid solution in ferrite. There are also some elements which primarily enter the carbide phase. Nitrogen is the main example of this behaviour, readily forming carbo-nitrides with iron and many alloying elements, and separate alloy nitride phases in the presence of titanium or aluminium, for example.

2.1.2 The effect of alloying elements and cooling rate on the γ/α transformation

The different tendencies of alloying elements to exist in ferrite or carbides result in the rate at which the decomposition of austenite occurs below A_{e_1} being sensitive to their concentrations in the steel. (A_{e_1} is the temperature of the eutectoid reaction.) Also increases in undercooling and the cooling rate from austenite limit the ability of alloying elements in iron, and the iron atoms themselves, to diffuse during the transformation to the equilibrium structure, and increases the likelihood of the formation of metastable structures.

The alloying elements are divided into two types, those in substitutional and those in interstitial sites. Substitutional elements (e.g. Cr, Mo etc.) occupy lattice sites within the iron lattice and require vacant sites in order to diffuse, whereas interstitial elements (e.g. C, N) can diffuse much more quickly, occupying and moving between interstices within the iron lattice. Diffusion of the interstitials can only be suppressed at high undercoolings. The reaction

process can be controlled by either of these diffusing species. In the case of diffusion of the substitutionals being dominant, it is found that growth occurs with partition of the element between α and γ under local equilibrium conditions. The ferrite grows at a slow rate determined by the diffusivity of the alloying element within the austenite. It is in fact more common for a reaction to be controlled by the diffusion of carbon (interstitial), in which case growth occurs with no partitioning of the alloying element. The observed growth rates, since they are controlled by the diffusivity of carbon, are relatively high. It is also possible to have a diffusionless transformation. Whether the reaction process and rate is controlled by either diffusion of interstitials or substitutionals, or is diffusionless, is determined by a combination of thermodynamic and kinetic constraints. Hence, both the cooling rate and alloy content are critical to the development of a particular microstructure.

The possible morphologies which can be produced are discussed in detail in the next section. This includes a brief discussion of the formation of allotriomorphic and idiomorphic ferrite, Widmanstätten ferrite, and more detailed discussion of the formation of bainite and martensite, because it is within these two microstructures that changes in carbide compositions are monitored.

2.1.3 Diffusional transformations—The reconstructive growth of ferrite

The f.c.c. lattice of austenite can undergo a reconstructive transformation to the b.c.c. ferrite if there is little undercooling and diffusion can occur. This can be thought of in the manner illustrated in Figure 2.1.

Diffusional ferrite in steels nucleates heterogeneously and is observed to grow in two forms, allotriomorphic and idiomorphic ferrite. The term allotriomorphic is used when the ferrite has a shape which does not reflect its crystal symmetry. Allotriomorphic ferrite nucleates at prior austenite grain boundaries and then grows preferentially along the grain boundary, where diffusivities are high, as illustrated in Figure 2.2.

Idiomorphic ferrite, however, has a shape which is related to its crystal structure. It nucleates and grows intragranularly, generally taking the form of equiaxed grains.

2.1.4 Widmanstätten ferrite

If undercooling occurs slightly below the A_{e_3} temperature for a particular alloy, the increase in free energy driving force for the reaction and the decrease in atomic mobility result in the formation of Widmanstätten ferrite. (The A_{e_3} temperature is the temperature at which austenite transforms to ferrite. For pure iron this occurs at 910°C, but transformation occurs at progressively lower temperatures as the carbon content of the steel is increased.) Diffusion

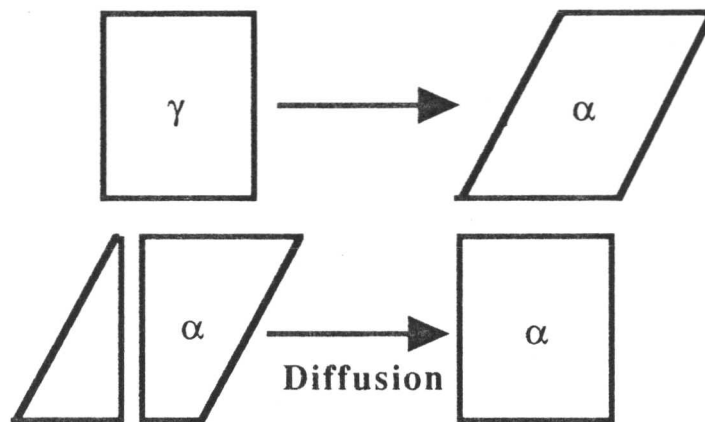


Figure 2.1: The reconstructive growth of ferrite.

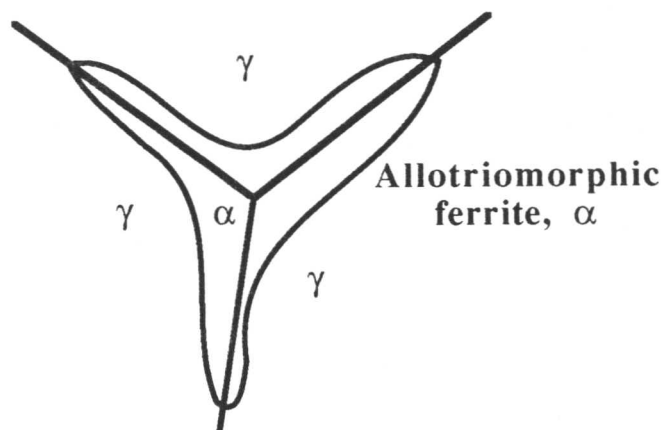


Figure 2.2: The growth of allotriomorphic ferrite along grain boundaries.

of carbon is a thermodynamic necessity and Widmanstätten ferrite forms with the equilibrium carbon concentration, therefore with carbon partitioning during the transformation. Growth is accompanied by an Invariant-Plane Strain (IPS) shape change, and there is no diffusion of substitutional solute or iron atoms. (A deformation which leaves a plane undistorted and unrotated is called an invariant-plane strain.) At these temperatures the available driving force is much less than the strain energy due to the shape change, and so to accommodate this strain energy, growth involves the simultaneous formation of two plates, appearing under an optical microscope as one, although they have different habit planes with respect to the parent austenite. The growth rate has been shown to be determined by carbon diffusion rates in the austenite at the glissile α_w/γ interface (Bhadeshia, 1981). This is illustrated in Figure 2.3.

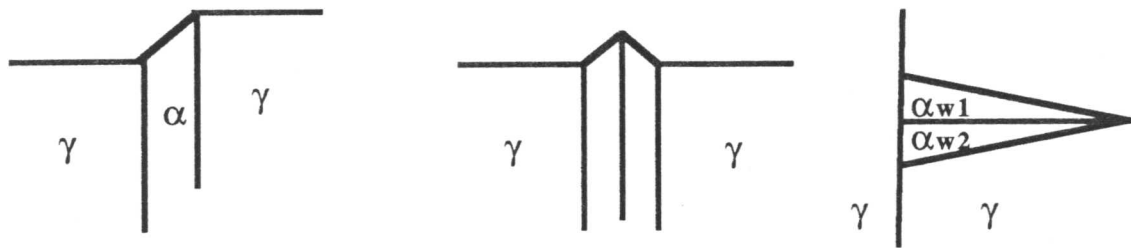


Figure 2.3: The growth of Widmanstätten ferrite planes.

2.2 Bainite

Bainite is a non-lamellar mixture of ferrite and carbides which is formed by the decomposition of austenite at a temperature above the martensite start temperature, M_s , but below the temperature at which pearlite can form. It has been shown that during the diffusionless formation of martensite there is a physical change in the shape of the parent phase, whereas a diffusional reaction requires mass transport to produce a change in structure without introducing strains (Bhadeshia, 1985). The bainite transformation, being intermediate between the diffusionless martensite and diffusional pearlite reactions has presented difficulties in interpretation in the past (Aaronson, 1986), although these are now beginning to be resolved (Christian and Edmonds, 1984; Bhadeshia, 1988; Bhadeshia and Christian, 1990).

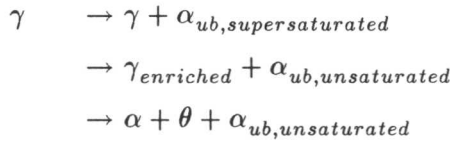
2.2.1 Morphology and carbide precipitation

Bainite consists of non-lamellar aggregates of ferrite and carbides, the ferrite being in the form of thin plates approximately $10 \mu\text{m}$ long and $0.2 \mu\text{m}$ thick, commonly referred to as sheaves (Hehemann, 1970). The growth of the sheaves is limited by hard impingement with the austenite grain or twin boundaries, and they have a relatively high dislocation density. Carbides are not an essential feature of bainite, and in fact they are completely absent in many cases. In particular, in alloys containing high concentrations of Si or Al, Fe_3C precipitation is so slow that to all intents and purposes the bainite consists only of bainitic ferrite and retained austenite.

The formation of bainitic ferrite leads to an increase in the carbon concentration of retained austenite. There are two different morphologies associated with bainite formation. Upper bainite forms at the higher temperatures within the range, the cementite precipitating from

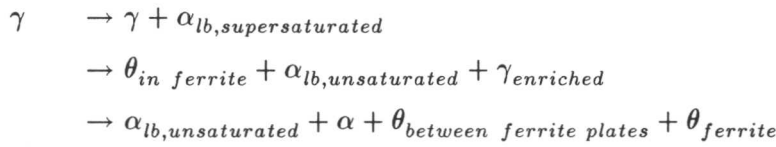
films of carbon-enriched austenite which separate the plates of bainitic ferrite. The platelets within a sheaf are all in the same orientation in space and the orientation between α_b and γ is the same as for α'/γ . In lower bainite, however, cementite also forms within the platelets of ferrite. In contrast to the cementite obtained after tempering supersaturated martensite, the carbides formed within any given lower bainitic plate usually occur in a single crystallographic orientation (Bhadeshia, 1988). There are therefore two kinds of cementite particles, those growing from carbon-enriched austenite and those precipitating from supersaturated ferrite. The precipitation of cementite generally occurs as a secondary reaction after the growth of bainitic ferrite (Hehemann, 1970). The precipitation sequences are summarised below.

1. Upper bainite

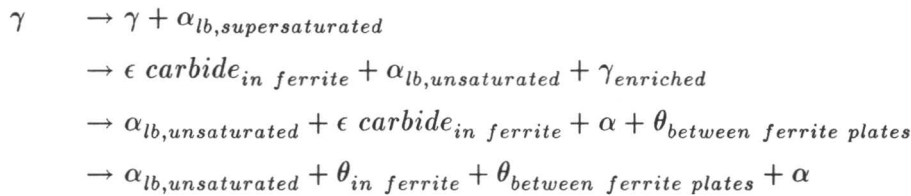


2. Lower bainite

a. High dislocation density



b. Low dislocation density



The two different morphologies of bainite are illustrated in Figure 2.4.

2.2.2 The shape change associated with the transformation

Bainite growth is also associated with an IPS shape change (Ko and Cottrell, 1952), as is the martensite reaction. The origin of this IPS shape change has been one of the prime areas of dispute in the proposed theories for the bainite reaction mechanism. It has been established (Bhadeshia and Waugh, 1982; Stark *et al.*, 1987) that iron and substitutional atoms do not diffuse during the reaction. Various observations imply that the formation of bainite involves the co-ordinated movement of the substitutional solute and iron atoms across a glissile transformation interface. These include the fact that the shape change gives rise to an elastically accommodated stored energy in the sheaves in the region of 400 J mol⁻¹. The high temperatures associated with the transformation result in the yield strength of both phases

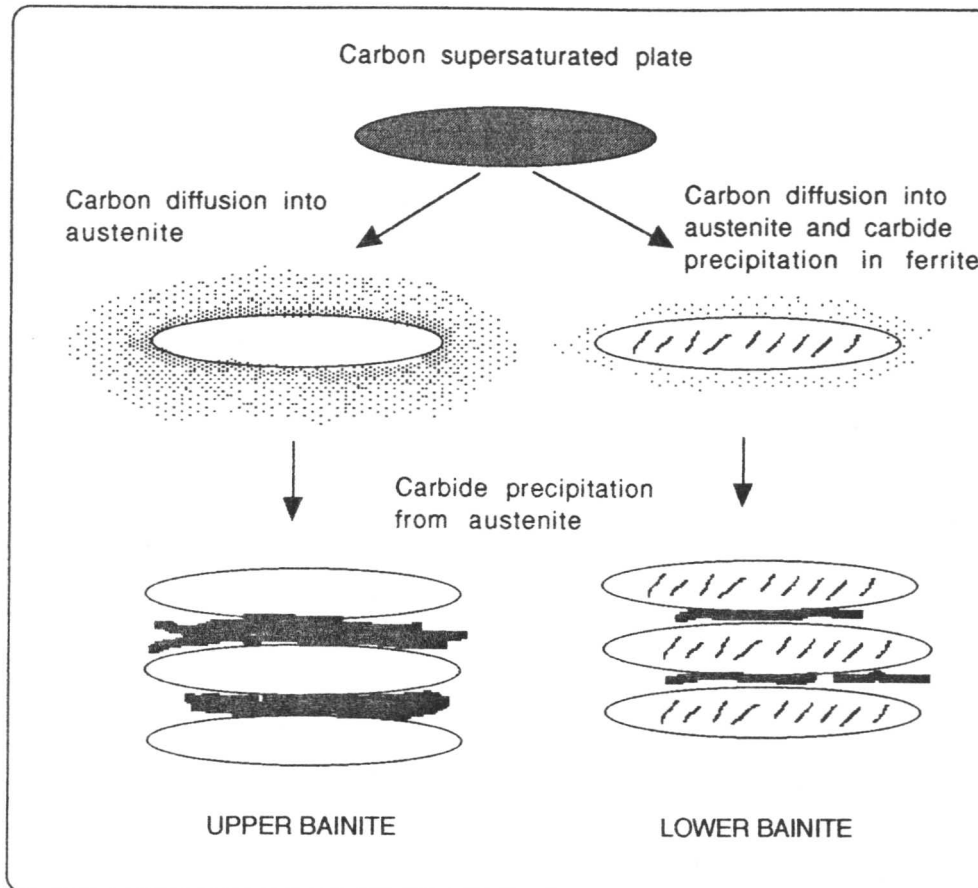


Figure 2.4: The morphologies of upper and lower bainite.

being comparatively low, and so plastic deformation can occur. The high dislocation density induced by attempts to relieve some of this strain is then responsible for hindering the advance of the transformation front, and thus limiting the size of the bainite sheaves (Bhadeshia and Edmonds, 1979). This can explain the observed limit on the growth of bainite in the absence of hard impingement. The ferrite plates always have a crystallographic orientation relationship with γ which is similar to that found between γ and α' . This type of co-ordinated movement cannot generally be sustained across randomly oriented grains, and so bainite growth is impeded by austenite grain boundaries. This is in contrast to diffusional transformations in which the product phase may readily grow across grains of the parent phase which are in different orientations.

It has been suggested (Kinsman *et al.*, 1975) that an IPS shape change can occur when a sessile semi-coherent interface is displaced by the motion of incoherent steps. However, there is no mechanism to explain how the systematic displacements implied by an IPS can

be caused by the unco-ordinated transfer of atoms across the steps. It should also be noted that allotriomorphic ferrite grows by a step mechanism, and despite it having the necessary semi-coherent interface, it does not show an IPS surface relief. The atomic correspondence implied by the shape deformation must be a property of a particle as a whole, rather than being dependent on interface orientation (Christian and Edmonds, 1984), also contradicting the above hypothesis.

2.2.3 The role of carbon in the bainite transformation

The precise role of carbon during the bainite transformation is difficult to determine (Christian and Edmonds, 1984; Bhadeshia, 1988). Bainite must always form below the T_0 temperature, at which α and γ of the same composition have the same free energy, which can be shown to make it thermodynamically possible for the transformation to be diffusionless. It is also possible to have a paraequilibrium transformation in which the substitutional lattice is configurationally frozen, but the carbon redistributes to equalise the chemical potential in all phases. An intermediate degree of partitioning is also possible. This is illustrated in Figure 2.5.

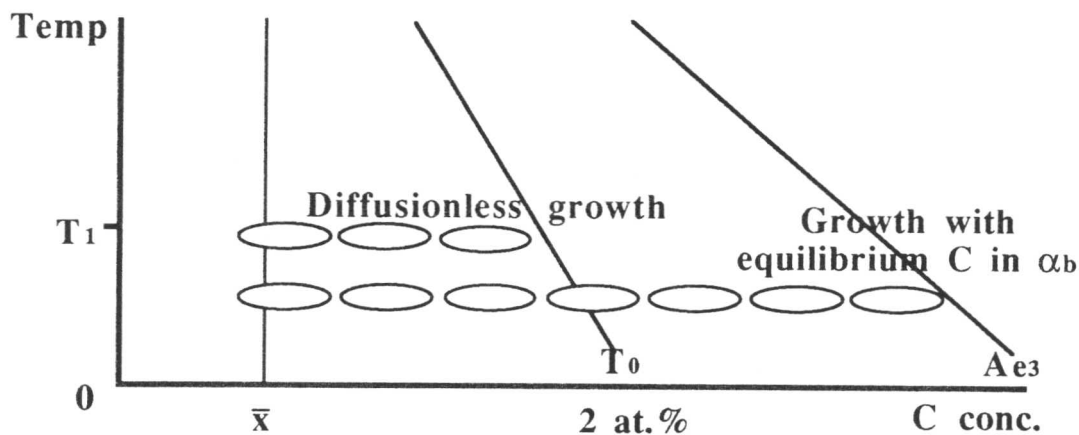


Figure 2.5: Bainite growth mechanisms.

If growth involves diffusionless transformation then any excess carbon in bainitic ferrite can partition into the retained austenite within a fraction of a second after the transformation because of the high diffusivity of interstitial carbon. It is not possible to determine directly the carbon concentration of the ferrite during its growth. The bainite reaction is found to stop before the carbon concentration of the retained austenite reaches that of the equilibrium or paraequilibrium phase boundary, i.e. when diffusionless transformation of carbon-enriched

austenite becomes thermodynamically impossible. The extent of the reaction is a function of temperature, increasing as the temperature is reduced. It is possible to extrapolate to find a bainite start temperature, B_s , above which bainite is not observed to form. This is known as the *incomplete reaction phenomenon*, in which the degree of transformation to bainite is always far less than that demanded by equilibrium.

Bhadeshia (1987) summarises the bainite reaction as a displacive transformation in which there is no diffusion of substitutional or iron atoms across the transformation interface. The excess carbon trapped in bainitic ferrite is removed by a combination of diffusion into the residual austenite, and by the precipitation of carbides between the ferrite. The retained austenite eventually decomposes by a diffusional transformation into a mixture of more carbides and ferrite. The plate morphology of bainite is explained by the minimisation of strain energy due to the IPS shape change associated with the displacive mechanism of the transformation. The kinetics of bainite are also shown to be consistent with the proposed diffusionless, displacive transformation mechanism.

2.3 Martensite

Martensite forms at the highest undercoolings, when the free energy change for the transformation is very large. Hence, rapid quenching of austenite to room temperature results in martensite, a very hard brittle structure in which carbon, originally in solid solution in austenite, remains in solution. Unlike the formation of ferrite or pearlite, the martensite reaction is a diffusionless shear transformation which is highly crystallographic in character and leads to a characteristic lath or lenticular microstructure.

The addition of alloying elements to a steel can affect the temperature, M_s , at which the martensite reaction can begin on cooling the parent phase. The extent to which the reaction proceeds depends on the undercooling below this temperature. Note that martensite can form at very low temperatures where atomic mobility is almost negligible because the transformation is diffusionless. The growth rate can be very high, limited by the speed of sound in the material concerned.

The fact that martensite can form at very low temperatures also means that any process which occurs during its formation also cannot depend on thermal activation, e.g. the interface between martensite and the parent phase must be able to move easily at very low temperatures. For the interface to have high mobility and velocity at low temperatures, it must be semi-coherent or fully incoherent (Christian and Knowles, 1981). It should be noted that fully coherent interfaces are only possible when the two lattices can be related by an IPS. In the γ/α

transformation the austenite lattice cannot transform to a b.c.c. martensite lattice by an IPS only (it occurs by the so-called Bain strain combined with a suitable rigid body rotation and a lattice invariant deformation which is either twinning or slip) and, therefore, the lattices are joined by semi-coherent interfaces. For the γ/α' interface to be glissile it must contain at least one invariant line along which interface dislocations lie.

The interface between the martensite and the parent plate is usually called the 'habit plane'. If the transformation is unconstrained, the habit plane is macroscopically flat, whereas in a constrained transformation it grows in the shape of a thin lenticular plate or lath, resulting in the interface being curved on a macroscopic scale. This is illustrated in Figure 2.6.

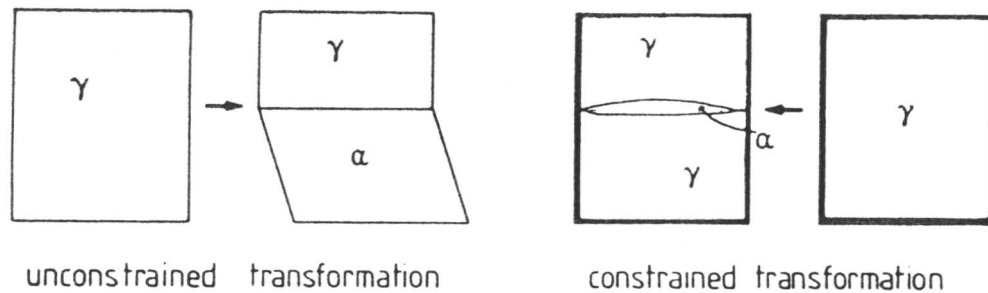


Figure 2.6: Unconstrained and constrained growth of martensite.

There are two kinds of martensite, a plate and a lath morphology. The extent of the martensite reaction has been found to be virtually independent of time. The volume fraction of martensite, f , formed as a function of undercooling below M_s is given by

$$1 - f = \exp[-0.011(M_s - T)] , \quad (2.1)$$

where T is the temperature to which the sample has been cooled below M_s . Since there is no diffusion during the martensite transformation, there will be reproducible orientation relationships between the parent and product lattices. The orientation relationship usually consists of approximately close-packed planes, and with corresponding close-packed directions also being approximately parallel e.g. Kurdjumov-Sachs

$$\{111\}_\gamma \parallel \{011\}_{\alpha'} \text{ and } \langle 10\bar{1} \rangle_\gamma \parallel \langle 11\bar{1} \rangle_{\alpha'} . \quad (2.2)$$

2.3.1 The shape deformation due to the martensitic transformation

When martensite grows there must be a change in shape because the pattern of atomic arrangement changes on transformation and the transformation is diffusionless, the change of shape being caused by the migration of interface dislocations. This is illustrated in Figure 2.7.

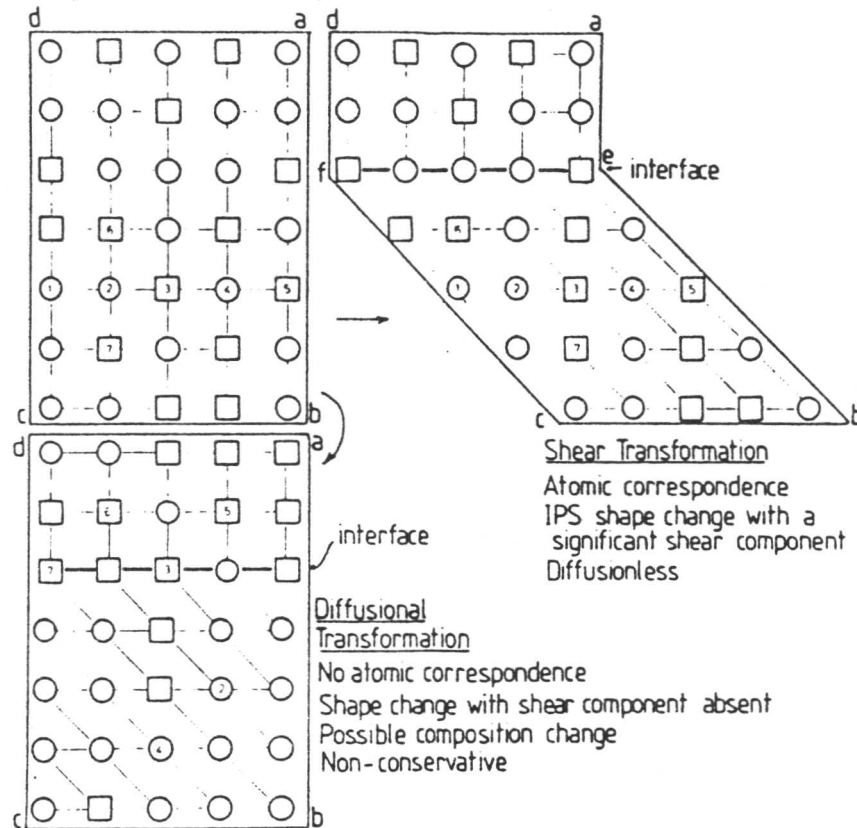


Figure 2.7: Diffusional and diffusionless transformations (Bhadeshia, 1987).

A comparison is made between diffusional and diffusionless transformations, the strain being an IPS and a fully coherent interface existing between the parent and product lattices. The occurrence of the shape deformation in martensite growth therefore implies there is an atomic correspondence between the parent and product lattices. It has been shown that in a constrained environment there is a distortion of the parent lattice around the martensite. The strain energy per unit volume is given by

$$E = \frac{c}{r}(s^2 + \delta^2)\mu, \quad (2.3)$$

where $\frac{c}{r}$ is the thickness/length ratio of the plate, μ is the shear modulus of the parent phase and s and δ are the shear and dilatational components of the shape deformation strain. This explains the plate morphology of martensite, for which E is minimised.

2.3.2 Martensite crystallography

It has been shown that the major feature of the martensite transformation is its shape change, macroscopically having the characteristics of an *invariant-plane strain*. There is an anomaly here because it is found that the Bain strain when combined with an appropriate rigid body rotation gives an *invariant-line strain*, which when applied to the f.c.c. lattice generates the martensite lattice. The Bain strain is illustrated in Figure 2.8.

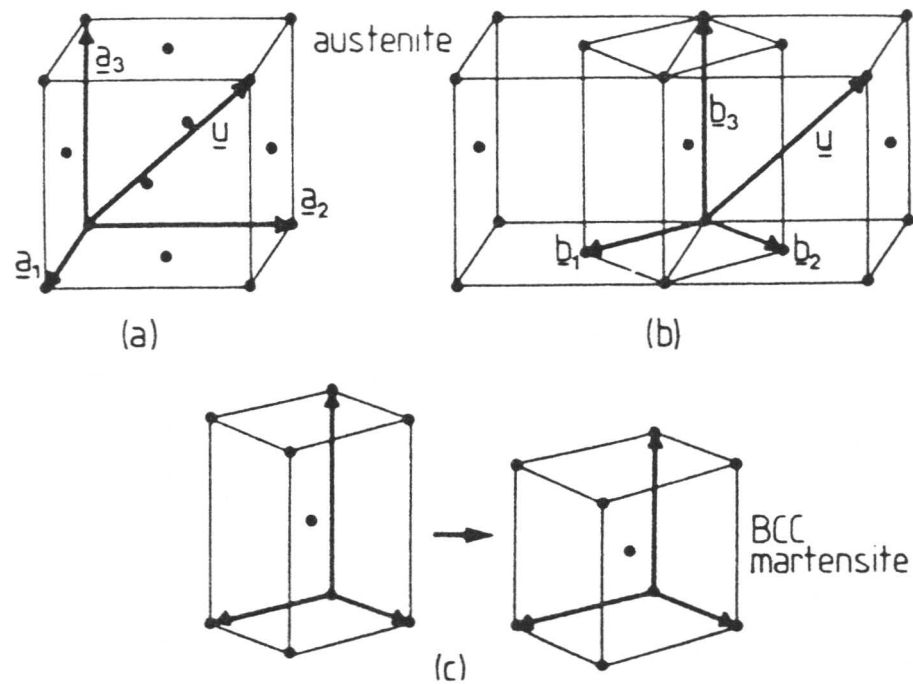


Figure 2.8: The Bain strain to transform austenite to martensite (Bhadeshia, 1987).

This is explained systematically in Figure 2.9. Figure 2.9 a) represents the shape of the initial f.c.c. austenite crystal. On martensitic transformation its shape alters to that in Figure 2.9 b) via an IPS. This is now an intermediate lattice which is not b.c.c., (an IPS on its own cannot convert f.c.c. \rightarrow b.c.c.). An invariant line strain (ILS) can, however, transform f.c.c. to b.c.c. and since an ILS can be factorised into two IPSs, it follows that the further deformation

needed to change the intermediate structure to the b.c.c. structure is another IPS. This now gives the correct lattice change but the wrong shape change. If another deformation is applied which alters the shape but without altering the crystal structure, i.e. is lattice invariant, this brings the experimental observations into agreement with theory. There are two possibilities for the lattice invariant deformation, twinning and slip.

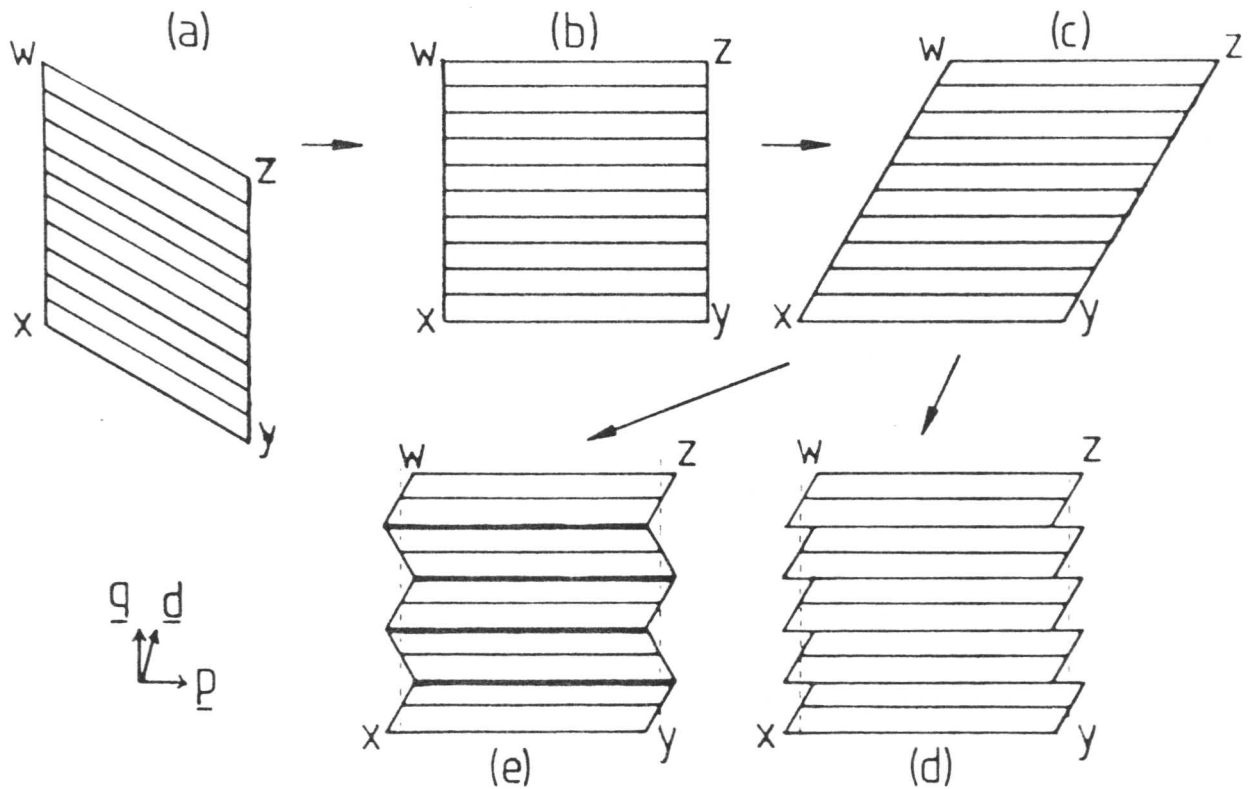


Figure 2.9: The formation of martensite (Bhadeshia, 1987).

This theory therefore explains the apparent contradiction that the lattice transformation strain is an ILS, but that the macroscopic shape deformation is an IPS, and also the experimentally observed transformation twins, and the peculiar habit plane indices, determined by the amount of lattice-invariant deformation.

2.3.3 The tempering of martensite

The presence of martensite in a quenched steel greatly improves the hardness, but it is normally very brittle and so almost all technological steels have to be heat treated to increase their toughness. Tempering is therefore normally carried out in the range 150–700°C. Martensite is a highly supersaturated solid solution of carbon in iron which, on tempering, rejects carbon

in the form of finely divided carbide phases. The microstructure after tempering is a fine dispersion of carbides in a ferrite matrix which often bears no resemblance to the as-quenched martensite. If the martensite reaction does not go to completion on quenching, there will also be some retained austenite which does not remain stable during the tempering process.

It is possible to define four distinct, but overlapping stages in the tempering of ferrous martensites, the discussion being initially restricted to plain carbon steels.

2.3.3.1 Stage 1: up to 250° C

Interstitial carbon atoms in martensite in steels of 0.3–1.5 wt.% C can diffuse within the tetragonal lattice at room temperature, increasing as the temperature is raised to 250°C. The primary stage of tempering is therefore the precipitation of close-packed hexagonal epsilon carbide, ϵ (composition $\text{Fe}_{2.4}\text{C}$) within the martensite. ϵ carbide precipitates as narrow laths on the cube planes of the matrix with a well-defined orientation relationship. It is also possible that cementite will be precipitated, but this will depend on the temperature and composition of the steel. After precipitation of ϵ carbide the martensite is still tetragonal, but has a much lower carbon content (low-carbon martensite). The microstructure at the end of the first stage of tempering consists of retained austenite, low-carbon martensite, and ϵ carbides.

2.3.3.2 Stage 2: 230–300° C

During the second stage the retained austenite decomposes. There is little experimental evidence, but it is thought that bainitic ferrite and cementite are formed. The reaction will only be important if there is an appreciable amount of retained austenite present, e.g. in medium or high carbon steels.

2.3.3.3 Stage 3

During the third stage of tempering cementite (Fe_3C) appears. The reaction commences as low as 100°C and is fully developed by 300°C, the particles being up to 200 nm long and approximately 15 nm in diameter. The most likely sites for the nucleation of the cementite are the ϵ carbide interfaces with the matrix; as the cementite grows the epsilon carbide will disappear. Nucleation and growth of the cementite can also occur on the twins occurring in the higher carbon martensites, with colonies of similarly oriented lath-shaped particles, distinguishable from the usual Widmanstätten distribution of rods. The matrix will no longer be tetragonal, being mainly ferrite saturated with carbon.

2.3.3.4 Stage 4

No further phase changes will occur as tempering proceeds, however the microstructure and mechanical properties will continue to alter. Hyam and Nutting (1956) suggest that the

coarsening and eventual spheroidisation of cementite particles constitutes a fourth stage of tempering. The final result in plain carbon steels is an equi-axed array of ferrite grains with coarse, spheroidised cementite particles, often in the grain boundaries.

2.3.3.5 Alloying elements

The tempering of martensite in an alloyed steel is clearly different than in a carbon steel, because the alloying elements generally move TTT (Time–Temperature–Transformation) curves to longer times. This results in a higher hardenability, because martensite structures can be achieved at slower cooling rates. Alloying elements can also depress the M_s (martensite start) temperature. The main difference in the tempering process is the replacement of cementite by alloy carbides.

The alloying elements will also have an effect on the formation of iron carbides. For example, Si can stabilise ϵ carbide so that it will still be present after tempering at 400°C in steels with 1–2 at. % Si, suggesting that Si enters the carbide structure. In steels containing Cr, Mo, W, V, Ti, Si etc. the tetragonality of martensite can be preserved up to 500°C, the alloying elements increasing the stability of the supersaturated Fe-C solid solution. Alloying elements can also slow down the coarsening of cementite in the range 400–700°C. The most important effect is that many elements (e.g. Cr, Mo, V, W and Ti) form carbides which are thermodynamically more stable than cementite.

Therefore, when strong carbide forming elements are present in a steel, their carbides will be formed in preference to cementite. Many alloy carbides do not usually form until 500–600°C, higher temperatures being necessary for the diffusion of the alloying elements prior to their nucleation and growth. There is often an associated marked increase in the strength of the steel, the phenomenon being termed secondary hardening, in which a relatively coarse cementite dispersion is replaced by a much finer alloy carbide dispersion.

2.4 Summary of transformation mechanisms

The characteristics of the formation of allotriomorphic ferrite, bainite and martensite have been discussed in the previous sections. This section summarises the mechanisms of these transformations. Figure 2.10 illustrates schematically the composition variation expected in the vicinity of the transformation interface. In the case of a reconstructive transformation the compositions of the two phases at the interface are defined by a tie-line of the phase diagram. In a binary alloy, the tie-line passes through the average alloy composition, however, for a ternary system it is not possible to satisfy the mass-balance condition for the three elements simultaneously. There are two possibilities. Firstly, to choose a tie-line which ensures that

the carbon composition in austenite at the interface is almost the same as that in the bulk alloy. This reduces the driving force for carbon diffusion almost down to zero and there will be a concentration gradient of substitutional solute ahead of the interface, implying extensive partitioning and a relatively slow growth rate. This is termed *partitioning local equilibrium* (P-LE). The second possibility is to choose a tie-line for which the concentration of substitutional solute in the austenite is approximately the same as that in the bulk alloy, resulting in a small amount of partitioning and a relatively fast growth rate. This is termed *negligible partitioning local equilibrium* (NP-LE).

In the NP-LE mode the concentration of solute remains the same everywhere except for a 'spike' at the interface, the width of the spike corresponding to the extent of the diffusion field. As the alloy is transformed at progressively lower temperatures the diffusion field gets smaller than atomic dimensions and local equilibrium breaks down. The substitutional element is then trapped across the advancing interface, although carbon is still mobile. This is termed *para-equilibrium*. In the case of martensitic transformations, neither the carbon or the substitutional solute atoms diffuse.

2.5 Carbide precipitation

In steels, pure binary carbides do not generally occur because there is always some solubility of the alloying elements in the various carbide phases, and in many cases solubilities are extensive. It is usual to denote a carbide by a general formula of the form $M_{23}C_6$, where M indicates a mixture of metal atoms. Much information on the composition, structure, morphologies and orientation relationships of various carbides has been obtained, usually with respect to specific steels (*e.g.* Goldschmidt, 1948; Kuo, 1953; Shaw and Quarrell, 1957; Baker and Nutting, 1959; Woodhead and Quarrell, 1965; Jack and Jack, 1973; Yakel, 1985).

Alloy carbides can form in a variety of ways. Sites for carbide precipitation include dislocations from the original α' structure, and at grain boundaries and sub-boundaries (which are energetically favourable sites, providing high diffusivity paths for the rapid diffusion of solute). In many cases the first alloy carbide to form is not the equilibrium carbide, leading to precipitation sequences as the first carbide is gradually replaced by more stable ones. There has been some controversy in past literature as to whether more stable alloy carbides nucleate 'in situ' or separately from the dissolving carbides. Transformations between particular carbides are discussed in the next section.

2.5.1 M_3C

Cementite containing no alloying element additions, Fe_3C , can be thought of as an ap-

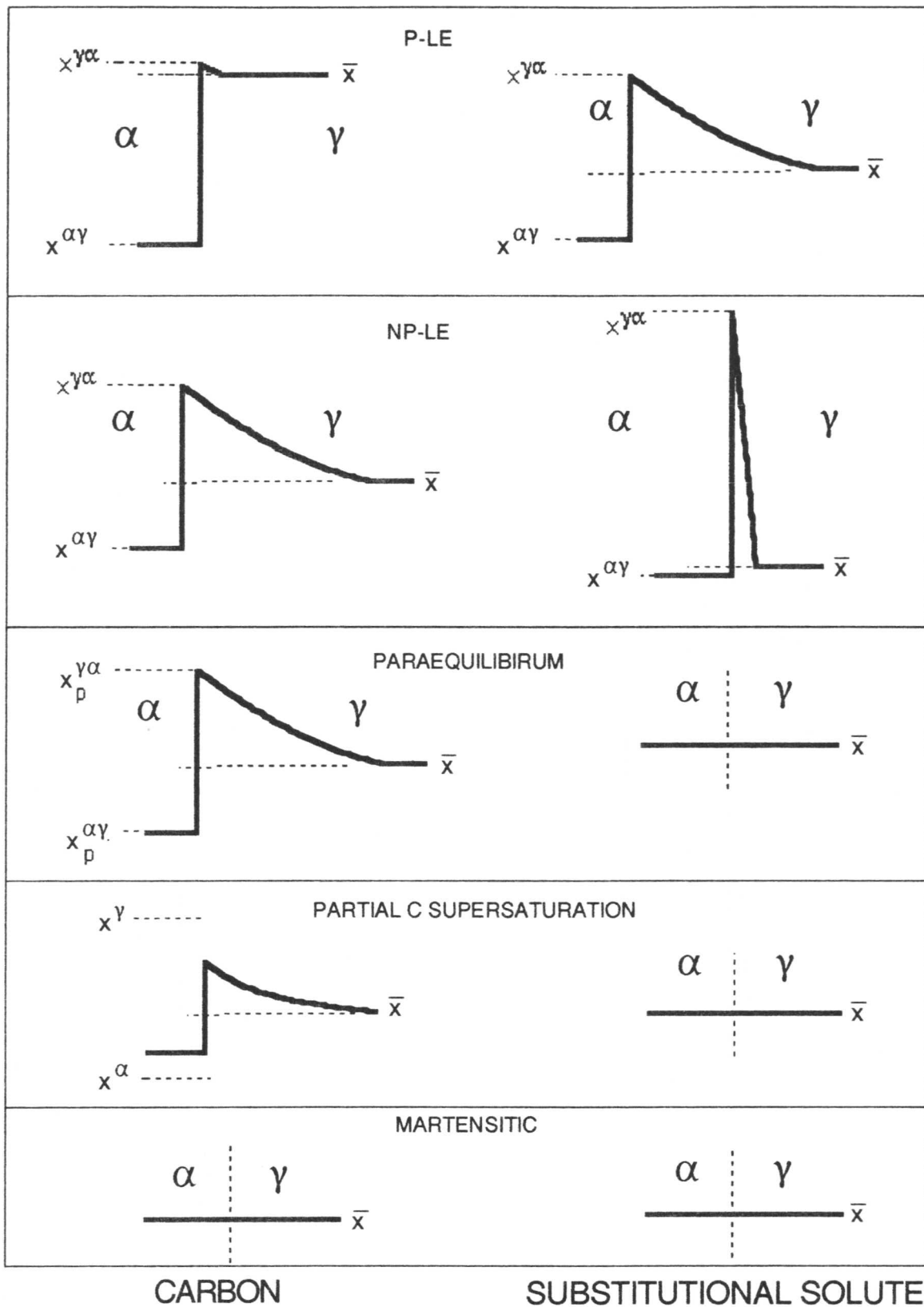


Figure 2.10: Schematic illustration of the composition variation in the vicinity of the transformation interface for a variety of growth mechanisms (Bhadeshia, 1992).

proximately hexagonal close-packed arrangement of metal atoms with localized distortions to accommodate the carbon atoms. Each carbon atom is surrounded by a triangular prism containing 6 iron atoms. This is illustrated in Figure 2.11 a). The prisms are then joined by corners and edges to form sheets stacked perpendicular to the *c*-axis, leading to the ‘pleated’ structure illustrated in Figure 2.11 b).

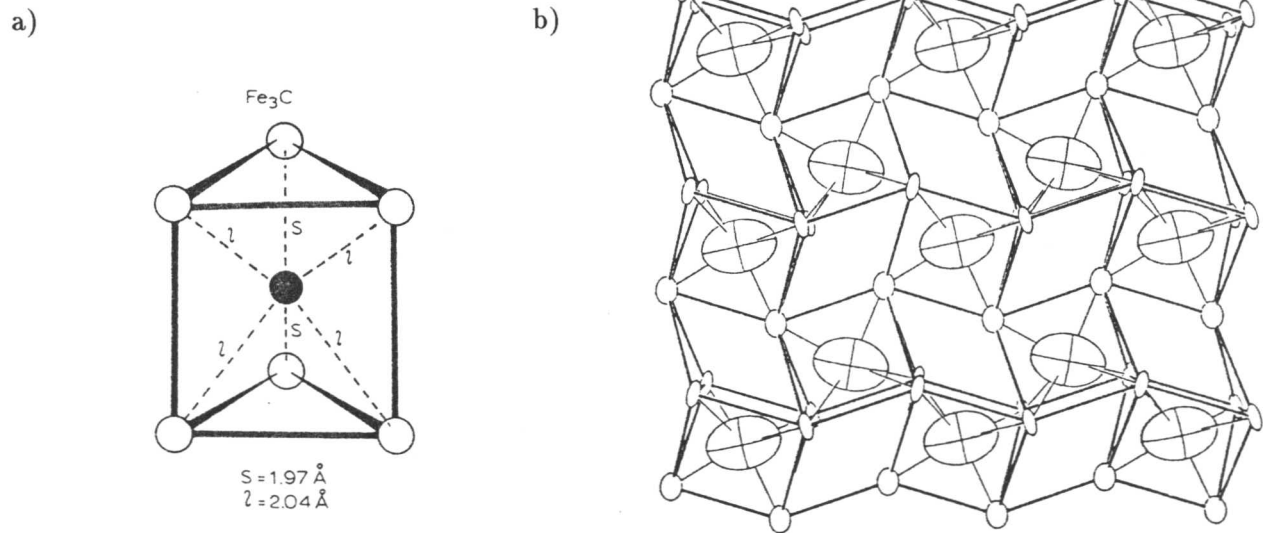


Figure 2.11: a) The triangular prism environment of iron atoms around carbon in Fe_3C (after Jack and Jack, 1973), and b) View of the atomic arrangement in cementite (after Yakel, 1985). Within each ellipse there is a 99.9% probability of finding the atom. The sizes of the ellipses depend on thermal vibration parameters, and hence the larger ellipses represent the carbon atoms.

M_3C is predominantly an iron-rich carbide with the same orthorhombic structure as Fe_3C , however several alloying elements can partition to this carbide in significant quantities. The unit cell dimensions are affected by partial substitution of alloying elements. Woodhead and Quarrell (1965) have found that Mn can dissolve in large quantities, as can Cr, with up to one fifth of the Fe atoms being replaced by Cr (specific to low alloy steels). Ni and Co can also dissolve as they form metastable orthorhombic carbides, although they usually partition to ferrite. Mo, W and V have also been found to have limited solubilities in M_3C . In general M_3C carbides can be referred to using the general formula $(\text{Fe,Cr,Mn,Mo})_3\text{C}$.

2.5.2 M_7C_3

This is a Cr-rich carbide with the trigonal structure of Cr_7C_3 , having a solubility of Fe up to 60% (although Titchmarsh (1978) has found that the Cr:Fe ratio can be greater than 1 in $2\frac{1}{4}\text{Cr1Mo}$ steel). Mn, V and Mo can also dissolve, with decreasing probabilities respectively.

Baker and Nutting (1959) state that nucleation of M_7C_3 can only occur in the vicinity of cementite or at the cementite/ferrite interface, which is supported by Kuo (1953) who states that separate nucleation is improbable because there is not enough Cr in the matrix. Beech and Warrington (1966) state that cementite particles on the point of dissolving may leave areas sufficiently rich in chromium in which M_7C_3 could precipitate since these will be the most favourable sites.

An interesting feature of M_7C_3 is that electron diffraction patterns show characteristic streaks, making it easily distinguishable from other carbides. The streaks have been attributed to faults lying on $\{10.0\}$ planes, with the fault vector being approximately half the unit cell repeat distance (Beech and Warrington, 1966).

2.5.3 $M_{23}C_6$

This is usually a Cr-rich carbide having the complex f.c.c. structure of $Cr_{23}C_6$, however, in steels containing significant amounts of Mo it can have the formula $Fe_{21}Mo_2C_6$. In steels containing both Cr and Mo its composition can be anywhere between the above. Mn has also been found to partition to $M_{23}C_6$ in small quantities. Baker and Nutting (1959) and others observe that $M_{23}C_6$ has never been found in the vicinity of M_7C_3 colonies. Beech and Warrington (1966) also support this view, finding no evidence supporting an 'in-situ' mechanism for the transformation $M_7C_3 \rightarrow M_{23}C_6$.

2.5.4 M_6C

M_6C is essentially a Mo-rich carbide with a f.c.c. structure. In a simple ternary system of Fe-Mo-C, it exists in the range Fe_2Mo_4C or Fe_3Mo_3C depending on the Mo content (Kuo, 1956). M_6C may also take small quantities of Cr and V into solution. It forms at grain boundaries, growing rapidly at the expense of all surrounding carbides, nucleating at existing particles. The transformation Mo_2C to M_6C occurs more rapidly in bainite than in ferrite.

2.5.5 M_2C

As with M_6C , M_2C is also a Mo-rich carbide with an f.c.c. structure and is usually denoted simply by Mo_2C . Cr and V have been found to be soluble in significant quantities, with a much smaller amount of Fe also dissolving. It commonly precipitates as fine needles parallel to the $\langle 110 \rangle_\alpha$ direction in ferrite. The orientation relationship is that of Pitsch-Schrader (1958):-

$$(0001)_{Mo_2C} \parallel (011)_\alpha \text{ and } [11\bar{2}0]_{Mo_2C} \parallel [100]_\alpha .$$

The precipitation of Mo_2C is usually said to be the major factor in conferring creep resistance on low alloy ferritic steels.

Table 2.1: A summary of data for the common alloy carbides found in steels, (Andrews *et al*, 1967).

Carbide	Structure	Lattice Parameter /Å	Formula Units /Cell	Density /g cm ⁻³
M ₃ C	Orthorhombic	a=4.5241 b=5.0883 c=6.7416	4	7.704
M ₇ C ₃	Trigonal	a=13.982 c=4.506	8	6.965
M ₂₃ C ₆	Cubic F	a=10.638	4	6.996
M ₆ C	Cubic F	a=11.082	16	6.325
M ₂ C	Hexagonal	a=3.002 c=4.724	1	9.188

Data for the various alloy carbides discussed above are summarised in Table 2.1.

2.6 Interphase precipitation

A number of studies (Berry and Honeycombe, 1970; Edmonds and Honeycombe, 1973; Tillman and Edmonds, 1974; Honeycombe, 1976; Dunlop and Honeycombe, 1976) have been made of the so-called *interphase precipitation* in isothermally transformed alloy steels. It was shown that direct decomposition of alloyed austenite containing a substantial amount of strong carbide-forming elements (e.g. V, Mo, Ti, Cr) can lead to a distribution of alloy carbide in the ferrite. Berry and Honeycombe (1970) investigated a number of alloys containing different amounts of Fe, Mo and C isothermally transformed in the range 600–900°C. They found two different morphologies of the carbide M₂C in the allotriomorphic ferrite; long, straight fibres growing from the prior austenite grain boundaries and sheets of smaller, needle-like, particles in a Widmanstätten ferrite array. It is these sheets of smaller particles which are termed ‘interphase precipitation’. It was found that the fibrous form of M₂C was favoured when the growth of allotriomorphic ferrite is slow, i.e. below the nose of the time-temperature transformation curve in the range 600–700°C, whereas the interphase precipitation was found at higher transformation temperatures. The orientation relationship derived between the M₂C fibres and the ferrite matrix was

$$(011)_\alpha \parallel (0001)_{\text{Mo}_2\text{C}}$$

$$(101)_\alpha \parallel (1\bar{1}01)_{\text{Mo}_2\text{C}}$$

$$[1\bar{1}1]_\alpha \parallel [1\bar{2}10]_{\text{Mo}_2\text{C}},$$

a relationship commonly observed for hexagonal phases precipitating within a b.c.c. matrix. The Widmanstätten ferrite type M_2C carbides were found to have the orientation relationship

$$(011)_\alpha \parallel (0001)_{M_2C}$$

$$(100)_\alpha \parallel (2\bar{1}\bar{1}0)_{M_2C}$$

$$[100]_\alpha \parallel [2\bar{1}\bar{1}0]_{M_2C},$$

which is also that describing the precipitation of M_2C in tempered martensite.

Edmonds and Honeycombe (1973) compared the microstructure and mechanical properties of a Fe-4Mo-0.2C steel both in the quenched and tempered and the isothermally transformed conditions. The isothermally transformed specimens showed elongation and high ductility when fractured, whereas the quenched and tempered specimens showed no elongation and there was evidence of cracking along the prior austenite grain boundaries. The ductile-brittle transition was found to be 30–40°C lower for the isothermally transformed alloy. These observations can be explained by the fact that the formation of alloy carbide in fibre or sheet form at the grain boundaries prevents the passage of dislocations, resulting in strong dispersion strengthening.

Honeycombe (1976) discusses the mechanism for the growth of the interphase precipitates. Early ideas for the mechanism of interphase precipitation were that the precipitates had nucleated on dislocations, known to be favourable sites for carbide nucleation. However, this would not explain the very regular precipitate arrays observed. Ferrite/austenite interfaces vary from high energy random boundaries to low energy planar boundaries which grow by step-by-step propagation. The nature of the interface itself is very important in determining the morphologies of the different carbide dispersions. The ferrite interfaces associated with interphase precipitation grow mainly by a ledge mechanism. Nucleation occurs on the planar boundary whereas the ledge itself is free from precipitates because of its higher mobility. The planar boundary is of low energy with limited mobility and therefore the growth of ferrite occurs by movement of a series of incoherent high energy steps. The fibrous carbides nucleate at the austenite boundary and then grow into the ferrite where the interface is more irregular with local curvature. Diffusivity along a disordered boundary is greater than on a coherent or semi-coherent one and therefore fibrous carbides are associated with lower temperatures and incoherent interfaces where there are enhanced diffusion paths.

CHAPTER 3

THEORETICAL STUDIES – AN INTRODUCTION

In this chapter a theoretical model for the diffusion of substitutional alloying elements to cementite particles is developed. Symmetric and asymmetric particle distributions are considered. The method of calculation of the equilibrium concentrations in the phases involved and choice of diffusion coefficients are discussed.

CHAPTER 3

THEORETICAL STUDIES – AN INTRODUCTION

3.1 Introduction

A large amount of experimental data has been collected over the years concerning the chemical composition of various carbides as a function of different tempering treatments. The aim of this work is to develop a sound theoretical basis for the assessment of these data. Carruthers and Collins (1981) and Afrouz *et al.* (1983) have attempted to explain the mechanism of composition changes in pearlitic and bainitic cementite in terms of diffusion-controlled coarsening theory (Wagner, 1961; Lifshitz and Slyozov, 1961). They therefore plotted composition changes as a function of $t^{\frac{1}{3}}$, where t is the time at the tempering temperature, and, finding approximately linear relationships, inferred that the changes occurred in the context of a coarsening reaction. However, it is well established (see for example Greenwood, 1969 and Christian, 1975) that coarsening reactions in alloys are dependent on the fact that the equilibrium composition of the matrix in contact with a particle is a function of the principal radii of curvature of the particle/matrix interface. For example, the matrix adjacent to smaller spherical particles would be expected to have a higher equilibrium concentration of solute than that adjacent to larger particles. Hence, a diffusion flux is stimulated from the smaller to the larger particles resulting in the larger particles growing at the expense of the smaller ones. The driving force for this process is the reduction in total interface energy.

However, the changes in cementite composition are fundamentally different from a coarsening reaction. The matrix is supersaturated in solute with respect to nearly all the particles and so the concentration of solute will at first increase in all particles irrespective of size. The flux of interest is that of solute into a particle from the surrounding matrix for both large and small particles. It is not correct therefore to explain the changes in particle composition in terms of coarsening theory. The enrichment behaviour only of cementite particles is discussed in this chapter. It should be noted, however, that coarsening in the true sense may occur at very long service times and also needs to be considered in the development of the model. The possibility that simultaneous coarsening and enrichment may occur is discussed in Chapter 9.

3.2 Partitioning in pearlitic and bainitic cementite

The precipitation of carbides during the bainite transformation has already been discussed in Chapter 2. After the formation of carbides, bainitic microstructures are a long way from

equilibrium. Hultgren (1947, 1951) established that upper bainitic cementite has a substitutional alloy content close to (or slightly higher than) that of the steel as a whole rather than its equilibrium concentration. Chance and Ridley (1981) investigated chromium partitioning during isothermal transformation for bainitic and pearlitic microstructures using analytical electron microscopy on carbon extraction replicas. They found that in upper bainite the partition coefficient, defined to be the ratio of chromium in cementite to that in ferrite, k_{Cr} , was close to unity. In the case of pearlitic cementite, the amount of partitioning increases with transformation temperature. At low temperatures (500–600°C) k_{Cr} remained approximately constant at $\simeq 4$, and rose to a value of $\simeq 15$ at 730°C. This is illustrated in Figure 3.1.

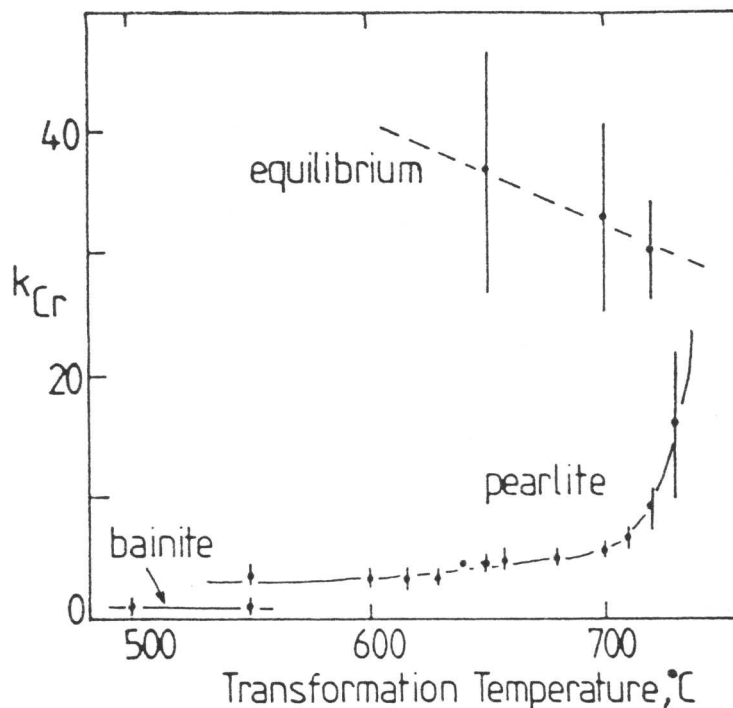


Figure 3.1: Partition coefficient between cementite and ferrite as a function of transformation temperature (Chance and Ridley, 1981).

The carbon concentration of cementite is substantially larger than that of austenite or ferrite, cementite (M_3C) containing 25 at.% of carbon to maintain the stoichiometry. A transformation to cementite, which has the same Fe/Cr ratio as the parent phase, should give a partition coefficient which is greater than unity. It can be concluded that the formation of cementite during transformation to upper bainite involves only a small degree of redistribution of elements such as chromium. This is consistent with the fact that upper bainitic cementite forms from carbon-enriched austenite, and so the driving force for cementite formation is higher allowing greater departure from the equilibrium composition.

For pearlitic cementite, however, it is found that its composition directly after transformation is always between equilibrium and paraequilibrium for alloy steels (Chance and Ridley, 1981; Al-Salman *et al.*, 1979; Williams *et al.*, 1979). Transformation to pearlite involves the co-operative growth of ferrite and cementite, with the reaction front providing a boundary along which the chromium can redistribute providing the reaction is not too rapid. There is at present no theory to predict the starting composition of pearlitic cementite from austenite, consequently modelling of the composition changes in carbides has so far focussed on bainitic cementite. If the starting composition of pearlitic cementite is known from experimental data, then the enrichment behaviour can be modelled. This is illustrated in Chapter 6.

3.3 Equilibrium compositions of cementite and ferrite

For many years the equilibrium compositions of the various carbides in alloyed steels were not known. Vengopalan and Kirkaldy (1978) determined expressions for the partition coefficient, k_z , of alloying elements between cementite and ferrite using empirical constants defined by the expression

$$k_z \approx \exp \frac{(A + BT)}{RT}, \quad (3.1)$$

for dilute alloys. The values of the constants A and B are given in Table 3.1.

Table 3.1: Parameters used for the calculation of partition coefficients (Vengopalan and Kirkaldy, 1978).

Element Z	A, J mol ⁻¹	B, J mol ⁻¹ K ⁻¹
Cr	47028	-17.45
Mn	42844	-20.21
Mo	27363	-5.86
Ni	-2619	-2.80
Si	0	-25.10

The partition coefficient k_z is defined to equal $c^{\theta\alpha}/c^{\alpha\theta}$, therefore using the condition for mass-balance at equilibrium (the Lever rule)

$$V_\theta = \frac{(\bar{c} - c^{\alpha\theta})}{(c^{\theta\alpha} - c^{\alpha\theta})}, \quad (3.2)$$

with respect to the carbon concentrations in the cementite and ferrite, $c^{\theta\alpha}$ and $c^{\alpha\theta}$, respectively the volume fraction of cementite in the alloy, V_θ , can be determined. \bar{c} is the average carbon concentration in the bulk alloy. Using the definition of the partition coefficient and the above

expression, the equilibrium compositions of the two phases can be calculated as a function of temperature using the equation:

$$c^{\theta\alpha} = \frac{\bar{c}}{V_\theta - \frac{V_\theta}{k_z} + \frac{1}{k_z}} \quad (3.3)$$

where $c^{\theta\alpha}$ and $c^{\alpha\theta}$ are now the concentrations of the substitutional alloying elements in the cementite and ferrite respectively.

However, implicit in this expression is the assumption that the solution is dilute, and it is not valid for steels with more than a few percent of the alloying elements. This method was used to find the equilibrium concentration of the various alloying elements between cementite and ferrite in the 12Cr1MoV steel discussed in Chapter 7, and was found to break down, predicting more than 100 at.% of chromium in the cementite!

It is now possible to calculate the equilibria in multicomponent alloys using experimentally determined thermodynamic data without using any dilute solution approximations and taking into account the effects of all the alloying elements in the steel. Phases other than cementite and ferrite can also be taken into account. In this work equilibrium calculations were performed using the National Physical Laboratory's Metallurgical and Thermodynamic Data Bank (MT-DATA), a computer package containing critically assessed thermodynamic data for a number of alloy systems. MTDATA allows the equilibria in multicomponent, multiphase systems to be calculated from a knowledge of the thermodynamic data for the subsystems. It is possible to calculate for a given temperature, pressure or volume, the phases present and the amounts of species within each phase by minimising the Gibbs free energy of the system for specified component amounts. Further details are given by Hodson (1989). The main database used for the calculations in this work is the solution database created by the Scientific Group Thermodata Europe.

For a specific steel composition and temperature the equilibrium phases can first be determined. The calculation yields information on the alloy content of the phases in question, their relative proportions and the Gibbs free energy of the system. If the equilibrium carbide phase is then suppressed and the calculation repeated, the new equilibria will contain the second most stable carbide. By repeating this process it is possible to predict the sequence of carbide formation on tempering steels alloyed with chromium and molybdenum. The results of specific calculations to determine the composition of the ferrite and carbide phases and precipitation sequences are presented in Chapters 5, 6 and 7 for the $2\frac{1}{4}\text{Cr}1\text{Mo}$, $\frac{1}{2}\text{Cr}\frac{1}{2}\text{Mo}\frac{1}{4}\text{V}$ and 12Cr1MoV steels respectively.

3.4 Diffusion coefficients

In a binary alloy an empirically defined diffusion coefficient is simply the proportionality constant relating the rate of transfer of diffusing substance through a unit area of section and the concentration gradient measured normal to the section. A *tracer diffusion coefficient* represents the diffusivity of radioactively labelled isotopes in an otherwise chemically homogeneous solution. When the radioactive tracer atoms are of the same species as the atoms of the medium, the tracer diffusion coefficient is called the *tracer self-diffusion coefficient*.

However, these two coefficients are not applicable if the diffusion is taking place in a concentration gradient. In the presence of a chemical composition gradient, an additional virtual force acts on the diffusing species due to the chemical potential gradient associated with the composition gradient. In order to take this into account and therefore represent the flux of one component, A, of a binary solid solution A–B in a concentration gradient of A, an *intrinsic diffusion coefficient* should be used.

In this work intrinsic chemical diffusion coefficients are used from the work of Fridberg *et al.* (1969). In order to calculate the overall diffusion coefficient, the expression

$$D = D_0 \exp\left(-\frac{Q}{RT}\right), \quad (3.4)$$

is used, where Q is the activation energy, R is the universal gas constant, T is the temperature in Kelvin and D_0 is the pre-exponential factor for diffusion. Fridberg states that the values for the self-diffusion of iron in austenite and ferromagnetic ferrite are given by

$$D_0 = 1.6 \text{ cm}^2\text{s}^{-1} \text{ and } Q = 240,000 \text{ J mol}^{-1}$$

$$D_0 = 0.5 \text{ cm}^2\text{s}^{-1} \text{ and } Q = 240,000 \text{ J mol}^{-1}$$

respectively. The intrinsic diffusion coefficients of the various alloying elements in ferrite are then determined by comparison with the self-diffusion of iron, the difference being described by a factor independent of temperature. These diffusion coefficients refer to the interdiffusion of the alloying element in a binary system, i.e. of chromium in ferrite, molybdenum in ferrite, and therefore do not strictly relate to diffusion in a multicomponent system. The values of interdiffusion coefficients used in this work are given in Table 3.2.

Table 3.2: Chemical interdiffusion coefficients (Fridberg *et al.*, 1969).

Element	$D_0/\text{m}^2\text{s}^{-1}$	$Q/\text{J mol}^{-1}$
Cr	1.5×10^{-4}	240,000
Mn	1.0×10^{-4}	240,000
Mo	1.0×10^{-4}	240,000

It is important to note that in this work it is assumed that the diffusion of the interstitial carbon is significantly faster than the diffusion of the substitutional alloying elements and that the flux of the latter will not be influenced by the former. Carbon diffusion in ferrite has been shown not to follow a simple Arrhenius-type relationship because of the possibility of carbon occupying both octahedral and tetrahedral sites in the lattice. Using the method due to McLellan *et al.* (1965) a value of $1.5 \times 10^{-11} \text{m}^2 \text{s}^{-1}$ is obtained for the diffusivity of carbon in ferrite at a temperature of 565°C . This is approximately eight orders of magnitude faster than the diffusion of chromium in ferrite. Diffusion of the alloying element only is therefore considered to be the rate-controlling step. In a more sophisticated treatment ternary diffusion, e.g. Fe-Cr-C, would need to be considered, although it should be noted that the interdiffusion coefficients allow for a flux of the alloying element within a flux of iron.

There is little information available in the literature on the diffusivity of the alloying elements in carbides. Törndahl (1968 – cited by Fridberg *et al.*, 1969) studied the rate of diffusion of manganese in cementite. His results seemed to indicate that the value of this diffusion coefficient lies between the values in ferrite and austenite. Recent work (Barnard *et al.*, 1987) using an atom probe has attempted to measure the chromium diffusivity in bainite and cementite. They found that the value in cementite was two orders of magnitude lower than corresponding measurements in ferrite. The diffusivity of chromium in ferrite measured was, however, different by an order of magnitude from that measured previously by Bowen and Leak (1970) and the value for the interdiffusion coefficient given above. The diffusion coefficient of chromium in cementite is discussed further in Chapter 8.

3.5 One dimensional modelling

A method to enable modelling of the diffusion of substitutional solute elements to cementite, for the case of a symmetric carbide distribution, was developed by Bhadeshia (1989). It is presented here in full in order that comparisons may be drawn with the improvements in the model discussed in the following sections. The problem of cementite enrichment is not easy to solve analytically because of the need to consider soft impingement[†]. The approach used in this work is to find solutions to the governing diffusion equations using numerical methods because they can easily take into account soft impingement.

3.5.1 Symmetric case – Definition of the problem

Cementite particles within a ferrite matrix are treated as a composite one dimensional

[†] Soft impingement is the overlap of the diffusion or temperature fields, or from active regions of the same particle. Hard impingement implies physical contact between the particles.

diffusion couple in which a slab of cementite, thickness x_θ , is sandwiched between two slabs of ferrite, thickness x_α , such that

$$\frac{x_\theta}{(2x_\alpha + x_\theta)} = V_\theta, \quad (3.5)$$

where V_θ is the equilibrium volume fraction of cementite in the alloy. This analysis is based on the idea that if all the cementite particles were to be massed together in a slab of width x_θ , they would occupy the same volume fraction as a number of individual carbides in a section of ferrite of length $x_\theta + 2x_\alpha$. This approximation will be a good one if the spatial distribution of plate-like carbide particles in the steel is appropriate. The thickness of the cementite is a parameter in the program chosen to represent an actual particle size in a steel at long ageing times, $\simeq 100$ nm. The equilibrium volume fraction of cementite in the alloy, V_θ , can be found by two alternative methods. Firstly, application of the Lever rule to the binary Fe–C phase diagram gives

$$V_\theta = \frac{(\bar{c} - c^{\alpha\theta})}{(c^{\theta\alpha} - c^{\alpha\theta})}, \quad (3.6)$$

where \bar{c} is the average carbon concentration in the alloy, $c^{\alpha\theta}$ and $c^{\theta\alpha}$ are the equilibrium carbon concentrations in the ferrite and cementite respectively. It is assumed that $c^{\alpha\theta} = 0$ and $c^{\theta\alpha} = 6.67$ wt.%. This method tended to overestimate V_θ by a small amount. A second, and more accurate method, is to use the volume fraction of cementite predicted by MTDATA for the ferrite/cementite equilibria. The advantage of this method is that it takes into account all the minor alloying element additions to the bulk alloy.

It is important to set the thicknesses of the ferrite and cementite to be consistent with the calculated volume fraction of cementite present at equilibrium. To this end, the size of the ferrite slice is calculated within the program for the chosen cementite particle size.

The diffusion equation must be obeyed separately in the cementite and ferrite phases:

$$\frac{\partial c^\theta}{\partial t} = D^\theta \frac{\partial^2 c^\theta}{\partial x^2} \quad (3.7)$$

$$\frac{\partial c^\alpha}{\partial t} = D^\alpha \frac{\partial^2 c^\alpha}{\partial x^2}. \quad (3.8)$$

The particle is of a fixed size and therefore the mass balance at the cementite/ferrite interface is given by

$$D^\theta \frac{\partial c^\theta}{\partial x} = D^\alpha \frac{\partial c^\alpha}{\partial x}, \quad (3.9)$$

where the gradients in this case are evaluated at the interface.

3.5.2 Symmetric case – Numerical solution

In the analysis non-dimensional variables are used. The advantage of this is that numbers occurring in the calculations cover roughly the same ranges for all calculations. Concentrations

are normalised with respect to the average concentration in the alloy and distances with respect to the thickness of the cementite, hence

$$x' = \frac{x}{x_\theta} \quad (3.10)$$

$$c' = \frac{c}{\bar{c}} \quad (3.11)$$

$$t' = \frac{Dt}{x_\theta^2}, \quad (3.12)$$

where D is the diffusion coefficient.

For the analysis the cementite and ferrite are divided up into a number of slices, n , of equal thickness, x_s such that,

$$n_\theta = \frac{x_\theta}{2x_s} \quad (3.13)$$

$$n_\alpha = \frac{x_\alpha}{x_s}. \quad (3.14)$$

This means that the x' - t' region is covered with a grid of rectangles of sides $\delta x'$ and $\delta t'$ respectively, hence the coordinates of a grid point (x', t') can be written $(i\delta x', j\delta t')$, where i and j are integers. The normalised concentration at that point (in ferrite) is denoted by $c'_{i,j}$. The use of finite-difference methods to obtain numerical solutions to the diffusion equation is discussed in detail by Crank (1975). The idea is that some, or all, of the derivatives in the diffusion equation are replaced by finite-difference approximations.

The explicit[†] finite difference approximation for diffusion in the ferrite matrix is given by

$$c'_{1,j+1} = c'_{i,j} + r(c'_{i-1,j} - 2c'_{i,j} + c'_{i+1,j}), \quad (3.15)$$

where

$$r = \frac{\delta t'}{(\delta x')^2},$$

and is taken to be 0.4. The value of r determines the accuracy of the method and also the computation time. A compromise value has been chosen by trial and error.

The finite difference method can be readily visualised using a graphical construction. If the value of r is taken to be $\frac{1}{2}$ for example, then equation 3.15 reduces to

$$c'_{1,j+1} = \frac{1}{2}(c'_{i-1,j} + c'_{i+1,j}). \quad (3.16)$$

[†] There are two methods of using finite difference approximations. Explicit formulae, as the name implies, express an unknown directly in terms of known values, whereas implicit formulae contain more than one unknown in each equation, necessitating the solution of a number of simultaneous equations. The latter method is usually considered to be more accurate but at the same time is very expensive in terms of computer time. The finite difference approximations are derived in Appendix I.

Hence, the concentration at a particular point after one time interval has passed is simply the arithmetic mean of the concentrations at the two adjacent points in the previous time interval. This is illustrated in Figure 3.2.

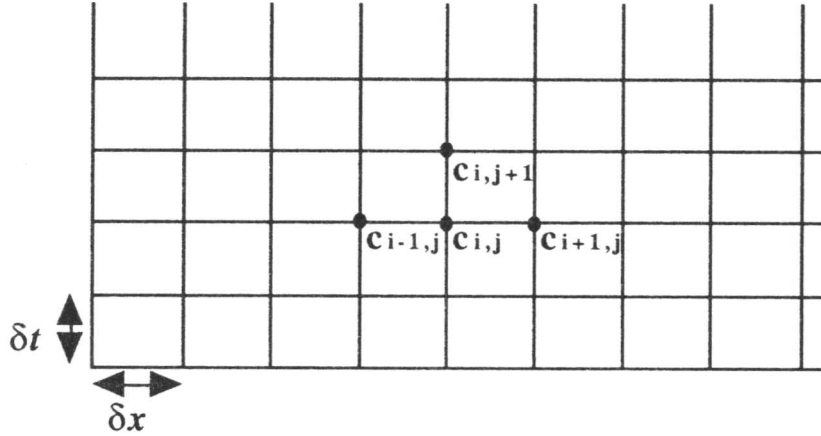


Figure 3.2: Graphical method to illustrate the finite difference model.

The normalised concentration $c_s^{\prime\alpha}$ in the α at the α/θ interface was initially set at $c^{\alpha\theta}/\bar{c}$, although the computer algorithm was designed to allow this to vary as soon as the flux matching condition at the interface necessitated changes. Then equation 3.15 was used to calculate the value of c at all points along successive time rows of the grid, for the initial conditions that $c_{0,0}^{\prime\alpha} = c^{\alpha\theta}/\bar{c}$, and $c_{i,0}^{\prime\alpha} = 1$ for all $i > 0$.

A similar analysis is applied to diffusion in the cementite. Finite difference approximations applied to the mass balance condition at the interface mean that $c_{0,j}^{\prime\theta}$ are determined by the equation

$$D_{\theta}(c_{0,j}^{\prime\theta} - c_{1,j}^{\prime\theta}) = D_{\alpha}(c_{1,j}^{\prime\alpha} - c_{0,j}^{\prime\alpha}), \quad (3.17)$$

where $c_{i,0}^{\prime\theta} = 1$ for all $i > 0$. It should be noted that the value of the concentration in cementite at the interface was not fixed by local equilibrium considerations, but increased gradually with time towards the equilibrium level. It is assumed that the diffusion coefficients in cementite and ferrite are equal for this work. This is discussed further in Chapter 8. In general $c^{\theta\alpha} \gg c^{\alpha\theta}$, therefore this condition ensures that the surface concentration of cementite at the θ/α interface, $c_{0,j}^{\prime\theta}$, is for a considerable period of time, less than $c^{\theta\alpha}/\bar{c}$.

For both phases, soft impingement will eventually occur. This means that the concentrations at the maximum values of i for both θ and α are eventually affected by the fluxes originating at the θ/α interface. The concentrations in the slices with $i = i_{max}$ (i.e. the extent of the ferrite and at the centre of the cementite particle) are therefore given by reflecting the concentration profile across an imaginary boundary located at i_{max} , hence

$$c_{i_{max},j+1}^{\theta} = c_{i_{max},j}^{\theta} + 2r(c_{i_{max}-1,j}^{\theta} - c_{i_{max},j}^{\theta}). \quad (3.18)$$

The diffusion couple and notation used are illustrated in Figure 3.3.

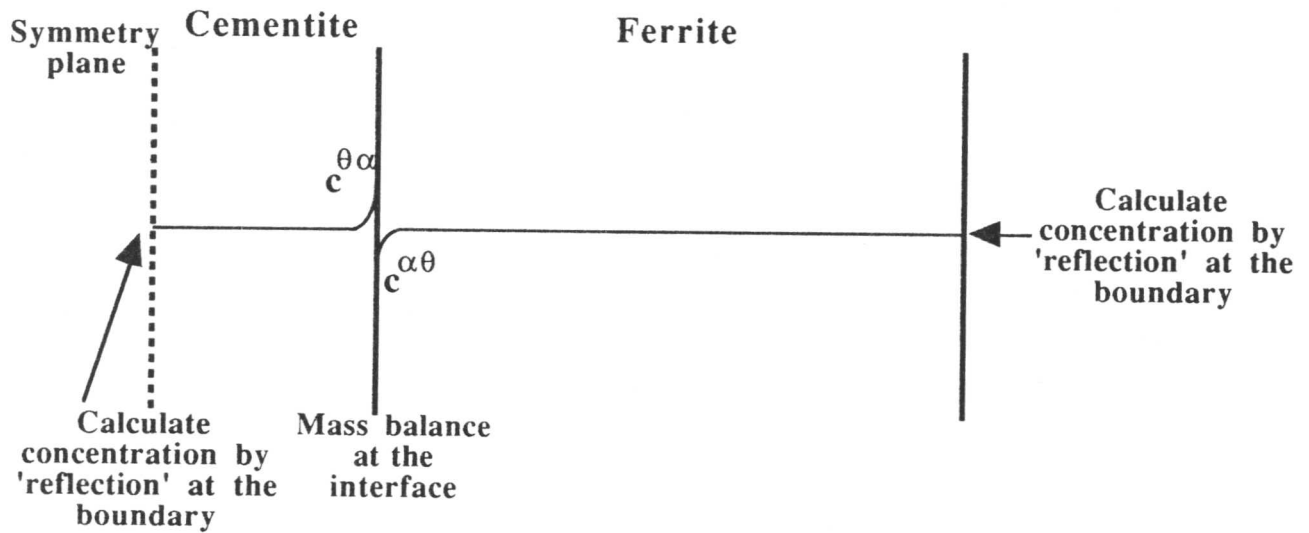


Figure 3.3: The diffusion couple and notation used for calculation of the enrichment rate of cementite in the symmetric case.

As the diffusion proceeds, $c_{0,j}^{\theta}$ eventually reaches $c^{\theta\alpha}/\bar{c}$ (at very long times). When this has occurred, it is diffusion in the cementite which begins to control the equilibration process, and the program switches to adjusting $c_{0,j}^{\alpha}$ to a value consistent with the condition for conservation of mass at the interface. The value of $c_{0,j}^{\alpha}$ then begins to increase to a value greater than $c^{\alpha\theta}/\bar{c}$.

It has already been stated that the diffusion coefficients of substitutional alloying elements in cementite are not known accurately. The sensitivity of the computer model to the value of the diffusion coefficient of Cr in cementite, D_{θ} , has been investigated. As the magnitude of the diffusion coefficient in cementite is reduced there are two main effects. The first is that the concentration in cementite at the particle/matrix interface rises more quickly as D_{θ} becomes

lower than D_α because of the need to satisfy the condition for mass balance at the interface (Equation 3.17). The second effect is an increase in the concentration gradient within the cementite particle because more time is necessary to redistribute the alloying element from the interface. For smaller particles, this will result in the overall enrichment rate being quicker because, although the diffusion coefficient is smaller, the diffusion distance is still comparable to the particle size and the increased concentration at the interface is able to redistribute across the particle. Larger particles, for which the diffusion distance is smaller than the size of the particle, are not affected significantly. (The diffusion distance, x , of a given element in a specific length of time, t , can be estimated using the formula $x^2 = Dt$ where D is an appropriate diffusion coefficient.)

Low-alloy steels used in the power generation industry, having been continuously cooled from the austenising temperature, are usually given a high temperature ($\simeq 700^\circ\text{C}$) stress-relief heat treatment before entering service at the lower temperature of $\simeq 565^\circ\text{C}$. Consequently, two computer programs have been developed, the first one (FINITE) is used for modelling the changes which take place during the stress-relief heat treatment, and the second (FINN), for which the input is the data generated by FINITE, to simulate the composition changes which occur during service after the stress-relief heat treatment. The computer program FINITE is presented in Appendix II.

The effect of temperature on the enrichment rate is illustrated in Chapter 5, the temperature dependence coming from the temperature dependence of the diffusion coefficient (equation 3.4) and the temperature variation of the equilibrium calculated level of substitutional alloying elements in cementite. Calculations are performed for a cementite particle in a $2\frac{1}{4}\text{Cr}1\text{Mo}$ steel, with a size of 60 nm at temperatures of 510, 565 and 620°C . The effect of particle size on the enrichment rate is discussed in Chapters 5 and 6 for $2\frac{1}{4}\text{Cr}1\text{Mo}$ and $\frac{1}{2}\text{Cr}\frac{1}{2}\text{Mo}\frac{1}{4}\text{V}$ steels respectively.

3.5.3 Asymmetric case – Definition of the problem

For the case in which the amount of ferrite on either side of the carbide plate is different, the central plane of the carbide is no longer a mirror plane and it becomes necessary to consider an asymmetric carbide distribution. The method of solution of the diffusion equations for an asymmetric carbide distribution is essentially the same as that for the symmetric case. Only the significant differences are highlighted below. The problem is initially set up with a slice of cementite of thickness x_θ in between two slices of ferrite (identified by the labels a and b) of

different thicknesses, $x_{\alpha a}$ and $x_{\alpha b}$ such that

$$\frac{x_{\theta}}{(x_{\alpha a} + x_{\theta b} + x_{\alpha b})} = V_{\theta}. \quad (3.19)$$

The input parameters for the calculation are the chosen particle size and volume fraction and a constant which represents the degree of inhomogeneity in the microstructure, the ratio of the thickness of ferrite (a) to ferrite (b). Hence, the program automatically calculates the thickness of the two ferrite slices to be consistent with the desired volume fraction and distribution of carbide.

The diffusion equation must be satisfied independently in both slices of ferrite and the cementite:

$$\frac{\partial c^{\theta}}{\partial t} = D^{\theta} \frac{\partial^2 c^{\theta}}{\partial x^2}, \quad (3.20)$$

$$\frac{\partial c^{\alpha a}}{\partial t} = D^{\alpha} \frac{\partial^2 c^{\alpha a}}{\partial x^2}, \quad (3.21)$$

$$\frac{\partial c^{\alpha b}}{\partial t} = D^{\alpha} \frac{\partial^2 c^{\alpha b}}{\partial x^2}. \quad (3.22)$$

3.5.4 Asymmetric case – Numerical solution

The number of slices in the cementite and ferrite are given by

$$n_{\theta} = \frac{x_{\theta}}{2x_s}, \quad (3.23)$$

$$n_{\alpha a} = \frac{x_{\alpha a}}{x_s}, \quad (3.24)$$

$$n_{\alpha b} = \frac{x_{\alpha b}}{x_s}. \quad (3.25)$$

The finite difference approximations to the diffusion equation are the same as in the symmetric case (equation 3.15) with an additional equation being added for the second ferrite slice. The boundary conditions are the same as for the symmetric case, although in the asymmetric case there are four, rather than two, boundaries to be considered. Soft impingement is taken into account at the extremes of the two ferrite slices in the same manner as equation 3.18. This allows the different fluxes originating from the two ferrite/cementite interfaces to be taken into account. The condition for mass balance (equation 3.17) is applied separately at the interfaces between cementite and ferrite (a), and between cementite and ferrite (b). Both $c^{\alpha \theta a}$ and $c^{\alpha \theta b}$ are initially set to $c^{\alpha \theta} / \bar{c}$, but are then allowed to vary independently because of the asymmetric carbide distribution. The numerical calculation of the level of substitutional solute in the cementite takes into account the differences in the interface values. The asymmetric diffusion

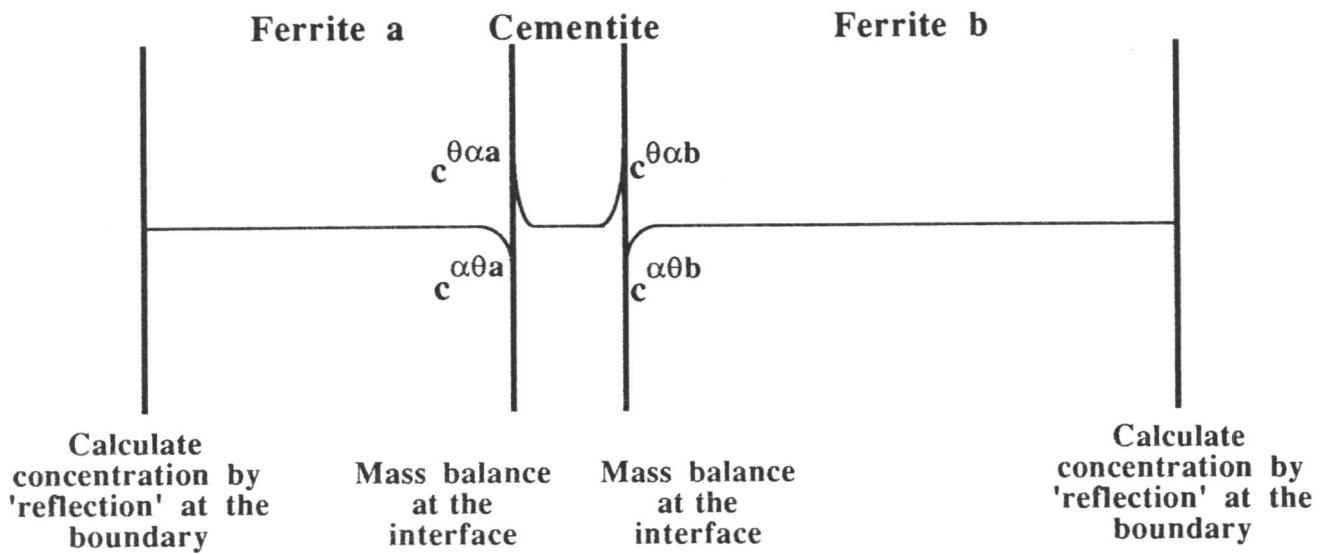


Figure 3.4: The diffusion couple and notation used for calculation of the enrichment rate of cementite in the asymmetric case.

couple and the notation used in the calculation of enrichment rate are illustrated in Figure 3.4. The computer program used in the asymmetric case (INHOMOG) is presented in Appendix III.

Figure 3.5 illustrates the effect of varying degrees of inhomogeneity in the microstructure. The chromium content of a cementite particle of size 60 nm is plotted as a function of the square root of time for a symmetric distribution, and for one ferrite slice being twice and five times as big as the other. The calculations were done at a temperature of 565°C for a 2 $\frac{1}{4}$ Cr1Mo steel. It can be seen that there is a marked reduction in the enrichment rate as the microstructure becomes more inhomogeneous. This is due to soft impingement in the smaller ferrite slice happening earlier than in the symmetric case and slowing down the rate of diffusion.

Figure 3.6 shows the actual chromium concentration profiles through the diffusion couple, one ferrite slice being twice the size of the other. The cementite particle size was chosen to be 50 nm and the calculations were again performed at 565°C for a 2 $\frac{1}{4}$ Cr1Mo steel. Four curves are shown on the graph representing intermediate times of 40, 100, 200 and 3,500 hours in the diffusion process. The average chromium concentration in the cementite particle can be seen to be gradually increasing as a function of time as it approaches equilibrium. After 3,500 hours the profiles are flat in both the cementite and ferrite, indicating that saturation has been reached.

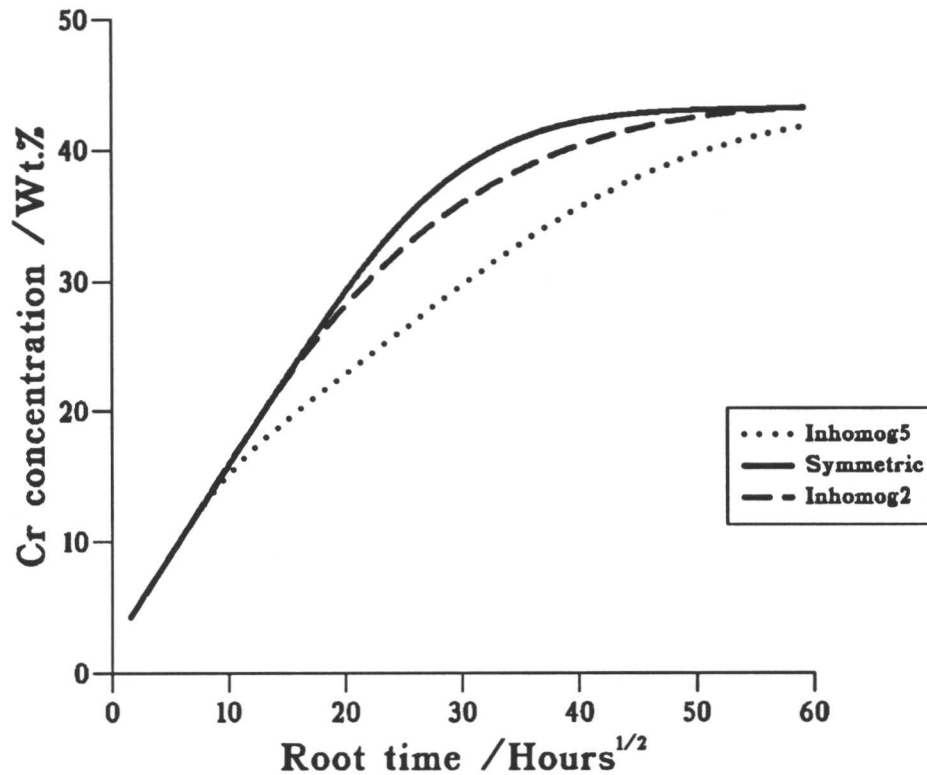


Figure 3.5: Chromium concentration in a cementite particle as a function of the square root of time for varying degrees of inhomogeneity in the microstructure.

Soft impingement can also be seen to be occurring more rapidly in the shorter ferrite slice; the concentration at the extent of the ferrite drops as it begins to be affected by fluxes originating at the interface.

The chromium profile inside the cementite particle used in Figure 3.6 is illustrated in Figure 3.7. The profile corresponds to a diffusion time of 100 hours. The slightly asymmetric profile in the cementite particle reflects the fact that soft impingement has occurred in the smaller ferrite slice. Comparison of the prediction of the asymmetric model with experimental results are made in Chapter 5.

3.6 Consideration of the effect of particle size

The use of the finite-difference model has highlighted the strong effect of particle thickness on its average composition during ageing. For a given flux across the θ/α interface, smaller particles will be sinks for solute and will enrich at a higher rate. Output from the model has indicated that the time t_c to reach a given composition varies as $(x_\theta)^2$, although this is only the case if soft impingement has not occurred in the ferrite (corresponding to approximately 8,000 hours of service life). It is possible to account for this analytically; however, the analysis

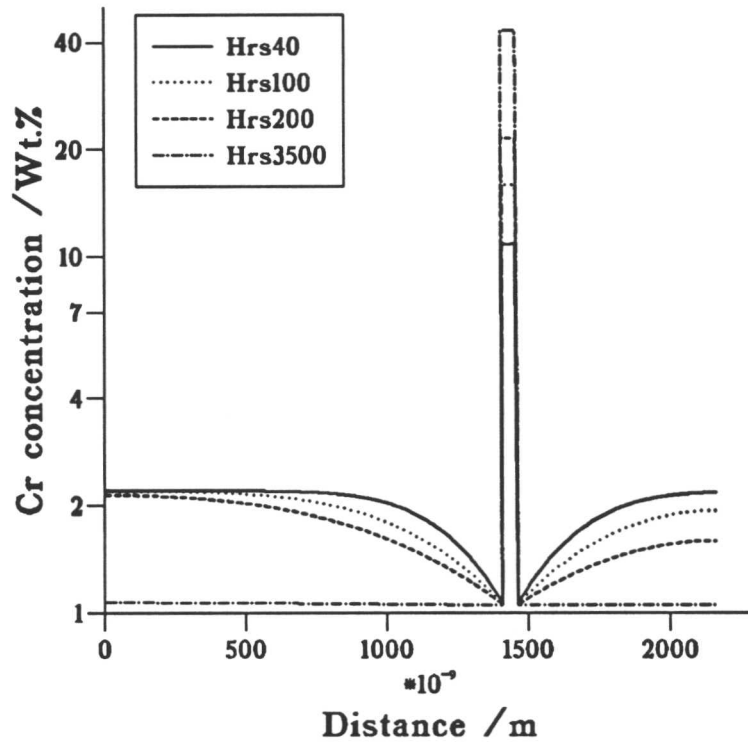


Figure 3.6: Chromium concentration profiles through a diffusion couple at times of 40, 100, 200 and 3500 hours during the diffusion process. The cementite particle size is 50 nm and the temperature 565°C.

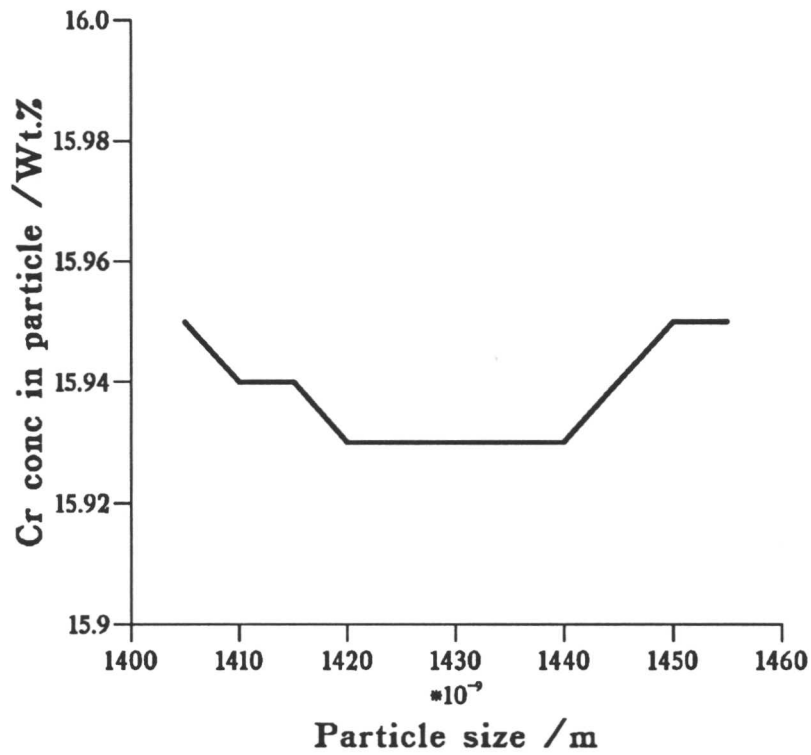


Figure 3.7: Schematic illustration of the chromium concentration profile within a cementite particle after 100 hours at 565°C.

cannot allow for the coupling of fluxes between the cementite and ferrite and so will tend to overestimate the time required to reach a given concentration.

Consider a slab of thickness x_θ embedded in an infinite matrix of ferrite (and no soft impingement in the ferrite). If the time required for the cementite to reach a concentration c^θ is t_c , then a standard mass balance procedure can be used (e.g. Crank, 1975) to show that

$$0.5x_\theta(c^\theta - \bar{c}) = \int_0^\infty c^\alpha(x, t_c) dx, \quad (3.26)$$

where

$$c^\alpha(x, t_c) = (\bar{c} - c^{\alpha\theta}) \operatorname{erfc} \left(\frac{x}{2\sqrt{D_\alpha t_c}} \right). \quad (3.27)$$

This equation can be solved to show that

$$t_c = \frac{\pi x_\theta^2 (\bar{c} - c^\theta)^2}{16D_\alpha (c^{\alpha\theta} - \bar{c})^2}. \quad (3.28)$$

It can be seen that, within the validity of the equation, the composition of cementite should vary with $t^{\frac{1}{2}}$ rather than with $t^{\frac{1}{3}}$. It should also be noted that, since $c^{\alpha\theta}$ is a relatively weak function of temperature, most of the temperature dependence of the ageing process comes from D_α . This means that for experiments carried out at various temperatures a plot of $\ln t_c$ against $1/T$ should give a positive slope corresponding to the activation energy for diffusion divided by the universal gas constant.

A similar analysis can be carried out for spherical particles, following Crank (1975). If the particle radius is a and the distance ahead of the particle is noted by r , then the solute distribution ahead of the particle is given by

$$c^\alpha(s, t_c) = \left[\frac{a(\bar{c} - c^{\alpha\theta})}{(a + s)} \right] \operatorname{erfc} \left(\frac{s}{2\sqrt{D_\alpha t_c}} \right). \quad (3.29)$$

Using the same procedure as above, it can be shown that

$$\frac{a^2(c^{\theta\alpha} - \bar{c})}{3(\bar{c} - c^{\alpha\theta})} = D_\alpha t_c + 2a\sqrt{\frac{D_\alpha t_c}{\pi}}. \quad (3.30)$$

In this case an initial enrichment proportional to $t^{\frac{1}{2}}$ is indicated, with a subsequent reduction in the time exponent. In both cases the enrichment also varies with the square of the particle radius in agreement with the numerical model. However, it is more difficult to interpret an activation energy for the spherical particles as the equation is no longer linear in D_α .

CHAPTER 4

EXPERIMENTAL PROCEDURE

The various techniques employed in the experimental studies of precipitation characteristics in $2\frac{1}{4}\text{Cr1Mo}$, $\frac{1}{2}\text{Cr}\frac{1}{2}\text{Mo}\frac{1}{4}\text{V}$ and 12Cr1MoV steels are described in this chapter.

CHAPTER 4

EXPERIMENTAL PROCEDURE

4.1 Introduction

This chapter includes a description of the experimental programme and the techniques employed, as summarised in Figure 4.1.

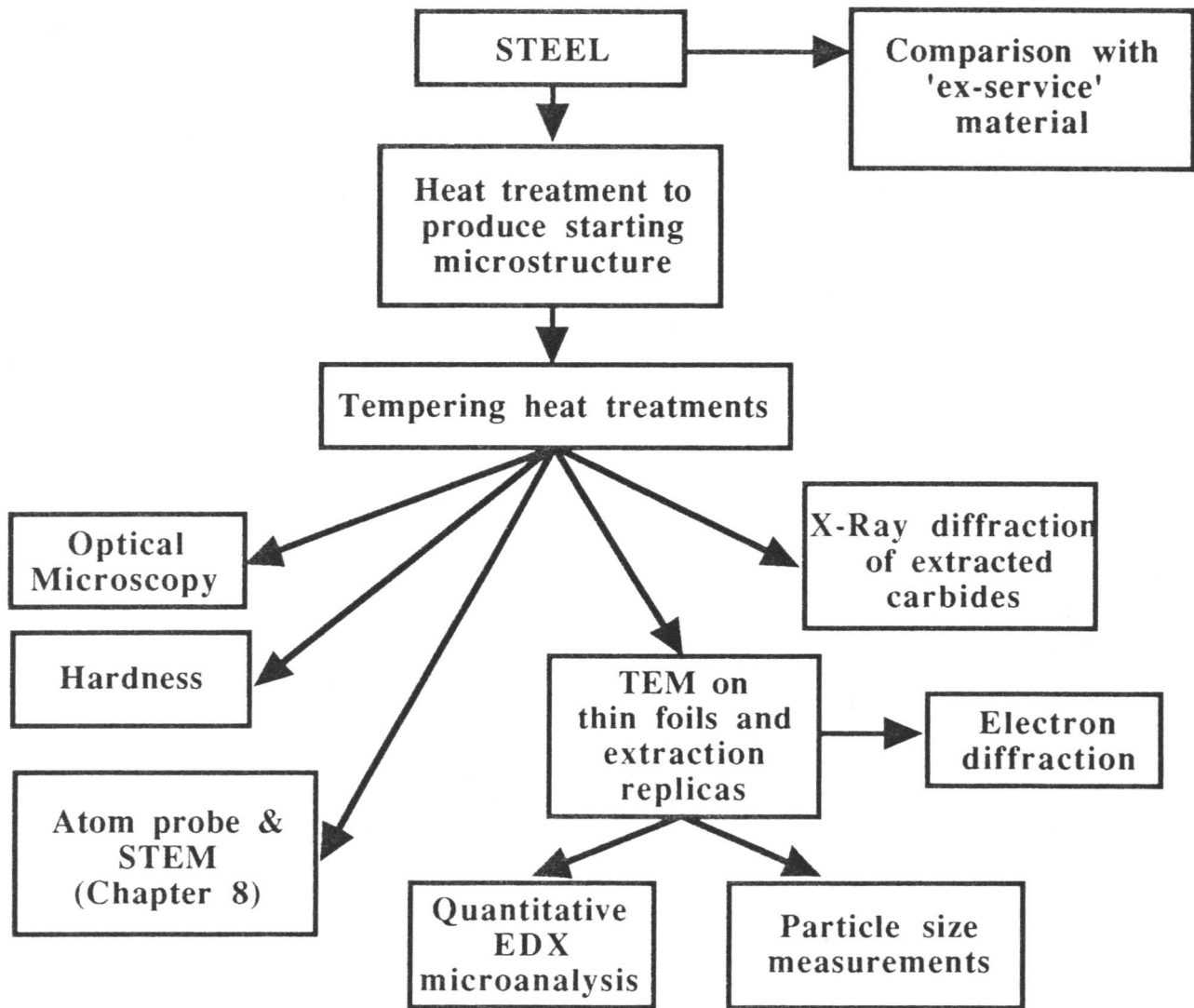


Figure 4.1: Flow chart illustrating the detailed experimental programme for three steels with different chromium contents.

4.2 Materials

The precipitation of cementite and other alloy carbide phases was examined for three typical power plant steels of varying chromium concentrations. The first was a $\frac{1}{2}\text{Cr}\frac{1}{2}\text{Mo}\frac{1}{4}\text{V}$ steel with a pearlitic microstructure which was expected to contain cementite as the dominant carbide phase at the temperatures of interest for several hundred years. The second contained slightly more chromium, $2\frac{1}{4}\text{Cr}1\text{Mo}$, the starting microstructure consisting of a mixture of bainite and martensite. Alloy carbides began to precipitate at the expense of cementite after a few hundred hours in this steel. The third steel was heavily alloyed with chromium, $12\text{Cr}1\text{MoV}$, resulting in the equilibrium alloy carbide precipitating within a few minutes on tempering at elevated temperatures. The chemical compositions of the steels used are given in Table 4.1. Further details of the materials supplied and heat treatments employed are given in Chapters 5, 6 and 7 for the $2\frac{1}{4}\text{Cr}1\text{Mo}$, $\frac{1}{2}\text{Cr}\frac{1}{2}\text{Mo}\frac{1}{4}\text{V}$ and $12\text{Cr}1\text{MoV}$ steels respectively. The $\frac{1}{2}\text{Cr}\frac{1}{2}\text{Mo}\frac{1}{4}\text{V}$ steel was supplied as prepared carbon extraction replicas from previous work by Du (1986). Details of the original method of preparation of the replicas are included below for completeness. Additional measurements were made on these specimens in order to relate particle size and chemical composition.

Table 4.1: Chemical composition of the steels used in wt. %

Steel	C	Si	Mn	P	S	Cr	Mo	V	Ni	Cu	Co	Nb+Ta	As	Sn
$\frac{1}{2}\text{Cr}\frac{1}{2}\text{Mo}\frac{1}{4}\text{V}$	0.14	0.23	0.61	0.007	0.023	0.36	0.66	0.26	0.21	0.13	–	–	–	–
$2\frac{1}{4}\text{Cr}1\text{Mo}$	0.15	0.29	0.49	0.01	0.025	2.20	0.96	0.01	0.14	0.18	0.02	–	0.03	0.02
12Cr1MoV	0.21	0.25	0.46	0.009	0.012	10.9	1.03	0.30	0.52	0.02	0.02	0.06	–	–
Ex-service 'X20CrMoV12'	0.18	0.22	0.58	0.01	0.007	12.4	1.07	0.28	0.64	0.13	0.03	<0.01	–	–

4.3 Heat treatments

4.3.1 Furnace heat treatments

Prior to the tempering heat treatments, the samples were sealed in silica tubes under a partial pressure of argon (150 mm Hg) to prevent any decarburisation or oxidation. The quartz tubes were then placed on ceramic boats inside furnaces to prevent any contamination by contact with the base of the furnace. The furnace temperatures were checked at regular intervals during the long term heat treatments with a Pt/Pt–13 wt.% Rh thermocouple.

4.3.2 Thermomechanical simulator heat treatments

A thermomechanical simulator ('Thermecmastor' manufactured by Fuji Electronic Industrial Co. Ltd.) was used in order to control and follow the initial heat treatments of the $2\frac{1}{4}\text{Cr1Mo}$ steel more accurately than could be achieved in a furnace. The Thermecmastor incorporates a sophisticated dilatometer, although is usually used for investigations of the effects of stress on transformation because the strains can be monitored in two orthogonal directions. It has a high frequency induction heating system, allowing homogeneous heating of the specimen to within $\pm 5^\circ\text{C}$, and is computer controlled enabling the heat treatment cycle to be programmed and monitored with ease. Heating can be done under a vacuum or with a gas atmosphere (Ar, N_2). Rapid heating and cooling at specified rates are also possible, with the gases Ar, He or N_2 being used for quenching. In this work heating was performed in an argon atmosphere and quenching was done with nitrogen gas. Temperature is measured using a Pt/Pt-13 wt.% Rh thermocouple resistance welded to the specimen. The dilation of the specimen in a radial direction during transformation is measured using a laser beam. Specimens for tests (under compression or with no applied load) are cylinders of 8 mm diameter and 12 mm long.

In order to prevent surface oxidation and nucleation effects (Strangwood and Bhadeshia, 1987), the specimens were nickel plated before use in the Thermecmastor. The nickel plating was carried out in two stages. Firstly, an adherent but rough layer of Ni was plated onto the surface by a 'striking' treatment in a solution of 250 g of nickel sulphate, 27 ml of concentrated sulphuric acid and 1 litre of water, with an applied current density of 7.75 mA mm^{-2} , for 6 minutes. After striking the samples were plated in a solution containing 140 g nickel sulphate, 140 g anhydrous sodium sulphate, 15 g of ammonium chloride and 20 g boric acid made up to a litre with distilled water. The applied current density was 0.4 mA mm^{-2} , and plating was carried out for 30 mins resulting in a nickel layer thickness of approximately 0.1 mm.

4.4 Hardness measurements

Macrohardness measurements were made using a Vickers pyramid hardness testing machine using a load of 30 kg and an $\frac{2}{3}''$ objective. Five measurements were taken over the whole sample area. Microhardness measurements were made with a Leitz miniload machine using a load of 0.981 N, and loading and dwell times of 15 seconds each. Twenty measurements were taken over the whole area of the specimen and the mean value calculated.

4.5 Optical microscopy

Samples were prepared for microstructural characterisation by hot mounting in acrylic moulding powder, followed by grinding on SiC paper to 1200 grit and polishing with $1 \mu\text{m}$ cloth

coated with diamond paste. Specimens of $2\frac{1}{4}\text{Cr1Mo}$ steel were etched in 2% nital (nitric acid in methanol) and specimens of the 12Cr1MoV steel were etched using Bain–Vilella’s reagent (5 ml hydrochloric acid, 1 g picric acid in 100 ml of methanol) for times of up to 3 minutes. Samples of the $\frac{1}{2}\text{Cr}\frac{1}{2}\text{Mo}\frac{1}{4}\text{V}$ steel were received already in the form of carbon extraction replicas; however, these were originally etched in 4% nital for cementite extraction from the shorter time heat treatments, and in Vilella’s reagent for extraction of the larger alloy carbides from the longer term heat treatments. Optical micrographs were taken with an Olympus microscope with a camera attached using Ilford Pan F film.

4.6 Transmission electron microscopy

Specimens for transmission electron microscopy (TEM) were prepared by both by the twin–jet electropolishing of thin foils and the carbon extraction replica technique.

4.6.1 Thin foil preparation

Thin 3 mm discs are required as the starting point for thin foil preparation. These were cut directly from the heat–treated 3 mm rods of the 12Cr1MoV steel using a SiC slitting wheel, whereas 3 mm discs were mechanically punched out of thin slices cut from the larger rectangular specimens of $2\frac{1}{4}\text{Cr1Mo}$ steel using a high–speed saw. The discs were then mechanically ground by hand to 50 μm and then twin–jet electropolished to electron transparency at 50 V, with the solution being cooled to 0°C using liquid nitrogen. The polishing solution used for the 12Cr1MoV steel contained 10% perchloric acid, 15% glycerol and 75% industrial methylated spirits, and that for the $2\frac{1}{4}\text{Cr1Mo}$ steel, 5% perchloric acid, 20% glycerol and 75% industrial methylated spirits. The thinned samples were examined in a Phillips 400T TEM operated at 120 kV.

4.6.2 Extraction replica preparation

The extraction replica technique is very useful for the identification or counting of carbide or precipitate phases in a metallic system. The main advantages of replicas over foils are that they eliminate any effects due to the steel matrix and thus enable the chemical composition of the carbides to be measured more accurately, and working with a magnetic specimen in the electron microscope is avoided. The replica is also very thin $\simeq 100 \text{ \AA}$, has no self–structure and will not burn in an electron beam.

Single–stage carbon extraction replicas were prepared using the method described by Smith and Nutting (1956) from surfaces prepared as for optical microscopy using a lighter etch. Shadowing of the carbon replica with gold (Mukherjee *et al.*, 1968) was not considered necessary

because only the particle sizes were measured, rather than volume fractions. The presence of gold on the replica would also have interfered with the electron diffraction and quantitative EDX measurements used to identify the second phase particles. A carbon coating of 200-300 Å (colour blue-brown) was deposited in a vacuum of 10^{-5} torr on to the etched specimens. The carbon film was scored using a sharp blade to enable removal of several small sections covering the whole area of the sample. The film was then removed by electrolytic etching in a solution containing 5% hydrochloric acid in methanol at +1.5 V. The film was then washed in industrial methylated spirits and floated off in distilled water and collected on 400 square mesh copper grids for examination in the TEM. Replicas from the $\frac{1}{2}\text{Cr}\frac{1}{2}\text{Mo}\frac{1}{4}\text{V}$ steel specimens were originally prepared using 4% nital for specimens previously etched in 4% nital, and 10% nital for those previously etched in Vilella's reagent.

4.6.3 Calibration of the camera constant

The settings of the various magnetic lenses within the column of a TEM affect the magnification of diffraction patterns. Usually the microscope is operated with the lenses at fixed settings and so the magnification of the diffraction pattern is a constant. This magnification factor is expressed in terms of an equivalent camera length necessary to produce the same magnification in a diffraction camera without the lenses. This is illustrated schematically in Figure 4.2.

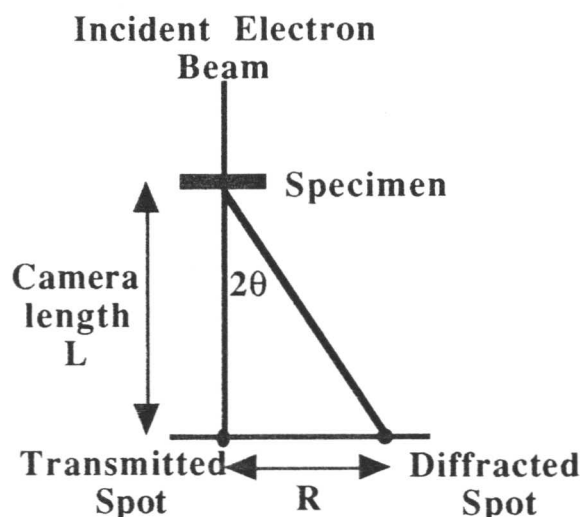


Figure 4.2: Schematic illustration of the magnification of a diffraction pattern by the microscope lenses.

The camera constant is denoted by the expression, corrected for relativistic effects,

$$Rd_{\{hkl\}} = L\lambda = \text{camera constant} \quad (4.1)$$

where R is the real distance measured on the diffraction pattern between the transmitted and the diffracted spot, L is the camera length (usually 575 mm or 800 mm in the Philips 400T TEM operated at 120 kV), $d_{\{hkl\}}$ is the spacing of the $\{hkl\}$ crystallographic planes and λ is the electron wavelength. λ is given by the following expression which is corrected for relativistic effects:-

$$\lambda = \frac{h}{2meV \left(1 + \frac{eV}{2mc^2}\right)} = 0.03335\text{\AA}, \quad (4.2)$$

where h is Planck's constant, m and e are the electron mass and charge respectively, V is the accelerating voltage of the electrons and c is the speed of light in vacuum.

It was very important for the identification of the various carbide phases which have similar lattice parameters to determine the camera constant accurately. This was done by examination of the diffraction pattern from a gold film sputtered onto a copper grid. A film produced by chemical vapour deposition consists of very fine grain size polycrystals. For a given electron beam direction a number of particles are oriented so as to satisfy the Bragg equation hence each plane gives rise to a number of reflections lying in a cone of angle 4θ . The resulting diffraction pattern therefore consists of a set of concentric rings corresponding to the $\{hkl\}$ planes which are diffracting.

To calculate the camera constant the diameters of the rings in the diffraction pattern were first measured. Then the ratios of the squares of the radii of the outer rings to those of the first or second low-index ring were determined. This enabled the N values corresponding to each of the rings to be found; N is given by the usual expression for cubic systems

$$N^2 = h^2 + k^2 + l^2, \quad (4.3)$$

where $\{hkl\}$ are the plane indices. The N values were then converted to d spacings using the formula

$$d = \frac{a}{\sqrt{N}} \quad (4.4)$$

for cubic systems. The accurate lattice parameter, a , for gold has been measured as 4.0780Å (Barrett and Massalski, 1968). Multiplication of the calculated d spacings by the radius of each individual ring gives a constant value. The average of all the values for the individual rings was used for the best accuracy. This method is illustrated in Table 4.2, which evaluates the camera constant for a current of 6.40 A through the objective lens at the eucentric specimen height. The diffraction pattern from the sputtered gold film is illustrated in

Figure 4.3. The calculated camera constants for a number of different nominal camera lengths and currents through the objective lens used in the characterisation of second phases are given in Table 4.3. The various carbides were identified using both selected area electron diffraction and convergent beam electron diffraction when the carbides were very small compared with the size of the selected area diffraction aperture.

Table 4.3: Calculated camera constants for a number of different nominal camera lengths and currents through the objective lens.

Nominal camera length /mm	Objective lens current /A	Calculated camera constant / $\times 10^{12}\text{m}^2$
800	6.40	2.66
800	6.20	2.71
575	6.20	1.86

4.7 Energy dispersive X-ray analysis (EDX)

For the detailed experimental results of particle size and composition on the $\frac{1}{2}\text{Cr}\frac{1}{2}\text{Mo}\frac{1}{4}\text{V}$, $2\frac{1}{4}\text{Cr1Mo}$ and 12Cr1MoV steels, detailed microanalyses were carried out on particles using carbon extraction replicas. At least 30 isolated particles on each specimen were analysed, depending on the particular measured composition variation, covering an area of several grid squares. In the early stages of tempering the cementite composition was found to vary so greatly between different particles that up to 100 analyses were needed to get a good estimation of the variation and a reasonable estimate of the average concentration. A LINK series 860 energy dispersive X-ray spectrometer attached to a Phillips 400T 120 kV TEM was used for all the analyses. X-ray spectra were recorded at a specimen tilt of 35° , and live times of at least 200 seconds were used to ensure statistically significant results, depending on the count rate from individual particles. The dead time was not allowed to exceed 25%. The data were analysed using the LINK RTS2-FLS software.

The original measurements on the $\frac{1}{2}\text{Cr}\frac{1}{2}\text{Mo}\frac{1}{4}\text{V}$ specimens made by Du (1986) were on extraction replicas in both a 100kV Philips 400T and a 200kV Hitachi H-700T transmission electron microscope, each equipped with an EDAX 9100 energy dispersive X-ray analysis facility. 50,000, 25,000 and 25,000 counts were preset in the Fe K_α , Mo K_α and V K_α windows respectively to keep a constant statistical error. Counts from the carbon replica background were kept at 200 ± 50 counts per second in the Hitachi H-700T and 100 ± 50 cpts in the Philips

400T microscopes to ensure a constant intensity beam. The incident spot size was 1000 Å and all the analyses were done with the spot covering the whole particle.

Chromium is chosen as an indicator of composition change because of its large concentration and partition coefficient; the iron content simply mirrors the changes in chromium content. The total manganese content is relatively small and therefore any errors will be relatively large. Molybdenum has a much larger atomic mass compared with iron, chromium or manganese. Since the microanalytic measurements are carried out assuming that all elements absorb the X-rays to a similar degree, the molybdenum data are likely to be flawed, the extent of the error depending on the thickness of the particle along the electron beam direction (a parameter which is very difficult to determine for each individual particle).

Typical EDX spectra for the various carbides in the three steels are presented in detail in the experimental chapters 5, 6 and 7.

4.7.1 Basis for quantification of EDX

Quantitative microanalysis involves the comparison of the intensities of an unknown peak with that from a measured or calculated standard, removal of the background, peak integration and correction for peak overlap. The intensity of a peak is proportional to the composition of the material being analysed. In order to avoid determination of various constants depending on mass, specimen thickness and diffraction conditions, ratios of the integrated characteristic intensities are related to the composition of the specimen using the equation due to Goldstein *et al.* (1986) for a binary system

$$\frac{C_A}{C_B} = k_{AB} \frac{I_A}{I_B}, \quad (4.5)$$

where C_A and C_B are the weight fractions of elements A and B in the analysed volume, I_A and I_B are the characteristic intensities of elements A and B (after subtraction of the background), and k_{AB} is an experimental constant. The number of similar equations for all the elements being analysed is necessarily less than the number of elements, therefore in order to solve these equations it is assumed that all the elements are detected and that the sum of the concentrations is 100%. It should be noted that due to the presence of a beryllium window on the front of the EDX detector, the carbon content of carbides cannot be allowed for. The results of the EDX analyses can be normalised to allow for the appropriate stoichiometric carbon content in the various carbides.

The factors k_{AB} , k_{AC} , k_{CB} etc. can be determined experimentally using pure elements or homogeneous compounds containing the desired element and the element chosen as a standard (Si in this case), e.g. chromium silicide, or by calculation from first principles. Experimental

determination is better due to difficulties into taking account of the detector response and other minor factors. The peak intensities and shapes from the standard compounds are used to determine the k-factors for every element to be analysed normalised with respect to Si. Pure compounds containing Si were used to determine the k-factors experimentally for the elements of interest when the EDX system was set up. The overall intrinsic system error is $\simeq 0.5\text{--}1.0\%$. The characteristic energies for the X-ray peaks of interest and the k-factors with respect to Si are given in Table 4.4.

Table 4.4: Characteristic X-ray peak energies for EDX. The average energy is given for the $K\alpha_1$ and $K\alpha_2$ peaks because, unlike X-ray diffraction, EDX is not usually able to resolve these peaks. The k-factors determined from standard compounds are included for the more intense α peaks only.

Element	Peak	Energy /keV	k_{Si}
Mo	$L_{\alpha_{1,2}}$	2.293	1.766
Mo	L_{β_1}	2.394	–
V	$K_{\alpha_{1,2}}$	4.948	1.197
Cr	$K_{\alpha_{1,2}}$	5.410	1.213
V	L_{β_1}	5.427	–
Mn	$K_{\alpha_{1,2}}$	5.898	1.291
Cr	K_{β_1}	5.946	–
Fe	$K_{\alpha_{1,2}}$	6.397	1.322
Mn	K_{β_1}	6.490	–
Fe	K_{β_1}	7.057	–
Cu	$K_{\alpha_{1,2}}$	8.037	1.595
Cu	K_{β_1}	8.940	–
Mo	$K_{\alpha_{1,2}}$	17.426	4.830
Mo	K_{β_1}	19.786	–

Correction for the absorption of characteristic X-rays in the particle analysed have been ignored, being close to unity for the average size of carbide present (< 100 nm). Characteristic X-ray fluorescence is of second order in magnitude to absorption and is therefore also ignored.

4.8 Particle size measurements

The size of each carbide particle was determined by measuring a number of random intercepts across it on the photographic negative. Hence, particle size is expressed in terms of a

mean linear intercept. This measure was chosen as it is closely related to the diffusion distance across the particle and can be used for irregular geometries. The particles are in the form of thin plates, so that most of the enrichment should be from diffusion in a direction normal to the plate plane. The linear intercept as measured above, should give a good description of the particle size along this diffusion direction.

4.9 Bulk extraction of carbides and X-ray diffraction

It is possible to isolate the carbide precipitates in steels by the electrochemical dissolution of the matrix. X-ray diffraction of the extracted particles can then be used for identification and quantitative analysis, including accurate lattice parameter measurements and volume fraction data for the various carbides formed in the steel during tempering. This technique is discussed in detail by Andrews and Hughes (1958), and more recently by Stuart and Ridley (1966), Leitnaker *et al.* (1975), Pilling and Ridley (1982) and Stevens and Lonsdale (1987).

In particular Stevens and Lonsdale (1987) investigated the experimental conditions necessary for optimum carbide extraction. The composition and strength of the electrolyte and the conditions of voltage or current density determine the efficiency with which dissolution of the matrix occurs whilst leaving the carbide precipitates intact. Chemical dissolution of the extracted precipitates in the electrolyte can occur. This is dependent on the electrolyte and the temperature and time of the extraction. The use of high voltages and associated high current densities results in large amounts of carbides being extracted in a short time; however, the likelihood of chemical dissolution of the precipitates may be increased by resistance heating of the electrolyte. The precipitates are more likely to separate from the specimen and fall into the solution thus increasing their risk of loss. The literature suggests that 5% aqueous hydrochloric acid is suitable for the extraction of low alloy steels, whereas 10% alcoholic hydrochloric acid is usually used for high alloy steels. The disadvantages of the alcohol as a base are that the lower associated current densities result in a higher acid concentration and longer extraction times having to be used, enhancing chemical dissolution of extracted carbides. Stevens and Lonsdale (1987) also suggest that for steels containing the carbide M_3C using alcohol as a base may mean that few of these carbides are extracted.

The specimen was anodically dissolved in a cell with a platinum cathode and a solution of 5% hydrochloric acid in water for the $2\frac{1}{4}Cr1Mo$ steel and 10% hydrochloric acid in methanol for the $12Cr1MoV$ steel as the electrolyte at a voltage of 1.5 V. Typical extraction times were 6–8 hours. The electrolyte was then decanted off and the precipitate thoroughly dried in an oven at approximately 60°C. Careful weighing at all stages of the extraction to an accuracy of 10 μg

was performed to find the exact amount of precipitate extracted. An internal standard, CeO_2 , was added to the precipitates. This was accurately weighed to approximately 25% of the total mass of the precipitate. A Siemens D500 diffractometer (CuK_α radiation) was used to scan between 30° and $65^\circ 2\theta$ at a step size of 1 second duration, corresponding to $0.004^\circ 2\theta$, where θ is the Bragg angle. The diffraction peak positions were located using Siemens DIFFRAC 500 software, also used to calculate the associated integrated intensities of the peaks.

CHAPTER 5

$2\frac{1}{4}$ Cr1Mo STEEL

Extensive studies of cementite composition changes in bainitic and mixed microstructures of bainite and allotriomorphic ferrite are discussed in this chapter. The observed composition changes are found to be highly dependent on the position of the carbides within the microstructure and on the particle size. The transformation of the cementite to alloy carbides is also studied. It is found that alloy carbides precipitate with a composition very close to their equilibrium composition and therefore subsequent enrichment is negligible.

CHAPTER 5

$2\frac{1}{4}$ Cr1Mo STEEL

5.1 Introduction

$2\frac{1}{4}$ Cr1Mo steel is widely used for superheater tubing in power plant, and as filler materials for joining $\frac{1}{2}$ Cr $\frac{1}{2}$ Mo $\frac{1}{4}$ V steam piping. Its creep properties, and their correlation with microstructural changes, have been studied widely (e.g. Baker and Nutting, 1959; Hale, 1975; Klueh, 1978). It is well established that the creep properties improve with subsequent tempering and then eventually degrade after the precipitation of the larger equilibrium alloy carbides. $2\frac{1}{4}$ Cr1Mo steel is usually given a stress-relief heat treatment at 700°C before going into service at a temperature of approximately 565°C. Klueh (1978) states that the creep rate is controlled initially by the motion of dislocations which contain atmospheres of carbon and possibly molybdenum clusters, and subsequently by atmosphere-free dislocations moving through M_2C precipitates.

The high temperature mechanical properties of the material are affected strongly by the metallurgical instability of the alloy involving carbide precipitation reactions. The tempering process results initially in the formation of iron carbides, which are subsequently replaced by more stable alloy carbides. Many studies of the precipitation sequences in $2\frac{1}{4}$ Cr1Mo steels have been made. Baker and Nutting (1959) discuss precipitation sequences in a commercial alloy in both quenched and normalised conditions in the temperature range 673–1023K. Andrews *et al.* (1972) have produced a comprehensive set of ‘near-equilibrium’ experimental diagrams relating to carbide stability. They used many steels in the composition ranges 0–6 wt.% Cr, 0–2 wt.% Mo and 0–1wt.% V, and tempered as-quenched microstructures for up to 1000 hours at 923 and 973K. Titchmarsh (1978) studied carbide precipitation in samples tempered at 933K for up to 200 hours in order to demonstrate the identification of various carbides using EDX analysis techniques. Hipsley (1981) also studied $2\frac{1}{4}$ Cr1Mo steel, although this was in the context of cracking during the stress-relief heat treatment in the bainitic Heat-Affected-Zone (HAZ) of welds. Pilling and Ridley (1982) investigated the effect of carbon content in three low carbon $2\frac{1}{4}$ Cr1Mo alloys, tempering at 700°C.

Baker and Nutting (1959) found that the sequences of carbide precipitation in the normalised (ferritic/bainitic) and quenched (autotempered martensite) microstructures were almost identical. The only difference being that precipitation of M_2C occurred in the early stages of tempering the normalised steel, and persisted in the ferrite phase, forming well-defined flat-

tened needles. They also found that bainitic carbides spheroidised quickly during tempering at 600°C. After 50 hours Cr_7C_3 was found in the bainite near the bainite/ferrite interface, M_{23}C_6 then being found in the bainitic regions, and only in the regions which were free from Cr_7C_3 . The experimental results of Baker and Nutting are presented in Figure 5.1.

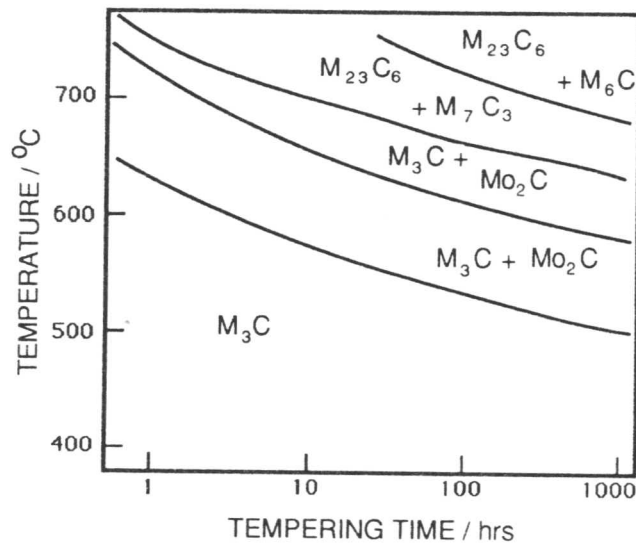


Figure 5.1: Carbide stability diagram for a $2\frac{1}{4}\text{Cr}1\text{Mo}$ steel. (Modified from Baker and Nutting, 1959)

There is evidence to suggest that small changes in chemical composition can alter the precipitation behaviour of the alloy. Yu (1989) has shown that increasing the silicon concentration stabilises M_6C , and accelerates the precipitation of M_2C . Similarly an increase in the manganese concentration was found to accelerate the precipitation of M_7C_3 . An analysis based on the thermodynamic stability as a function of chemistry and temperature could in principle be used to explain these results. However, no information can be obtained on the rate of precipitation from such calculations. In stating such precipitation sequences, it is important to relate them to the part of the microstructure in which they occur. Lee (1989) has recently confirmed that the starting microstructure can have a profound effect on the tempering sequence. In a Fe-1Cr-0.5Mo-0.15C wt.% steel detailed differences between pearlitic, bainitic and ferritic microstructures were demonstrated, and it was also shown that the carbide type was sensitive to position within the microstructure. The predicted equilibrium carbides in the steel utilised in this work using MTDATA were M_6C and M_{23}C_6 in the temperature range 500–650°C.

5.2 Materials

The $2\frac{1}{4}\text{Cr}1\text{Mo}$ steel was supplied in the form of a cylindrical bar approximately 100 mm in diameter and 300 mm long. Rectangular specimens of size 10×10×60 mm were machined from

the bar for furnace heat-treatment, and smaller cylindrical specimens of 8 mm diameter and 12 mm length were also machined for use in the thermomechanical simulator. The chemical composition of the steel (in wt. %) is given in Table 5.1.

Table 5.1: Chemical composition of $2\frac{1}{4}$ Cr1Mo steel in wt. %

C	Si	Mn	P	S	Cr	Mo	V	Ni	Cu	Al	Co	As	Sn
0.15	0.29	0.49	0.01	0.025	2.20	0.96	0.01	0.14	0.18	< 0.01	0.02	0.03	0.02

5.3 Initial heat treatments

The initial microstructure for use in power plant is formed by continuously cooling a thick section of material, resulting in a mixture of allotriomorphic ferrite and bainite (with some martensite). In this work it was decided to investigate both a predominantly bainitic microstructure (also containing some areas of martensite) and a mixed microstructure of approximately 50% allotriomorphic ferrite and bainite. [The former microstructure is henceforth referred to as ‘fully bainitic’ for brevity, although it should always be understood that it consists of a mixture of bainitic ferrite and martensite.] The bainite in the specimens containing 50% allotriomorphic ferrite forms from carbon-enriched austenite and therefore the enrichment kinetics of the cementite are expected to be different from those in the fully bainitic microstructure. In order to determine the heat treatments required to produce these two starting microstructures it is necessary to calculate the time-temperature-transformation (TTT) diagram for the steel.

5.3.1 Calculation of the TTT curve and phase diagram

A model developed by Bhadeshia (1982) was used to calculate the TTT curve and phase diagram for the $2\frac{1}{4}$ Cr1Mo steel; the results are presented in Figure 5.2 and Figure 5.3. (The ‘kinks’ in the dot-dashed line in Figure 5.2 and in the Ae_3' line in Figure 5.3 are artefacts of the computer program.) The phase diagram shows three distinct lines: the line T_0 is the locus of points where ferrite and austenite of identical composition have equal free energy and the T_0' line is a modification of this which allows for the strain energy involved in the transformation (400 J mol^{-1}). The line Ae_3' is the paraequilibrium phase boundary indicating equilibrium between ferrite and austenite when the ratio of iron to substitutional solute atoms is constant everywhere, i.e. when there is no substitutional alloying element partitioning during transformation. The start temperatures B_s and M_s for the bainite and martensite reactions respectively are also marked on the TTT curve. The TTT curve was then used to determine a suitable heat treatment cycle. To produce a mixed microstructure of allotriomorphic ferrite and bainite it can be seen

that holding the specimen at 700°C will allow the growth of allotriomorphic ferrite and further transformation at 480°C, within the bainite phase field, will produce bainite. A fully bainitic microstructure can be produced by simply holding the specimen at 480°C.

5.3.2 Calculations to determine the volume fraction of allotriomorphic ferrite

A model has been developed by Bhadeshia *et al.* (1987) to calculate the volume fraction of allotriomorphic ferrite formed in steel weld deposits. This theory was applied to the 2 $\frac{1}{4}$ Cr1Mo steel to estimate the volume fraction of allotriomorphic ferrite in a sample after a given time for transformation at 700°C. The calculation of the growth rate of allotriomorphic ferrite uses the methods discussed by Avrami (1939) and Cahn (1956) to calculate the isothermal reaction kinetics for ferrite allotriomorphs forming at grain boundaries, modified to incorporate parabolic growth kinetics. The allotriomorphs are modelled as discs parallel to grain boundary planes with a half-thickness, q . Geometrical considerations lead to the following approximate expression when the austenite boundary is decorated with uniform layers of allotriomorphic ferrite

$$-\ln(1 - \zeta) = \frac{2S_v}{\phi} \alpha_1 t^{\frac{1}{2}}, \quad (5.1)$$

where S_v is the austenite grain surface area per unit volume, α_1 is the one-dimensional parabolic thickening rate constant and t is the reaction time in seconds. ϕ is the equilibrium volume fraction of ferrite, given by

$$\phi = \frac{x^{\gamma\alpha} - \bar{x}}{x^{\gamma\alpha} - x^{\alpha\gamma}}, \quad (5.2)$$

where $x^{\gamma\alpha}$, $x^{\alpha\gamma}$ and \bar{x} are the carbon concentrations in the austenite, ferrite and the bulk alloy respectively. ζ is the calculated volume fraction of allotriomorphic ferrite divided by ϕ .

The values of $x^{\gamma\alpha}$, $x^{\alpha\gamma}$ and α_1 were determined using the same computer model as that for calculating the TTT curve. At 700°C these were 2.28 at.%, 0.0669 at% and 0.1014×10^{-3} cm s $^{-\frac{1}{2}}$ respectively. \bar{x} was 0.69 at.%. Assuming an initial austenite grain size of approximately 150 μ m, estimated from the prior austenite grain size in the bainitic specimens, gives a value of S_v equal to 13.33×10^3 m $^{-1}$. Therefore, for transformation at 700°C for 1 hour, theory predicts a volume fraction of allotriomorphic ferrite of $\simeq 0.6$. It can also be shown using the approximation $q = \alpha_1 t^{\frac{1}{2}}$, that a tempering time of 1 hour at 700°C is consistent with the above calculation. It was therefore decided that the transformation to allotriomorphic ferrite should be carried out initially for 1 hour at 700°C.

5.3.3 Starting bainitic microstructure

The rectangular specimens were first dip-coated in a commercial application (containing a dispersion of clays and refractory solids in a solution of an organic resin in solvent) whose

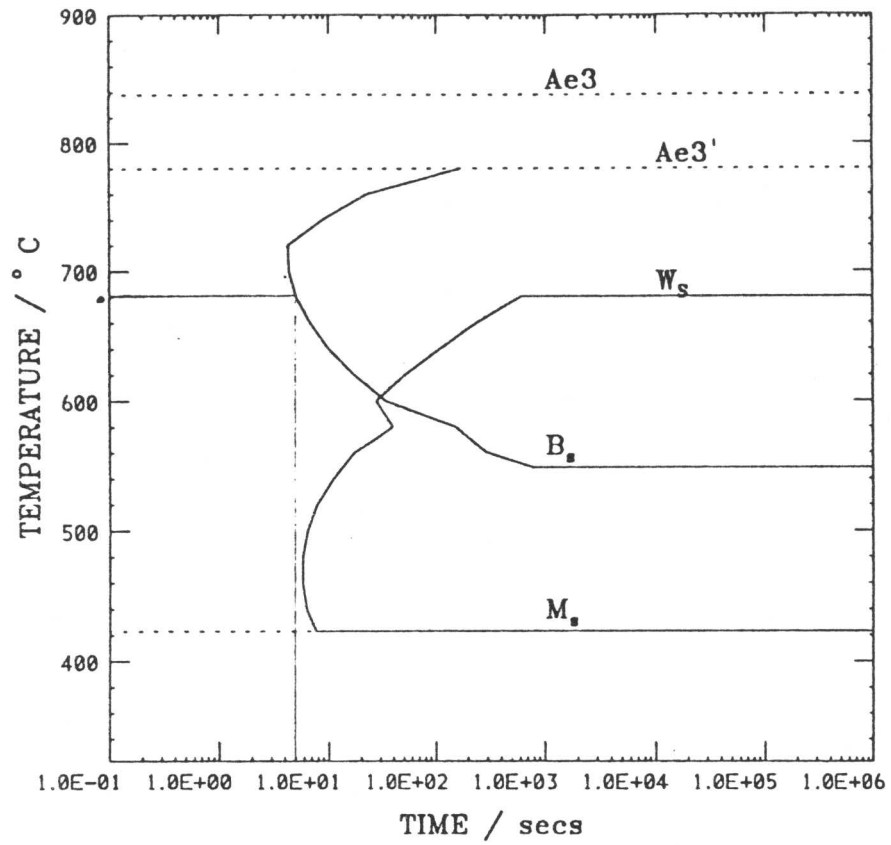


Figure 5.2: Calculated Time-Temperature-Transformation curve for $2\frac{1}{4}$ Cr1Mo steel.

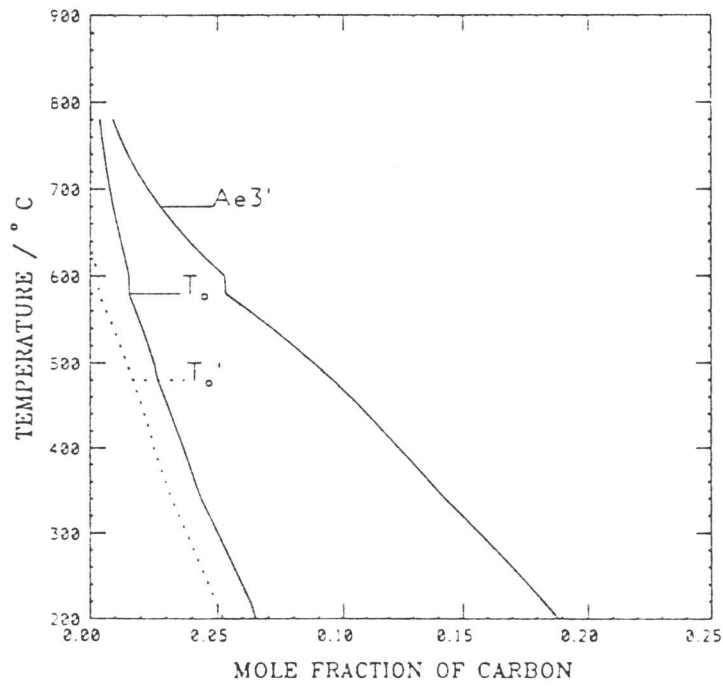


Figure 5.3: Calculated section of the phase diagram for $2\frac{1}{4}$ Cr1Mo steel.

function was to limit any decarburisation which might occur during heat treatment. They were then austenitised at 1050°C for 15 minutes in a furnace before transfer to an adjacent fluidised bed at 480°C for 30 minutes. Optical and scanning electron micrographs illustrating the predominantly bainitic microstructure with small islands of martensite are presented in Figure 5.4a) and b). It is well known that the bainite reaction does not go to completion when cementite formation does not accompany the growth of bainite. It is then possible to calculate the expected volume fraction of bainite at 480°C using the equation

$$V_b = \frac{x_{T_0} - \bar{x}}{x_{T_0} - x_\alpha}, \quad (5.3)$$

where x_{T_0} is the mole fraction of carbon remaining in austenite when the reaction stops, \bar{x} is the average carbon concentration in the alloy and x_α is the carbon concentration in bainitic ferrite (assumed to be zero). The phase diagram in Figure 5.3 predicts a value for x_{T_0} of $\simeq 0.026$ at 480°C and \bar{x} is 0.0069, giving a volume fraction of $\simeq 0.7$ at 480°C. This is in good agreement with the observed volume fractions in Figure 5.4. As the transformation temperature is lowered the volume fraction of bainite will increase.

The initial microstructure was also characterised in the TEM using thin foil specimens. The micrograph in Figure 5.5 illustrates the bainitic and martensitic areas, the martensite being heavily dislocated. There is also a small amount of retained austenite present at the edges of the bainite sheaves; the electron diffraction pattern in Figure 5.6 shows reflections attributable to the retained austenite.

A carbon extraction replica taken from the as-transformed fully bainitic specimen is presented in Figure 5.7. It is interesting to note that there are no cementite particles in the bainitic regions immediately after isothermal transformation. This implies that it is upper bainite which forms at 480°C because lower bainite would contain carbides as a consequence of the transformation mechanism. The bainite reaction has been discussed extensively in Chapter 2. The formation of upper bainite results in the rejection of carbon into the austenite surrounding the bainite plates. Some of this enriched austenite is retained on quenching after isothermal transformation. Immediately tempering begins, the austenite starts to decompose to a mixture of ferrite and cementite. This cementite will initially have a composition consistent with formation by a paraequilibrium mechanism owing to the large differences in the diffusion rates of carbon and substitutional solute elements.

Whether it is upper or lower bainite which can be found in the microstructure following isothermal transformation above M_s has been investigated widely for plain Fe-C steels. Oka and Okamoto (1986) proved that steels with more than 0.8 wt.% of carbon do not contain any upper

bainite, observing only lower bainite at all transformation temperatures above M_s . In addition, Ohmori and Honeycombe (1971) found only upper bainite in plain carbon steels containing less than 0.4 wt.% carbon. Few similar studies have been made for alloy steels. The steel used in this work has a carbon concentration of 0.15 wt.%. It is of great interest, therefore, to investigate whether or not lower bainite can be formed by isothermal transformation near M_s . To this end, the value of M_s was first determined by austenitising a specimen in a thermomechanical simulator at 1050°C for 15 mins, followed by quenching to room temperature using nitrogen gas. Graphs in which the relative length change is plotted against temperature and time are presented in Figure 5.8a) and b) respectively. The M_s temperature was found to be 420°C. This is in good agreement with the value of 390°C predicted by the model described in section 5.3.1.

Two similar isothermal transformations experiments to those used to create the starting bainitic microstructure used in the majority of this work were then carried out, again in the thermomechanical simulator. In both cases specimens were austenitised at 1050°C for 15 mins and then one specimen was isothermally transformed at 450°C, and the other at 400°C, each for 30 mins. It is important to note that although 400°C is slightly below M_s , a considerable volume fraction of bainite is to be expected on isothermal transformation so near M_s . Graphs showing plots of temperature against time and relative length change against time for the transformation at 450°C are presented in Figures 5.8c) and d), and at 400°C in Figures 5.8e) and f). The specimen isothermally transformed at 400°C was then examined in the TEM to determine if there was any lower bainite present in the microstructure.

A low magnification transmission electron micrograph is presented in Figure 5.9. Careful examination of the picture reveals that there are large areas of both lower and upper bainite. A higher magnification image of the upper bainitic region presented in Figure 5.10 clearly shows plates of upper bainite separated by films of retained austenite. Low and high magnification images of the lower bainitic region are presented in Figure 5.11 and Figure 5.12 respectively. The most striking feature of these images is that the cementite precipitates are in one orientation only with respect to the lower bainitic ferrite. There is also evidence of some films of retained austenite in the lower bainitic regions, but it is not as extensive as in the upper bainitic regions. The microstructure contained approximately 45% lower bainite, 45% upper bainite and also 10% martensite. A martensite lath is illustrated in Figure 5.13. The cementite within the lath is found in three different orientations, in contrast to that in the lower bainite. It should be noted that this martensite has formed during isothermal transformation just below M_s and has tempered on continued holding at 400°C. This is still consistent with the fact that there are no

carbides found in the specimens transformed at 480°C which contained a mixture of martensite and bainite. In that case the martensite formed on quenching and therefore no tempering occurred allowing cementite precipitation, and the bainite was all upper bainite and therefore did not contain any carbides.

The differences in scale of both the laths and the carbide precipitation in the lower bainite and the martensite are clearly illustrated in Figure 5.14. The martensite lath is much coarser than the bainite, whereas cementite precipitation is on a much finer scale in the martensite due to the increased carbon concentration and occurs in more than one orientation. Chapter 2 discussed the rejection of carbon from plates of upper bainite during growth. As a consequence of this, the austenite matrix will become richer in carbon. In the later stages of transformation the bainite growing from the enriched austenite may then decompose to lower bainite. This explains why the mixture of upper and lower bainite is observed in this case.

5.3.4 Starting mixed allotriomorphic ferrite and bainitic microstructure

The necessary heat treatment cycle to produce a mixed microstructure is austenitisation at 1050°C for 15 minutes, followed by holding at 700°C for 1 hour, then further transformation at 480°C for 30 minutes, then finally quenching to room temperature. It proved extremely difficult to control the amount of decarburisation in the specimens using a furnace at 1050°C and two fluidised beds at 700 and 480°C respectively. The heat treatments were therefore performed on the smaller 8 × 12 mm cylindrical specimens in a thermomechanical simulator. This enabled the exact heating cycle and cooling rates to be accurately programmed. The experiments were essentially performed in vacuum, however, nitrogen gas was introduced into the chamber to quench the specimen between the transformation temperatures. The vacuum pumps were then switched back on to pump out the gas once the specimen had reached the next required transformation temperature. Three test experiments were performed in which the only difference was the speed with which the vacuum pumps were activated after the introduction of the N₂ gas to quench the specimen from 1050°C to 700°C. The heat treatment cycle and graphs showing the relative length change versus time for three of the test specimens are presented in Figure 5.15a)–d).

It can be seen from Figure 5.15b) that specimen 1 shows the maximum relative length change of $\simeq 0.01$, with specimens 2 and 3 showing relative length changes of $\simeq 0.008$ and $\simeq 0.007$ respectively. The relative length change corresponds to the amount of growth of allotriomorphic ferrite and therefore specimen 1 should contain the highest volume fraction of ferrite, with specimens 2 and 3 having progressively lower volume fractions. Optical micrographs of specimens 1, 2 and 3 are presented in Figure 5.16, Figure 5.17 and Figure 5.18 respectively. It can be seen that

a)



b)

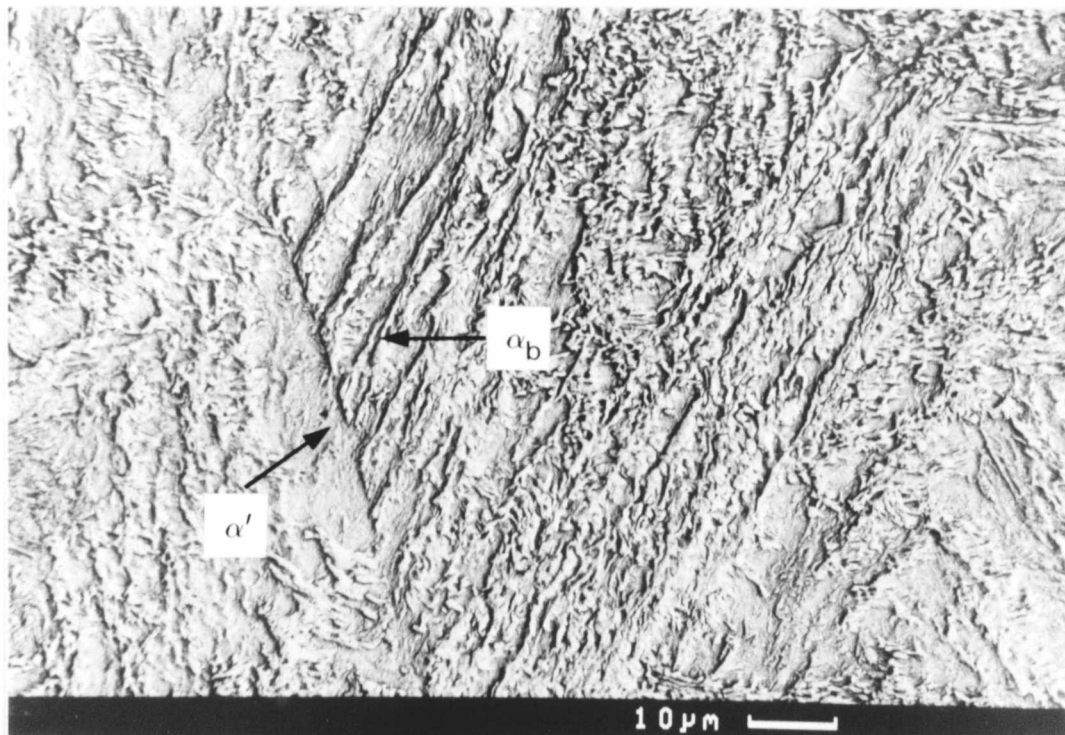


Figure 5.4: a) Optical and b) scanning electron micrographs of the starting bainitic microstructure – Austenitised 1050°C 15 minutes, 480°C 30 minutes and then water quenched.

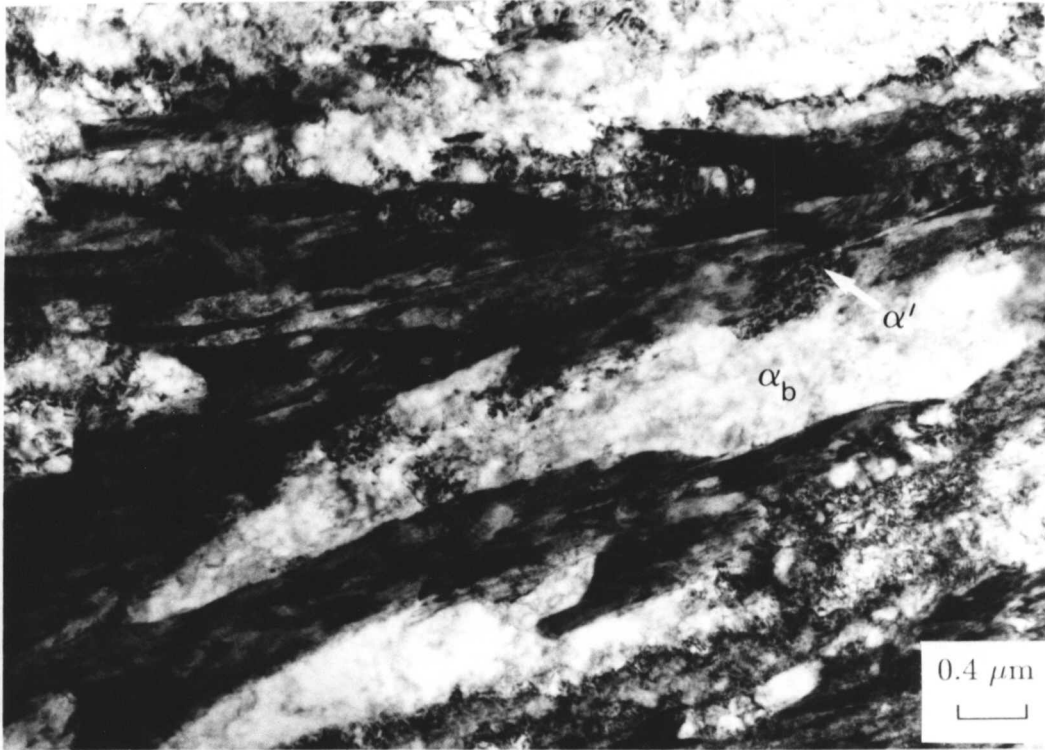


Figure 5.5: Transmission electron micrograph showing a mixture of bainite and martensite, the martensite being heavily dislocated. There is also a small amount of retained austenite – Austenitised 1050°C 15 minutes, 480°C 30 minutes and then water quenched.

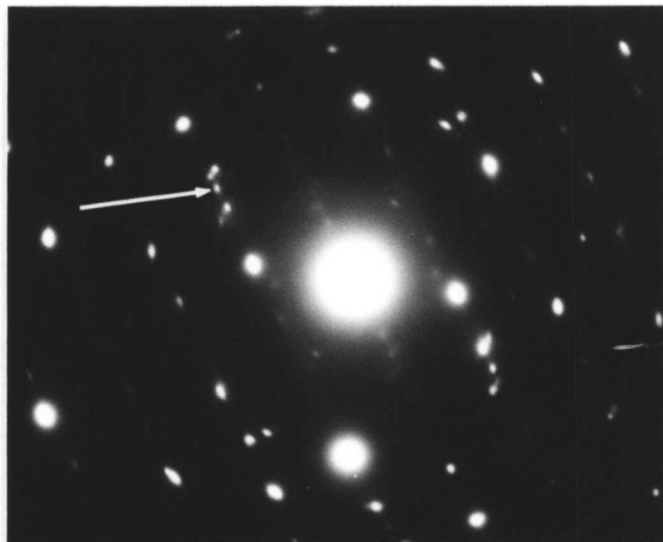


Figure 5.6: Selected area electron diffraction pattern showing reflections due to retained austenite within the microstructure.



Figure 5.7: Carbon extraction replica taken from the as-transformed fully bainitic microstructure illustrating that there are no carbides present.

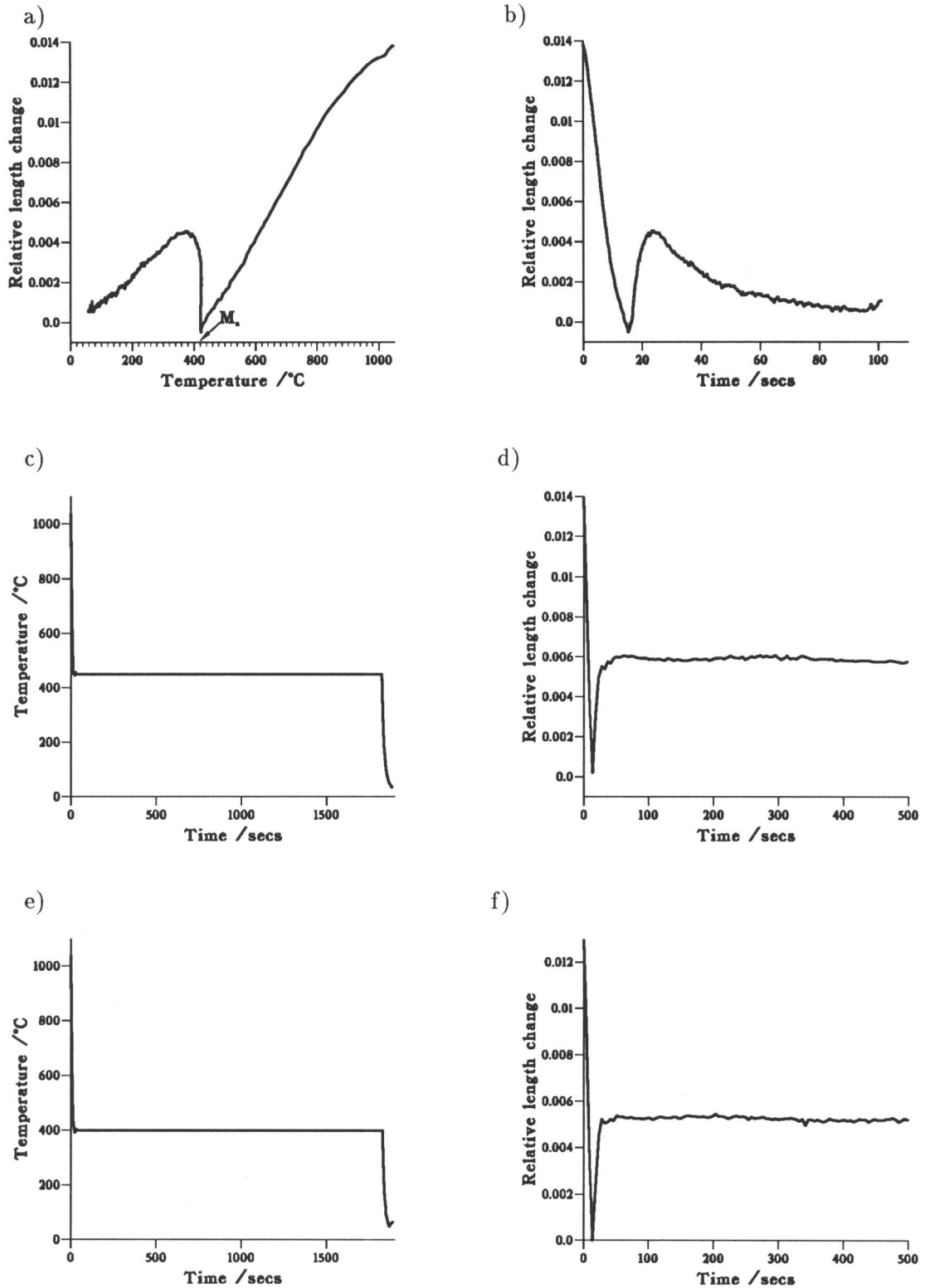


Figure 5.8: Relative length change against temperature a) and time b) for gas quenching a specimen from austenite to determine the M_s temperature. Temperature against time and relative length change against time for isothermal transformation at 450°C c) and d), and at 400°C e) and f).

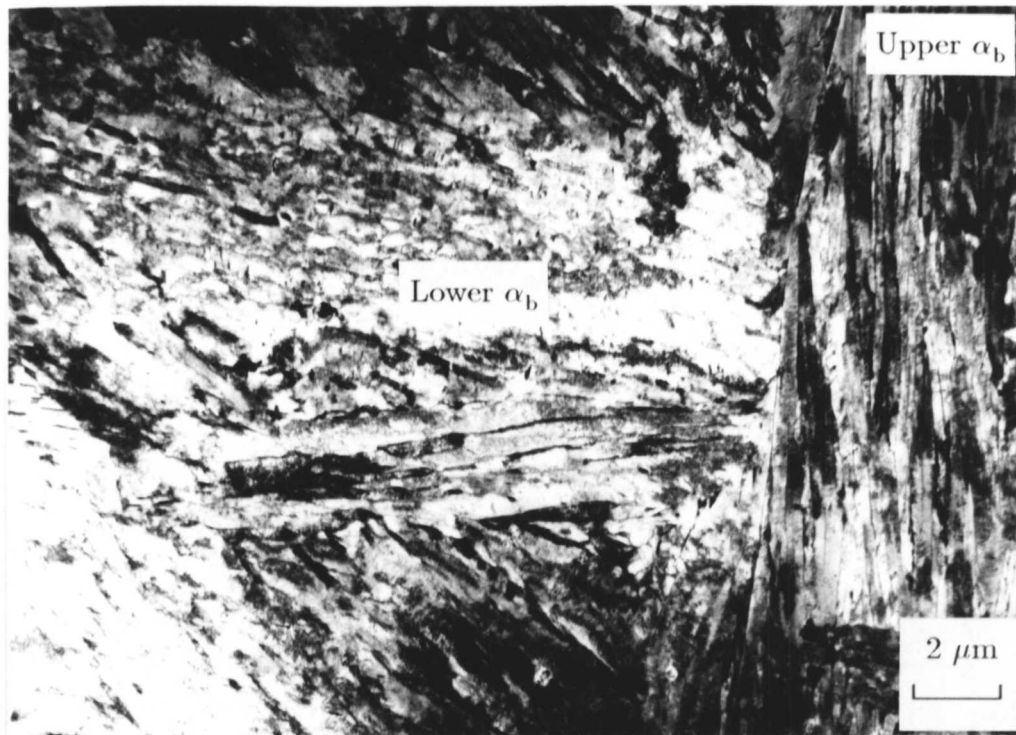


Figure 5.9: Low magnification image illustrating lower and upper bainitic regions in a specimen austenitised at 1050°C for 15 mins followed by isothermal transformation at 400°C for 30 mins.

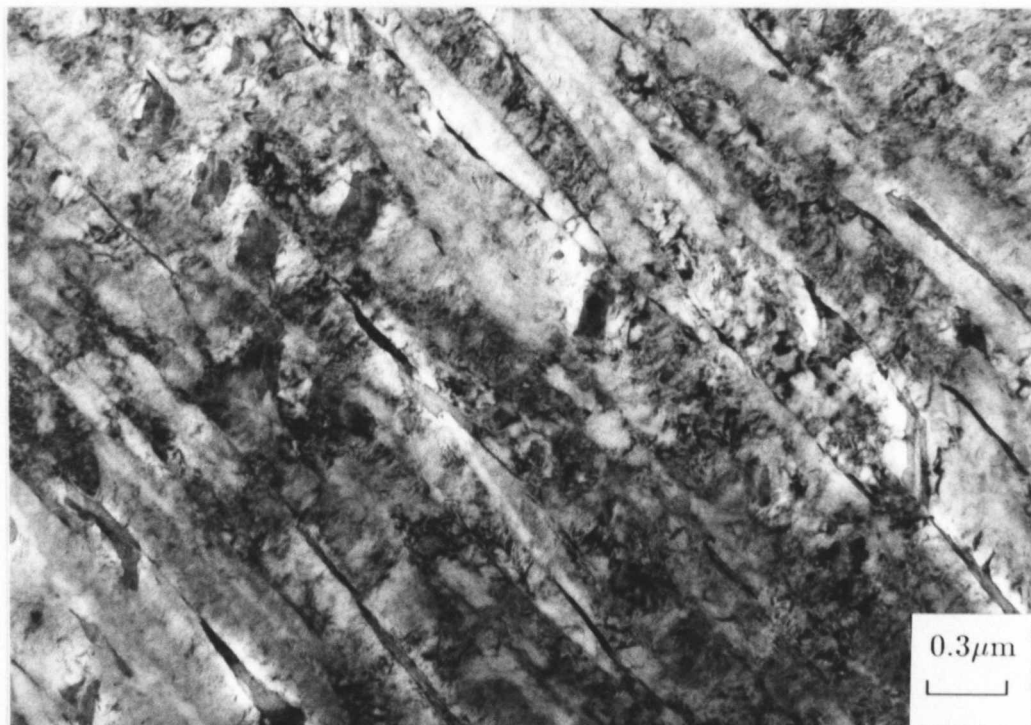


Figure 5.10: Transmission electron micrograph illustrating plates of upper bainite with films of retained austenite in between.

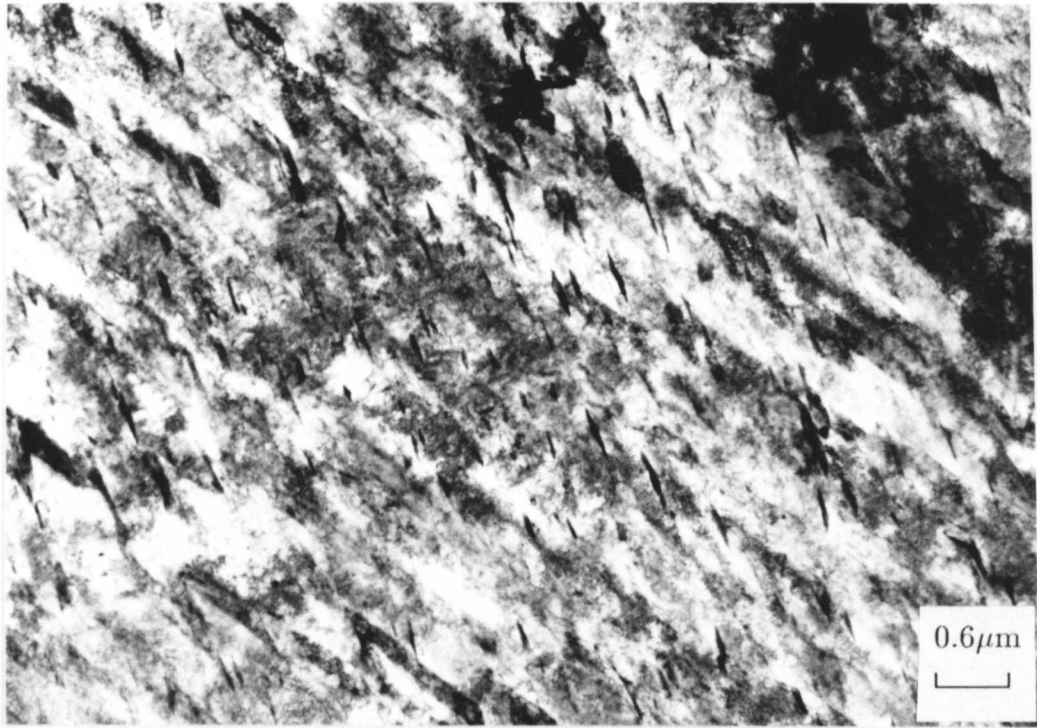


Figure 5.11: Low magnification image illustrating a lower bainitic region in the specimen isothermally transformed at 400°C for 30 mins. Cementite particles are observed in only one orientation with respect to the bainitic ferrite.



Figure 5.12: High magnification image of a lower bainite plate in this case showing cementite precipitation parallel to the axis of the plate.

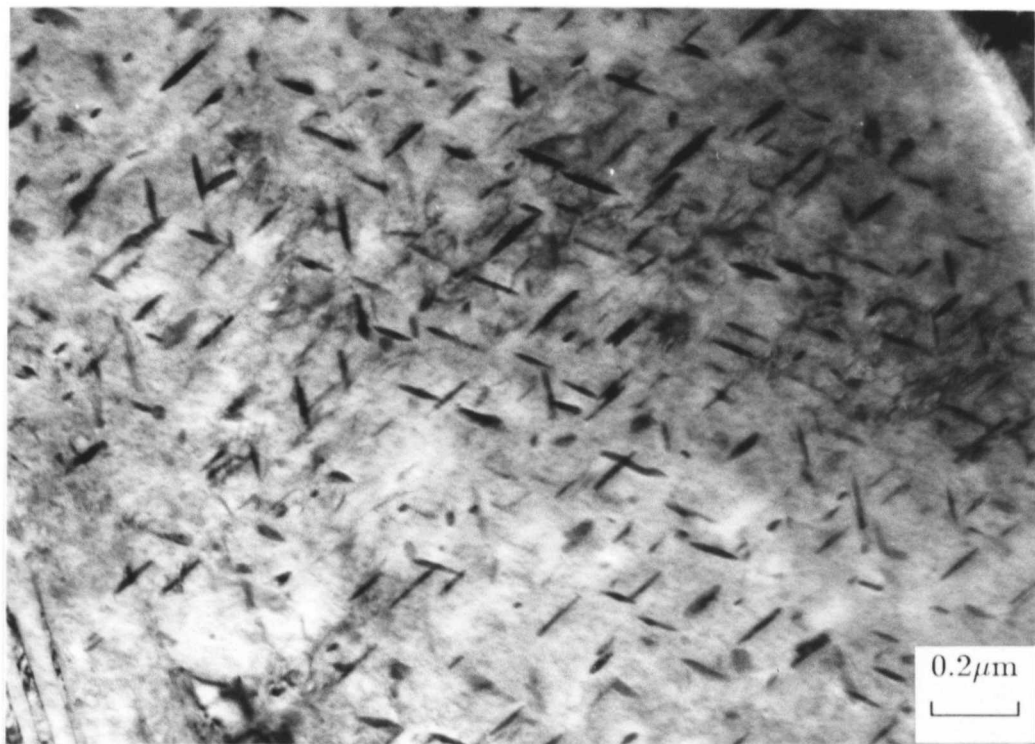


Figure 5.13: High magnification image illustrating a tempered martensite lath in a specimen austenitised at 1050°C for 15 mins followed by isothermal transformation at 400°C for 30 mins. Note that the cementite precipitates in more than one orientation to the martensite lath.

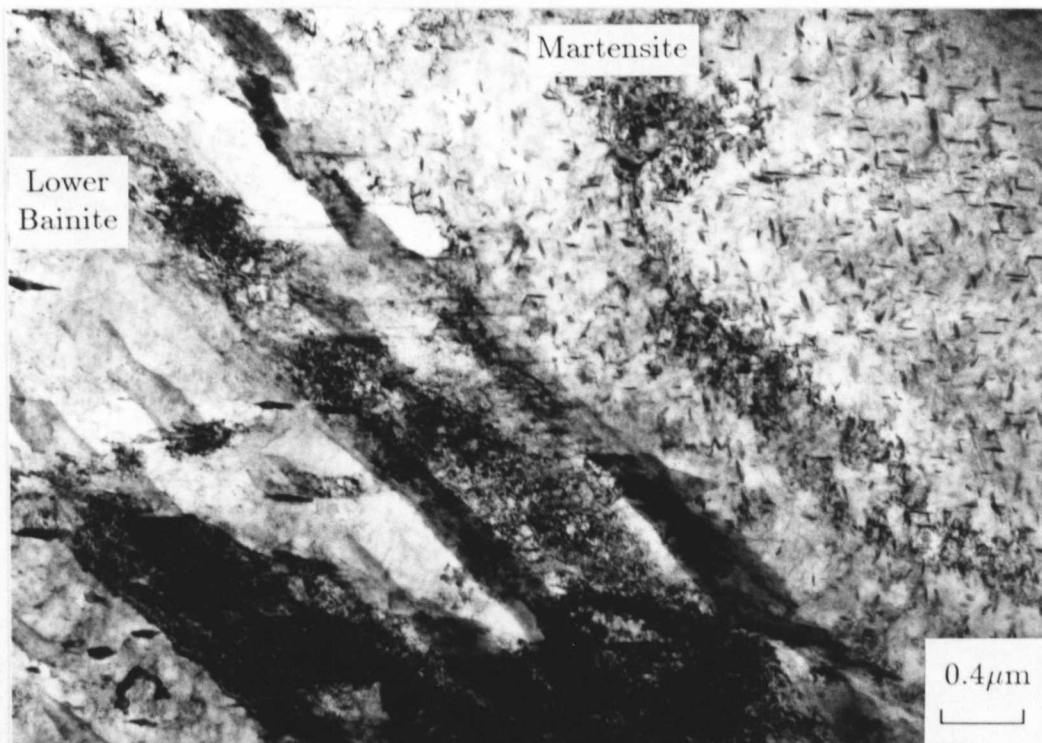


Figure 5.14: A clear illustration of the differences between a coarse martensite lath and smaller plates of lower bainite, particularly with respect to the cementite precipitation.

the observed volume fractions of allotriomorphic ferrite are approximately 0.5, 0.25 and 0.15 respectively. The difference between the three specimens is only the time before the removal of the quenching gas at 700°C. These results are not understood because there was no evidence that any decarburisation had taken place. The desired volume fraction was $\simeq 50\%$ and therefore subsequent specimens for production of the starting microstructures for the tempering heat treatments were heat treated under the same conditions as specimen 1. A TEM micrograph showing two adjacent grains of allotriomorphic ferrite within the bainitic/martensitic matrix is presented in Figure 5.19.

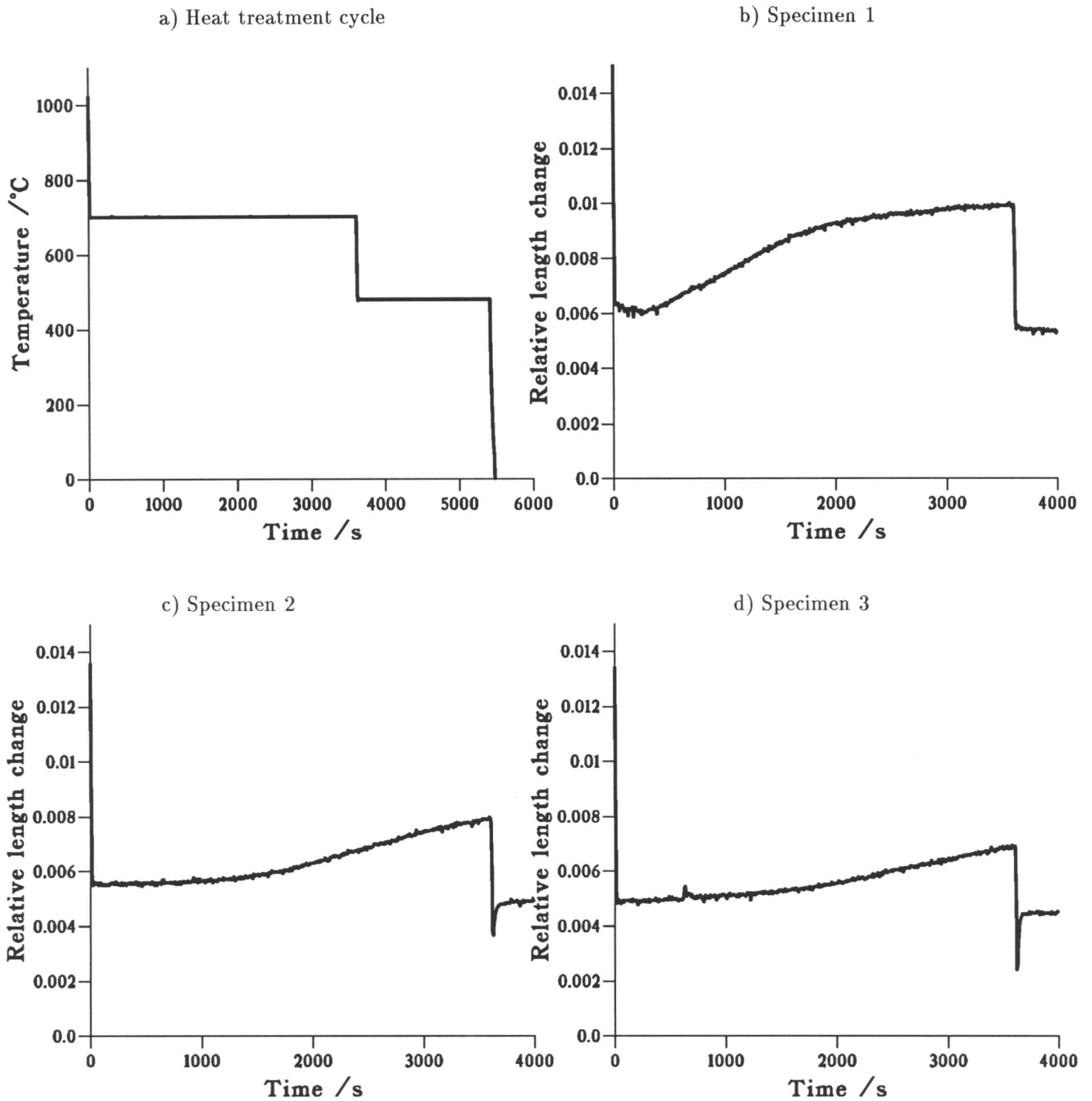


Figure 5.15: a) Heat treatment cycle and b)-d) graphs showing relative length change against time for specimens 1, 2 and 3 heat treated in the thermomechanical simulator to produce mixed microstructures of allotriomorphic ferrite and bainite.

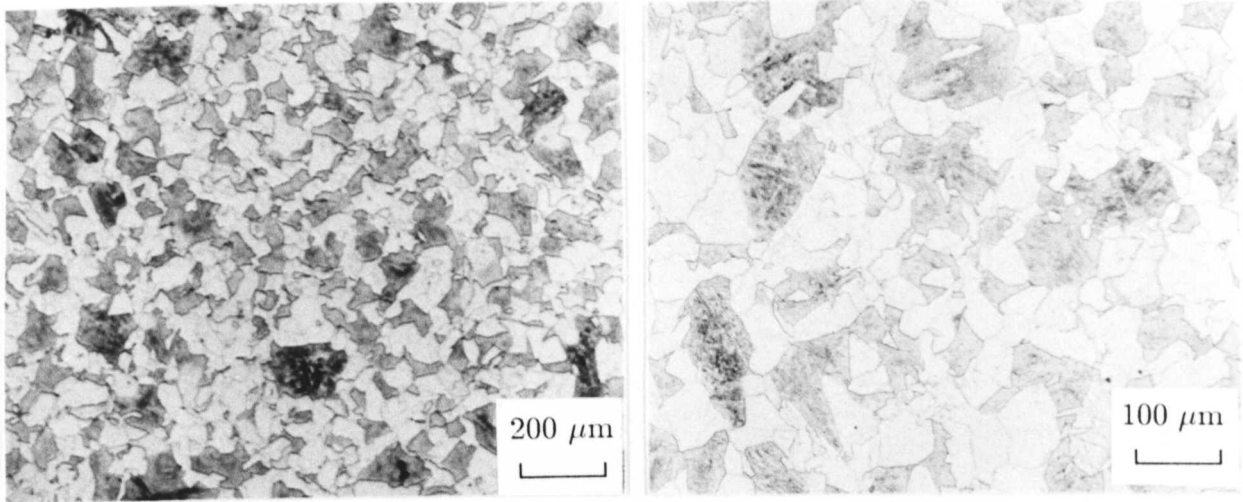


Figure 5.16: Optical micrographs of specimen 1 – Heat treated in the thermomechanical simulator – Austenitised 1050°C 15 minutes, 700°C 1 hour and 480°C 30 minutes. Gas cooled.

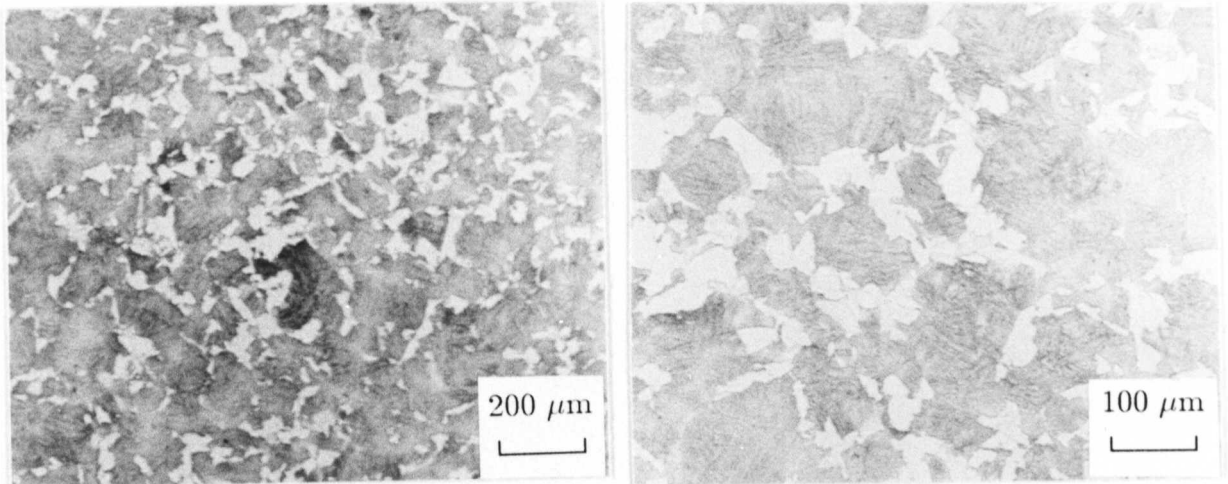


Figure 5.17: Optical micrographs of specimen 2 – Heat treated in the thermomechanical simulator – Austenitised 1050°C 15 minutes, 700°C 1 hour and 480°C 30 minutes. Gas cooled.

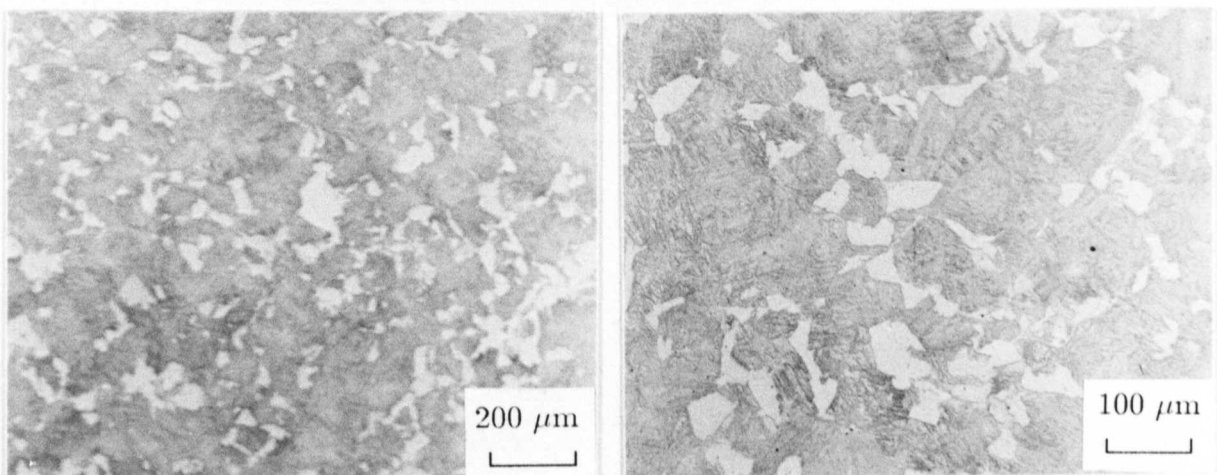


Figure 5.18: Optical micrographs of specimen 3 – Heat treated in the thermomechanical simulator – Austenitised 1050°C 15 minutes, 700°C 1 hour and 480°C 30 minutes. Gas cooled.

5.4 Tempering heat treatments

Prior to entering service $2\frac{1}{4}\text{Cr1Mo}$ steel is usually given a stress-relief heat treatment at 700°C for varying times depending on the specimen size. In these experiments the stress-relief heat treatment was not given. The main purpose of the experimental work was to investigate changes in cementite composition, both with time and with the onset of alloy carbide precipitation, with a view to improving predictive models for $\frac{1}{2}\text{Cr}\frac{1}{2}\text{Mo}\frac{1}{4}\text{V}$ and $1\text{Cr}\frac{1}{2}\text{Mo}$ steels rather than predicting the remanent life of $2\frac{1}{4}\text{Cr1Mo}$ steel *per se*.

5.4.1 Calculation of the enrichment rate of cementite in $2\frac{1}{4}\text{Cr1Mo}$ steel

Power stations operate at temperatures close to 565°C , and therefore it was decided to temper the majority of the specimens at this temperature. Specimens were also tempered at 620°C and 510°C , being 55°C above and below this temperature, in order to investigate the temperature dependence of enrichment rates. Suitable tempering times at these temperatures were chosen with the aid of the computer model described in chapter 3. MTDATA calculations were carried out to determine the equilibrium chromium content in cementite and ferrite at these three temperatures. Cementite and ferrite were the only phases allowed to exist in the MTDATA calculations, and therefore the predicted rates of cementite enrichment do not take into consideration the effect of alloy carbide precipitation. This point will be discussed later on in this chapter.

The calculated equilibrium chromium levels in cementite and ferrite at the temperatures of the tempering heat treatments are presented in Table 5.2. The predicted volume fraction of cementite was 0.022; this was almost independent of temperature in the range of interest. Finite difference calculations were then carried out using these calculated equilibrium values to set the interface concentrations. The calculations assumed an average particle size of 60 nm, determined by preliminary TEM investigations. The results of the calculations are presented in Figure 5.20.

Table 5.2: Equilibrium chromium levels in cementite and ferrite calculated using MTDATA at temperatures 510, 565 and 620°C .

Temperature / $^\circ\text{C}$	Cementite		Ferrite	
	At.%	Wt.%	At.%	Wt.%
510	51.51	61.99	0.95	0.88
565	45.22	53.99	1.13	1.05
620	38.91	46.11	1.32	1.23

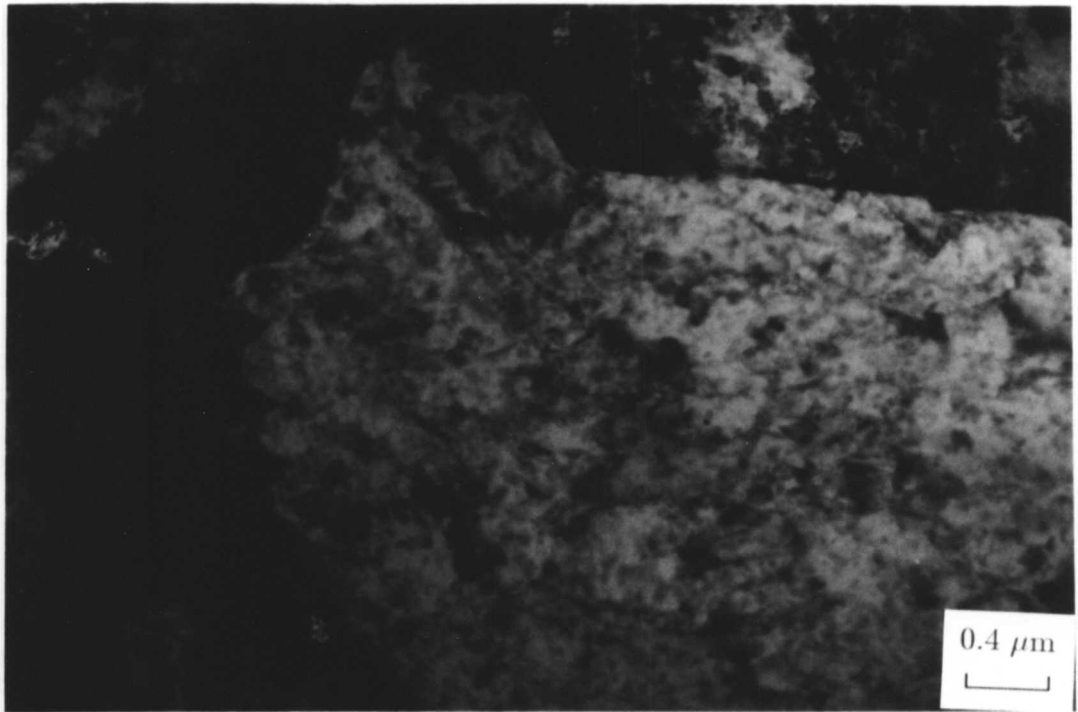


Figure 5.19: A transmission electron micrograph showing two adjacent grains of allotriomorphic ferrite within the bainitic/ martensitic matrix – Austenitised 1050°C 15 minutes, 700°C 1 hour and 480°C 30 minutes.

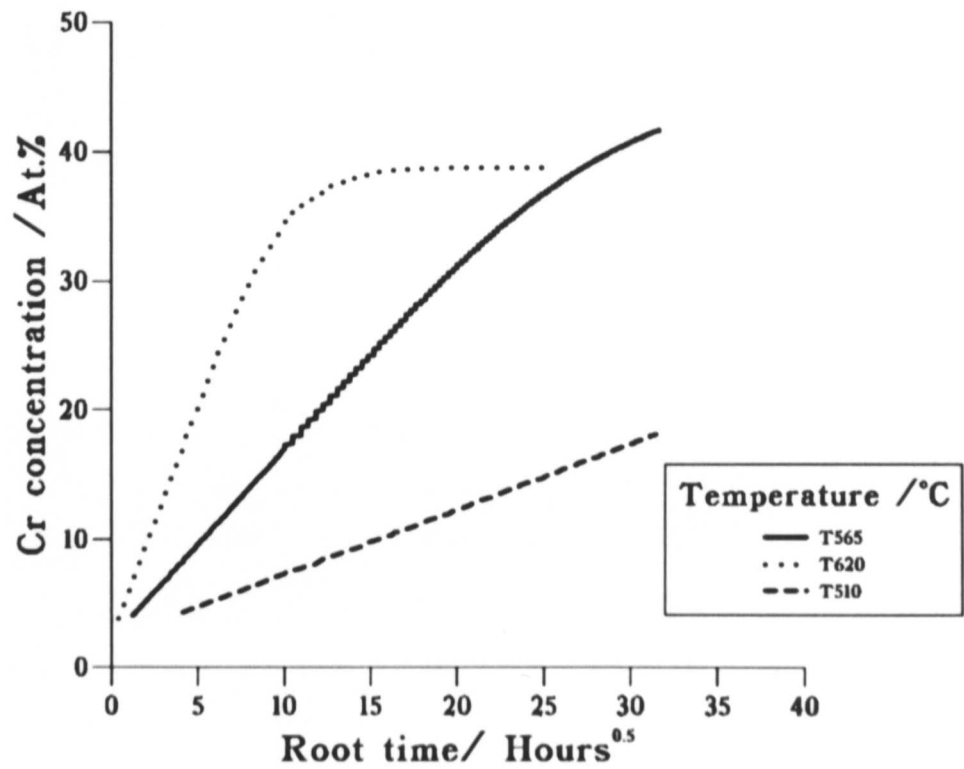


Figure 5.20: Calculated rate of cementite enrichment at 510, 565 and 620°C using finite difference model.

5.4.2 Tempering times for bainitic microstructures

The tempering times at temperatures 510, 565 and 620°C decided upon using the results of the calculations described above are presented in Table 5.3.

Table 5.3: Tempering heat treatment temperatures and times for the bainitic specimens

Temperature /°C	Time /Hours
510	1, 128, 256
565	$\frac{1}{6}$, 1, 4, 7, 32, 64, 128, 178, 239, 512, 1048, 2072
620	1, 10, 25

5.4.3 Tempering times for mixed microstructures

The mixed microstructures were tempered at 565°C only because the purpose of this investigation was to determine any changes in the rate of enrichment compared with the fully bainitic microstructures and therefore to study the effect of temperature was not the main purpose of the investigation. These specimens were tempered for a few times, given in Table 5.4, covering the range during which cementite was known to exist in the fully bainitic specimens.

Table 5.4: Tempering heat treatment temperatures and times for the mixed microstructure specimens

Temperature /°C	Time /Hours
565	1, 46.5, 80, 128, 180

5.5 Results and discussion from bainitic microstructures

5.5.1 Hardness measurements

Macrohardness measurements on all the bainitic specimens are presented in Figure 5.21. The starting hardness was 373 HV, which then decreased gradually as tempering proceeded. For the series of specimens tempered at 565°C there was a peak in hardness observed corresponding to the precipitation of M_2C after 32 hours, and a slight peak possibly corresponding to the precipitation of M_7C_3 after 128 hours. The specimens tempered at 510°C and 620°C showed slower and faster drops in hardness respectively compared with those tempered at 565°C. This is to be expected as microstructural changes will be accelerated as the temperature is increased.

5.5.2 Microstructural evolution during tempering at 565°C

Changes in the microstructure observed optically with tempering at 565°C were slight. This is demonstrated in Figure 5.22 which shows an optical micrograph for the specimen tempered

for 2072 hours. The bainitic and martensitic regions are, however, more distinguishable than in the microstructure prior to tempering.

The evolution of carbides within the different regions of the microstructure was extensively studied on carbon extraction replicas. Detailed microanalyses from the carbide particles are discussed in section 5.5.3. A TEM image from a carbon extraction replica of the specimen tempered at 565°C for 10 minutes is presented in Figure 5.23, and from a thin foil in Figure 5.24. Both illustrate the early stages of carbide precipitation. The micrograph from the thin foil illustrates a plate of martensite which has begun to precipitate cementite in three distinct orientations on tempering. The replica image illustrates cementite plates precipitating parallel to the direction of the bainitic sheaves; this is probably from the carbon rich retained austenite in between the upper bainite.

Figure 5.25 shows that further cementite precipitation has occurred after tempering for 64 hours. It would seem that not all the cementite precipitates immediately after isothermal transformation, but that there is further precipitation as tempering proceeds; any cementite precipitating after tempering for some time may not have an initial composition given exactly by a paraequilibrium mode of formation.

Figure 5.26, Figure 5.27 and Figure 5.28 illustrate the microstructure after tempering for 128 hours. Figure 5.26 is a very low magnification TEM image showing carbide particles delineating lath boundaries in the bainitic and martensitic regions. The bars across the image are the copper grid on which the replica is supported. Figure 5.27 illustrates cementite precipitation which occurs in the martensitic regions in the Widmanstätten pattern usually associated with the tempering of alloy martensites. Figures 5.28a) and b) are low and high magnification images respectively showing that cementite precipitation occurs in the bainitic regions mainly on the boundaries of the sheaves, whereas there is extensive precipitation of needle-shaped M_2C within the sheaves coexisting with only a few cementite particles. The fine M_2C needles also precipitate in a regular Widmanstätten array.

The difference in the precipitation behaviour within the bainitic and martensitic regions becomes more marked after tempering for 178 hours. The cementite in the martensitic regions continues to enrich with respect to all the substitutional solute elements. The low and high magnification images in Figure 5.29a) and b) illustrate this dense cementite precipitation in regular Widmanstätten arrays. There are very few needles of M_2C carbide within the vicinity of this cementite. Convergent beam and selected area electron diffraction patterns are presented in Figure 5.29c) and d), confirming that the carbide with this composition is cementite. The typical composition of the cementite in these regions measured by EDX (not allowing for the

carbon concentration) is

25 wt.% Cr, 5 wt.% Mn, 7 wt.% Mo, and 63 wt.% Fe.

Precipitation in the bainitic regions is illustrated in Figure 5.30. There is extensive precipitation of M_2C within the sheaves. The cementite in between the sheaves appears to have dissolved to some extent compared with Figure 5.28a) showing cementite in a similar position after tempering for 128 hours. The M_2C actually contains a considerable amount of dissolved chromium, a typical composition being

25 wt.% Cr, 0.5 wt.% Mn, 70.5 wt.% Mo, and 4 wt.% Fe.

It was found that the cementite adjacent to the regions of M_2C precipitation had a different composition from that in the martensitic regions. The average composition was

16 wt.% Cr, 6 wt.% Mn, 0.5 wt.% Mo, and 77.5 wt.% Fe,

from which it can be seen that the Mo content is reduced to almost nothing, and the Cr content has also been reduced by a significant amount. Two such cementite particles are marked with arrows in Figure 5.30b). It would appear that the precipitation of the more thermodynamically stable M_2C has drawn both Mo and Cr from the less stable cementite, which has started to dissolve. It was confirmed by selected area electron diffraction (Figure 5.30c) that the carbide with a lower Mo content than that found in the martensitic regions was indeed still cementite. There were also a few larger Cr-rich particles found at the edges of some of the regions containing M_2C . These were identified as M_7C_3 , and can be seen in the lower right of Figure 5.30a).

A thin foil was also examined made from the specimen tempered for 178 hours at 565°C. Figure 5.31 illustrates the upper bainitic sheaves dominant in the microstructure. A few cementite particles and a larger M_7C_3 particle can be seen on the lath boundaries; there is also extensive M_2C precipitation within the laths. Figure 5.32 illustrates a similar upper bainitic region; a large MnS inclusion can be seen within the microstructure, and there is extensive cementite precipitation on the plate boundaries and M_2C within the sheaves. Figure 5.33 is a nice illustration of the differences between the different regions of the microstructure. There is dense cementite precipitation in the martensitic region and much finer M_2C precipitation in the bainitic region. A selected area electron diffraction pattern is illustrated in Figure 5.34. The larger spots are from ferrite, and the smaller spots in between from the cementite within the martensitic region. The pattern exhibits the well known Bagaryatski (1950, cited by Bhadeshia, 1992) orientation relationship for cementite in tempered martensite:–

$$\{001\}_\theta \parallel \{211\}_{\alpha'}$$

$$\langle 100 \rangle_{\theta} \parallel \langle 0\bar{1}1 \rangle_{\alpha'}$$

After 238.5 hours the microstructure consists predominantly of M_7C_3 and M_2C . The cementite in the bainitic regions has been completely replaced by M_2C with some larger M_7C_3 particles on the boundaries between sheaves. Some cementite with the higher chromium remains in the martensite, although there is also precipitation of M_7C_3 on the edges of these regions. This is illustrated in Figure 5.35a). A selected area electron diffraction pattern from an M_7C_3 particle is presented in Figure 5.35b); characteristic streaks from the presence of stacking faults in the structure (discussed in Chapter 2) are clearly visible. The specimens tempered for 512 and 1048 hours (Figure 5.36 and Figure 5.37 respectively) showed further precipitation of M_7C_3 at the expense of the martensitic cementite. All the cementite had dissolved in the specimen tempered for 1048 hours. There was a slight enrichment of the M_7C_3 with respect to the chromium concentration with increasing tempering time; this is discussed in section 5.5.4. After 2072 hours the M_7C_3 precipitates have coarsened slightly (Figure 5.38). The carbide M_6C has also begun to precipitate at the expense of some of the M_2C needles which have dissolved. This is illustrated in Figure 5.39a) which shows aligned M_2C carbides together with some smaller, squarer particles which have been identified by selected area electron diffraction as M_6C (Figure 5.39b). A selected area diffraction pattern from the M_2C needles is also presented in Figure 5.39c). The needles of M_2C were too fine to take selected area electron diffraction patterns, except from a cluster, prior to this tempering time.

It has been shown above that the carbide type is very sensitive to position within a given microstructure. After a short period of tempering M_2C dominates within the bainitic plates, whereas mixtures of M_2C , M_7C_3 and M_3C are to be found at the bainite plate boundaries and predominantly M_3C in the martensitic regions. This is probably because far less carbon is available within the upper bainitic plates, whereas the plate boundaries are the sites for cementite precipitation during the growth of upper bainite. More carbon is available (in the form of cementite, or dissolved in carbon-enriched retained austenite) in the vicinity of the plate boundaries which can stimulate the formation of a variety of alloy carbides.

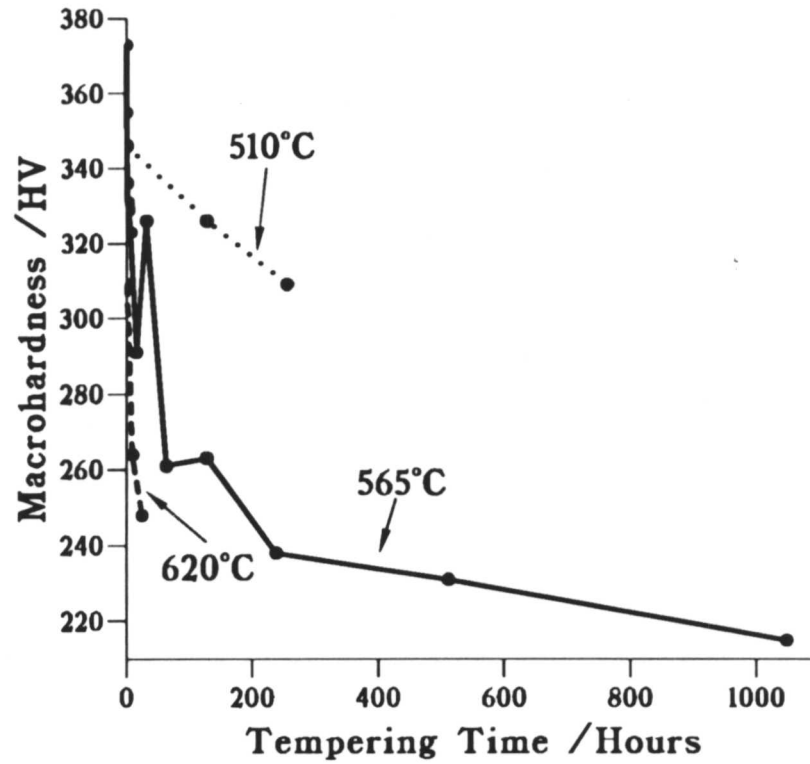


Figure 5.21: Macrohardness measurements as a function of time for specimens tempered at 510, 565 and 620°C.

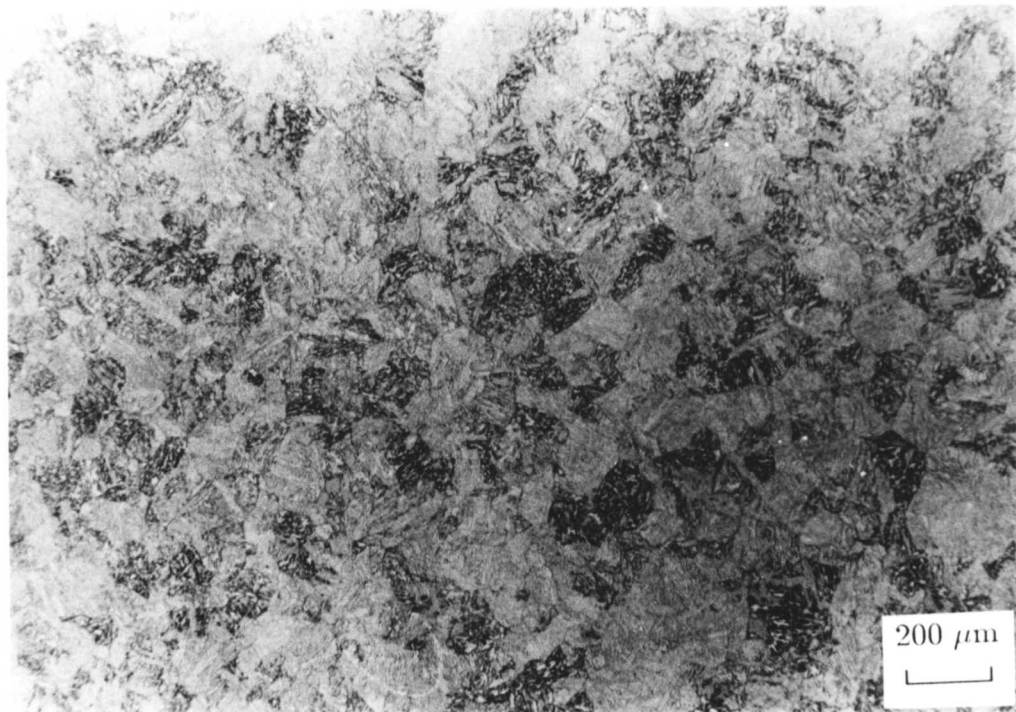


Figure 5.22: Optical microstructure from the fully bainitic specimen tempered for 2072 hours at 565°C.



Figure 5.23: Carbon extraction replica from the fully bainitic specimen tempered for 10 minutes at 565°C showing that cementite has begun to precipitate, in particular in between and parallel to the plates of upper bainite.



Figure 5.24: Transmission electron micrograph from a thin foil specimen from the fully bainitic specimen tempered for 10 minutes at 565°C showing a plate of tempered martensite containing cementite in three distinct orientations.

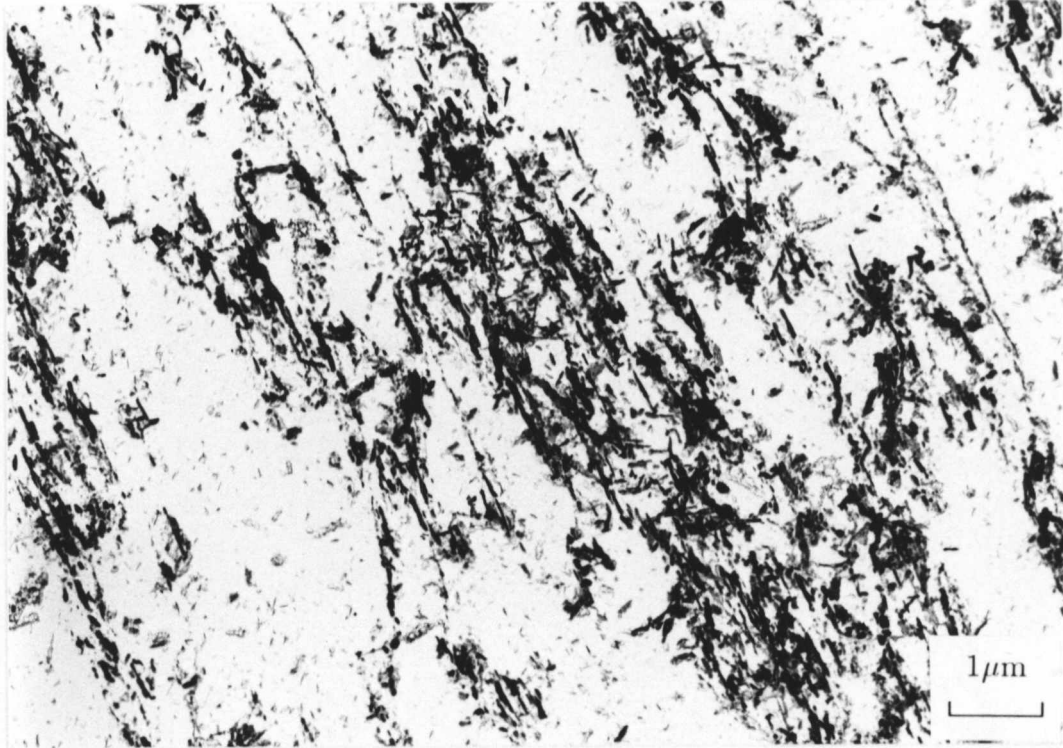


Figure 5.25: Carbon extraction replica from the fully bainitic specimen tempered for 64 hours at 565°C.

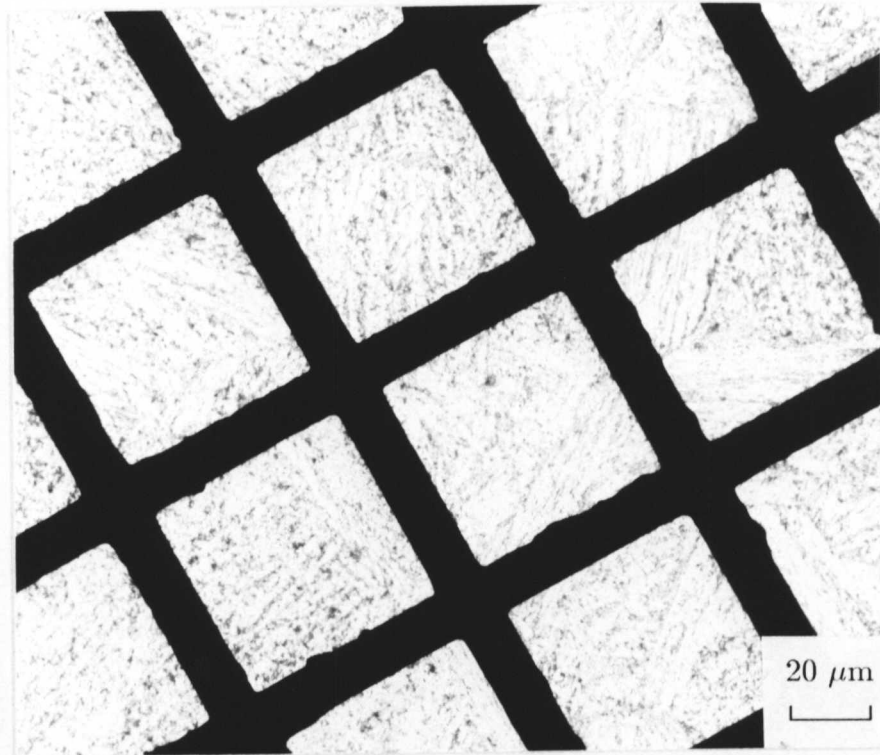


Figure 5.26: Low magnification transmission electron micrograph showing carbide particles delineating lath boundaries in the bainitic and martensitic regions after tempering at 565°C for 128 hours. The grid bars across the image are the copper grid on which the replica is supported.

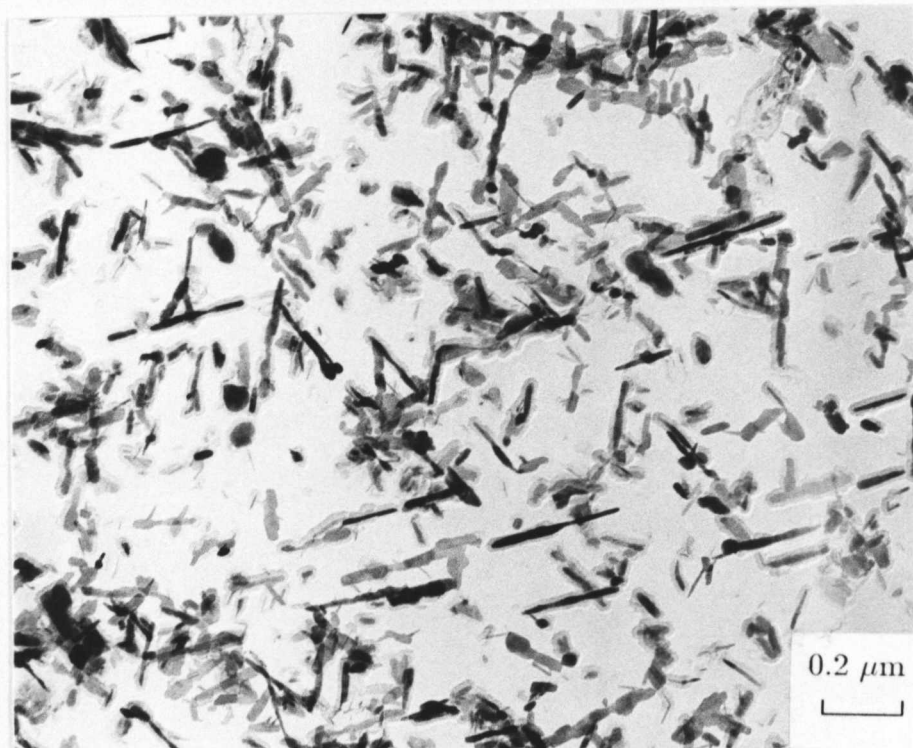
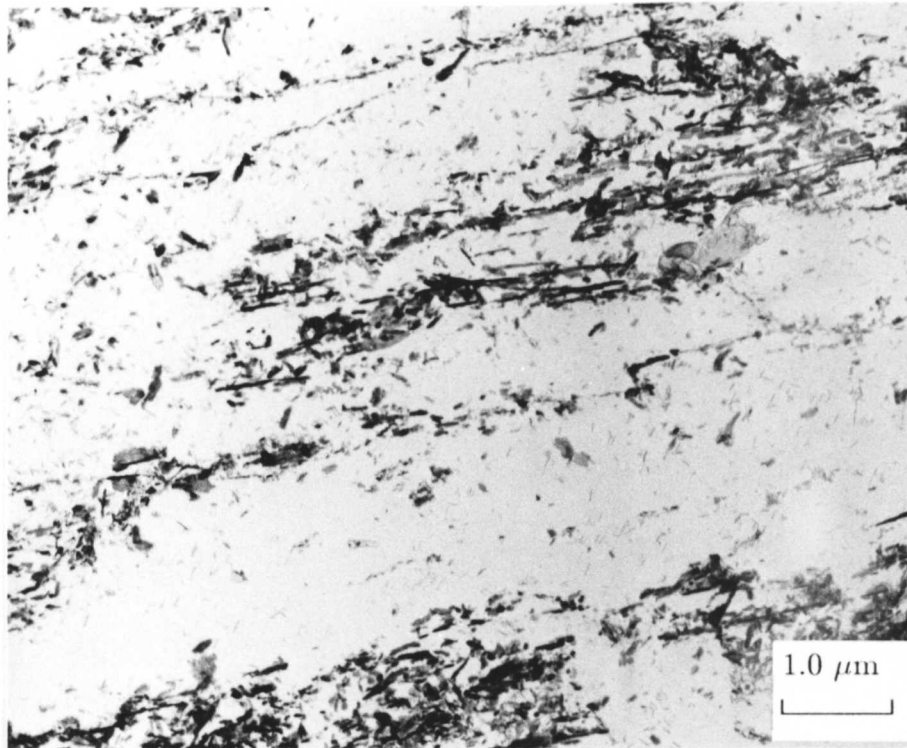


Figure 5.27: Cementite precipitation in the martensitic regions of a specimen tempered for 128 hours at 565°C in a Widmanstätten array.

a)



b)

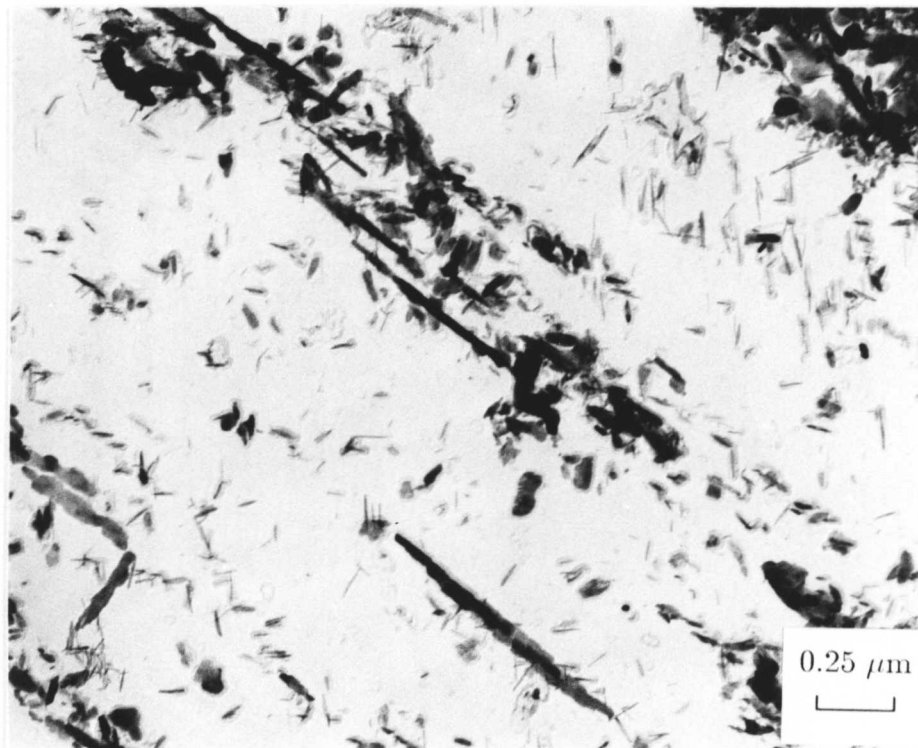


Figure 5.28: a) Low and b) high magnification carbon extraction replicas from the specimen tempered at 565°C for 128 hours showing cementite precipitation on the boundaries of the bainitic regions which contain extensive precipitation of M_2C needles in a Widmanstätten array.

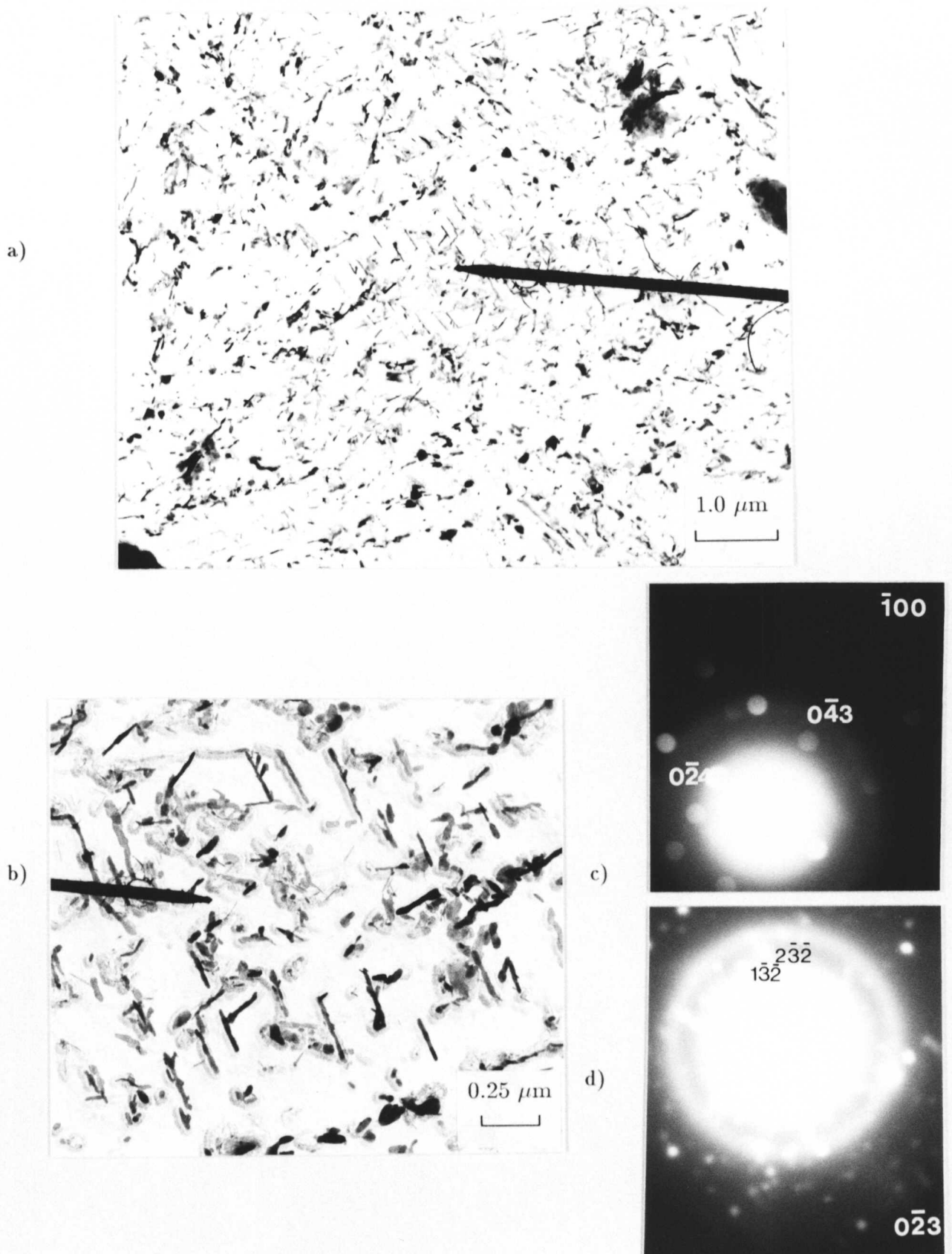


Figure 5.29: Low a) and high b) magnification transmission electron micrographs illustrating dense cementite precipitation in Widmanstätten arrays in martensitic regions of specimens tempered for 178 hours at 565°C. Convergent beam c) and selected area d) electron diffraction patterns from cementite particles in this region.

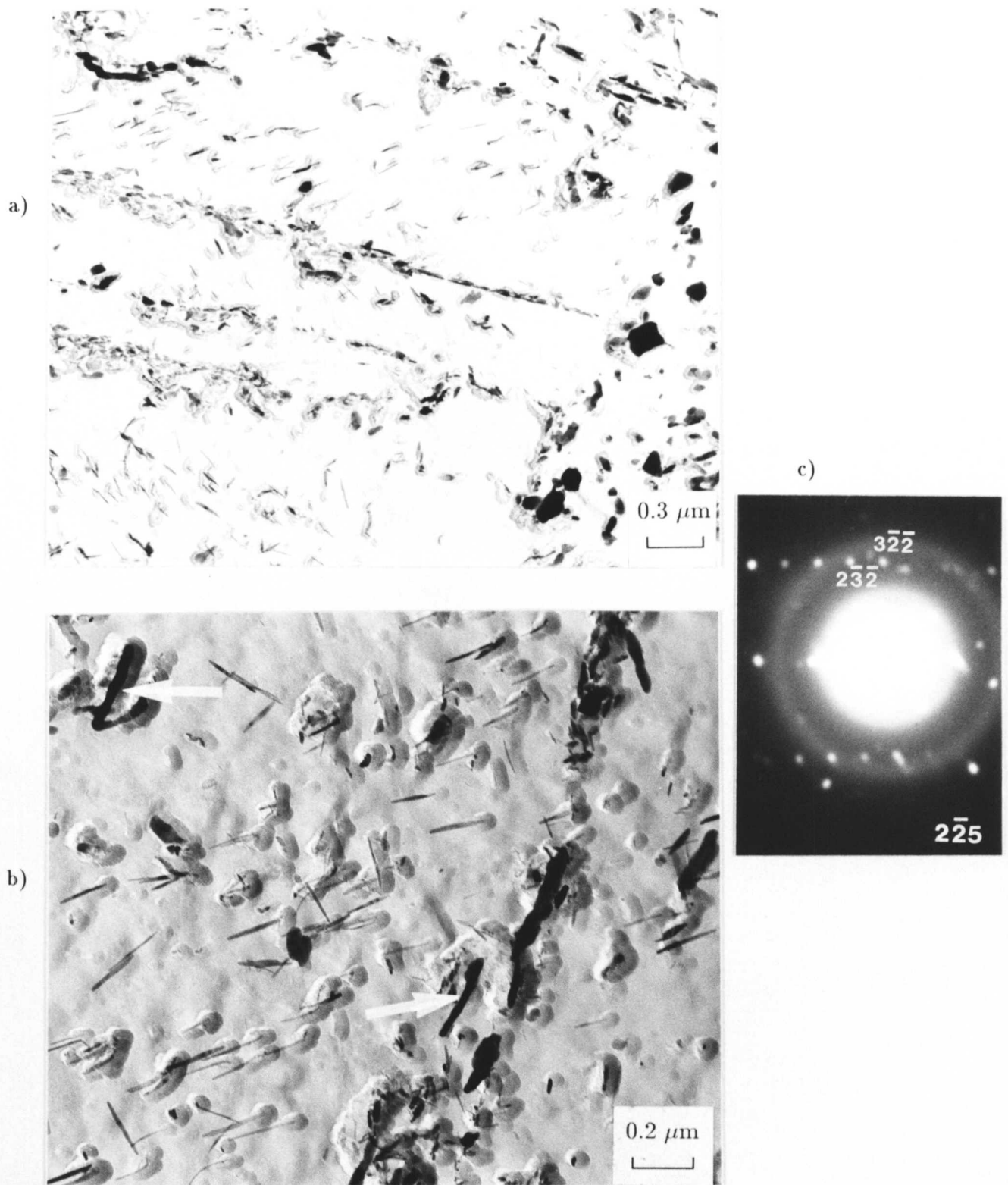


Figure 5.30: Low a) and high b) magnification transmission electron micrographs illustrating extensive M_2C precipitation between bainitic sheaves for specimens tempered for 178 hours at 565°C. The two carbides marked with arrows in b) contain virtually no Mo. A selected area electron diffraction pattern c) confirms that these particles are cementite.

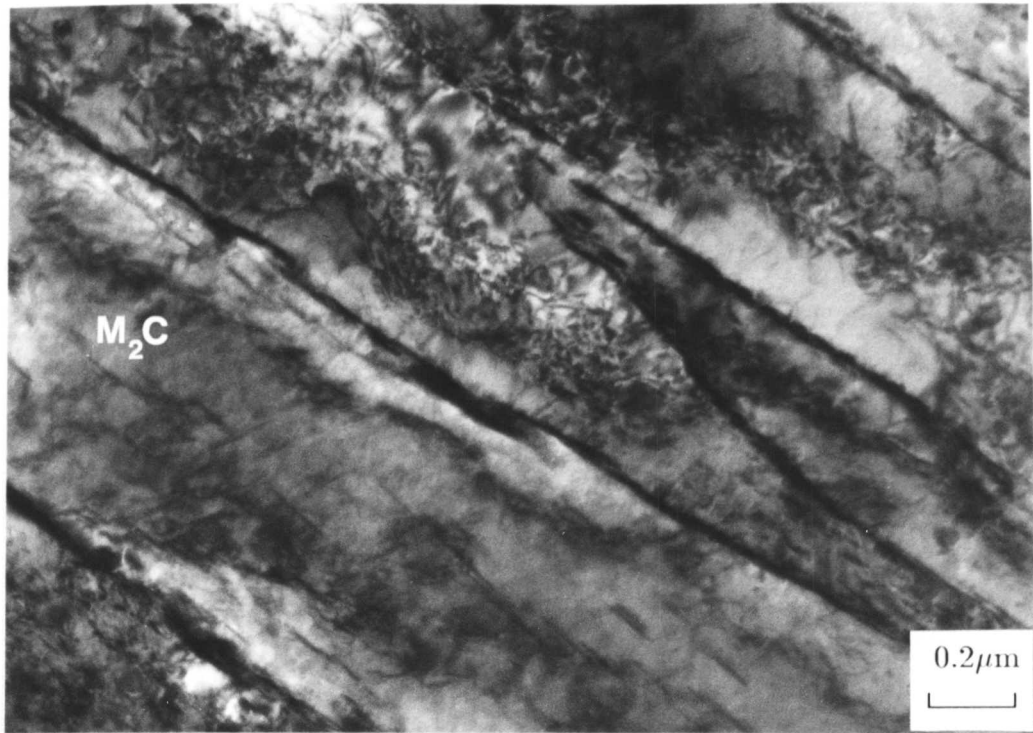


Figure 5.31: Transmission electron micrograph from a thin foil from a specimen tempered for 178 hours at 565°C showing the upper bainitic sheaves dominant in the microstructure. A few cementite particles and a larger M_7C_3 particle can be seen on the lath boundaries; there is also extensive Mo_2C precipitation within the sheaves.



Figure 5.32: A similar upper bainitic region; a large MnS inclusion can be seen within the microstructure, and there is extensive cementite precipitation on the plate boundaries and Mo_2C within the sheaves.

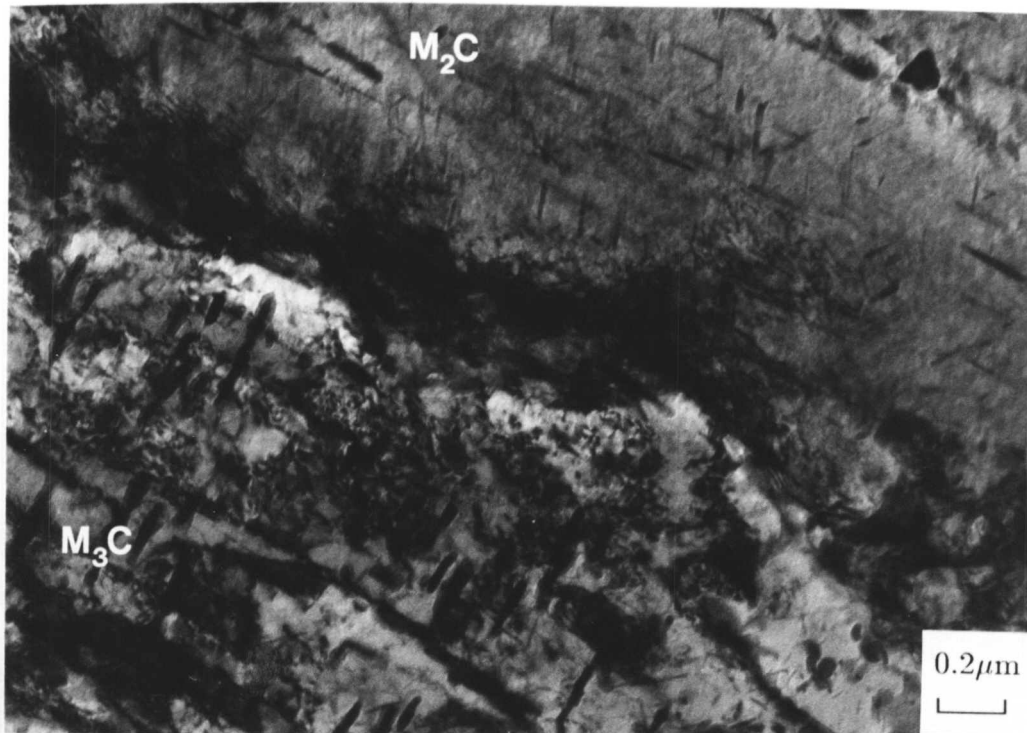


Figure 5.33: A thin foil from the specimen tempered for 178 hours at 565°C illustrating the differences between the different regions of the microstructure. There is dense cementite precipitation in the martensitic region and much finer Mo_2C precipitation in the bainitic region.

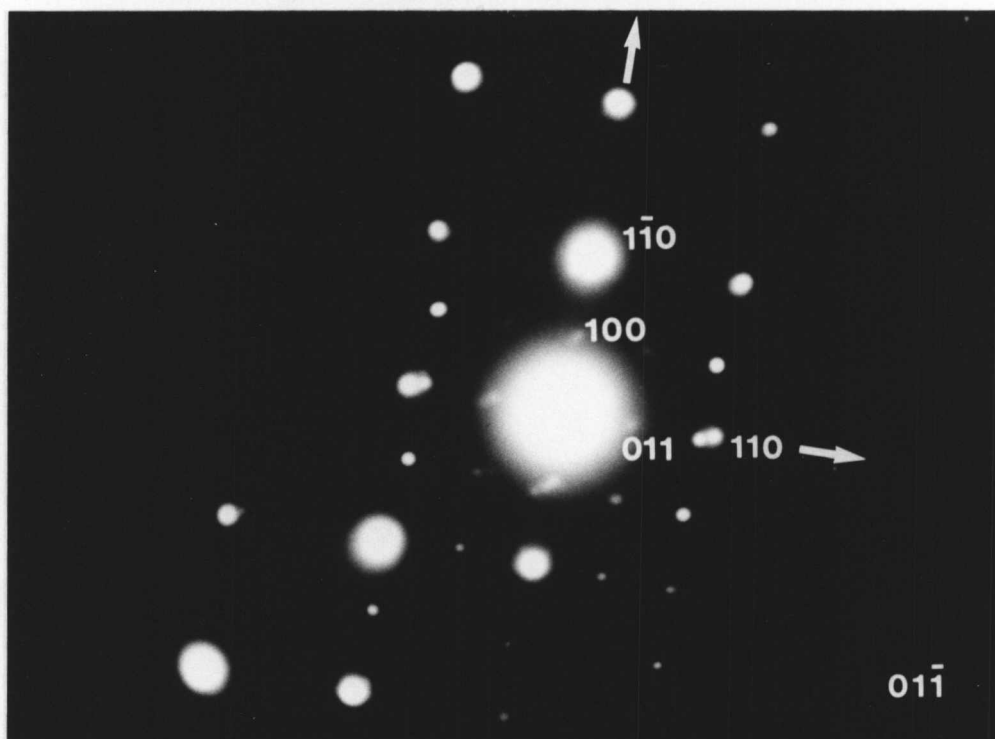


Figure 5.34: A selected area electron diffraction pattern from the martensitic region exhibiting the well known Bagaryatski (1950) orientation relationship.

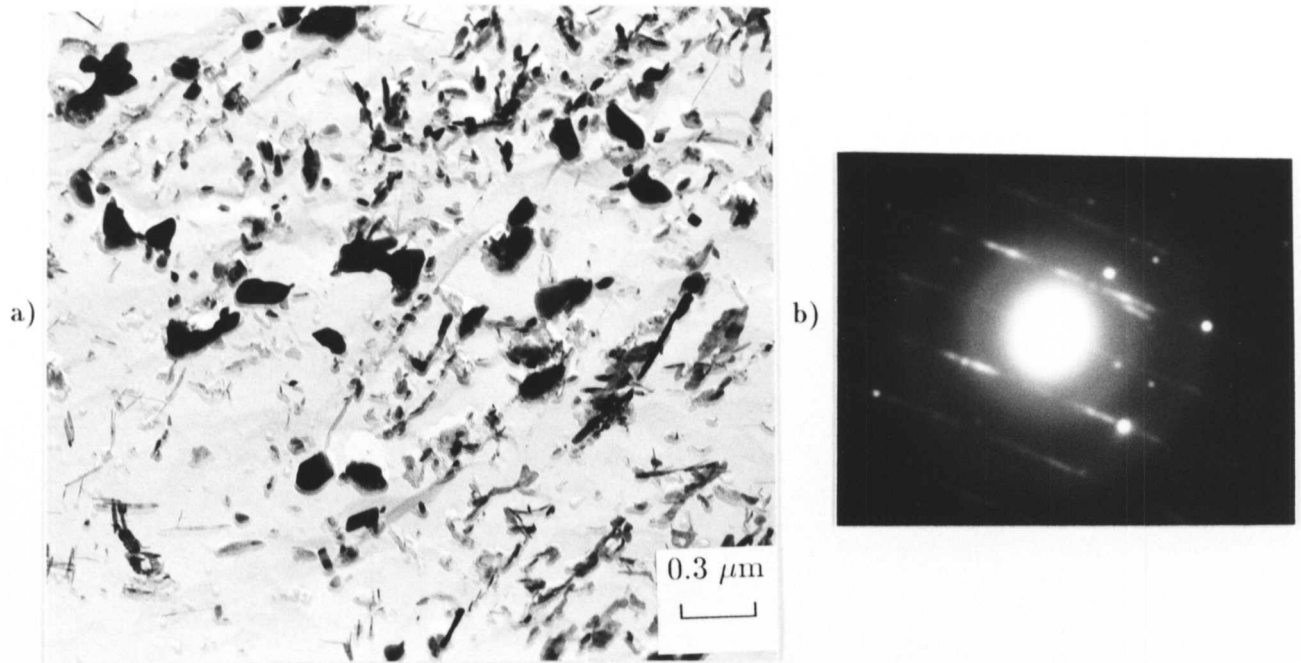


Figure 5.35: a) Carbon extraction replica from a specimen tempered for 238.5 hours at 565°C illustrating that the microstructure consists predominantly of M_7C_3 and M_2C . b) A selected area electron diffraction from M_7C_3 showing characteristic streaks due to the presence of stacking faults within the lattice.

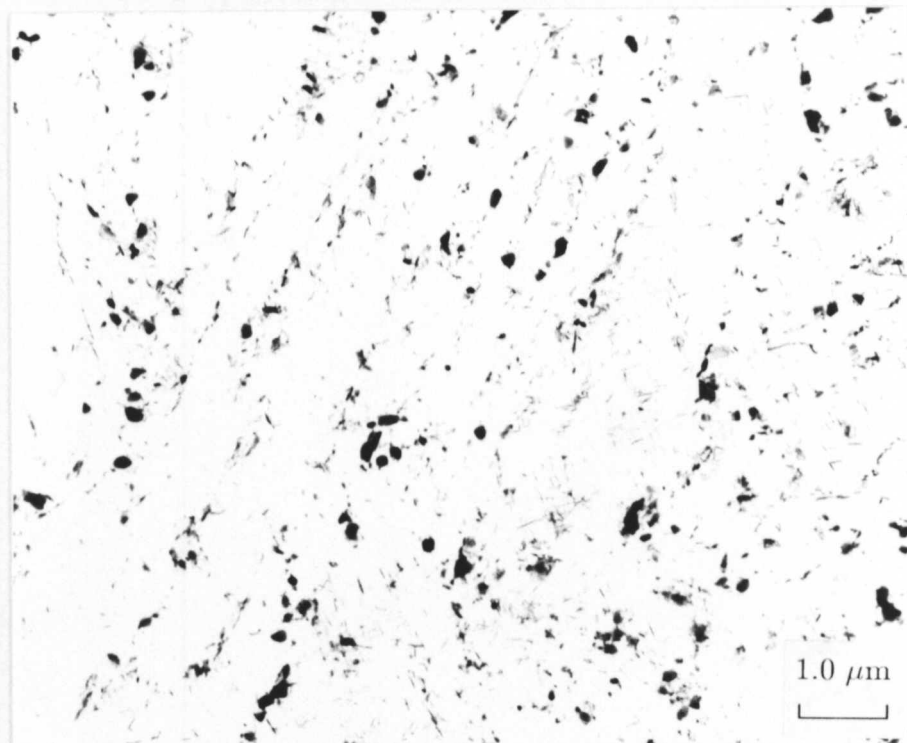


Figure 5.36: Carbon extraction replica from specimen tempered for 512 hours at 565°C, showing increasing precipitation of M_7C_3 at the expense of cementite.

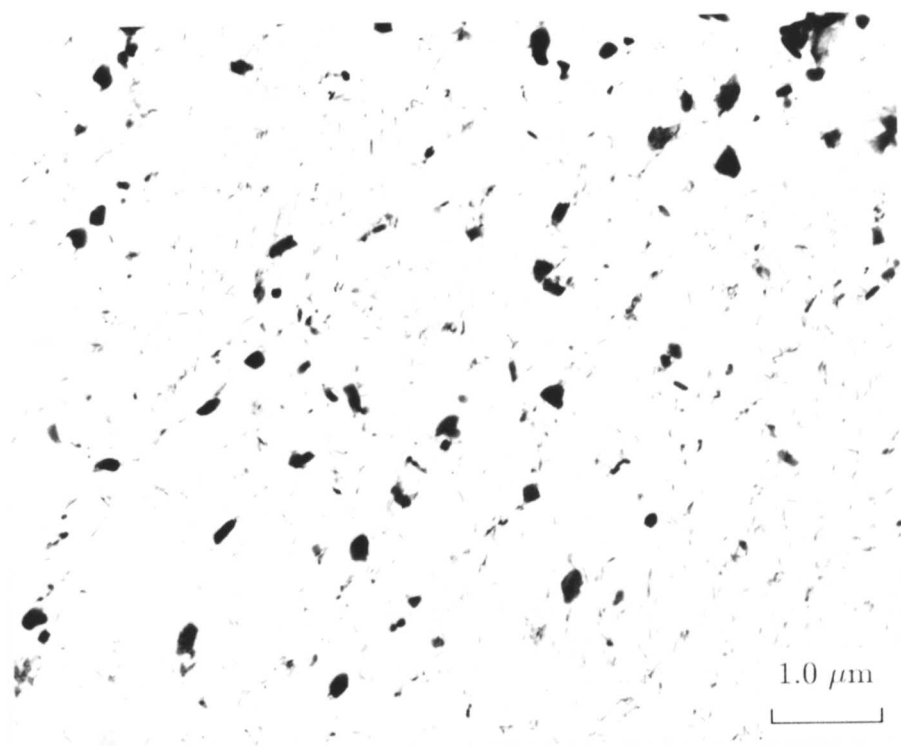


Figure 5.37: Carbon extraction replica from specimen tempered for 1048 hours at 565°C showing that the microstructure consists predominantly of large M_7C_3 and fine M_2C particles.

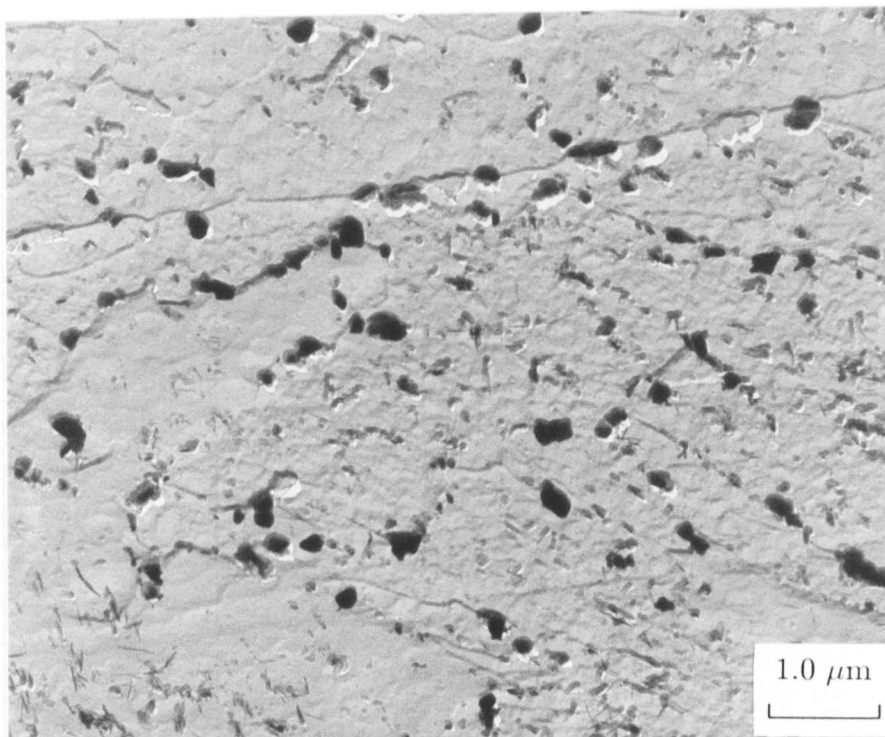


Figure 5.38: Carbon extraction replica from specimen tempered for 2072 hours at 565°C showing that the microstructure consists predominantly of large M_7C_3 and fine M_2C particles.

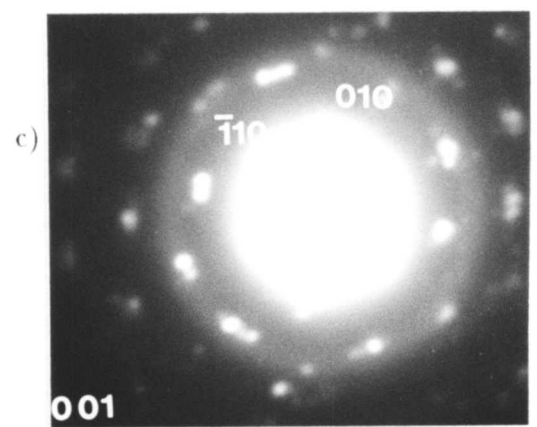
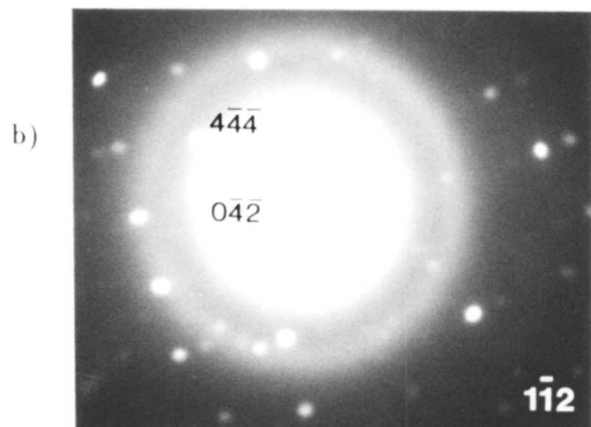
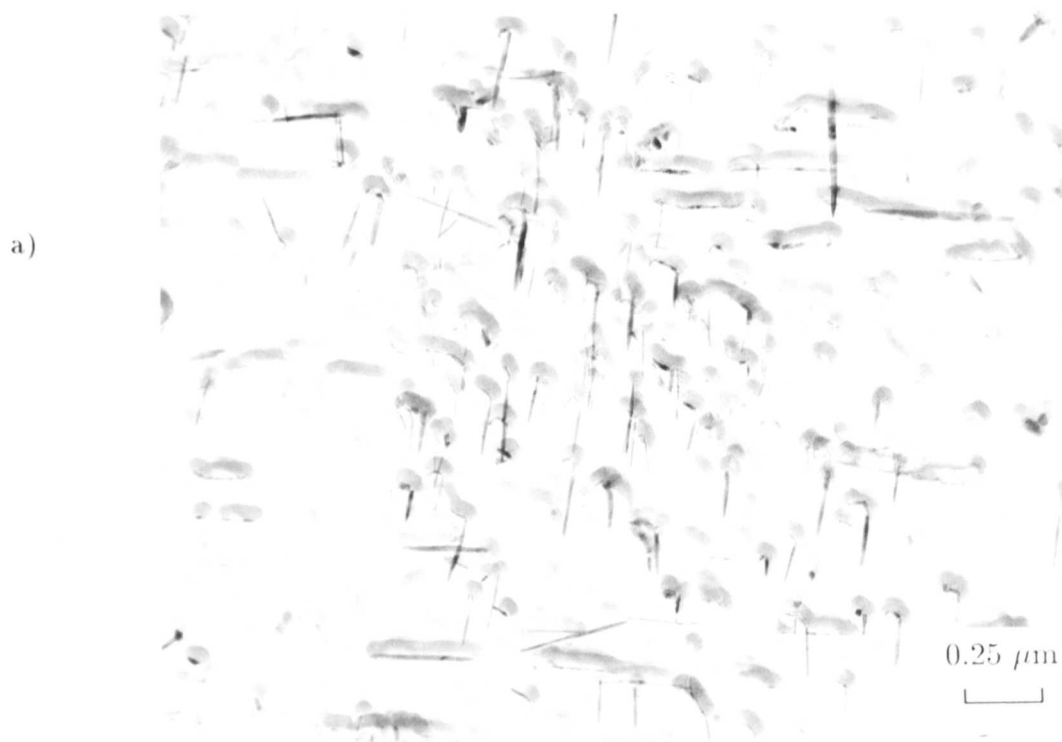


Figure 5.39: a) Carbon extraction replica from specimen tempered for 2072 hours at 565°C showing aligned M_2C particles with small, squarer M_6C carbides in between. Selected area electron diffraction patterns from M_6C carbides b) and a cluster of M_2C c).

5.5.3 EDX measurements of the Cr content of cementite at 565°C

The composition of isolated cementite particles was measured using EDX. A photograph was taken of each individual particle analysed in order to correlate the particle size with composition. Graphs are presented in Figure 5.40a)–g) showing the measured Cr concentration in cementite plotted as a function of the reciprocal particle size for the specimens tempered up to 128 hours at 565°C. The calculated regression line has been plotted on each graph. The correlation coefficient for each plot, the average particle size and the average Cr concentration are presented in Table 5.5.

Table 5.5: Summary of experimental measurements of Cr concentration and particle size for specimens tempered up to 178 hours at 565°C.

Tempering time /Hours	Correlation coefficient	Average Cr conc. /wt.%	Average particle size /nm
$\frac{1}{6}$	0.57	6.70	52
1	0.65	15.04	56
4	0.82	14.96	68
7	0.43	17.85	58
32	0.27	18.06	56
64	0.36	26.91	65
128	-0.05	25.30	65
178 (Martensitic)	–	24.57	72
178 (Bainitic)	–	16.34	75

It can be seen from the graphs that there is a definite trend for the smaller particles to be richer in Cr, although there is some scatter about the regression line. The correlation coefficient is observed to steadily increase with tempering time initially and then to decrease. This is to be expected because initially all the particles are formed under paraequilibrium conditions and have the same concentration as the matrix, then as tempering proceeds the smaller particles will enrich at a faster rate than large particles. This will initially result in an increase in the correlation coefficient, however, at increasing tempering times other effects dominate over the size dependence of the enrichment rate. These include the precipitation of alloy carbides with the subsequent dissolution of cementite in the bainitic regions of the specimens and soft impingement of the cementite particles as they approach the equilibrium concentration. The very poor correlation coefficient and scatter in the measured Cr concentrations for the 128 hour

specimen correspond with the precipitation of the Cr rich M_7C_3 .

The measured Cr content of the cementite in the specimen tempered for 178 hours is presented separately in Figure 5.41a)–c). It has already been noted that two separate populations of cementite were observed in the bainitic and martensitic regions of the microstructure. Figure 5.41c) clearly shows the dichotomy of the cementite compositions; the upper points (marked with triangles) are from martensitic regions of the microstructure free from alloy carbide precipitation whereas the lower points (marked with circles) are from cementite particles in bainitic regions in which extensive alloy carbide precipitation has occurred. The two distributions are shown separately in Figure 5.41a) and b). The average Cr level in the martensitic and the bainitic regions are included in Table 5.5.

It has been shown that the Cr content of a cementite particle is dependent on its size. It is therefore important when finding the average Cr content after a given tempering time of a distribution of cementite particles to take an unbiased sample of particle sizes. To this end histograms have been plotted in Figure 5.42a)–f) showing the number of carbides analysed of different sizes for the specimens tempered for 10 minutes, 1, 4, 7, 32, and 64 hours at 565°C. Although the size distributions are not all identical, it is important to note that there is no significant bias for any of the tempering times towards smaller or larger particles.

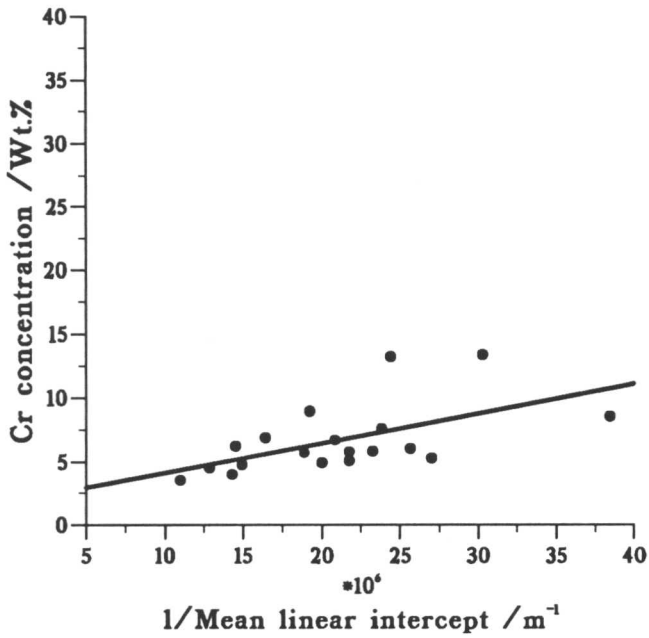
5.5.4 Enrichment of M_7C_3 with tempering time

The carbide M_7C_3 was found to precipitate after tempering at 565°C for approximately 128 hours and then to coexist with cementite for some time before the cementite dissolves. The composition of the M_7C_3 was monitored along with the cementite by EDX. The average composition (measured from at least 10 particles per specimen and not taking into account carbon content) of the M_7C_3 is presented in Table 5.6. It was found that there was a gradual increase in the Cr concentration with tempering time from 58 to 65.5 wt.%. The Mn concentration was found to correspondingly decrease with tempering time. The Mo data as a function of tempering time were scattered. Some of the scatter can be attributed to the inherent difficulty in measuring the Mo content accurately with EDX because of the failure to account for absorption errors. It seems that the absolute level also depends on the particles surrounding the M_7C_3 particles. A similar effect to that already described for cementite particles in the vicinity of M_2C particles was observed; a few M_7C_3 carbides within clusters of M_2C needles contained very little molybdenum. No significant dependence of the composition on the particle size was observed for the M_7C_3 carbides for each tempering time.

Thermodynamic calculations were performed using MTDATA to investigate the equilibrium chromium levels of both M_7C_3 and $M_{23}C_6$ in equilibrium separately with ferrite. It was

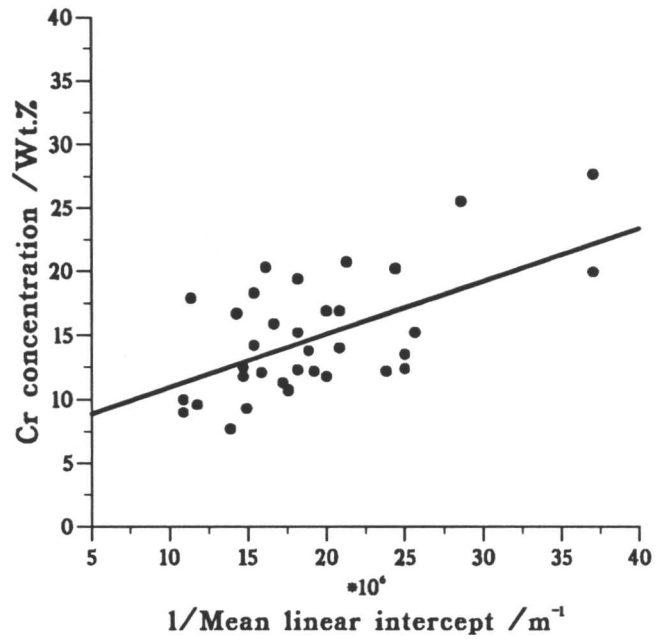
a)

2.25Cr1Mo Steel-10 mins at 565°C



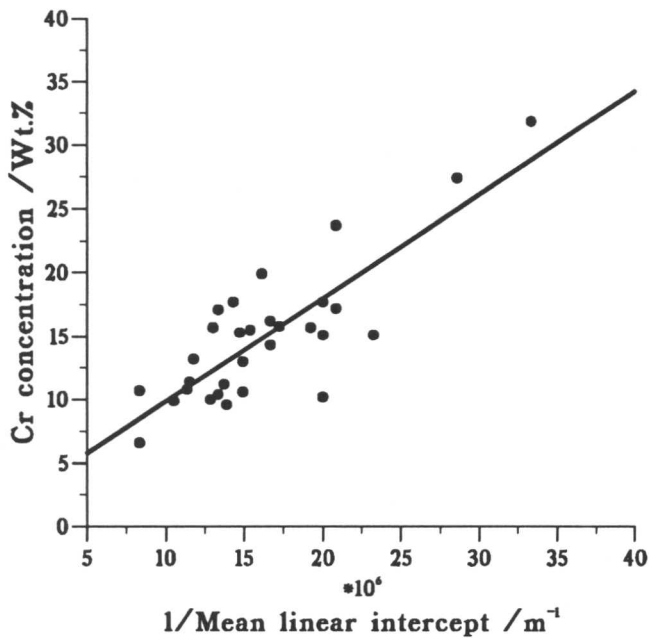
b)

2.25Cr1Mo Steel-1 hour at 565°C



c)

2.25Cr1Mo Steel-4 hours at 565°C



d)

2.25Cr1Mo Steel-7 hours at 565°C

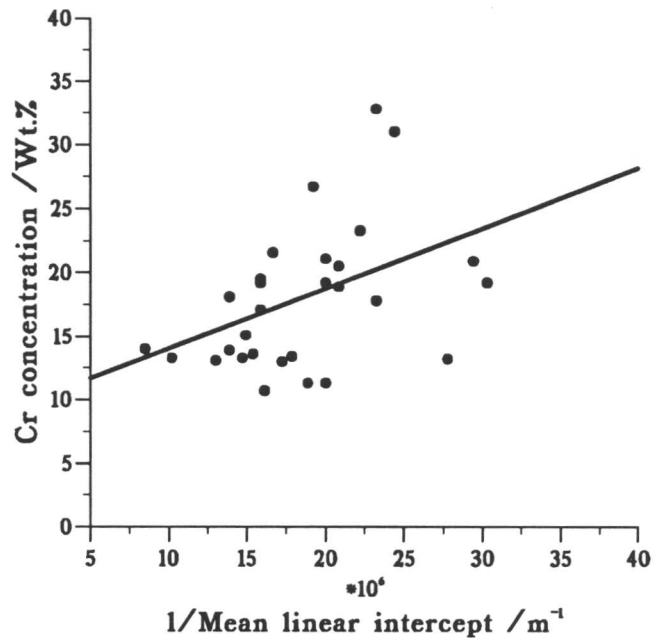
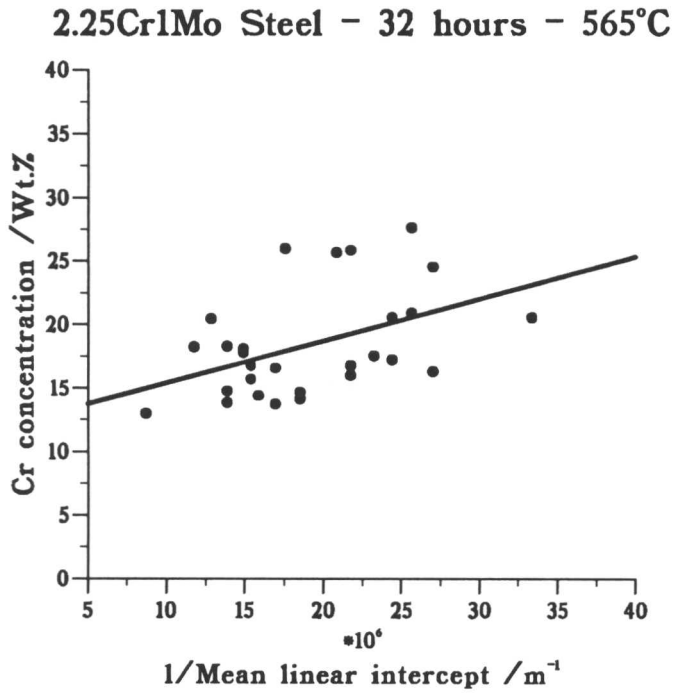
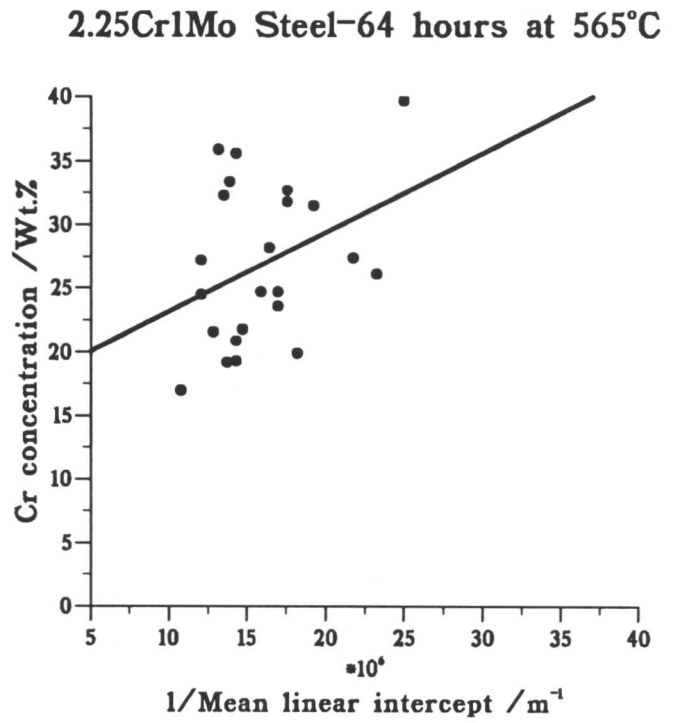


Figure 5.40: a)–g) Chromium concentration in cementite plotted as a function of reciprocal particle size for various tempering times at 565°C for fully bainitic microstructures.

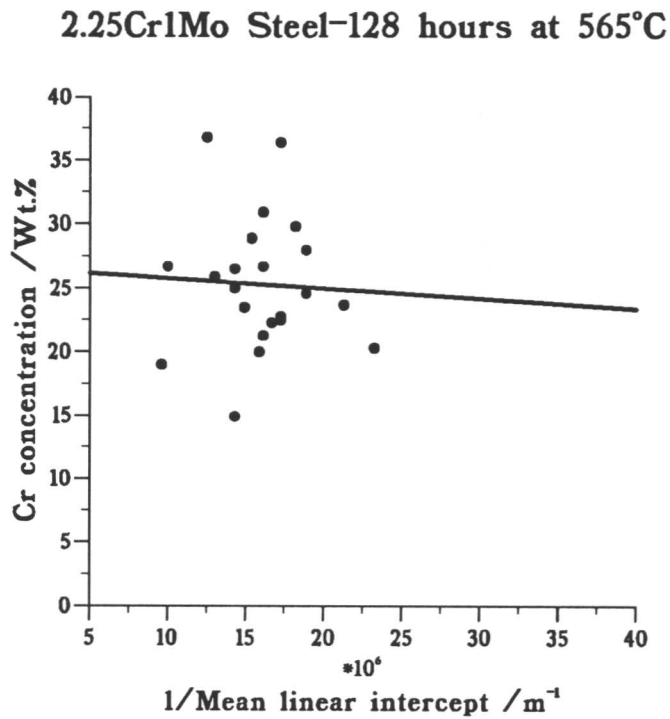
e)



f)



g)



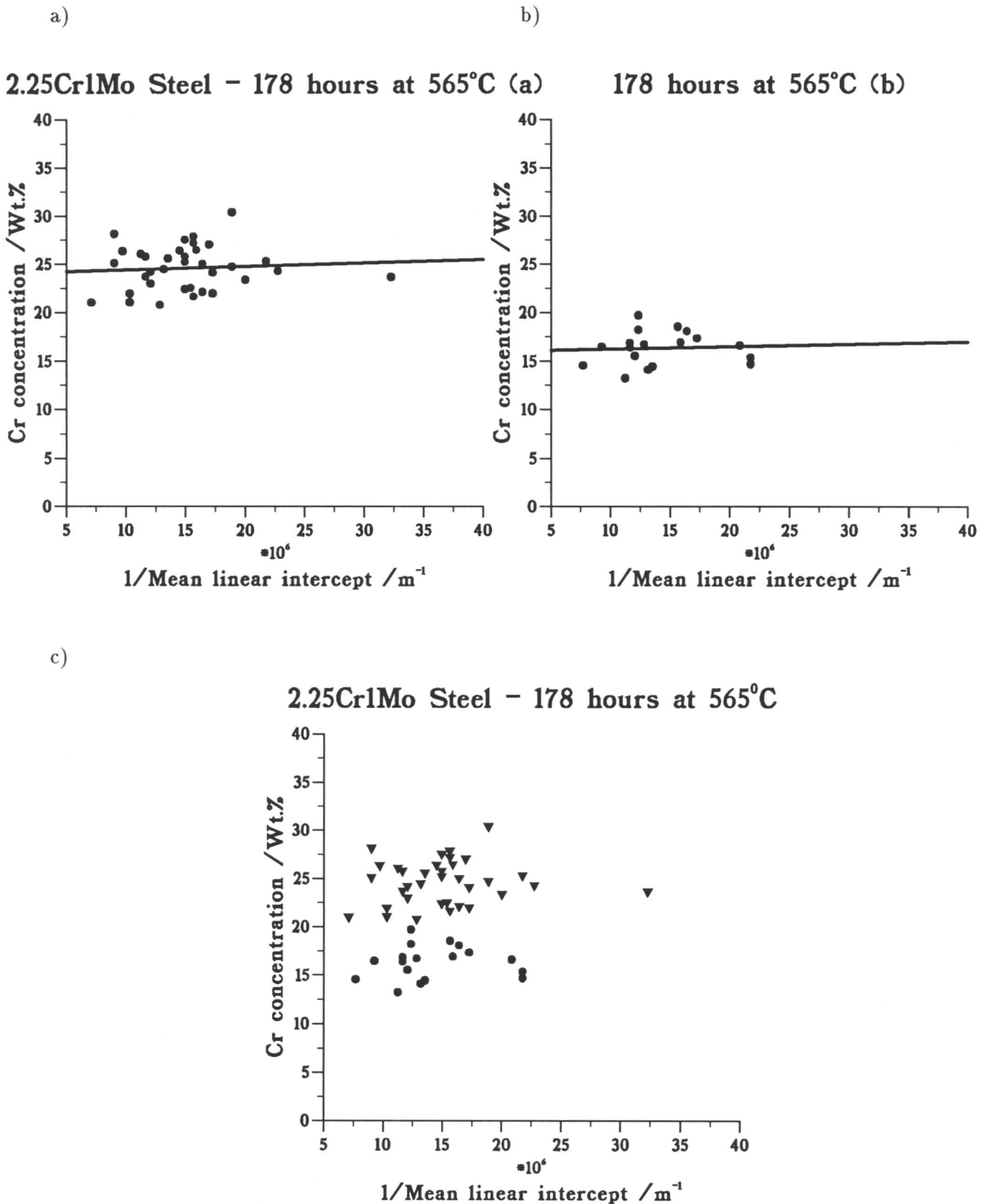


Figure 5.41: a)-c) Chromium concentration in cementite plotted as a function of reciprocal particle size for specimen tempered for 178 hours at 565°C for fully bainitic microstructures.

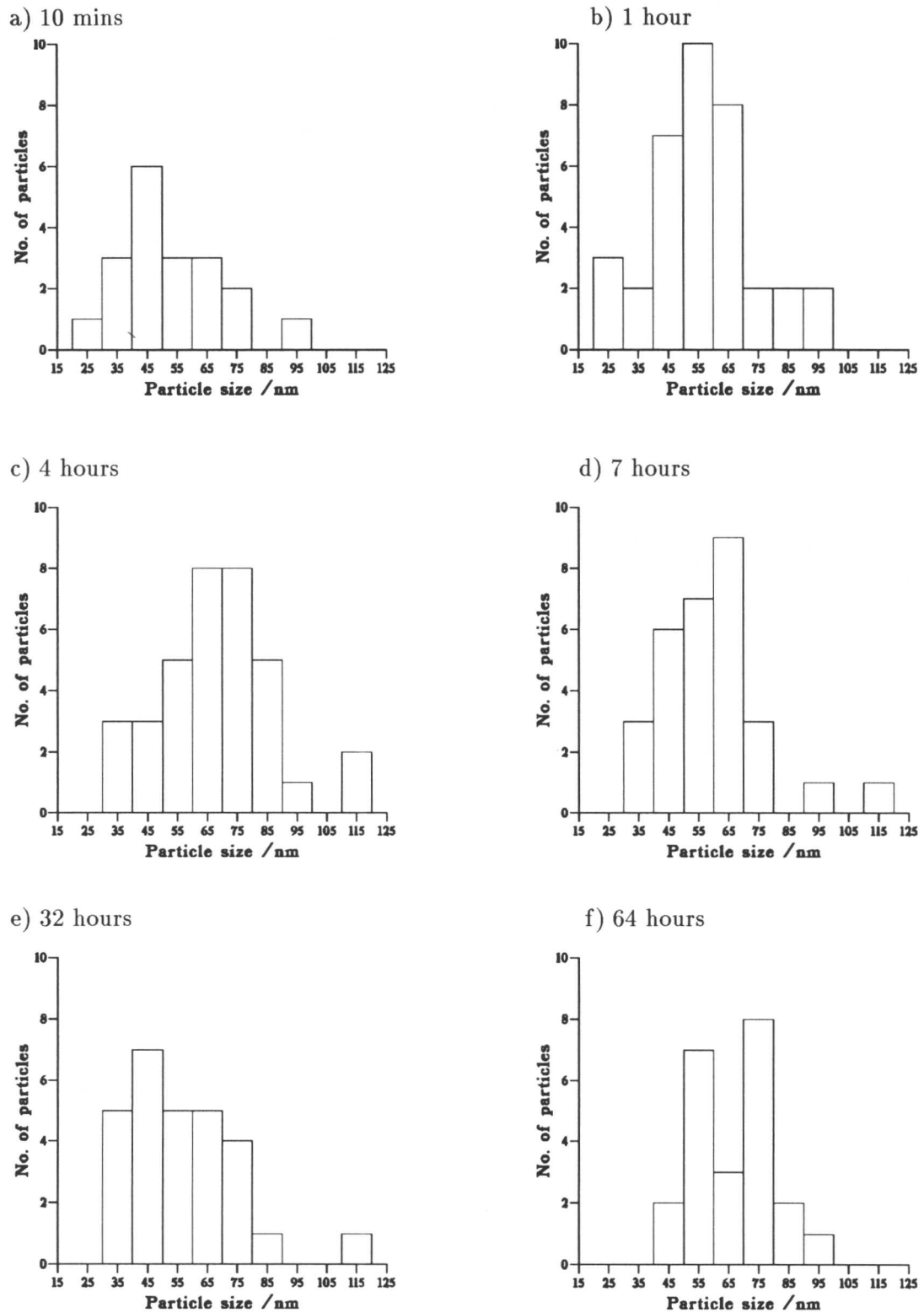


Figure 5.42: Histograms showing the distribution of particles sizes measured after a) 10 mins, b) 1 hour, c) 4 hours, d) 7 hours, e) 32 hours, f) 64 hours tempering at 565°C for the fully bainitic specimens.

Table 5.6: Composition of M_7C_3 with tempering time at 565°C measured by EDX.

Time /Hours	Cr /wt.%	Mn /wt.%	Mo /wt.%	Fe /wt.%
128	58	8	11	23
178	59	6	9	26
238.5	61	4.5	9	25.5
512	62	6.5	3	28.5
1048	63.5	5	7	24.5
2072	65.5	5	5	24.5

not possible to allow M_7C_3 and M_2C , and $M_{23}C_6$ and M_2C to coexist with ferrite. The calculations therefore give an idea of the chromium level only in each carbide because much of the molybdenum would be tied up in M_2C in the real situation. The calculated equilibrium chromium levels in M_7C_3 and $M_{23}C_6$ as a function of temperature are presented in Table 5.7. The predicted equilibrium level of $\simeq 59$ wt.% Cr in M_7C_3 at 565°C is in reasonable agreement with the measured concentrations using EDX. The slightly lower value predicted compared with the observed value can be explained by the fact that some of the Mo predicted to be in the M_7C_3 would actually be in M_2C , leading to an increase in the predicted Cr level in the M_7C_3 .

Table 5.7: Calculated equilibrium Cr levels in M_7C_3 and $M_{23}C_6$ as a function of temperature using MTDATA scaled to remove the stoichiometric carbon concentration to enable direct comparison with EDX measurements.

Temperature /°C	M_7C_3 Cr level /wt.%	$M_{23}C_6$ Cr level /wt.%
750	52.2	30.4
700	54.5	34.5
650	56.5	39.2
600	58.0	44.4
565	58.7	48.2
550	58.8	49.8

5.5.5 Enrichment of Mo_2C with tempering time

It has been observed (Pilling and Ridley, 1982) that the carbides M_2C and M_6C become richer in molybdenum as a function of tempering time in a $2\frac{1}{4}Cr1Mo$ steel. These tempering heat treatments were carried out at 700°C. In this study, the M_2C carbide needles formed at

565°C are very fine and therefore attempts at measuring their composition by EDX are subject to considerable error, especially with respect to the concentration of molybdenum. M_6C was found to precipitate after 1048 hours tempering and contained $\simeq 60$ wt.% molybdenum. This is in good agreement with the equilibrium composition calculated using MTDATA at 565°C, which suggests that there would be no further enrichment on prolonged tempering. At the higher temperatures used by Pilling and Ridley (1982) the molybdenum-based alloy carbides will precipitate quickly and therefore may not quite be at their equilibrium composition, whereas at lower temperatures they do not precipitate until much later tempering times. In this case the carbides appear to precipitate very close to their equilibrium compositions.

5.5.6 Consideration of the precipitation of $M_{23}C_6$

It was important to exclude completely the possibility that the cementite observed in the bainitic regions coexisting with M_2C could in fact be some other carbide, such as $M_{23}C_6$, because conclusive proof with selected area electron diffraction was difficult. Therefore, a fully bainitic specimen was tempered at 750°C for 48 hours in order to accelerate the precipitation of $M_{23}C_6$. The microstructure after this heat treatment presented in Figure 5.43a) consisted of two different carbide dispersions. The larger carbides were identified as $M_{23}C_6$ by both EDX and selected area electron diffraction (Figure 5.43b), and the smaller carbides as M_7C_3 . The average composition of the $M_{23}C_6$ was

31 wt.% Cr, 2 wt.% Mn, 9 wt.% Mo, and 58 wt.% Fe,

and that of the M_7C_3 as

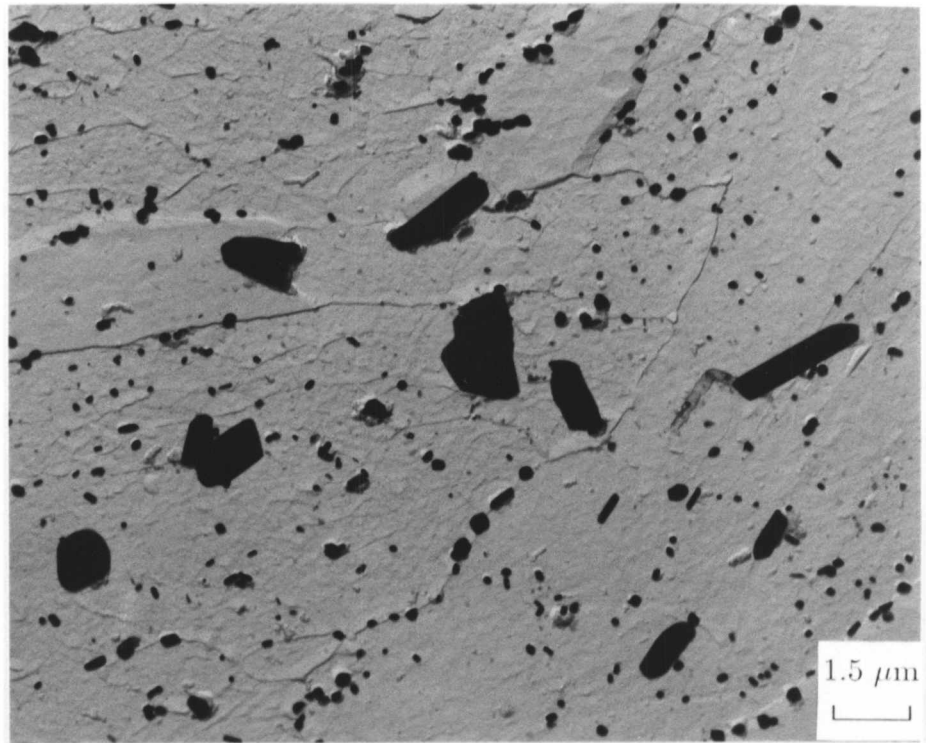
51 wt.% Cr, 2.5 wt.% Mn, 7 wt.% Mo, and 39.5 wt.% Fe.

These Cr levels are in excellent agreement with those predicted by MTDATA (see Table 5.7 above) for tempering at 750°C, and confirm that the amount of Cr each carbide can support increases as the tempering temperature decreases. The predicted Cr level in $M_{23}C_6$ at the lower temperature of 565°C of 48 wt.% can therefore be assumed to be accurate. This means that were $M_{23}C_6$ to be present in the specimens tempered at 565°C it should contain 48 wt.% Cr, ruling out any possibility that the cementite with reduced Mo content and lower Cr levels in the bainitic regions could be $M_{23}C_6$. $M_{23}C_6$ was not observed in the bainitic microstructure for tempering times up to 3000 hours at 565°C.

5.5.7 Microstructural evolution during tempering at 510°C

The microstructural changes in specimens tempered at 510°C were considerably slower than at 565°C. The optical microstructure after tempering for 256 hours is presented in Figure 5.44.

a)



b)

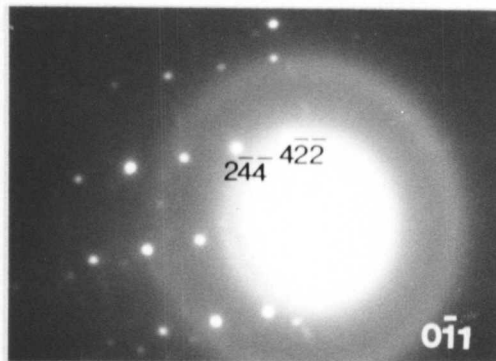


Figure 5.43: a) Carbon extraction replica from a fully bainitic specimen tempered for 48 hours at 750°C showing large particles of $M_{23}C_6$ and smaller particles of M_6C . b) Selected area electron diffraction pattern from an $M_{23}C_6$ carbide.

There are no observable differences compared with the starting microstructure. Figure 5.45 is a transmission electron micrograph from a replica taken from a specimen tempered for 1 hour; comparison with Figure 5.23 shows that the initial precipitation of cementite is much slower at the lower temperatures, as expected. Tempering for up to 256 hours allowed cementite to precipitate and enrich as in the specimens tempered at 565°C. The enrichment rate of the cementite was found to be a lot slower and no M_2C precipitation was found after 256 hours, compared with M_2C being found after 32 hours in the specimens tempered at 565°C.

5.5.8 EDX measurements of the Cr content of cementite at 510°C

The plots of Cr concentration against the reciprocal of particle size are presented in Figure 5.46a)–c) for the specimens tempered at 510°C. There is considerable scatter in the compositions measured after tempering for 1 hour, however, the slope of the regression line increases after tempering for 128 and 256 hours as the effect of the smaller particles enriching more quickly than the larger particles becomes more prominent. The results of these analyses are summarised in Table 5.8.

Table 5.8: Summary of experimental measurements of Cr concentration in cementite and particle size for specimens tempered up to 256 hours at 510°C.

Tempering time /Hours	Correlation coefficient	Average Cr conc. /wt.%	Average particle size /nm
1	-0.43	11.8	45
128	0.13	15.9	62
256	0.40	20.1	64

5.5.9 Microstructural evolution during tempering at 620°C

Microstructural changes at 620°C were rapid compared to those at 565°C. This is illustrated in Figure 5.47 which shows extensive cementite precipitation after tempering for only 1 hour taken from a carbon extraction replica. A MnS inclusion is also marked in the figure. The steel contains quite a number of MnS particles as a result of the manufacturing process, however, these are distributed evenly throughout the microstructure and therefore have no influence on the changes which occur. After 10 hours tempering there is extensive precipitation of M_7C_3 together with fine M_2C needles. After 25 hours the M_7C_3 is widespread, illustrated in Figure 5.48. M_7C_3 did not appear until after tempering for 128 hours at 565°C. It was clear that there were two different types of cementite, one richer in Cr and Mo, and one containing

less Cr and virtually no Mo, in the specimens tempered for only 25 hours at 620°C. This is illustrated in Figure 5.49. The two cementite particles marked with arrows at the boundary between two sheaves and in regions in which there is extensive M_2C precipitation both have the composition

15 wt.% Cr, 3 wt.% Mn, 0 wt.% Mo, and 82 wt.% Fe,

whereas the cementite particles in the martensitic regions have an average composition

23 wt.% Cr, 4.5 wt.% Mn, 5.0 wt.% Mo, and 67.5 wt.% Fe.

5.5.10 EDX measurements of the Cr content of cementite at 620°C

The plots of Cr concentration against the reciprocal of particle size are presented in Figure 5.50a)–c) for the specimens tempered at 510°C for 1, 10 and 25 hours respectively. These results exhibit considerably more scatter than do those at 510 and 565°C. The explanation of this is that microstructural changes are accelerated at the higher temperature with alloy carbide precipitation being present to some extent in all the specimens. The results are summarised in Table 5.9. The cementite has started to dissolve (corresponding to a drop in the experimentally measured cementite concentrations) after only 25 hours at 565°C.

Table 5.9: Summary of experimental measurements of Cr concentration and particle size for specimens tempered up to 25 hours at 620°C.

Tempering time /Hours	Correlation coefficient	Average Cr conc. /wt.%	Average particle size /nm
1	0.35	17.6	73
10	0.13	25.5	81
25	0.14	23.2	79

5.5.11 Coexistence of M_7C_3 with cementite

It has been noted that M_7C_3 precipitated whilst cementite was still present in the microstructure, and then the two coexisted for some time. The cementite in the immediate vicinity of M_7C_3 particles was found to have a lower Cr content than the average measured for an isolated cementite particle. It was thought that in the same way as the precipitation of M_2C appears to draw Mo from the cementite, precipitation of the Cr-rich M_7C_3 drew Cr away from any cementite particles nearby. This is illustrated in Figure 5.51 which shows a cementite



Figure 5.44: Optical micrograph for a fully bainitic specimen tempered at 510°C for 256 hours.

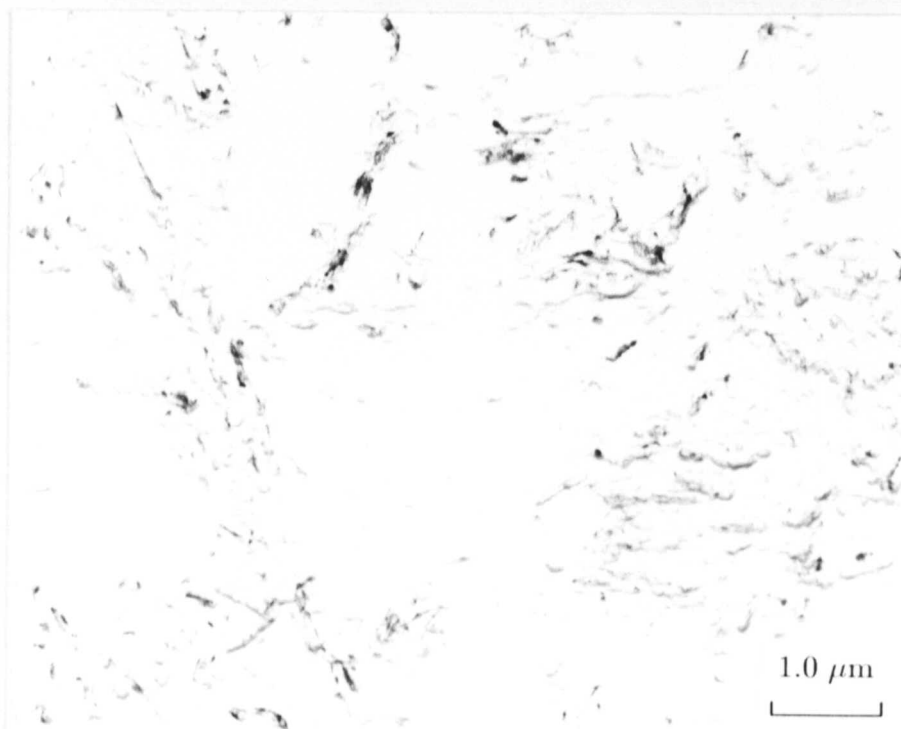


Figure 5.45: Carbon extraction replica taken from a bainitic specimen tempered at 510°C for 1 hour showing that cementite precipitation is very slow at this temperature.

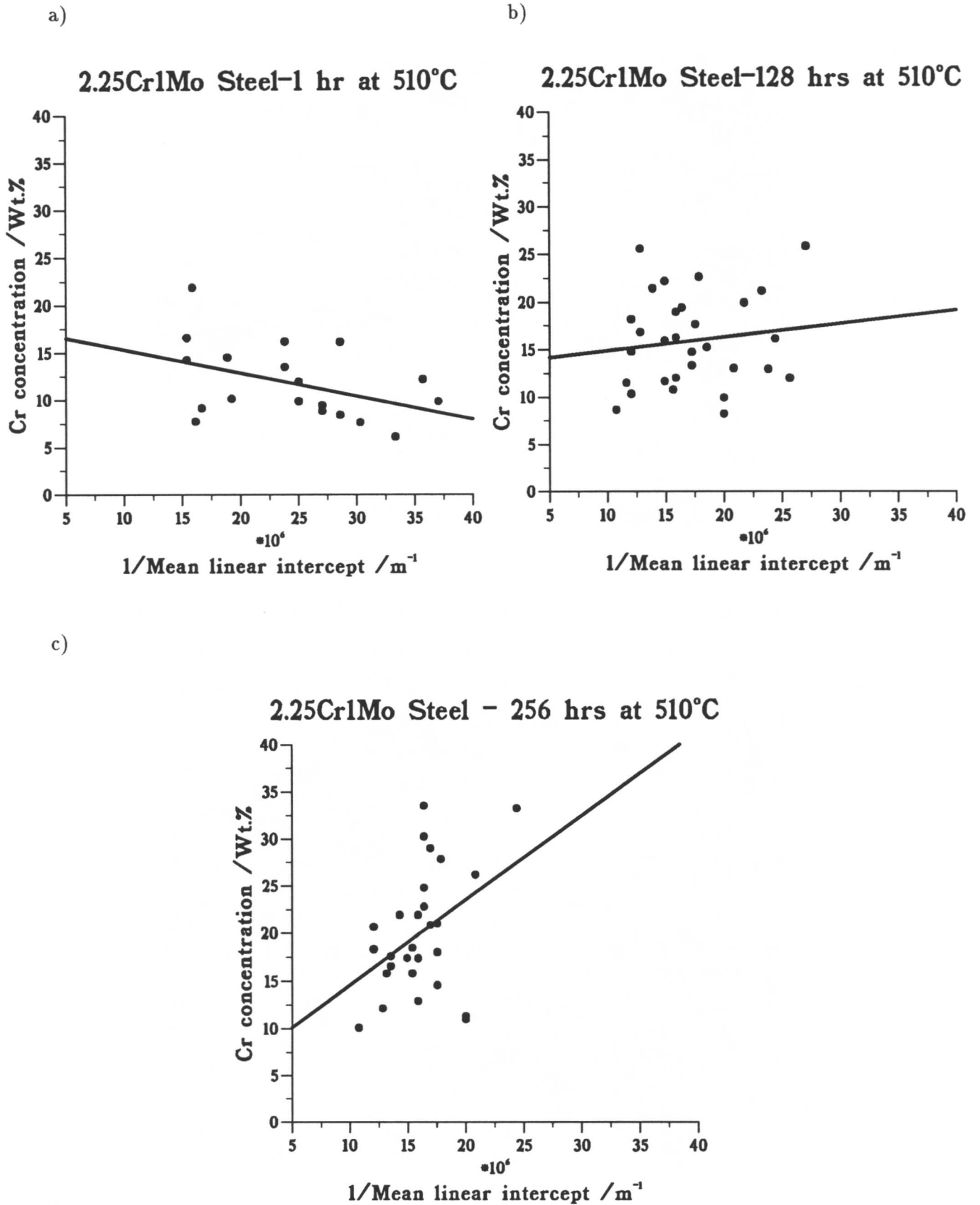


Figure 5.46: a)-c) Chromium concentration in cementite plotted as a function of reciprocal particle size for specimens tempered for various times at 510°C for fully bainitic microstructures.

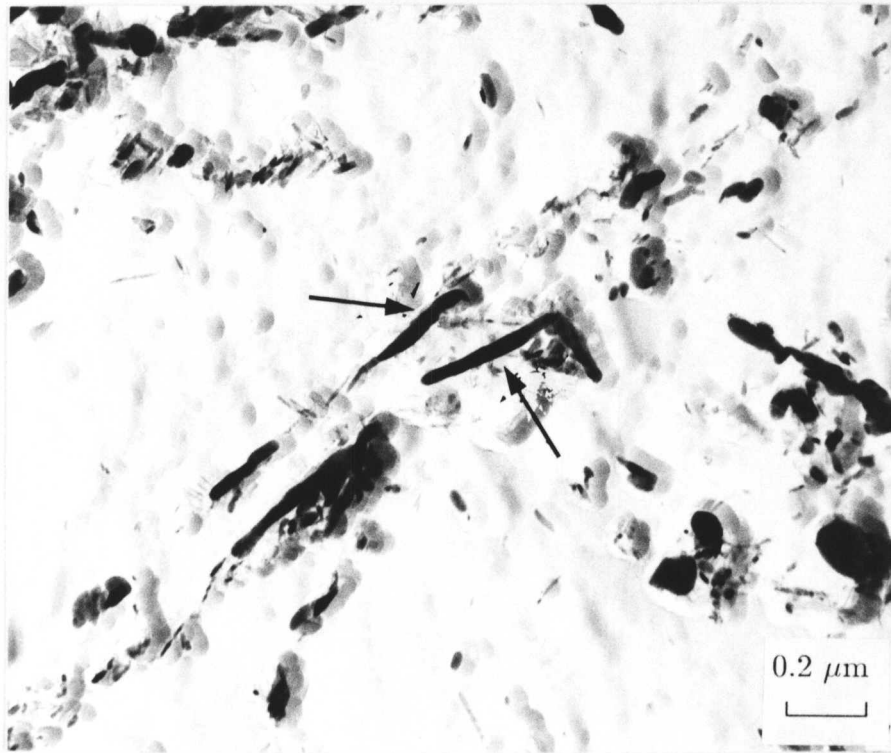
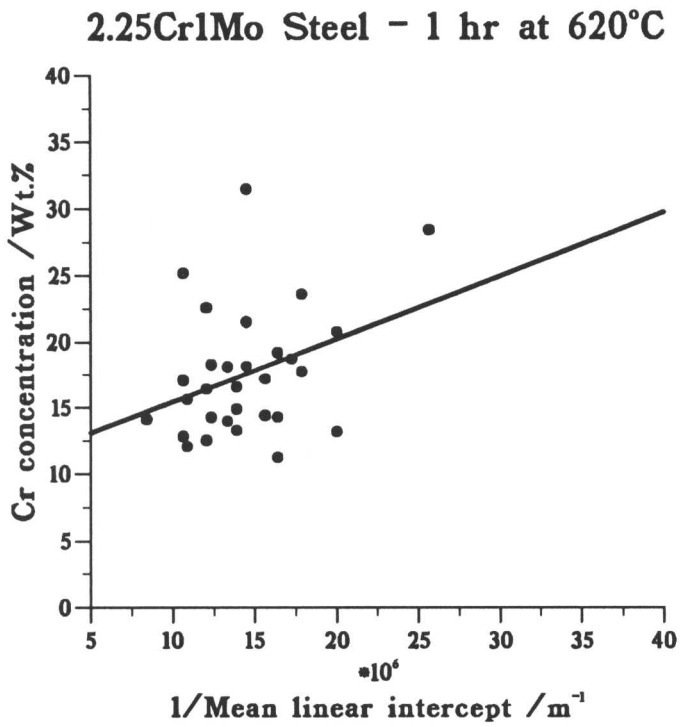
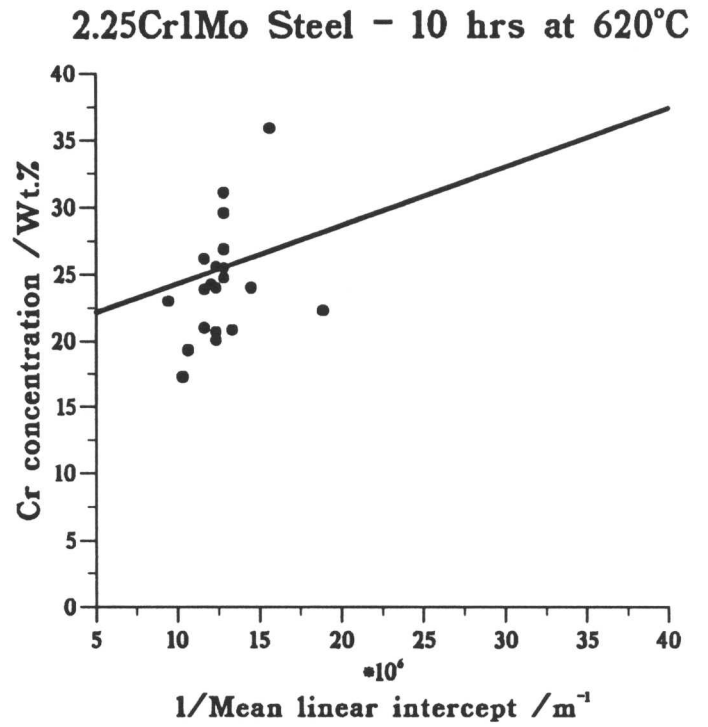


Figure 5.49: Carbon extraction replica from the fully bainitic specimen tempered for 25 hours at 620°C showing cementite particles with reduced Mo content in a region of extensive M_2C precipitation.

a)



b)



c)

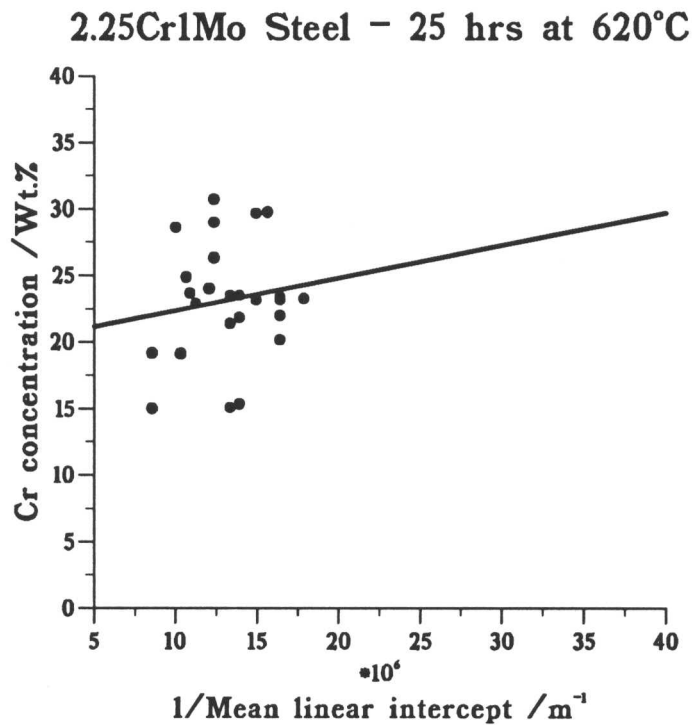


Figure 5.50: a)-c) Chromium concentration in cementite plotted as a function of reciprocal particle size for specimens tempered for various times at 620°C for fully bainitic microstructures.

particle next to an M_7C_3 particle in a fully bainitic specimen tempered for 10 hours at 620°C. The cementite has a composition

19 wt.% Cr, 4 wt.% Mn, 1 wt.% Mo, and 76 wt.% Fe,

compared with the Cr level in an isolated cementite particle of comparable size of

24 wt.% Cr, 4 wt.% Mn, 6 wt.% Mo, and 66 wt.% Fe.

The M_7C_3 particle contains 51 wt.% Cr. By considering the equilibrium Cr levels in cementite and ferrite and in M_7C_3 and ferrite using MTDATA it can be established whether there is a flux of Cr through the ferrite from cementite towards an M_7C_3 particle.

It was not possible to allow both cementite and M_7C_3 to exist at 565°C for the composition of the $2\frac{1}{4}\text{Cr1Mo}$ steel used because MTDATA calculates the carbides present at equilibrium. When the three phases cementite, ferrite and M_7C_3 were allowed to coexist MTDATA correctly calculates the microstructure to consist of M_7C_3 and ferrite only. In order to investigate the possibility of a Cr flux from cementite to M_7C_3 when the two coexist as a consequence of kinetic factors, the bulk carbon concentration was increased until the cementite became thermodynamically stable again and coexists with the M_7C_3 . This is a somewhat artificial procedure in that the calculated absolute equilibrium values in the three phases will not relate to the real situation, but it will allow the possibility of a Cr flux from cementite to M_7C_3 to be studied. Care was taken that as the bulk carbon concentration was increased to force the three phases to exist, the Fe/Cr ratio in the alloy overall was kept constant. Figure 5.52 shows the calculated equilibrium Cr level in cementite as a function of the bulk carbon concentration. It can be seen that for high carbon concentrations only cementite is the stable carbide, and for low carbon concentrations M_7C_3 is stable; for intermediate compositions M_7C_3 and cementite coexist. The lowest carbon concentration at which M_7C_3 and cementite were in equilibrium with ferrite, 0.75 wt.%, was chosen to perform further calculations because this point would be most closely related to the composition of the $2\frac{1}{4}\text{Cr1Mo}$ steel. The equilibria between cementite and ferrite and between M_7C_3 and ferrite were then investigated separately at this overall concentration to find the Cr level in the ferrite at the interface between each of the particle types. The results of these calculations are presented in Figure 5.53. It can be seen that because the Cr level in the ferrite matrix surrounding a cementite particle is higher than that surrounding an M_7C_3 particle, a flux of Cr is stimulated from the cementite to the M_7C_3 , hence explaining the drop in Cr level in a cementite particle in the vicinity of an M_7C_3 particle.

5.5.12 Coexistence of Mo₂C with cementite

A similar calculation was performed to that described in the previous section to study the coexistence of M₂C and cementite. Once again, in order to force MTDATA to allow M₂C and cementite to coexist in ferrite, the carbon concentration in the bulk alloy was increased, keeping the Fe/Cr ratio constant. Below 0.5 wt.% C only M₂C was stable, but further increasing the carbon concentration allowed M₂C and cementite to coexist. As the carbon concentration increased, the volume fraction of cementite was predicted to increase at the expense of the M₂C. The results of the calculation for an overall concentration of 0.5 wt.% C are presented in Figure 5.54. It can be seen that the increase in the matrix concentration of Cr and Mo around a cementite particle would result in a flux of both to the M₂C. This is consistent with the experimentally observed fact that once there is extensive M₂C precipitation within the bainitic plates, the cementite between the plates begins to 'lose' both chromium and molybdenum.

5.5.13 Calculation of the diffusion constants from experimental results

The enrichment kinetics of cementite particles were studied for various times at three different temperatures in order that the diffusion coefficient and the activation energy could be calculated for the diffusion of chromium in ferrite. The dependence of the diffusion coefficient of chromium in ferrite, D_α , is given by the analytical equation (3.28)

$$t_c = \frac{\pi x_\theta^2 (\bar{c} - c^\theta)^2}{16D_\alpha (c^{\alpha\theta} - \bar{c})^2}.$$

The most accurate way of performing this calculation is to use all the experimental data gathered in the TEM and evaluate the quantity

$$\frac{\pi x_\theta^2 (\bar{c} - c^\theta)^2}{16(c^{\alpha\theta} - \bar{c})^2} \quad (5.4)$$

for each individual particle analysed at each of the different tempering temperatures and times. Regression of the tempering time, t_c , against the expression 5.3 should then give a straight line passing through the origin with a gradient equal to the reciprocal of the diffusion coefficient. The tempering times and temperatures used in this analysis only included those specimens in which enrichment of the cementite was taking place rather than the dissolution due to the precipitation of Cr-based alloy carbides. This therefore included tempering times up to 64 hours at 565°C, all the specimens tempered at 510°C and excluded the 25 hour specimen tempered at 620°C.

The value of $c^{\alpha\theta}$, the equilibrium concentration of Cr in the ferrite, varies with temperature. The values used for the calculations of the diffusion coefficient were calculated using MTDATA

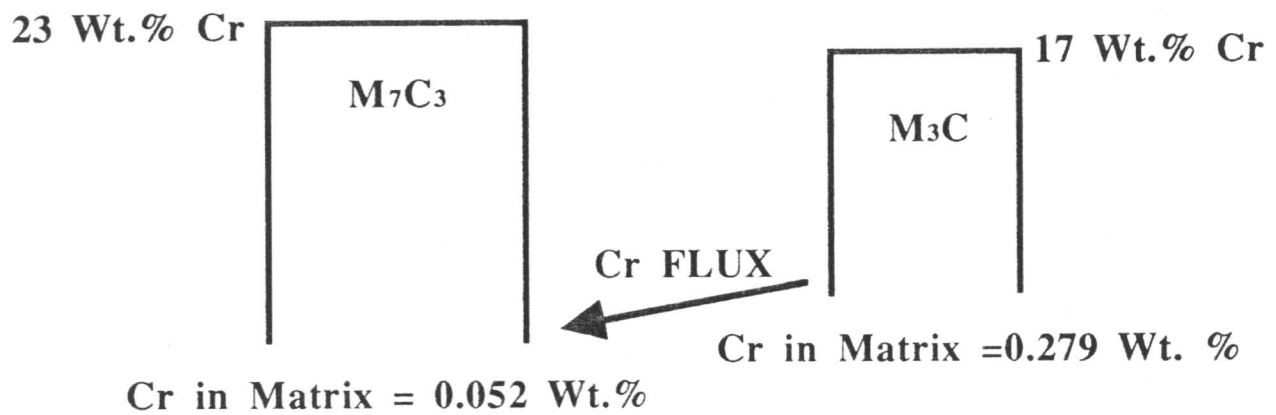


Figure 5.53: Schematic illustration of a cementite particle next to an M_7C_3 particle showing calculated equilibrium concentrations in the particles and the matrix using MTDATA.

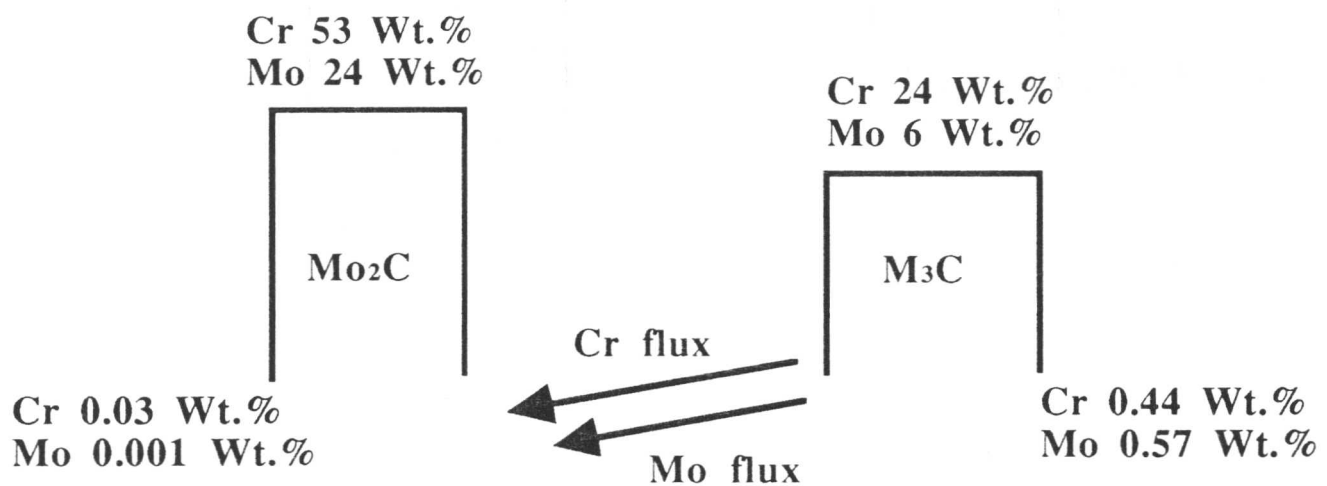


Figure 5.54: Schematic illustration of a cementite particle next to an M_2C particle showing calculated equilibrium concentrations in the particles and the matrix using MTDATA.

allowing only the phases cementite and ferrite to exist. These data have been presented in Table 5.2. The predicted chromium level in the cementite is higher than that observed in the particles experimentally (because of the precipitation of Cr-based alloy carbides discussed above) and therefore the predicted of $c^{\alpha\theta}$ should be slightly higher than that used in the calculations. The effect of this difference will be very small because it will not change the value of the regression constant, and hence the value of D_{α} , at any one temperature because it would simply be changing the absolute value of the constant in the denominator of expression 5.3. The volume fraction of cementite is small compared to the ferrite and therefore any changes in the overall concentration in the matrix due to changes in the cementite composition will also be small.

The equilibrium values also take into account the carbon content of the cementite, which the EDX data do not. The EDX measurements were therefore scaled to allow for 6.67 wt.% of C to be contained in the cementite (the stoichiometric carbon content for M_3C).

A computer program was written to calculate the regression coefficient, and therefore the diffusion constant, at each of the three tempering temperatures. The results of the calculations are presented in Table 5.10.

Table 5.10: Calculated diffusion coefficient as a function of temperature for the fully bainitic specimens.

Temp /°C	$D_{\alpha} / m^2 s^{-1}$
510	$3.5 \pm 0.2 \times 10^{-19}$
565	$2.5 \pm 0.1 \times 10^{-18}$
620	$2.7 \pm 0.3 \times 10^{-17}$

The calculated value of the diffusion coefficients at the three temperatures were then used to calculate the activation energy for the diffusion of Cr in ferrite using the Arrhenius relationship

$$D = D_0 \exp\left(-\frac{Q}{RT}\right), \quad (5.5)$$

where Q is the activation energy, R is the universal gas constant, T is the temperature in Kelvin and D_0 is the pre-exponential factor. Taking the natural logarithm of equation 5.5 results in the expression,

$$\ln D = -\frac{Q}{R} \frac{1}{T} + \ln D_0 \quad (5.6)$$

from which it can be seen that plotting a graph of the logarithm of D_{α} against reciprocal temperature yields a slope equal to $-\frac{Q}{R}$. Such a graph is plotted in Figure 5.55; a regression line is plotted through the experimental points. The correlation coefficient for these three data

points was found to be 0.99. The value for the activation energy of diffusion, Q , was found to be $230,000 \pm 10,000 \text{ J mol}^{-1}$, and the pre-exponential factor was found to be $7.0 \pm 0.3 \times 10^{-4} \text{ m}^2 \text{ s}^{-1}$. The values given by Fridberg *et al.* (1969) for the inter-diffusion of Cr in ferrite are an activation energy of $240,000 \text{ J mol}^{-1}$, and a pre-exponential factor of $1.5 \times 10^{-4} \text{ m}^2 \text{ s}^{-1}$.

5.6 Results and discussion from mixed microstructures

5.6.1 Precipitation within the allotriomorphic ferrite

A carbon extraction replica from the isothermally transformed mixed microstructure before tempering showed that although there was no precipitation in the bainitic regions of the microstructure, extensive precipitation had occurred in the ferrite. Fibrous carbides were found to exist in the allotriomorphic ferrite, both at grain boundaries with other ferrite grains (Figure 5.56 and Figure 5.57) and at the ferritic/bainitic grain boundaries (Figure 5.58). The fibres were approximately 30 nm thick and up to 2 μm long. Selected area electron diffraction (Figure 5.58c) from a cluster of such fibres (Figure 5.58a) showed that a unique spot diffraction pattern could be obtained from the cluster suggesting all the fibres had the same orientation. A dark field electron micrograph from one such spot is presented in Figure 5.58b), again illustrating that parallel fibres can be illuminated from a single diffraction spot. The selected area electron diffraction pattern is attributable to hexagonal M_2C . EDX analyses were possible on clusters of fibres and they were found to have a chemical composition of 50 wt.% Mo, 40 wt.% Cr with small amounts of Fe and Mn, consistent with the electron diffraction results. A second morphology of M_2C clusters was also observed in the ferrite. These particles, illustrated in Figure 5.59, were much smaller than the fibres (length $\simeq 60 \text{ nm}$, $\simeq 20 \text{ nm}$ thick), precipitating in a Widmanstätten array usually parallel to the prior austenite grain boundaries. The M_2C fibres and small particles present in the as-transformed microstructure persisted throughout tempering, also being observed in the specimens tempered for 180 hours at 565°C . This interphase precipitation of M_2C has been discussed in Chapter 2. Larger precipitates, identified by EDX as both M_2C and M_6C , were also found on ferrite-ferrite grain boundaries. Precipitation of this type is illustrated at a triple point in Figure 5.60. The M_6C precipitates become larger during tempering at the expense of some of the smaller M_2C particles.

5.6.2 Precipitation within the bainitic regions

The characteristics of precipitation in the bainitic regions of the mixed microstructures are broadly the same as in the fully bainitic specimens. However, cementite precipitation in the bainitic regions of the mixed microstructure specimens is very dense compared with the

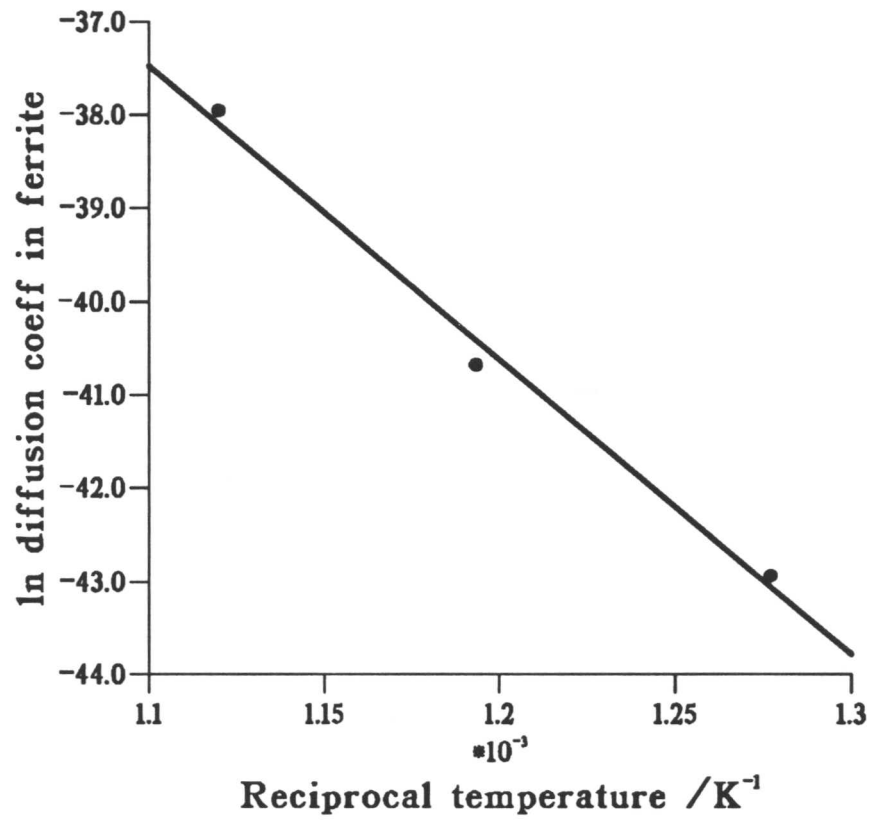


Figure 5.55: Plot of the logarithm of the calculated diffusion coefficient in ferrite as a function of temperature showing the regression line through the points

fully bainitic specimens. This is to be expected because of the increased carbon concentration in the bainitic regions due to the rejection of carbon into the austenite as the allotriomorphic ferrite forms. The carbon extraction replica taken from a specimen tempered for 47 hours at 565°C presented in Figure 5.61 illustrates this point. The contrast between the dense cementite precipitation in the bainitic regions and the empty ferritic regions is illustrated in Figure 5.62. Large M_6C particles are also visible on the ferrite grain boundaries. Figure 5.63 shows a replica from a specimen tempered for 180 hours. Widmanstätten type cementite is clearly visible within a martensite lath.

It has been shown that the bainitic and martensitic regions contain extensive cementite precipitation, whereas the ferritic regions contain M_2C (which is replaced by M_6C on prolonged tempering). This difference must be related to the mechanism of transformation. The ferrite forms reconstructively and therefore the atomic mobility inherent in this process could also permit the simultaneous precipitation of alloy carbides. The growth of bainite and martensite is displacive, precluding the formation of alloy carbides during transformation.

5.6.3 EDX measurements of the Cr content of cementite in mixed microstructures

The plots of Cr concentration against the reciprocal of particle size are presented in Figure 5.64a)–e) for the mixed microstructure specimens tempered at 565°C for 1, 47, 80, 128 and 180 hours respectively. The calculated regression lines are plotted on the first four plots, however the results for the 180 hour specimen were beginning to show a division of the cementite particles into those associated with bainitic and martensitic regions, and therefore it was not thought appropriate to find a single regression line for two different distributions. The results of these analyses are summarised in Table 5.11.

Table 5.11: Summary of experimental measurements of Cr concentration in cementite and particle size for mixed microstructure specimens tempered at 565°C.

Tempering time /Hours	Correlation coefficient	Average Cr conc. /wt.%	Average particle size /nm
1	0.74	9.1	76
47	0.44	15.9	68
80	0.55	20.2	59
128	0.41	21.9	71
180	–	26.2	63

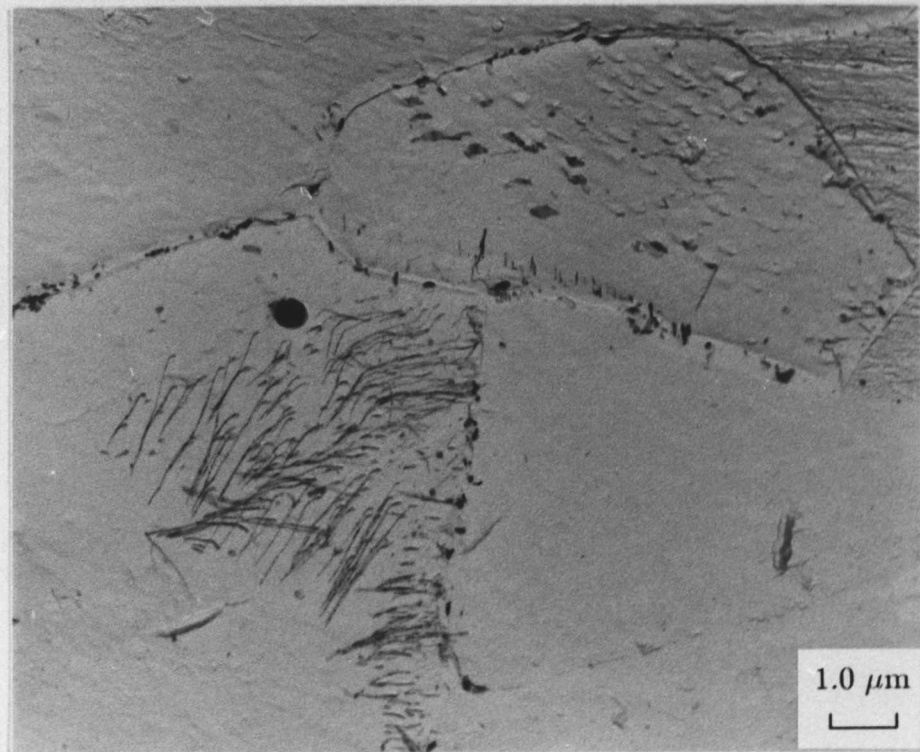


Figure 5.56: Carbon extraction replica from the as-transformed mixed microstructure showing fibrous M_2C carbides at ferritic/ferritic grain boundaries.

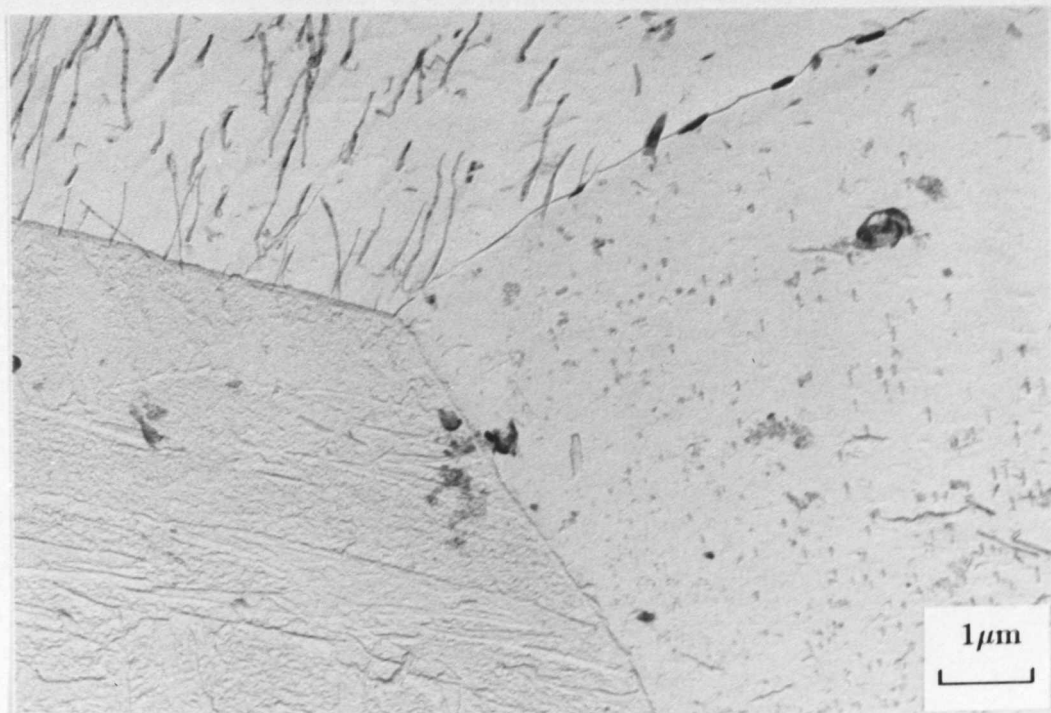
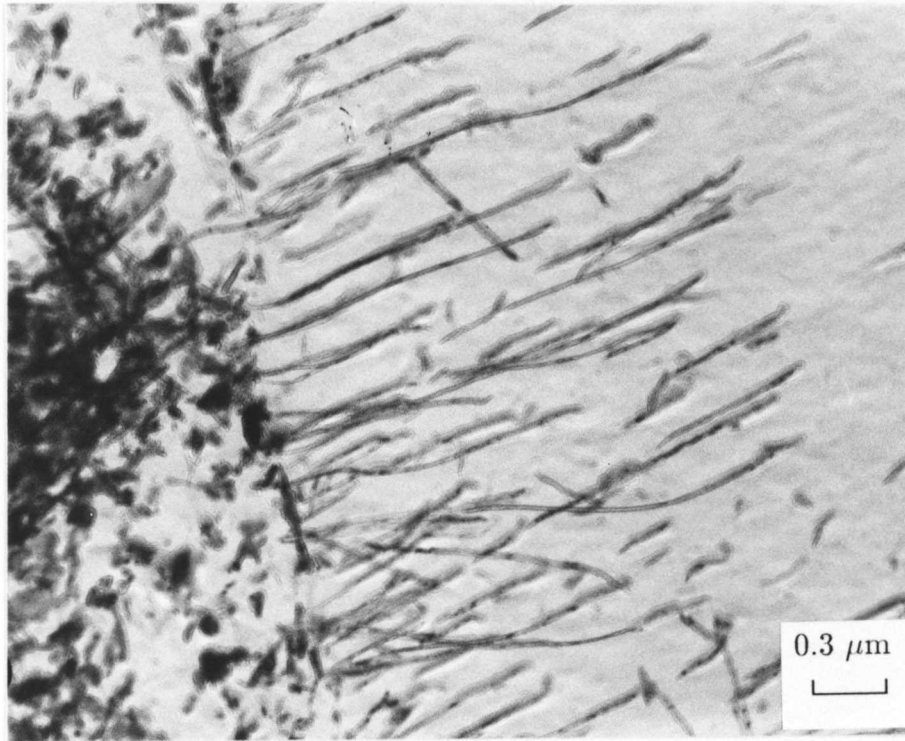
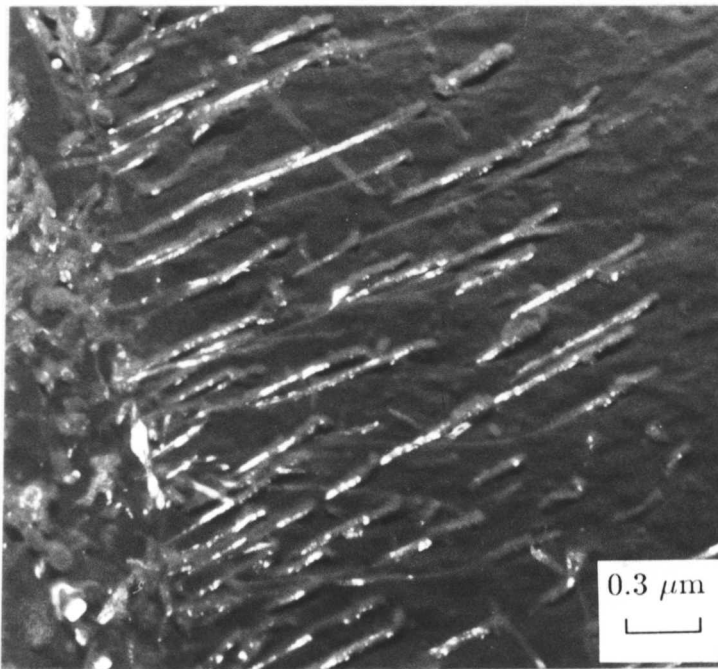


Figure 5.57: Carbon extraction replica from the as-transformed mixed microstructure showing fibrous M_2C carbides at ferritic/bainitic grain boundaries.

a)



b)



c)

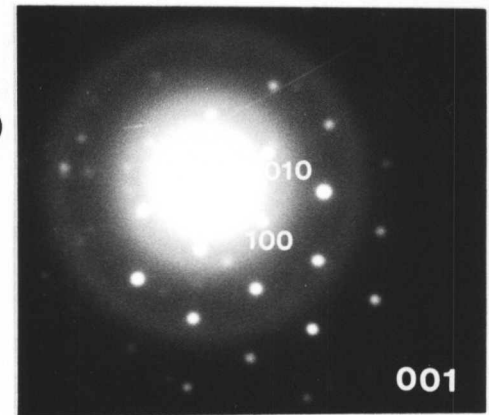


Figure 5.58: Carbon extraction replica from the mixed microstructure after tempering for 180 hours at 565°C. a) Bright field and b) dark field images of fibrous M_2C particles showing that all the fibres have the same orientation. c) Selected area electron diffraction pattern from a cluster of the fibres showing that a single spot pattern is obtained.

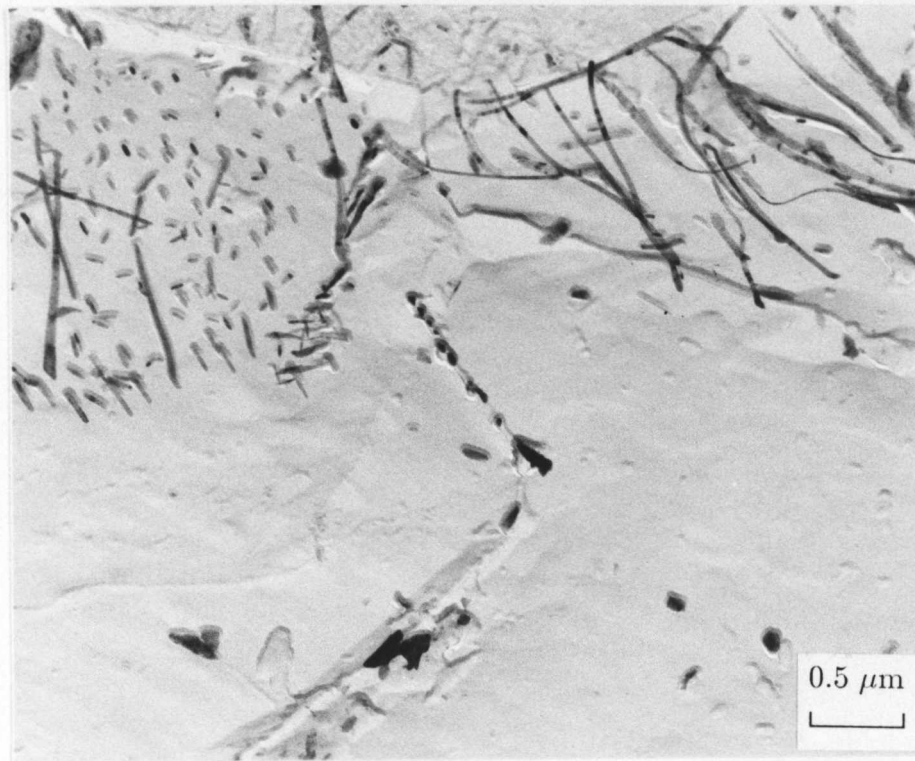


Figure 5.59: Carbon extraction replica from the as-transformed mixed microstructure showing a second morphology of M_2C clusters precipitating in a Widmanstätten array.

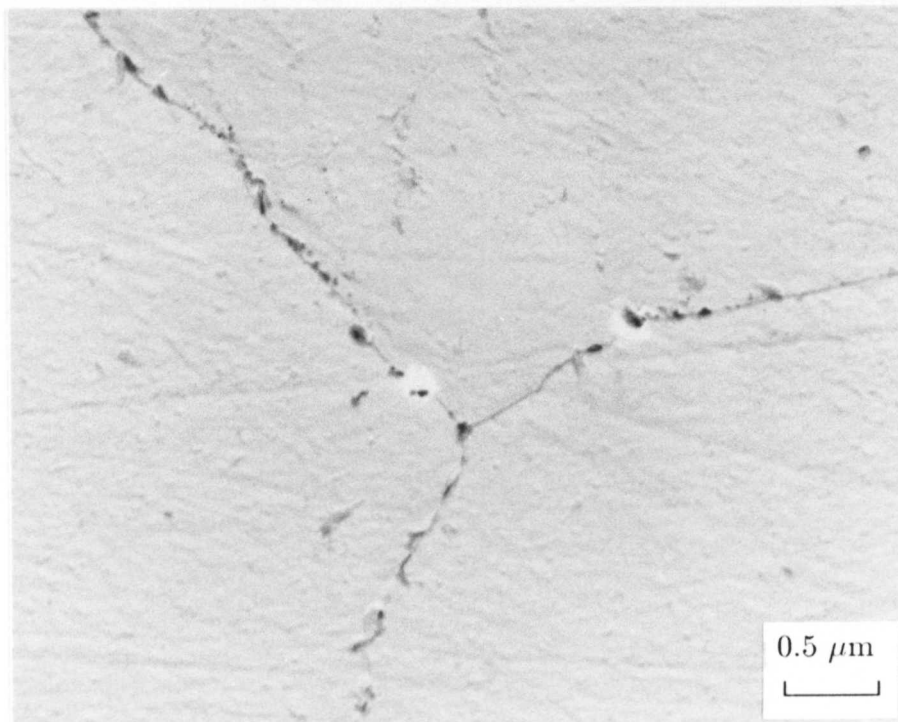


Figure 5.60: Carbon extraction replica from the as-transformed mixed microstructure illustrating precipitation of M_6C at a triple point between ferrite grains.

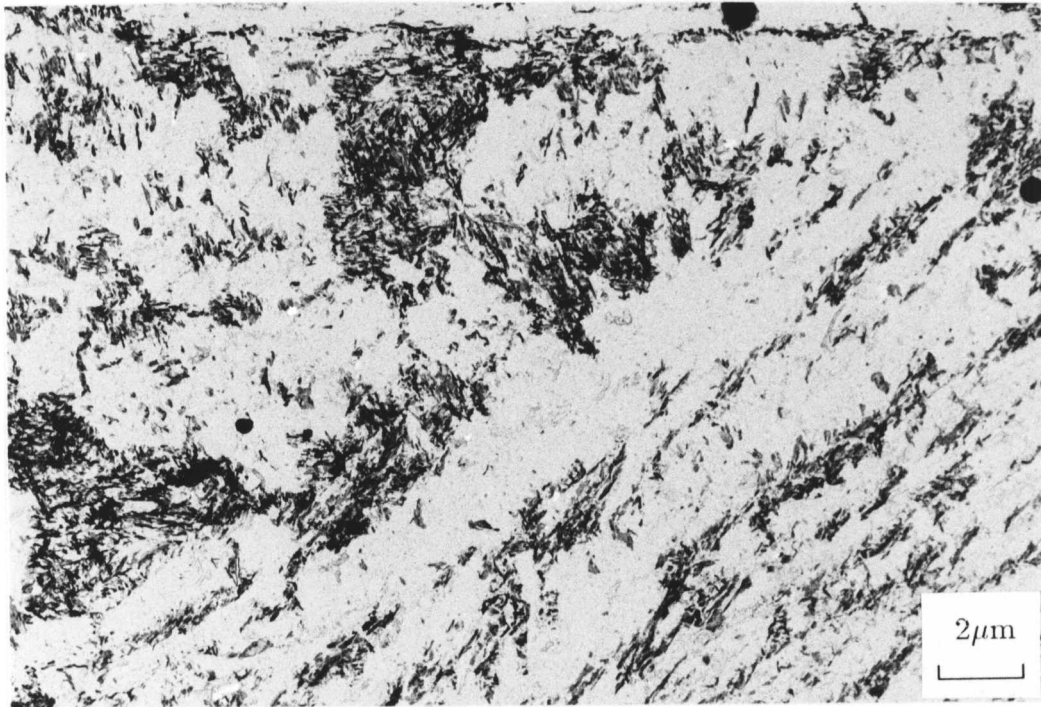


Figure 5.61: Carbon extraction replica from a mixed microstructure specimen tempered for 47 hours at 565°C showing dense cementite precipitation.

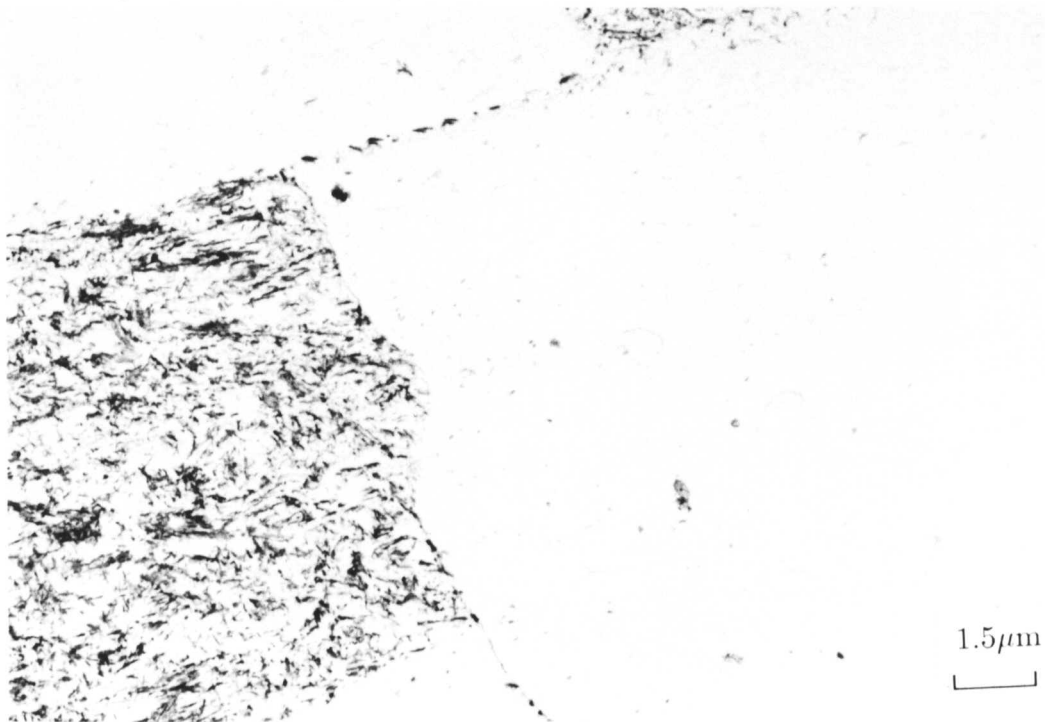


Figure 5.62: Carbon extraction replica from a mixed microstructure specimen tempered for 47 hours at 565°C showing the contrast between the dense cementite precipitation in the bainitic regions and the empty allotriomorphic ferrite regions.

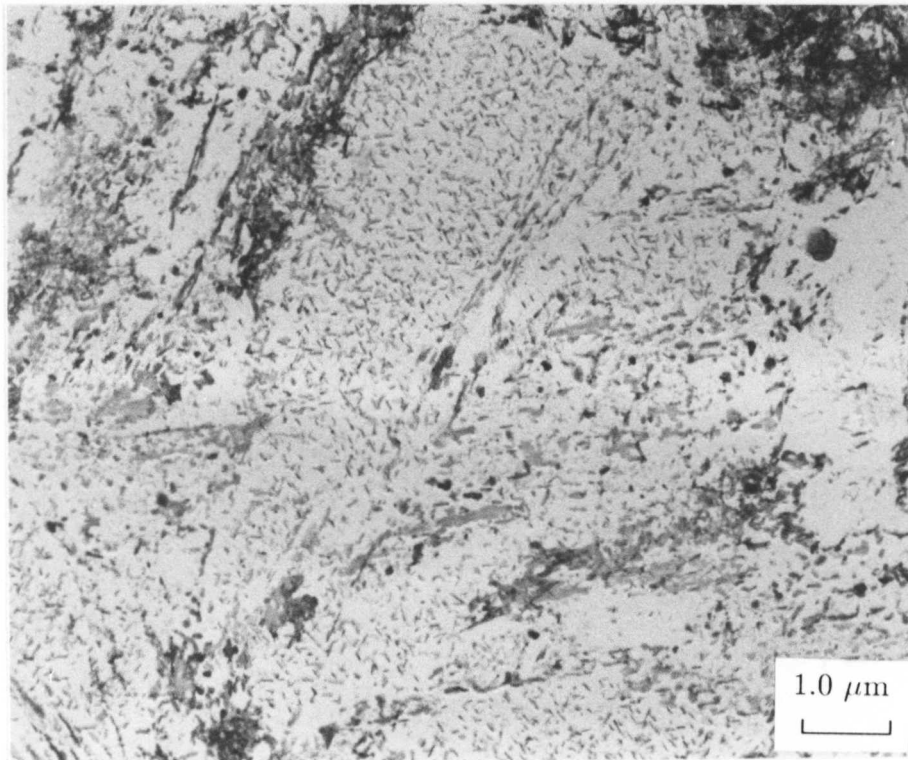


Figure 5.63: Carbon extraction replica from a mixed microstructure specimen tempered for 180 hours at 565°C showing Widmanstätten type precipitation of cementite within a martensite lath.

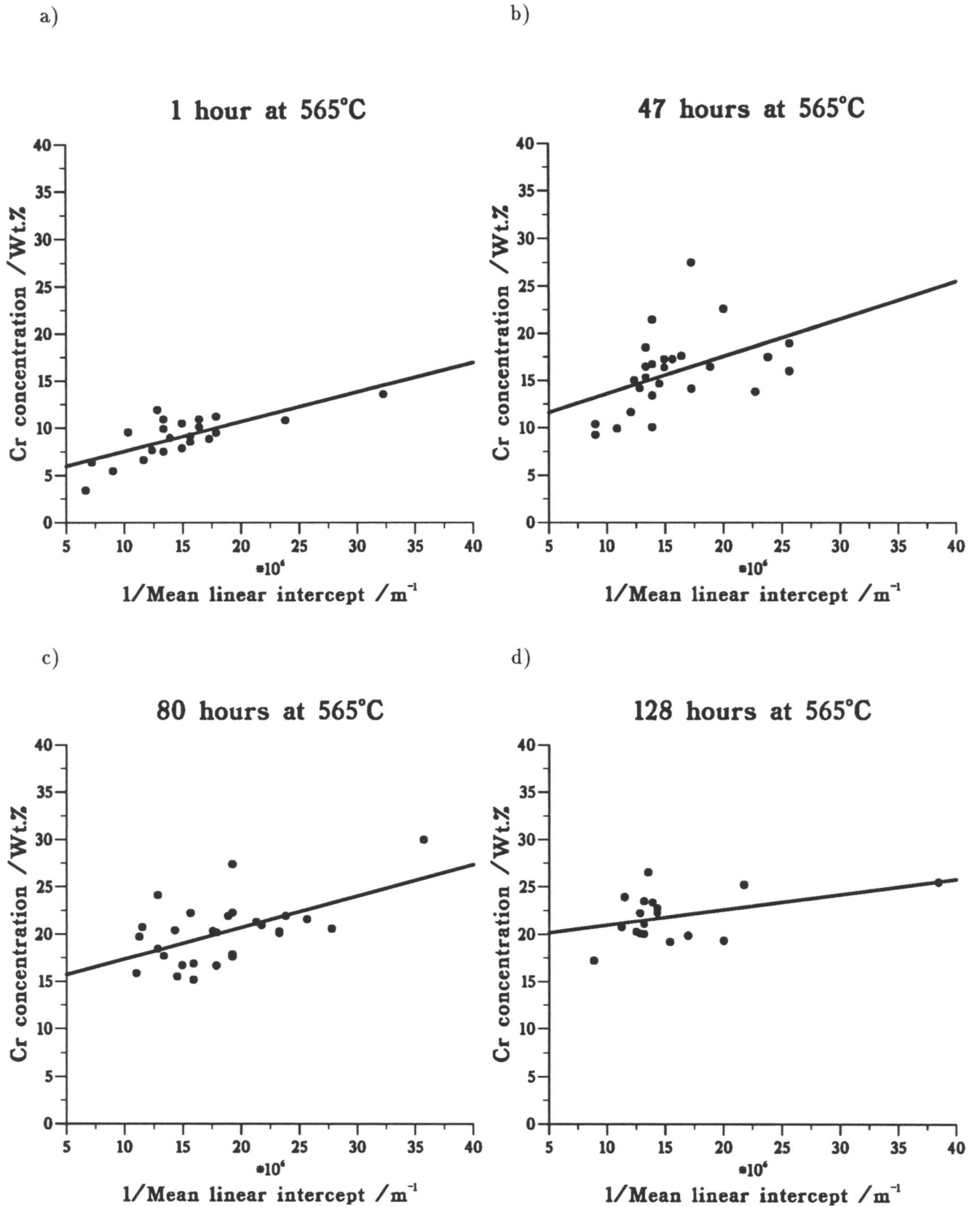
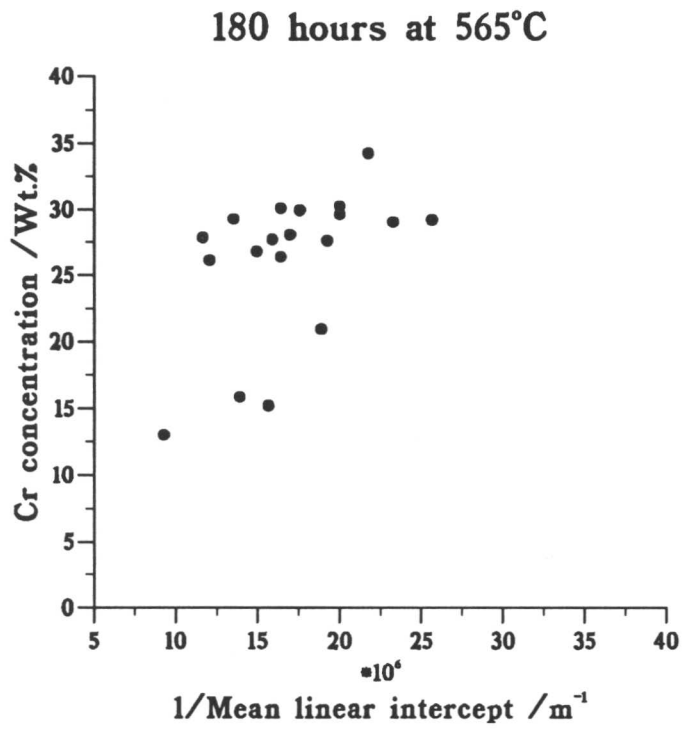


Figure 5.64: a)–e) Chromium concentration in cementite plotted as a function of reciprocal particle size for various tempering times at 565°C for mixed microstructure specimens.

e)



5.7 Comparison of experimental results and theoretical predictions

The experimental measurements of Cr concentration in cementite in the fully bainitic and mixed microstructure specimens are summarised in Figure 5.65. It can be seen that the cementite in the fully bainitic specimens enriches more quickly than in the specimens containing only 50% bainite. This is to be expected because the formation of allotriomorphic ferrite in the mixed microstructure specimens causes an increase in the carbon concentration of the bainitic regions. The carbon concentration in the two different regions can be determined from a simple mass balance equation:-

$$\bar{x} = V_{\alpha}x_{\alpha} + (1 - V_{\alpha})x_{\gamma} , \quad (5.7)$$

where \bar{x} is the average carbon concentration in the alloy, V_{α} is the volume fraction of allotriomorphic ferrite, and x_{α} and x_{γ} are the carbon concentrations in the ferrite and the austenite respectively. \bar{x} is 0.15wt.%, V_{α} is 0.5 in the specimens used, x_{α} (determined from the program used to calculate the TTT curve in section 5.3.1) = 0.0228 wt.% and hence x_{γ} is calculated to be 0.277 wt.%. This is by definition the carbon concentration in the bainite which forms from the carbon-enriched austenite. There is therefore approximately twice as much carbon available for carbide precipitation initially in the mixed microstructure specimens than in the fully bainitic specimens.

The symmetric and asymmetric finite difference methods discussed in Chapter 3 can be used to predict the enrichment rate of cementite in the fully bainitic and mixed microstructures respectively. Both calculations were carried out at 565°C, and for average particle sizes of 60 nm in the bainitic and 70 nm in the mixed microstructures. These are consistent with the particle sizes measured experimentally. The two curves are shown in Figure 5.66, plotted as a function of time. Experimentally it is observed that the bainite in the mixed microstructure specimens, which has formed from enriched austenite, contains cementite which enriches more slowly than that in the fully bainitic specimens. This is consistent with the predictions of the model.

Figure 5.67 and Figure 5.68 show the predicted curves for the bainitic and mixed microstructures respectively, for short times only, plotted against the experimental results. The deviation of the experimental points tempered for more than 64 hours in the fully bainitic specimens corresponds to the precipitation of M_7C_3 and the subsequent dissolution of the cementite particles. It can be seen that the model is consistently underpredicting the value of chromium in cementite after a given time compared with the experimental results. The most probable explanation for this is that the value of the diffusion coefficient of chromium in cementite is a little high. A lower value would cause the predicted enrichment rate to be higher, increasing the

predicted concentration for a given tempering time. The relatively small size of the particles (≈ 60 nm) increases the sensitivity of the model to the values of the diffusion constants used. This point is discussed further in Chapters 3 and 8. However, it is important to note that the experimental results clearly show a linear dependence of enrichment rate on the square root of tempering time, as predicted by the model.

The experimental results have highlighted the dependence of enrichment on particle size, smaller particles enriching more quickly than larger ones. Figure 5.69 shows the results of a calculation using the finite difference model of the enrichment rate at 565°C for three different particle sizes, 50 nm, 75 nm and 100 nm. The model predicts a difference of ≈ 20 wt.% Cr between the 50 and 100 nm particles after tempering for 100 hours. This is consistent with the measured variation of composition with size, and illustrates the importance of making the two measurements simultaneously.

5.8 Conclusions

Detailed experimental studies of cementite composition changes in fully bainitic and mixed ferritic/bainitic microstructures have been made. The enrichment rate has found to be slower in the bainitic regions of the mixed microstructures than in the fully bainitic specimens. A strong dependence of enrichment on particle size has been observed, the smaller particles enriching more quickly than the larger ones. Both of these observations are consistent with the predictions of the computer model. Differences in precipitation behaviour between bainitic, martensitic and ferritic regions of the microstructure have been established. This has important consequences for remanent life assessment in that a simple measurement of cementite composition is not sufficient; the size and position in the microstructure must be simultaneously determined.

The calculated value for the activation energy of chromium diffusion in ferrite, and hence the diffusion coefficient, show good agreement with previously measured values. The need for a measurement of the diffusivity of chromium in cementite has been highlighted. The usefulness of equilibrium thermodynamic calculations in predicting the microstructural changes which occur has also been demonstrated.

No significant dependence of the composition of the chromium-rich alloy carbide, M_7C_3 , on size or tempering time has been found. Indications are that once alloy carbides have precipitated any further enrichment is too small to be useful in estimating the average temperature experienced by the microstructure. This is discussed further in Chapter 7.

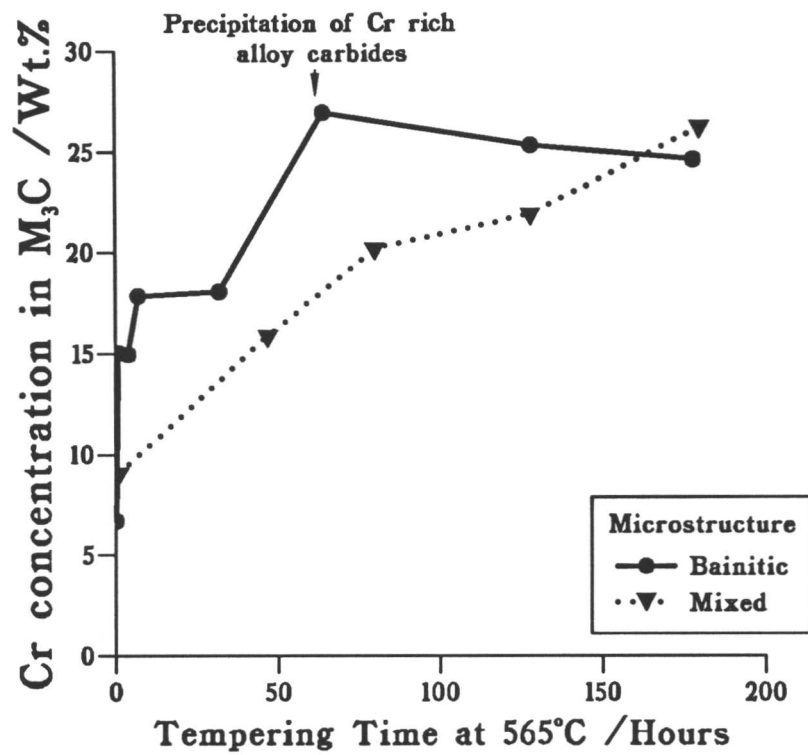


Figure 5.65: Comparison of the average chromium content in cementite in fully bainitic and mixed microstructure specimens as a function of tempering time at 565°C.

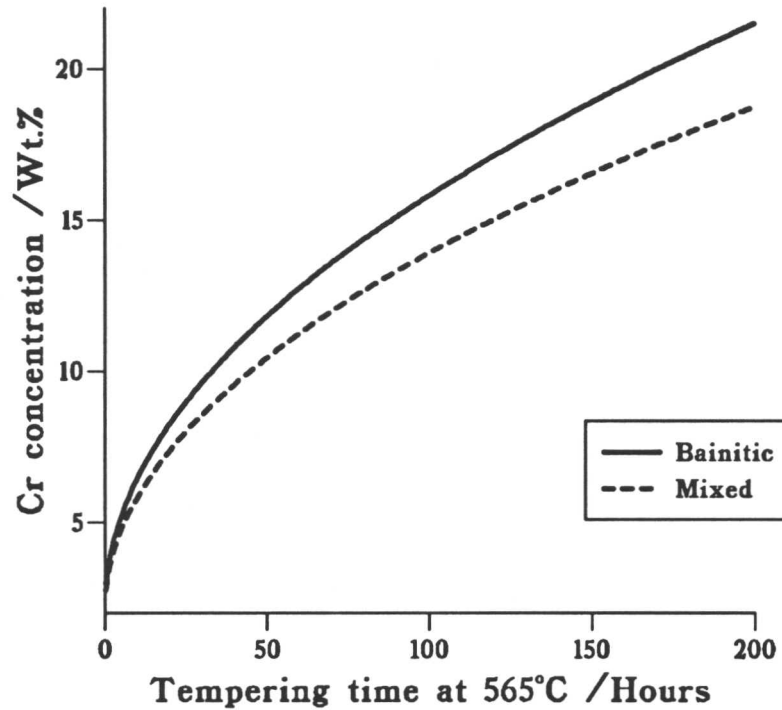


Figure 5.66: Predicted rate of enrichment in cementite in the bainitic and mixed microstructure specimens using the asymmetric finite difference model described in Chapter 3.

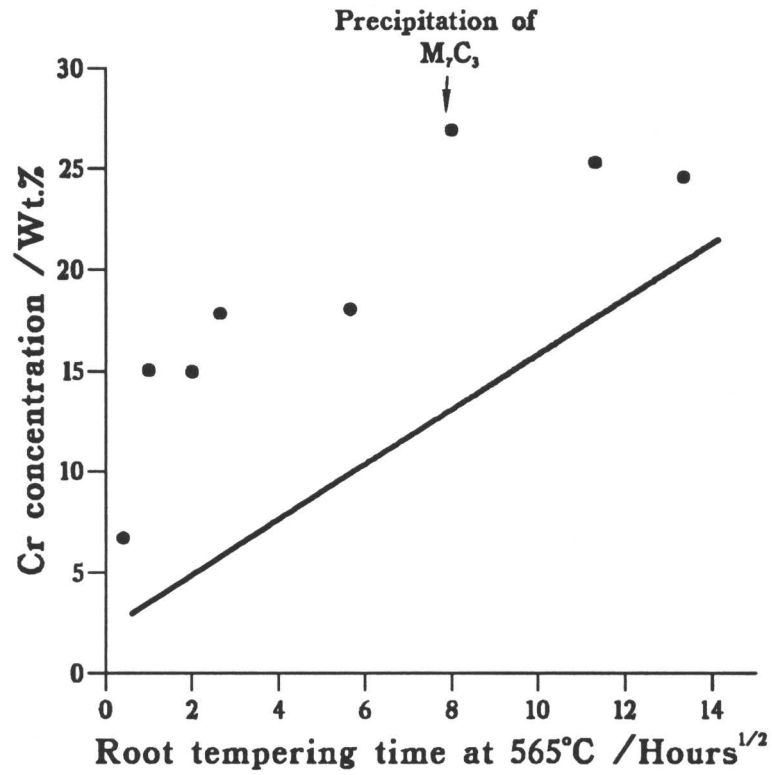


Figure 5.67: Comparison of the experimentally measured Cr concentration in cementite in the bainitic specimens with the predicted rate of enrichment using the asymmetric model described in Chapter 3.

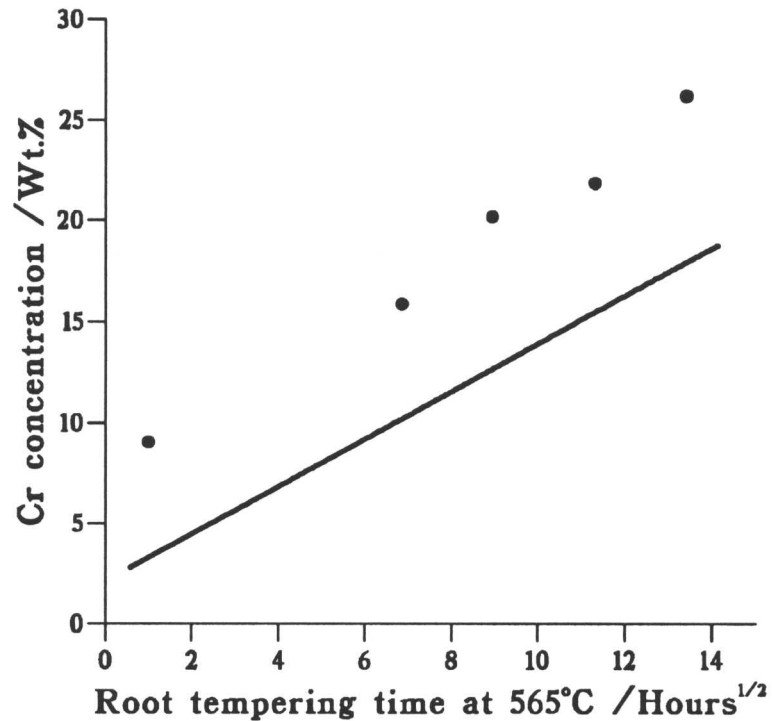


Figure 5.68: Comparison of the experimentally measured Cr concentration in cementite in the bainitic regions of the mixed microstructure specimens with the predicted rate of enrichment using the asymmetric model described in Chapter 3.

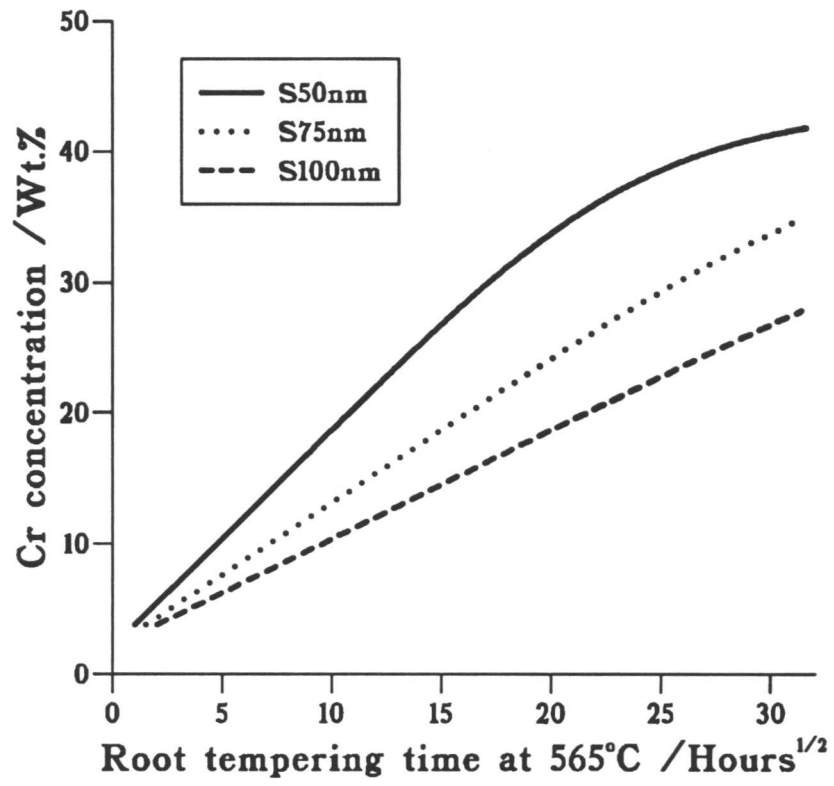


Figure 5.69: Illustration of the dependence of the enrichment of cementite on the particle size calculated at 565°C using the finite difference model.

CHAPTER 6

$\frac{1}{2}\text{Cr}\frac{1}{2}\text{Mo}\frac{1}{4}\text{V}$ STEEL

Measurements of composition changes in cementite over long periods of time in a pearlitic $\frac{1}{2}\text{Cr}\frac{1}{2}\text{Mo}\frac{1}{4}\text{V}$ steel have been carried out at a variety of tempering temperatures. The original measurements were made by Du (1986), although only empirical expressions describing the results were found. In this chapter additional measurements made by myself on the original specimens to determine the variation of cementite concentration with particle size are discussed. Having obtained the particle size data, the composition changes are modelled theoretically. Very good agreement is found between theory and experiment.

The material described in this chapter has been published in *Materials Science and Engineering A*, **155**, 1992, p. 197–205.

CHAPTER 6

$\frac{1}{2}\text{Cr}\frac{1}{2}\text{Mo}\frac{1}{4}\text{V}$ STEEL

6.1 Introduction

In bainitic microstructures in which cementite grows without partitioning of the substitutional alloying elements, the initial composition of bainitic cementite can be readily estimated. This work, however, focusses on the ferritic/pearlitic microstructures in a $\frac{1}{2}\text{Cr}\frac{1}{2}\text{Mo}\frac{1}{4}\text{V}$ steel. Investigations by Carruthers and Collins (1980) on this material have shown that changes in the substitutional solute concentration of cementite may be a viable technique for the estimation of an effective service temperature. $\frac{1}{2}\text{Cr}\frac{1}{2}\text{Mo}\frac{1}{4}\text{V}$ steel is probably the most widely used low alloy steel in power plant.

The pearlite reaction is fundamentally different from that of bainite in that it is a reconstructive transformation in which growth occurs at an incoherent interface with the parent austenite. Diffusion of all the elements is therefore an integral part of the reaction, and the partitioning of substitutional elements has been reported (Al-Salman *et al.*, 1979; Chance and Ridley, 1981) for all transformation conditions. Paraequilibrium growth of pearlite does not occur, nor does the cementite have an equilibrium composition. Therefore, there is an uncertainty about the starting chemistry of pearlitic cementite. In addition, the cementite is rather coarse compared with that associated with bainite. In fact, each pearlite colony is a bicrystal of cementite and ferrite, the so-called cementite lamellae being interconnected in three dimensions (Hillert, 1962). Consequently it is of considerable interest, both from an industrial and an academic point of view, to investigate any changes in carbide characteristics with tempering heat treatments.

6.2 Materials and heat treatment

The material used in these experiments was a standard $\frac{1}{2}\text{Cr}\frac{1}{2}\text{Mo}\frac{1}{4}\text{V}$ steel supplied by National Power designated as cast M1. The chemical composition is given in Table 6.1. The samples were normalized from an austenitising temperature of 950°C and then tempered at 690°C for one hour in order to simulate the commercial stress-relief heat treatment for this steel. Specimens were then machined to 10×20 mm and tempered at a variety of temperatures between 640 and 525°C in a specially designed furnace (Carruthers and Collins, 1980) for varying times. Within the furnace, the samples were screwed into a nimonic 80a bar to ensure an even temperature distribution. The temperature error at any specimen position was

$\pm 2^\circ\text{C}$. There was no significant oxidation or decarburisation of the threaded test pieces during tempering. Tempering was discontinuous because the specimens were removed at various time intervals to prepare samples for examination in the transmission electron microscope, and then put back for further heat treatment. It was confirmed in a separate experiment that the cementite compositions of samples tempered continuously and discontinuously were, as expected, the same within experimental error.

Table 6.1: Chemical composition of the $\frac{1}{2}\text{Cr}\frac{1}{2}\text{Mo}\frac{1}{4}\text{V}$ steel in wt.%

Cast	C	Si	Mn	P	S	Cr	Mo	V	Ni	Cu
M1	0.14	0.23	0.61	0.007	0.023	0.36	0.66	0.26	0.21	0.13

6.3 Experimental results

6.3.1 Microstructure and carbide morphologies

The microstructures after the normalisation heat treatment at 950°C were mixtures of ferrite, pearlite and bainite. The development of the microstructure as tempering proceeds is illustrated in Figure 6.1; the transmission electron micrographs were taken from carbon extraction replicas and are therefore specific to the carbide distribution. After the stress-relief heat treatment at 690°C for one hour the main ferritic and pearlitic regions were still clearly defined, however, it can be seen from Figure 6.1b) that the pearlitic cementite had already begun to spheroidise. Further coarsening occurs during prolonged tempering. Figures 6.1c) and d) illustrate this in specimens tempered at 640° for 483 and 2996 hours respectively. Cementite particles located at the ferrite grain boundaries were generally found to be coarser than those within the grains. The coarsening process ultimately dissolved most of the intragranular cementite particles, leaving relatively few large particles on the boundaries. It is found that eventually very much larger alloy carbides, M_{23}C_6 and M_6C , precipitate at the expense of the cementite which dissolves completely. The transformation to alloy carbides was found to be much faster at the higher tempering temperatures. M_{23}C_6 is found after 5,850 hours at 640°C and M_6C after 9,353 hours, whereas after 9,381 hours at 565°C only M_{23}C_6 is found, and cementite remains the stable carbide after 12,887 hours tempering at 525°C .

In addition to the chromium-rich M_3C , M_{23}C_6 and M_7C_3 carbides, a fine dispersion of molybdenum and vanadium based carbides, M_2C and MC respectively, also precipitated during the stress-relief heat treatment and persisted throughout the tempering process.

6.3.2 Composition of the carbides

The representative energy dispersive X-ray spectra of the various carbides are presented in Figure 6.2. M_3C is characterised by a low vanadium and molybdenum concentration, whereas $M_{23}C_6$ has a much higher chromium and molybdenum content. M_6C contains a slightly smaller chromium content than $M_{23}C_6$, but can be identified by its high molybdenum and silicon contents. Figure 6.2d) illustrates the characteristic spectra from MC, a vanadium based carbide which can dissolve some molybdenum, and Figure 6.2e) that from M_2C , which is molybdenum-rich, although it contains a significant amount of vanadium, and traces of chromium, manganese and iron.

The experimentally determined composition bands spanning the ranges of temperatures studied of the alloying elements in the carbides in atomic % , allowing for the stoichiometric carbon content in each alloy carbide (for example, 25 at.% of carbon in cementite) are summarised in Table 6.2.

Table 6.2: Chemical composition ranges of the carbides M_3C , $M_{23}C_6$ and M_6C in at. %

Carbide	V	Cr	Mn	Mo	C
M_3C	0.7–1.1	2.0–7.6	2.0–10.0	0.6–1.0	25.0
$M_{23}C_6$	0.3–0.6	9.0–15.0	6.0–8.0	3.0–5.0	20.7
M_6C	2.0–3.0	5.5–8.0	6.0–8.0	16.0–20.0	14.3

The chromium content of the cementite was found to increase steadily with time at the tempering temperature, the rate of enrichment being higher at the higher tempering temperatures. Manganese was found to diffuse into the cementite faster than the chromium, and saturated at a higher concentration. At the lower tempering temperatures saturation was not observed within the time periods studied. The saturation levels of chromium and manganese were also found to increase with decreasing tempering temperature. In the $M_{23}C_6$ the chromium content also appeared to increase slightly with tempering time, whereas the manganese content decreased. However, much longer service times are needed before the enrichment kinetics of $M_{23}C_6$ can be established with confidence. The vanadium content of the $M_{23}C_6$ was much lower than that in the other carbides. M_6C was found to have an almost constant composition at all stages of tempering.

The dissolution of cementite and precipitation of $M_{23}C_6$ occurred after the cementite had reached saturation. The literature suggests that the alloy carbide sequence usually involves first a transformation to M_7C_3 prior to $M_{23}C_6$, but this sequence was not observed experimentally.

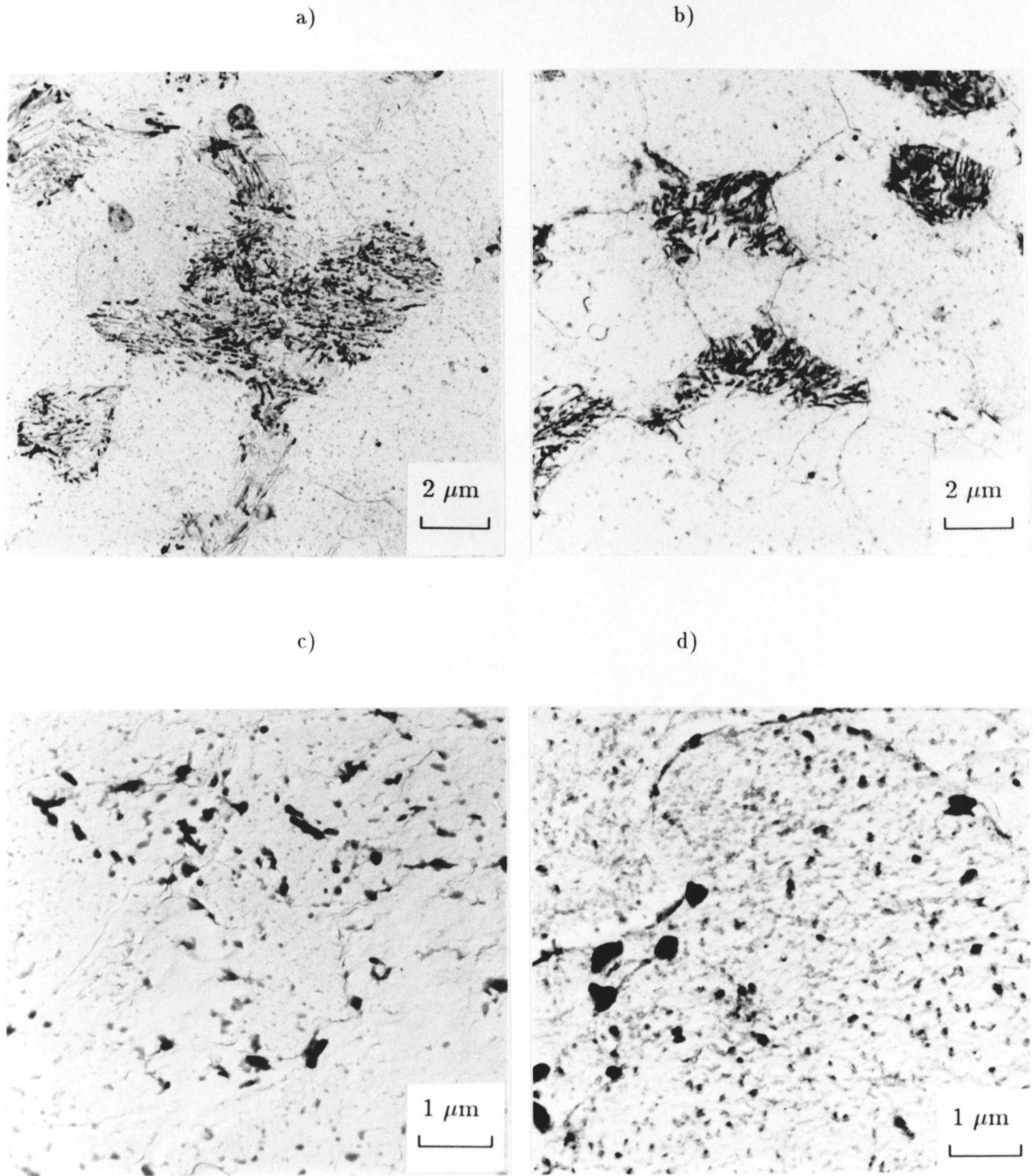


Figure 6.1: The development of the carbide distribution during long term tempering at 640°C; a) after normalizing at 950°C, b) as a), but additionally tempered at 690°C for 1 hour, c) further tempered at 640°C for 483 hours and d) tempered at 640°C for 1996 hours.

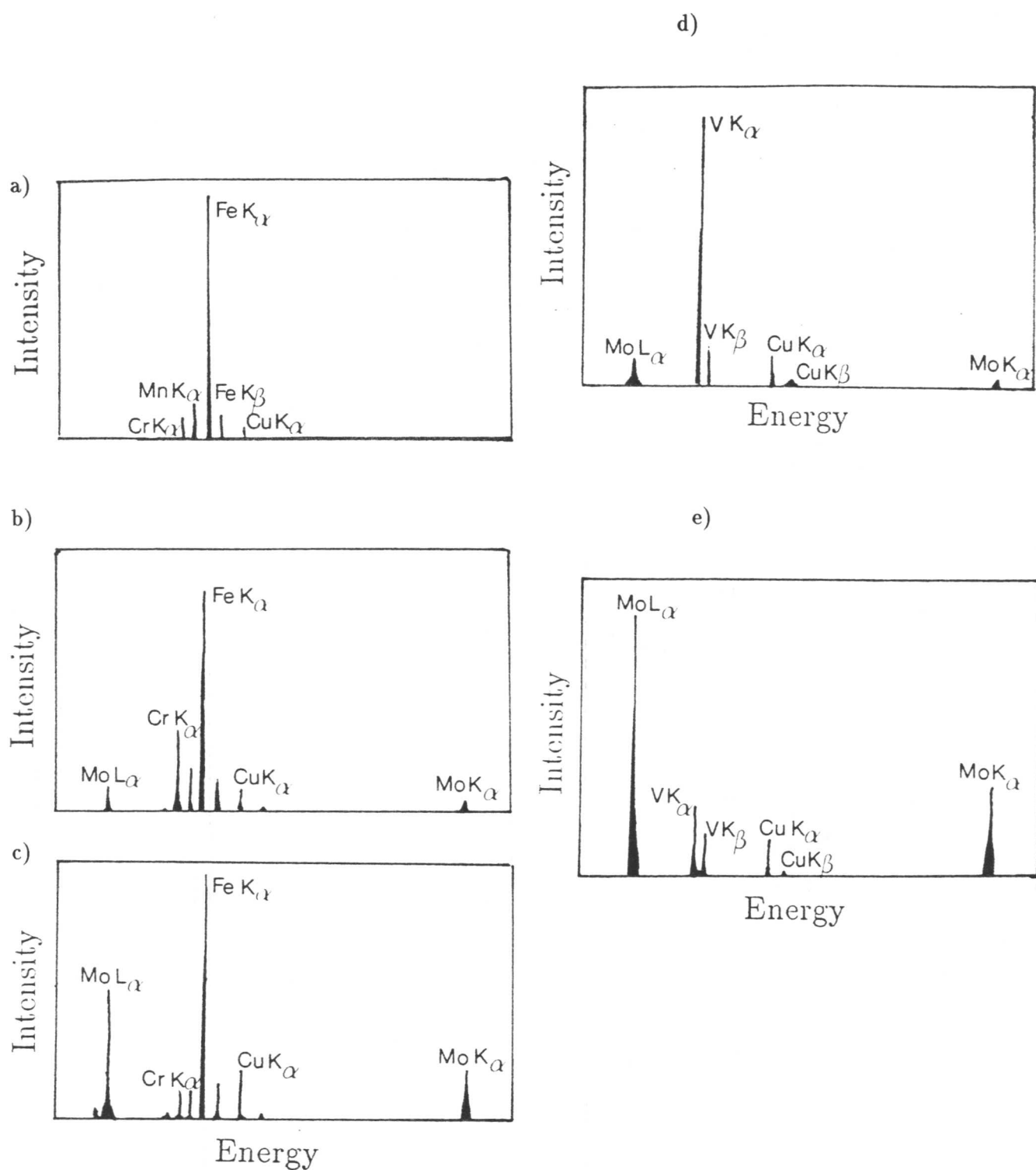


Figure 6.2: Characteristic energy dispersive X-ray spectra for the various alloy carbides found to precipitate during the tempering heat treatments: a) M_3C , b) $M_{23}C_6$, c) M_6C , d) MC and e) M_2C .

A possible explanation for this is that the chromium content of the steel, and its ratio to molybdenum was too low for M_7C_3 to form. It is also probable that the small molybdenum-based carbides in the matrix limited the molybdenum content of the larger $M_{23}C_6$ and M_6C carbides, and stabilized the $M_{23}C_6$ to longer times.

6.4 Modelling of the diffusion process

6.4.1 Thermodynamic calculations

Thermodynamic calculations were performed to calculate the equilibrium carbides expected in M1 steel as a function of temperature, and to study the metastable equilibrium between ferrite and cementite. The calculations allowed for the elements Fe, Cr, Mn, Mo, C, V, Si, Ni, Sn, Cu, P and S and the phases M_3C , M_7C_3 , M_6C , $M_{23}C_6$, M_2C , VC, austenite and ferrite.

The equilibrium carbides at all temperatures were found to be $M_{23}C_6$, M_6C and VC which is in good agreement with the carbides observed after long ageing times in all the specimens (Mo_2C is assumed to have all transformed to M_6C under equilibrium conditions). Calculations were then performed by suppressing all carbides except cementite, thereby allowing the equilibria between the metastable cementite and the ferrite matrix to be studied. The calculated chromium levels in the ferrite and cementite are presented in Table 6.3. These data are also plotted in Figure 6.3. It can be seen that the maximum permitted concentration of chromium in cementite increases with decreasing temperature, as observed experimentally.

Table 6.3: Equilibrium concentration (at.%) of chromium in ferrite and cementite calculated using MTDATA as a function of temperature in steel M1.

Phase	690°C	640°C	630°C	620°C	610°C	590°C	575°C	565°C	525°C
Ferrite	0.25	0.23	0.22	0.22	0.21	0.20	0.19	0.18	0.16
Cementite	5.53	6.35	6.53	6.72	6.91	7.31	7.63	7.85	8.77

The equilibria between ferrite/ $M_{23}C_6$ and ferrite/ M_6C can also be calculated. The calculated equilibrium chromium concentration in $M_{23}C_6$ varies between 7–9 at.% from 690–525°C respectively, and that in M_6C from 2–4 at.% over the same temperature range. These equilibrium calculations also predict that the level of molybdenum at equilibrium is 10 at.% in $M_{23}C_6$ and 45 at.% in M_6C .

6.4.2 Finite difference modelling

Calculations were performed using the model described in Chapter 3 to predict the enrichment rate of cementite for comparison with the experimental results. The initial compositions

in the cementite and ferrite are obtained by assuming that there is no partitioning of the substitutional solute elements during transformation. The particle size used in the model was 175nm; this represented the mean value obtained from particle size measurements over many specimens. The effect of the chosen particle size on the enrichment rate is illustrated in Figure 6.4 for particles of 150, 175 and 200nm at 590°C. Obviously there is no effect on the saturation level of chromium which is determined by equilibrium thermodynamics, but the enrichment rate is slightly faster for a smaller particle.

In order to simulate the industrial heat treatment, calculations were carried out in which the composition changes in cementite resulting from a stress-relief heat treatment at 690°C for one hour were evaluated prior to the modelling of long term tempering at the lower service temperatures. As an initial approximation it is assumed that there is no redistribution of substitutional solute elements during the formation of pearlite. The starting concentrations were therefore set to be the bulk chromium composition of the alloy in both the ferrite and cementite. The interface concentrations used were the equilibrium concentrations of chromium in the cementite and ferrite respectively, calculated using MTDATA as described in the previous section. The measured chromium concentrations are compared with the theoretical predictions in Figure 6.5a)–h), for specimens tempered at 640, 630, 620, 610, 590, 575, 565, and 525°C. It should be noted that the saturation level in cementite predicted by MTDATA is slightly different from that measured experimentally. This is thought to be due to the presence of the fine M_2C in the steel, precipitated during the stress-relief heat treatment, which reduces the molybdenum content in the cementite and raises the chromium content above that predicted if only cementite and ferrite are allowed to exist. The experimentally determined chromium contents of $M_{23}C_6$ and M_6C are also plotted to illustrate the time at which the cementite transforms to alloy carbides at the various tempering temperatures. The absolute chromium levels in the alloy carbides are higher than those predicted by thermodynamic calculations. The high molybdenum concentrations predicted in $M_{23}C_6$ and M_6C are not observed experimentally, resulting in larger chromium concentrations being measured in the alloy carbides than their predicted values. Again this can be attributed to the fact that molybdenum is tied up in fine M_2C precipitates, reducing the amount of molybdenum available for inclusion in $M_{23}C_6$ and M_6C . The effect of the M_2C precipitation altering the absolute chromium levels predicted in carbides is very small in the case of cementite, where the predicted level is 2–3 at.% and the measured level is approximately 1 at.%.

It has already been mentioned in the introduction that the chemical composition of cementite in pearlitic steels is found to be somewhere in between equilibrium and paraequilibrium

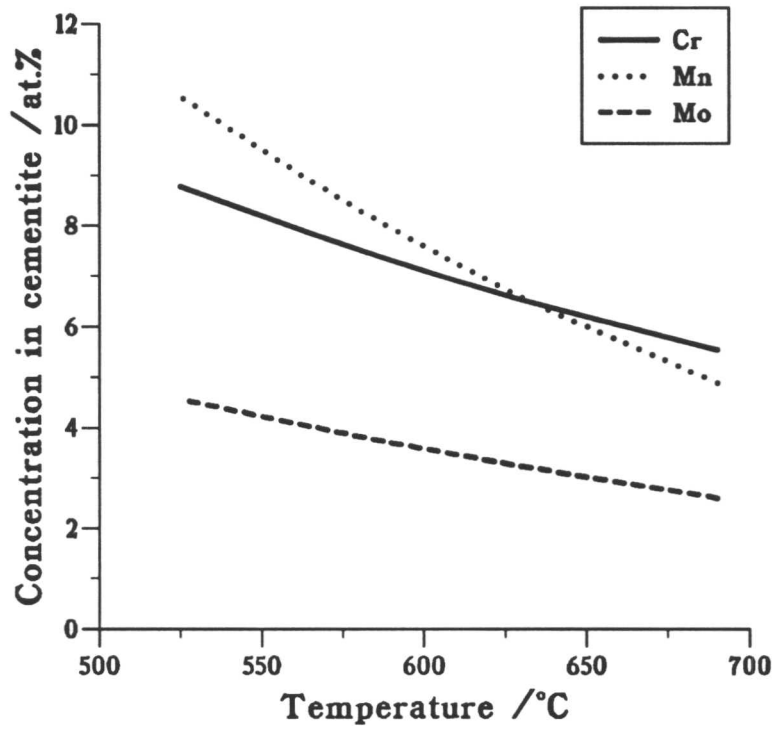


Figure 6.3: Equilibrium substitutional alloying content of cementite as a function of temperature calculated using MTDATA.

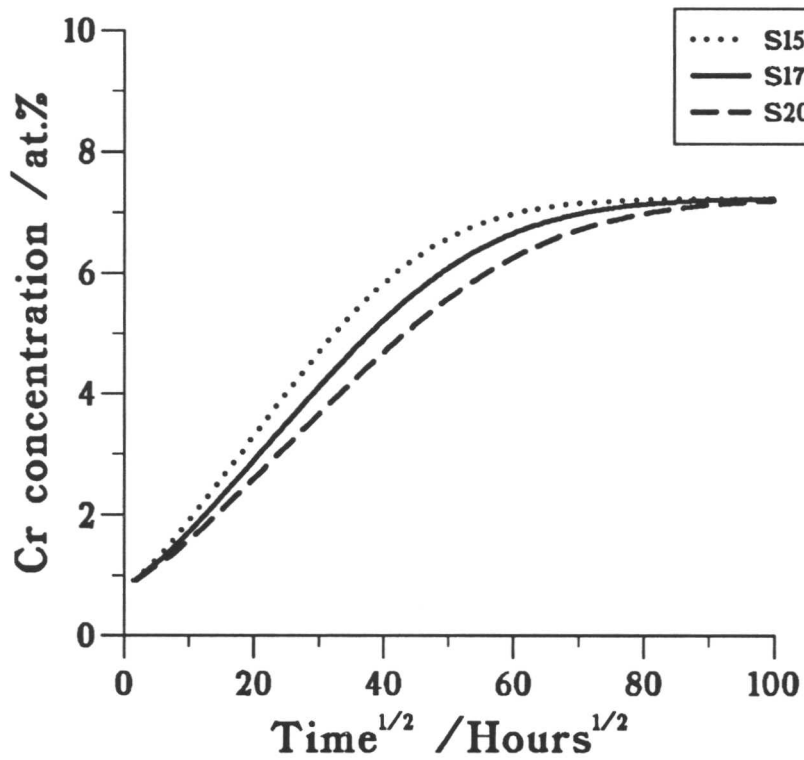


Figure 6.4: The effect of particle size on the enrichment kinetics of cementite.

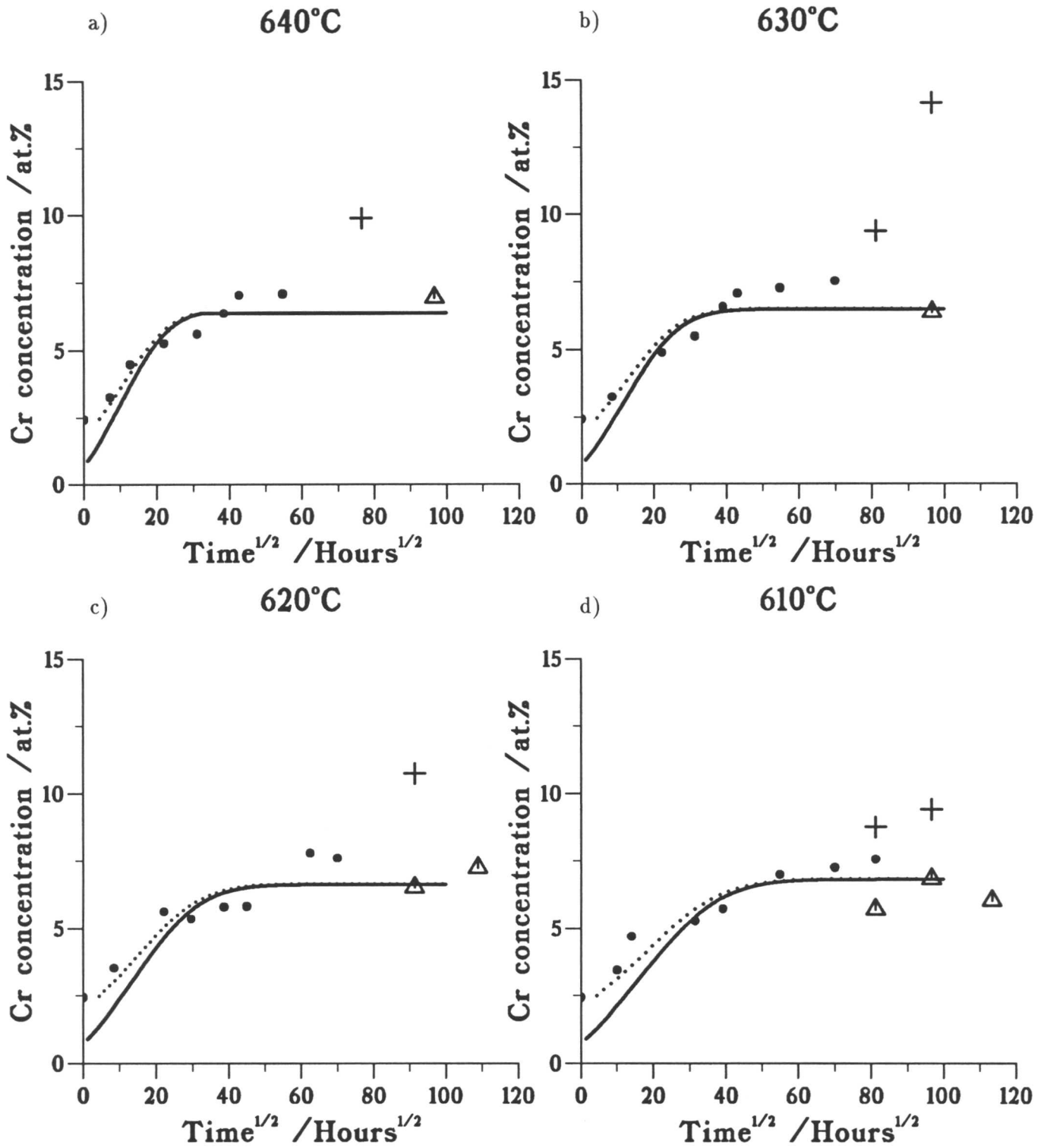
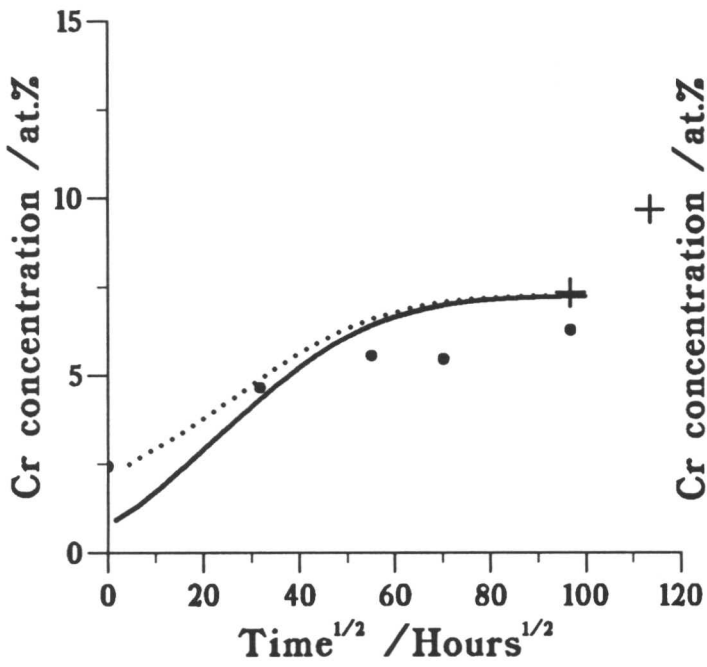


Figure 6.5: a)–h) A comparison of experimental measurements of chromium concentration in cementite, ●, with the finite difference model (solid line). The dotted line represents the predictions of the model in the case where partitioning of some chromium is allowed for. The chromium concentration of the alloy carbides occurring at long service times is plotted for comparison: + $M_{23}C_6$, Δ M_6C .

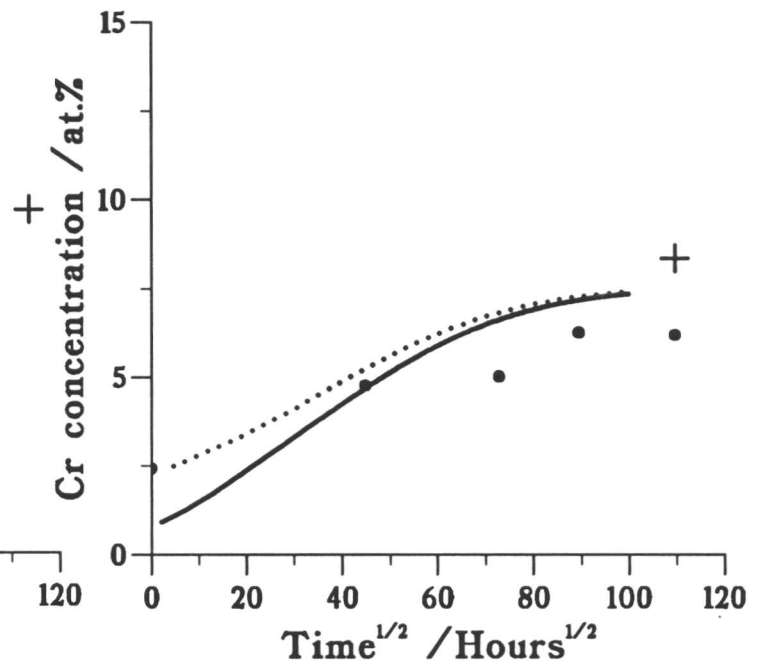
e)

590°C



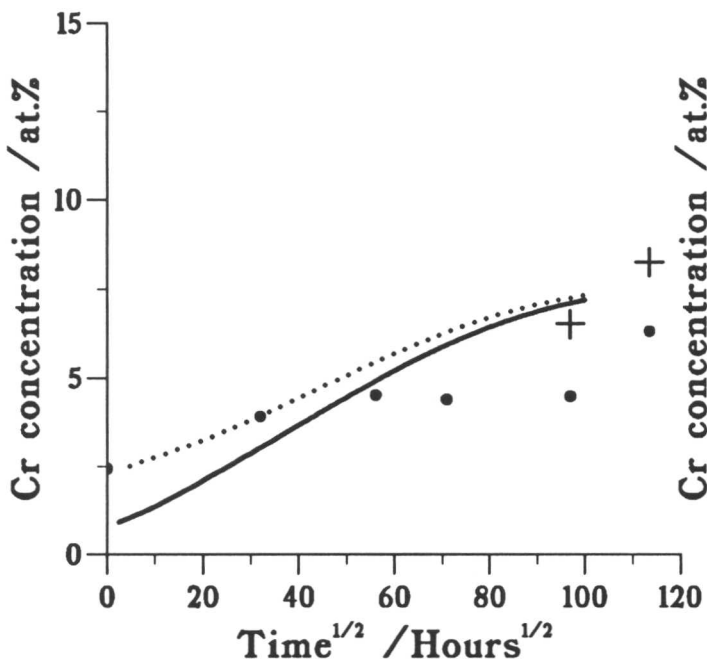
f)

575°C



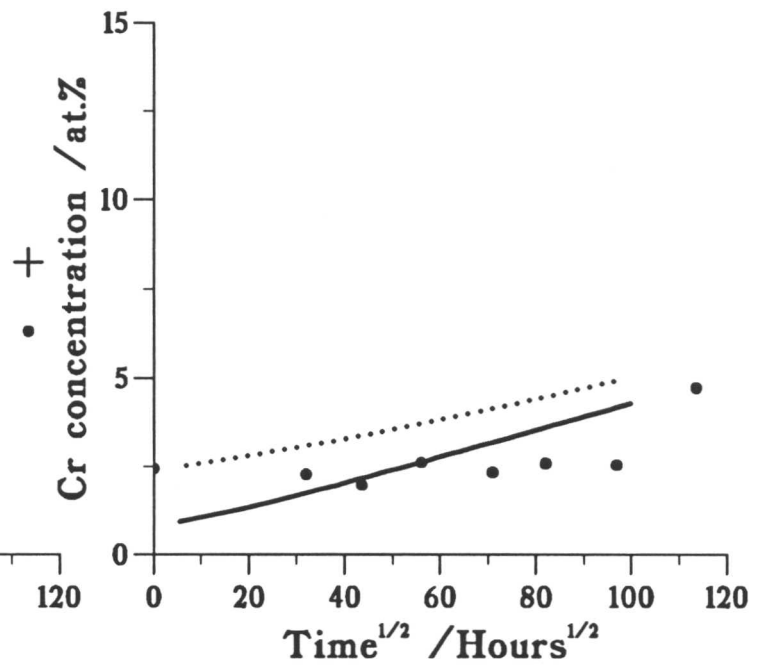
g)

565°C



h)

525°C



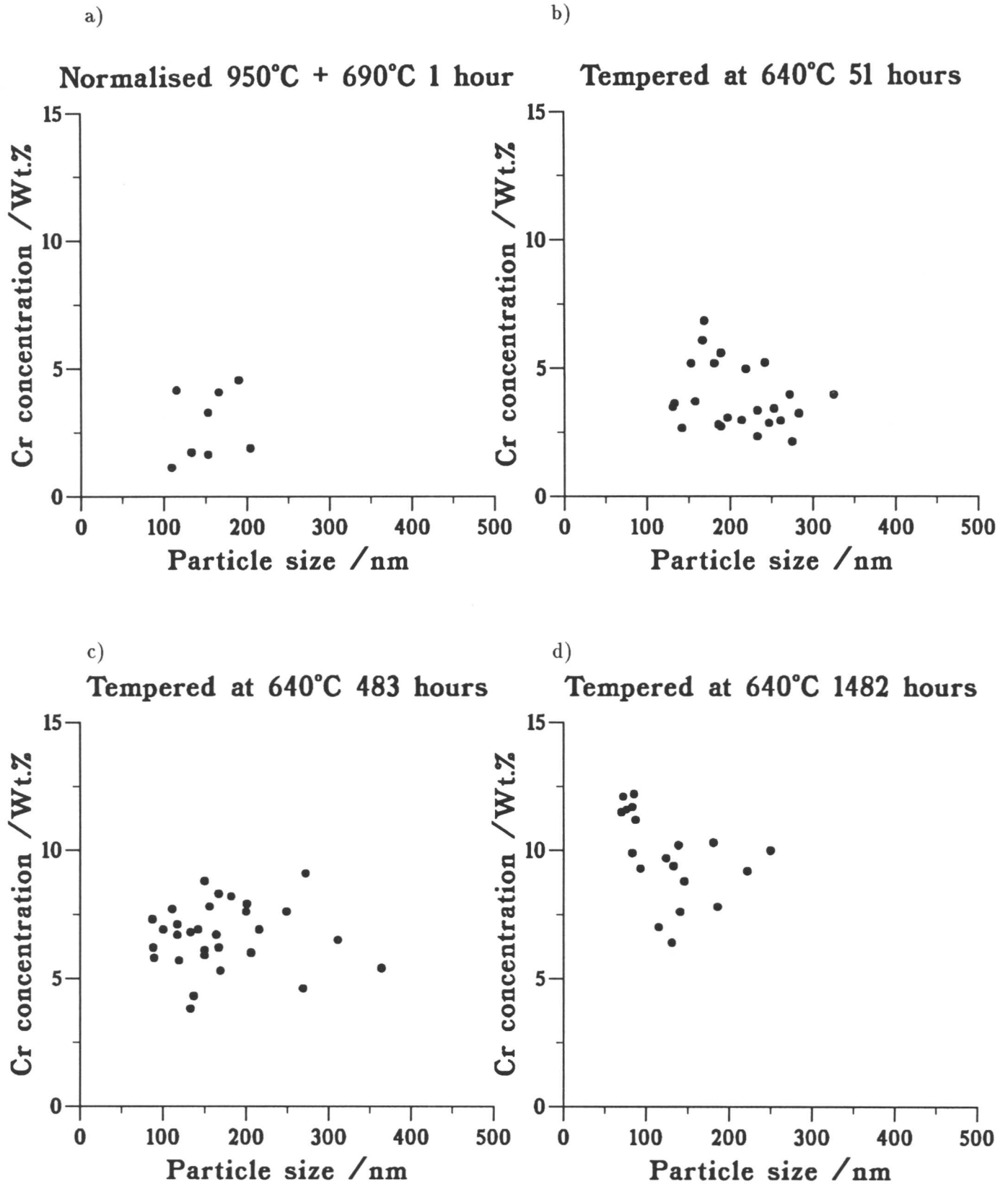
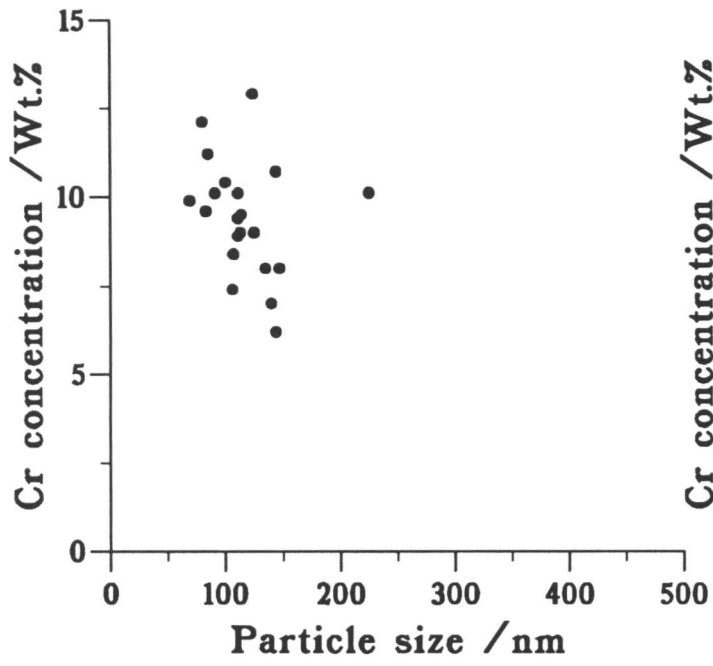


Figure 6.6: a)–f) Chromium concentration in cementite plotted against particle size for specimens tempered for varying times at 640°C.

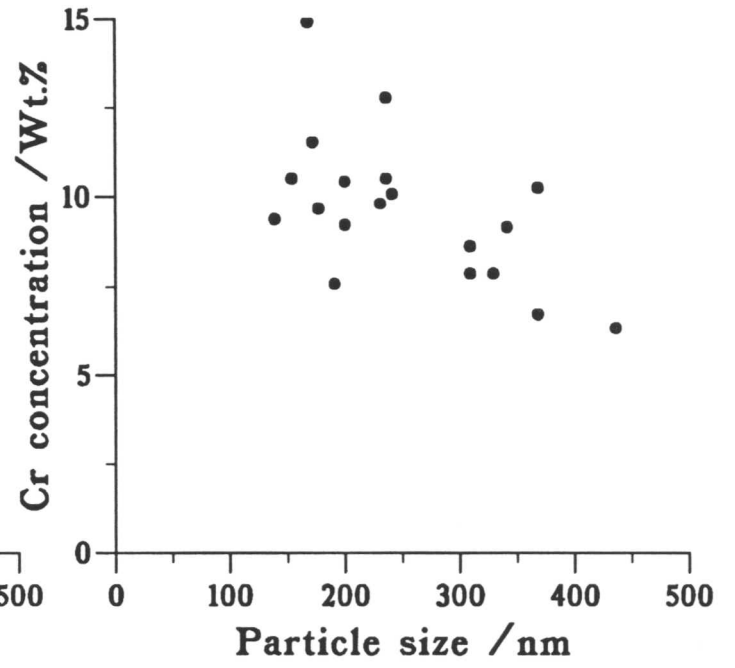
e)

Tempered at 640°C 1824 hours



f)

Tempered at 640°C 2996 hours



after transformation, and there is as yet no theory to predict the starting composition of the cementite. This is in contrast to bainitic cementite in which it can be assumed that there is negligible partitioning of substitutional solute elements during transformation. It can be seen in Figure 6.5 that there is an error in the predicted starting composition of the pearlitic cementite after the stress-relief heat treatment because any partitioning occurring on transformation is not taken into account. To allow for this problem with the initial stage of modelling, the simulation of the stress-relief heat treatment was allowed to run until the composition of the cementite had reached that measured experimentally. This corresponded to a period of tempering at 690°C for 18 hours rather than the one hour experienced in the practical situation. This is an artificial procedure because it considers partitioning to occur during the stress-relief heat treatment rather than on transformation, but it simply allows the use of the correct starting composition of the pearlitic cementite. The improvement in the agreement between the predicted and measured values is shown by the dotted line superimposed on the graphs in Figure 6.5. This problem will be overcome when a theoretical basis for the precipitation of pearlitic cementite during transformation can be established.

6.4.3 Particle size

The size and concentration of a series of particles were examined in specimens tempered at 640°C. Plots of chromium concentration against particle size are presented in Figure 6.6a)–f). The situation is complicated by the fact that the initial cementite lamellae appear to spheroidise and coarsen during tempering.

The physical explanation of the size effect is that the total amount of solute that any particle can hold scales with particle size. A smaller particle will therefore reach its equilibrium concentration at an earlier stage in the tempering process. Therefore, size effects are unlikely to be easily detected during the early stages of tempering when most of the particles are below their saturation concentration and capable of accumulating solute. It is expected therefore that the size effect becomes more prominent during the later stages of ageing. A second point to note is that at any given ageing time, the average concentration of the solute in the particle, c^θ , varies inversely with particle size, x^θ . Thus c^θ will only be sensitive to x^θ when the latter is small. This is illustrated in Figure 6.4, where variations in x^θ within the expected range for the present study do not cause very large changes in c^θ when compared with experimental error. Nevertheless it is evident from the data presented in Figure 6.6 that the dependence of c^θ on x^θ begins to emerge with statistical significance only at the longest tempering time studied. Longer times could not be studied because of the onset of alloy carbide formation.

6.5 Conclusions

In a $\frac{1}{2}\text{Cr}\frac{1}{2}\text{Mo}\frac{1}{4}\text{V}$ steel after normalisation at 950°C followed by a stress-relief heat treatment at 690°C for an hour, the cementite composition varies on further tempering at temperatures in the range $640\text{--}525^\circ\text{C}$. The chromium and manganese content of the cementite increase with tempering time at the expense of the ferrite content. After the equilibrium composition of the cementite has been reached, transformation to the alloy carbides M_{23}C_6 and M_6C occurs. The diffusion of the substitutional solute elements to cementite has been modelled and very good agreement has been found with the experimentally determined compositions. Further theoretical work is necessary to model the formation of cementite from austenite so that the starting composition of pearlitic carbides can be predicted. The dependence of composition on particle size was found not to be significant due to the relatively large size of the pearlitic cementite, and the fact that the calculated equilibrium concentration of chromium in cementite in this steel was relatively low, approximately 8 at.%. This is contrast to the particle size dependence of alloy element concentration discussed in the previous chapter for bainitic cementite. Comparison of the experimentally determined chromium concentration in cementite, after a particular operating time, with the predictions of the numerical model of the diffusion process can therefore be used to estimate the service temperature of $\frac{1}{2}\text{Cr}\frac{1}{2}\text{Mo}\frac{1}{4}\text{V}$ steel power plant components.

CHAPTER 7

12Cr1Mo STEEL

Carbide precipitation studies in 12Cr1MoV steel are discussed in this chapter. As a result of the very high chromium concentration of 12Cr1MoV steel, the reaction kinetics are rapid compared to those in low alloy steels. It is found that the equilibrium alloy carbide precipitates during the commercial stress-relief heat treatment and does not change in composition during further tempering. This is an important result; indications are that once the cementite transforms to alloy carbides, any changes in their composition are not large enough for this method to be used as a quantitative estimation of remanent life. (Low alloy steels, however, contain cementite for a considerable fraction of their useful service life.)

The material described in this chapter has been published in *Metallurgical Transactions A*, **23A**, 1992, p. 1171–1179.

CHAPTER 7

12Cr1Mo STEEL

7.1 Introduction

The vast majority of creep-resisting steels used in power plant or in the petrochemical industry are based on low-carbon, low-alloy steels containing carbide forming elements such as chromium, molybdenum and vanadium as deliberate additions. In addition to creep resistance, prolonged service at elevated temperatures also requires good oxidation and hot-corrosion resistance, possibly in environments containing hydrogen and sulphur. In the United Kingdom, the steels are often used within the temperature range 480–565°C, the service stresses being of the order of 15–30 MPa over time periods of some thirty years. There is currently considerable research in progress to implement higher alloy steels with the aim of improving the creep strength so that the service temperature can be increased (Alberry and Gooch, 1983; Middleton, 1986). Alternatively, the higher strength can be exploited by reducing section size, which can be beneficial from the viewpoint of welding, thermal fatigue and the reduced cost of support structures. A lot of the effort to date has focussed on 12Cr1MoV steel. The purpose of this work was to examine the effect of representative heat-treatments on the chemistry and some other characteristics of the carbides to be found in 12Cr1MoV type steels.

7.2 Materials and heat treatment

The material used in this work was a 12Cr1MoV steel supplied by National Power Technology and Environment Centre, Leatherhead, from heat 60348. The steel was supplied in the form of a rod of diameter 4 cm×1 m long. Thinner rods of 3 mm diameter and bars 1×1×4 cm were machined from the original sample. Experimental results were compared with ‘ex-service’ material (i.e. steel which has been in service in a power station), courtesy of Laborelec, Belgium. The service history of this latter pipe was 68,646 hours at 592°C followed by 146,000 hours at 587°C, both at a pressure of 175 bar. The compositions of both steels, which are both within British Standard, BS3604, and the German standard X20 for 12Cr1MoV steels, are given in Table 7.1. In spite of this, it is worth noting that the chromium concentration of the ex-service steel is significantly higher.

Heat treatments were carried out in order to recreate the microstructures used in the commercial condition when the steels are first implemented for service. The material is metallurgically complex and requires careful control of the heat treatment to ensure that the starting

Table 7.1: Chemical compositions of the 12Cr1MoV steels in wt. %

	C	Si	Mn	P	S	Cr	Mo	V	Ni	Cu	Al	Co	Nb+Ta
12Cr1MoV	0.21	0.25	0.46	0.009	0.012	10.9	1.03	0.30	0.52	0.02	<0.005	0.02	0.06
Ex-service X20CrMoV12 1	0.18	0.22	0.58	0.01	0.007	12.4	1.07	0.28	0.64	0.13	0.01	0.03	<0.01

microstructure is 100% martensitic. The specimens were sealed in silica tubes containing a partial pressure of argon of 150 mm Hg. Austenitisation was carried out at 1060°C for 15 minutes. It has been shown by Barraclough and Gooch (1985) that the austenitising temperature for 12Cr1MoV steels is crucial in determining the microstructure and mechanical properties. Too low a temperature will cause heavily spheroidised microstructures with dramatically reduced creep resistance, and too high a temperature can result in the formation of δ ferrite and a large austenite grain size, which is undesirable. Yet the temperature must be high enough to ensure the complete dissolution of carbides. After austenitisation the specimens were air-cooled, and re-sealed in silica tubes and tempered for up to 2 hours at 700°C, in order to simulate the commercial stress-relief heat treatment, and then further tempered at 565°C to simulate service conditions.

7.3 Results

7.3.1 Microstructural changes

A typical optical micrograph is shown in Figure 7.1. It can be seen that the microstructure is 100% martensite and does not contain any δ ferrite. TEM micrographs of the as-quenched microstructure are presented in Figure 7.2. Figure 7.2a) shows martensite platelets containing some internal twins, confirmed by selected area electron diffraction. Figure 7.2b) demonstrates the fact that there are no carbides in the as-quenched microstructure, i.e. that no autotempering has occurred. Gooch (1982) reported that the microstructure obtained by cooling from 1100°C contained a fine dispersion of cementite particles. This difference is attributed to the relatively slower speed of the quench.

Figure 7.3a) and b) illustrate the carbides beginning to form at prior austenite grain and lath boundaries, and also intra-lath, in a specimen which has been tempered at 700°C for 15 minutes. The carbides were identified by selected area electron diffraction as both M_7C_3 and $M_{23}C_6$.

The carbide M_7C_3 was also found in specimens aged for up to 30 minutes at 700°C, but these had all dissolved at the end of the stress-relief heat treatment. Figure 7.4 shows that

M_7C_3 was mainly found within the martensite laths and distant from the clustered $M_{23}C_6$ precipitates. This is in agreement with Beech and Warrington (1966) who found that $M_{23}C_6$ and M_7C_3 were both present from an early stage of tempering, and that on spheroidisation the particles within the martensite laths disappeared. The diffraction pattern in Figure 7.4 illustrates the characteristic streaks of M_7C_3 resulting from its faulted structure compared with that of pure Cr_7C_3 (Westgren *et al*, 1928). No difference in morphology was found between M_7C_3 and $M_{23}C_6$, apart from a tendency for the former carbides to be much finer.

A typical carbon extraction replica from a sample which had been given the commercial stress-relief heat treatment, i.e. tempering at 700°C for 2 hours, is shown in Figure 7.5. The distribution of the carbides in relation to the martensite boundaries is clearly illustrated. The carbides at the end of the stress-relief heat treatment were found to consist chiefly of a dispersion of $M_{23}C_6$ particles concentrated on the austenite grain and lath boundaries.

A comparison between the distribution of coarse $M_{23}C_6$ carbides in the ex-service material and in a specimen isothermally heat treated at 700°C for 1173 hours is presented in Figure 7.6. The empirical Larson-Miller (Larson and Miller, 1952) parameter, defined as $T(20 + \log t)$, where T is the temperature in Kelvin and t is the time in hours, indicates that these two different heat treatment conditions are comparable. The carbide size and distribution is similar in the two materials, although for reasons which are not clear there appears to be a tendency for increased clustering of the carbides in the ex-service material.

Macrohardness measurements were made on all the specimens using a 30 kg load. These results are presented in Table 7.2. Each data point is the average of three measurements on each sample, with the total scatter being no more than 10 HV. The macrohardness data confirms that the microstructure of the ex-service material and the 12Cr1MoV steel are similar, and that little change in carbide precipitation occurs on tempering.

Table 7.2: Macrohardness measurements

Specimen	Macrohardness /HV
Pre-tempering	622
700 °C-15 mins	315
700 °C-30 mins	309
700 °C-60 mins	296
700 °C-120 mins	315
700 °C-1173 hours	293
Ex-service material	302

The appearance of additional phases, such as Laves phase, on tempering a 12Cr1MoV steel depends critically upon the base composition of the steel. In the steels used in this work no additional phases were found during tempering which is consistent with the work of Briggs and Parker (1965).

7.3.2 Thermodynamic calculations

Thermodynamic calculations were performed using MTDATA in order to calculate the equilibrium phases in the 12Cr1MoV steel. The carbide $M_{23}C_6$ was found to be the stable carbide, coexisting with ferrite, at all temperatures in the range of interest, 400–800°C. The equilibrium solution temperature of the carbides was found to be 950°C. Barraclough and Gooch (1985) found that 30 minutes at 950°C was not an adequate solution heat treatment, although 30 minutes at 1000°C was satisfactory. The temperature at which delta ferrite became stable on heating was calculated as 1220°C in the 12Cr1MoV steel, and as 1110°C in the ex-service material, which contained an additional 1.5 wt.% chromium. This difference is consistent with the work of Irvine *et al.* (1960) who found that an increase in chromium content of 1 wt.% led to an increase in δ -ferrite content of $\simeq 14\%$. This confirms that the commercial austenisation temperature range of 1020–1070°C is adequate to completely dissolve carbides and will not produce large amounts of δ -ferrite.

$M_{23}C_6$ was found to be the most stable carbide, then M_7C_3 , followed by cementite. A precipitation sequence of $M_3C \rightarrow M_7C_3 \rightarrow M_{23}C_6$ is therefore possible.

The results of the thermodynamic calculations for 700°C (the stress-relief heat treatment) and for 565°C (the service temperature) are presented in Table 7.3. The alloying element content of the two carbides of interest, M_7C_3 and $M_{23}C_6$, is presented as a function of temperature in Figure 7.7a) and b).

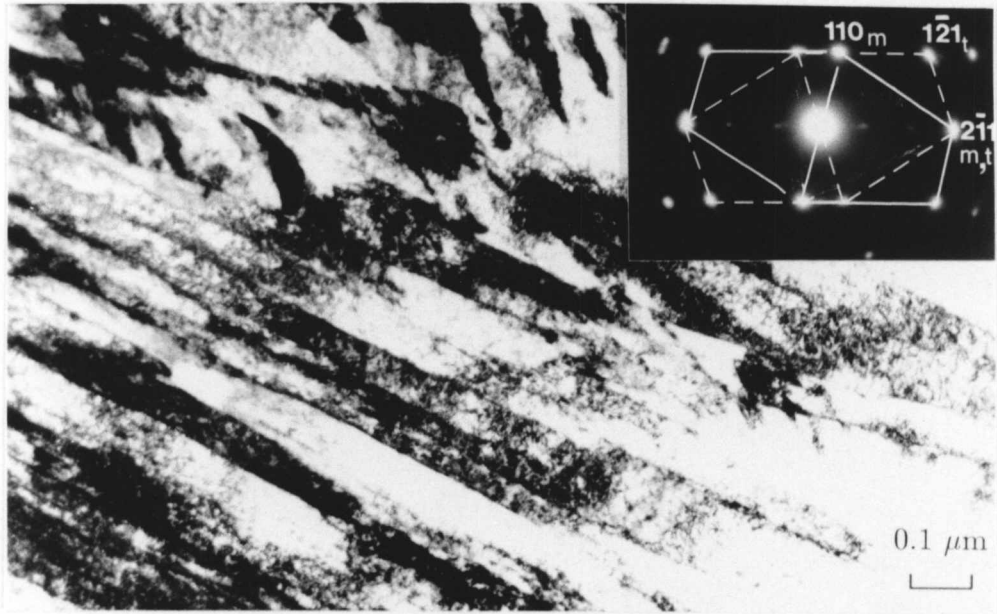
Table 7.3: Chemical compositions of the carbides in both the 12Cr1MoV steels used in wt.%. The calculations were performed using MTDATA at 700°C and 565°C respectively.

	12Cr1MoV Steel					'Ex-service' 12Cr1MoV steel				
	Fe	Cr	Mo	Mn	C	Fe	Cr	Mo	Mn	C
700°C										
M_7C_3	5.2	82.2	3.1	0.6	8.9	4.6	83.2	2.7	0.7	8.8
$M_{23}C_6$	10.7	65.1	19.1	–	5.1	9.0	66.4	19.5	–	5.1
565°C										
M_7C_3	1.6	84.4	4.5	0.7	8.8	1.4	85.1	4.0	0.7	8.8
$M_{23}C_6$	4.2	70.3	20.4	–	5.1	3.6	70.9	20.4	–	5.1



Figure 7.1: Optical micrograph for specimen austenitised at 1060°C 15 mins, air cooled, and tempered for 2 hours at 700°C.

a)



b)

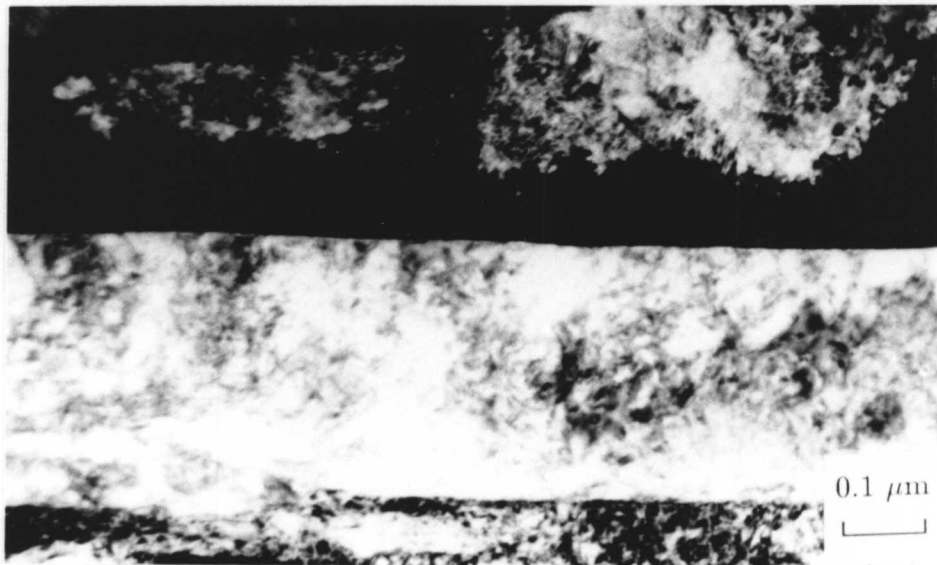
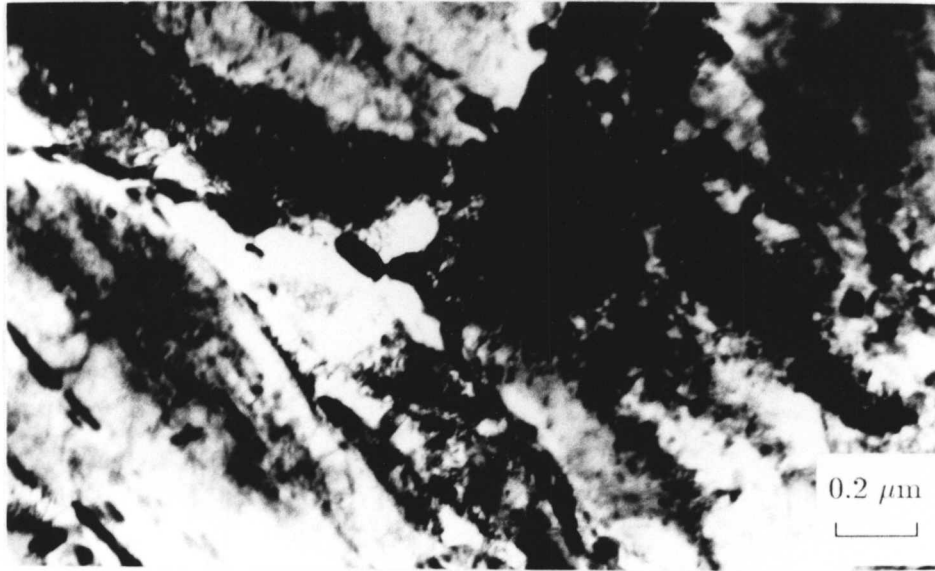


Figure 7.2: Transmission electron micrographs from the as-quenched microstructure. a) illustrates the twinned martensite microstructure; the inset is a selected area diffraction pattern showing the twin (t) and matrix (m) reflections. The twin plane is $2\bar{1}1$. b) is a higher magnification image showing that no auto-tempering has occurred.

a)



b)

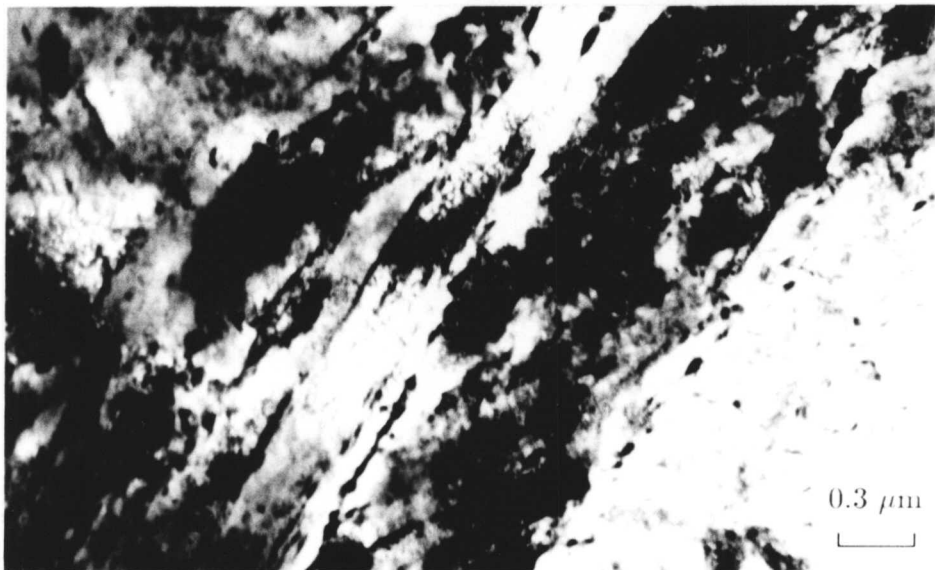


Figure 7.3: Transmission electron micrographs illustrating carbide formation at both the grain a) and lath b) boundaries in a specimen tempered for 15 minutes at 700°C.

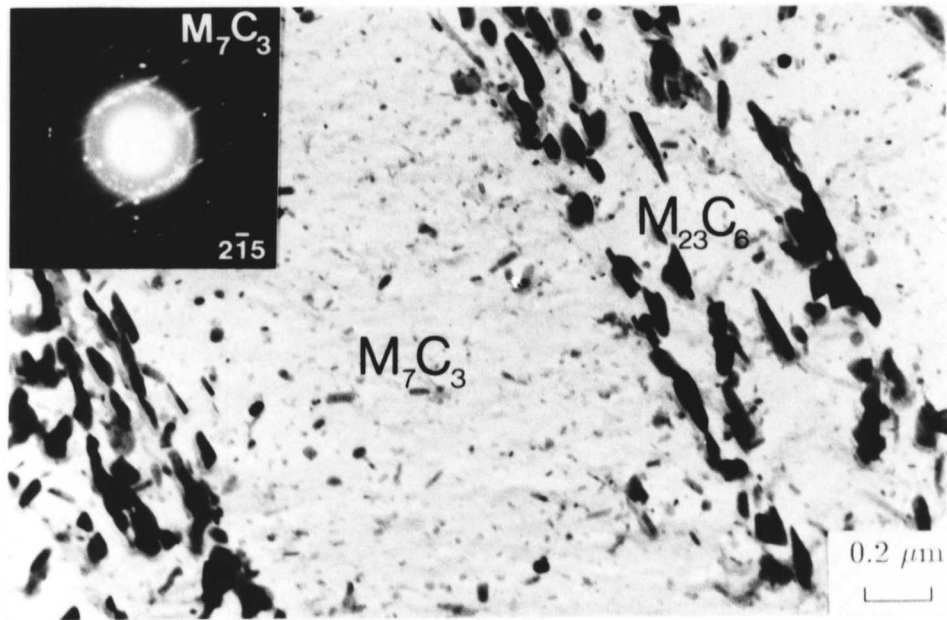


Figure 7.4: Carbon extraction replica showing small M_7C_3 particles distributed within the martensite laths and distant from the larger $M_{23}C_6$ particles clustered on the lath boundaries. The inset is a selected area diffraction pattern of M_7C_3 , the zone axis being $[2\bar{1}5]$ and showing characteristic streaks.

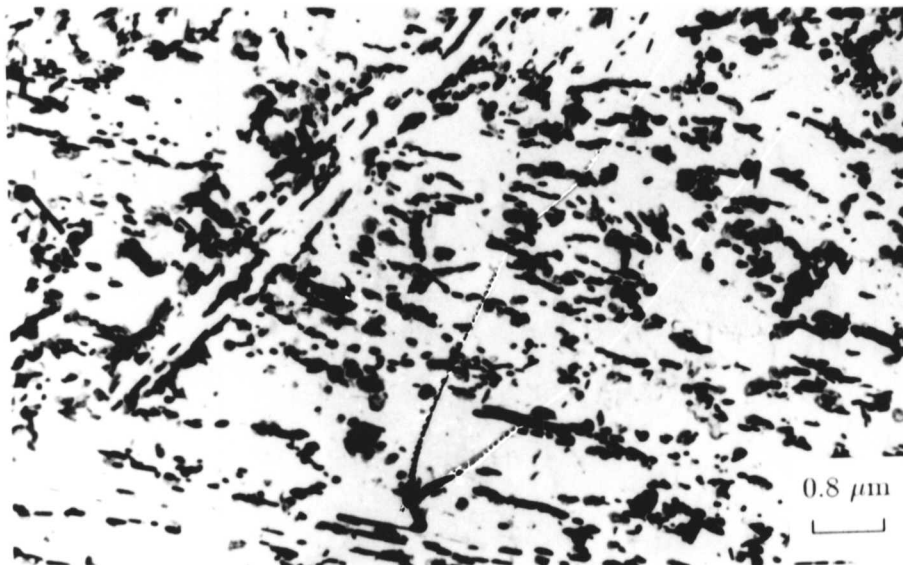


Figure 7.5: Carbon extraction replica from a specimen tempered for 2 hours at 700°C illustrating the distribution of $M_{23}C_6$ carbides with respect to martensite lath boundaries.

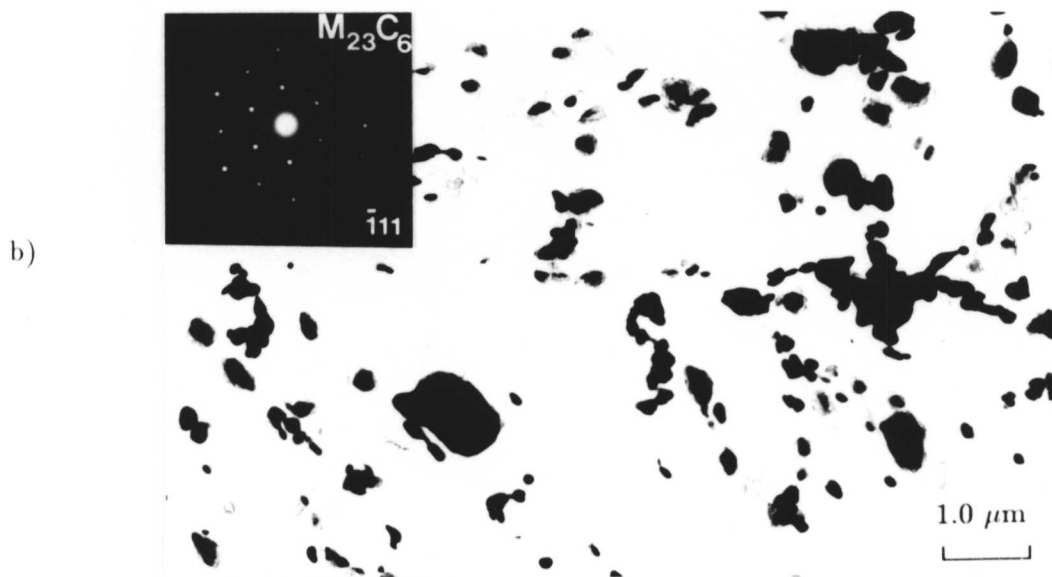
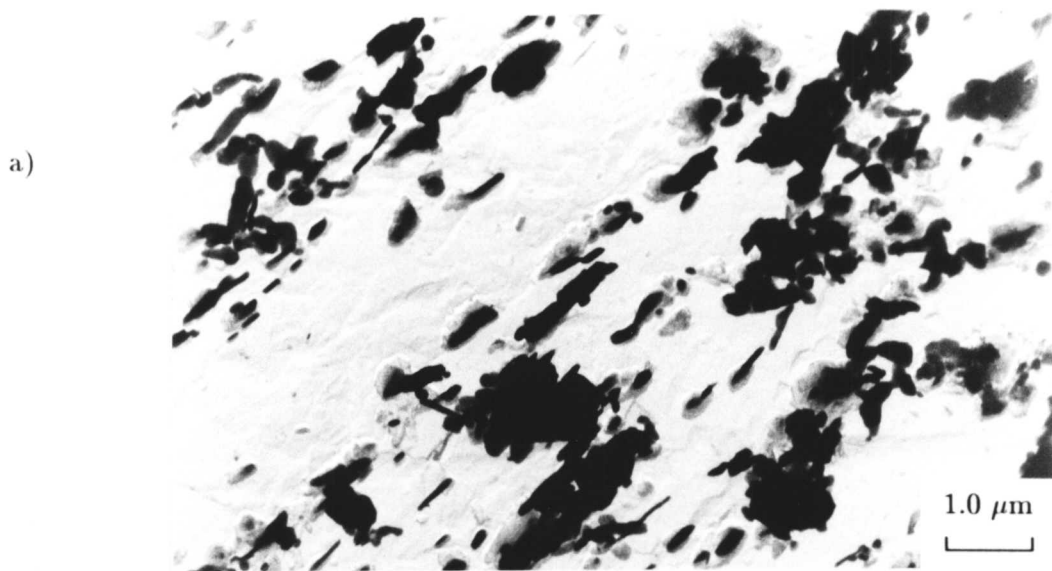


Figure 7.6: A comparison between the distribution of $M_{23}C_6$ carbides in the ex-service material a) and in the specimen isothermally heat treated for 1173 hours at 700°C b) which represent comparable heat treatments according to the empirical Larson–Miller parameter. The inset in figure b) is a selected area electron diffraction pattern of $M_{23}C_6$ in the $[\bar{1}11]$ orientation.

The carbides found in the microstructural investigation were M_7C_3 and $M_{23}C_6$, in good agreement with the sequence predicted by thermodynamic calculations. The EDXS results show that the equilibrium chromium content of the carbide M_7C_3 is higher than that in $M_{23}C_6$. The absolute levels of Cr and Mo predicted to be in the carbides are slightly higher than those observed experimentally (e.g. 65 wt.% Cr and 20 wt.% Mo are predicted in $M_{23}C_6$, whereas 60 wt.% Cr and 10 wt.% Mo, allowing for 5 wt.% C, are measured experimentally), however, there is good general agreement. The chromium content of both carbides in the ex-service material is larger due to the increased bulk chromium content of the alloy. The carbides can support a greater substitutional alloying content as the temperature is lowered. It is possible, therefore, that when the steel is in service at the lower temperature of 565°C, after the stress-relief heat treatment, the chromium content of the $M_{23}C_6$ may increase by approximately 4–5 wt.%. It is likely, however, that this approach to equilibrium will be extremely slow and difficult to detect within the experimental error of energy-dispersive X-ray spectroscopy.

7.3.3 Cementite precipitation

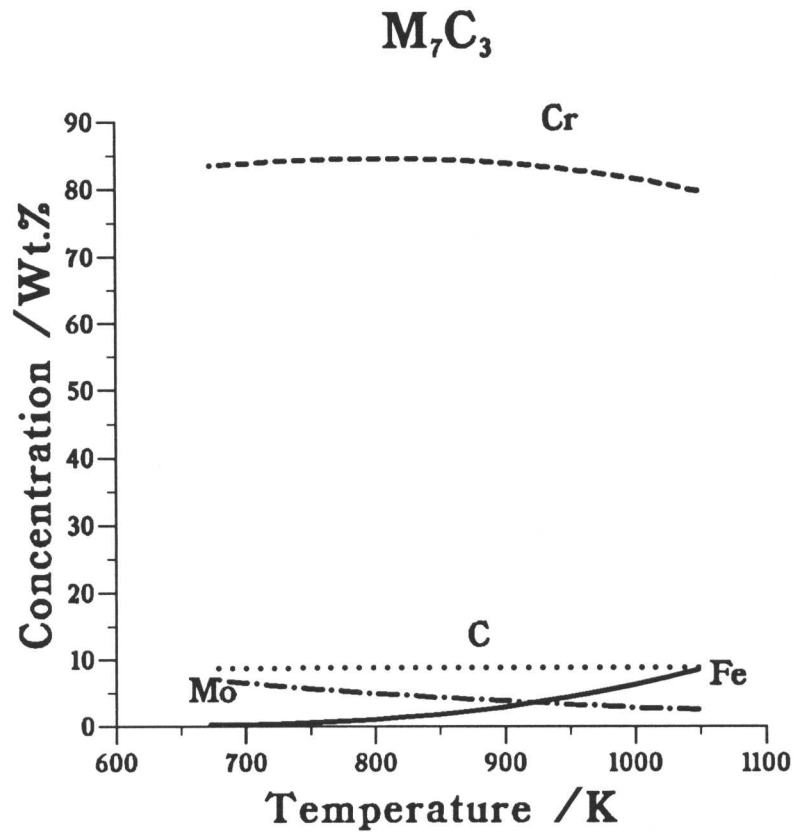
It is interesting to note that no cementite was found in any of the specimens, even during the earliest stages of tempering, because cementite is usually expected to be the first carbide to form on tempering martensite. Therefore the computer model described in Chapter 3 was used to investigate the time for cementite, with an initial composition determined by assuming a paraequilibrium transformation mechanism, to reach its predicted equilibrium composition. The results of these calculations are presented in Figure 7.8. The chromium concentration in the cementite is plotted against the time allowed for diffusion at 700°C for a range of particle sizes between 10 and 30 nm. It can be seen that cementite in fact saturates in an extremely short time, of the order of a few minutes. It is concluded that with the large amount of chromium in the base composition of the steel, the driving force for alloy carbide precipitation is large, and that cementite will only be seen in this steel if tempering takes place at a much lower temperature, or possibly immediately after tempering has begun.

7.3.4 X-ray microanalysis

Extensive measurements of carbide composition and particle size were performed on carbon extraction replicas using EDX. The results of the analyses on the carbides contained in specimens tempered at 700°C for 15, 30, 60 and 120 minutes respectively are presented in Figure 7.9a)–d) as plots of the chromium concentration against particle size, measured in terms of a mean linear intercept.

It can be seen in the 15 minute specimen that M_7C_3 (with a composition of approximately

a)



b)

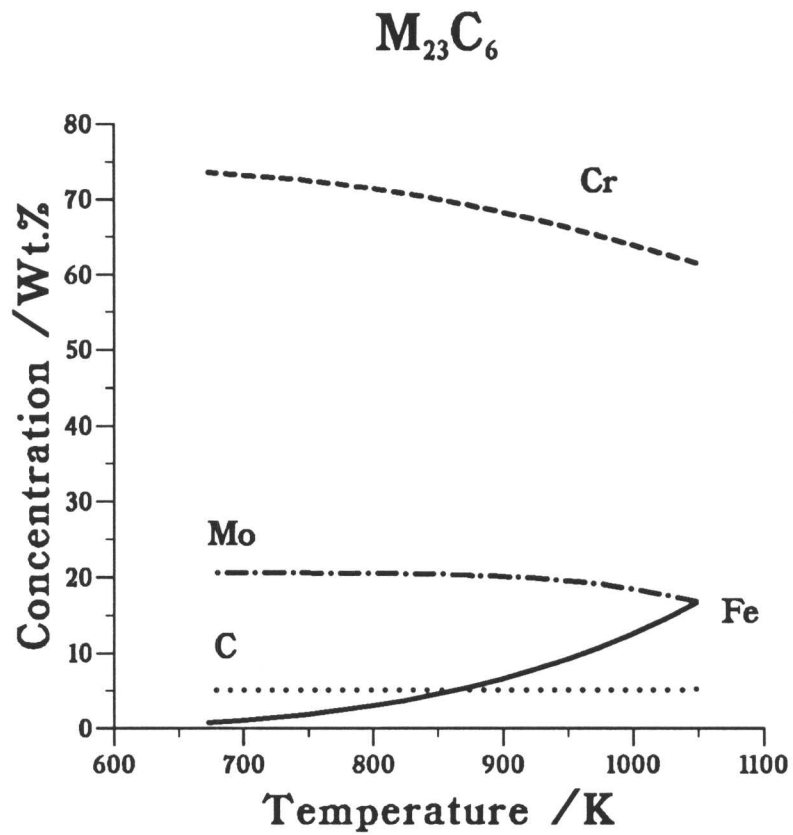


Figure 7.7: Alloying element content of M_7C_3 a) and $M_{23}C_6$ b) carbides as a function of temperature in the 12Cr1MoV steel.

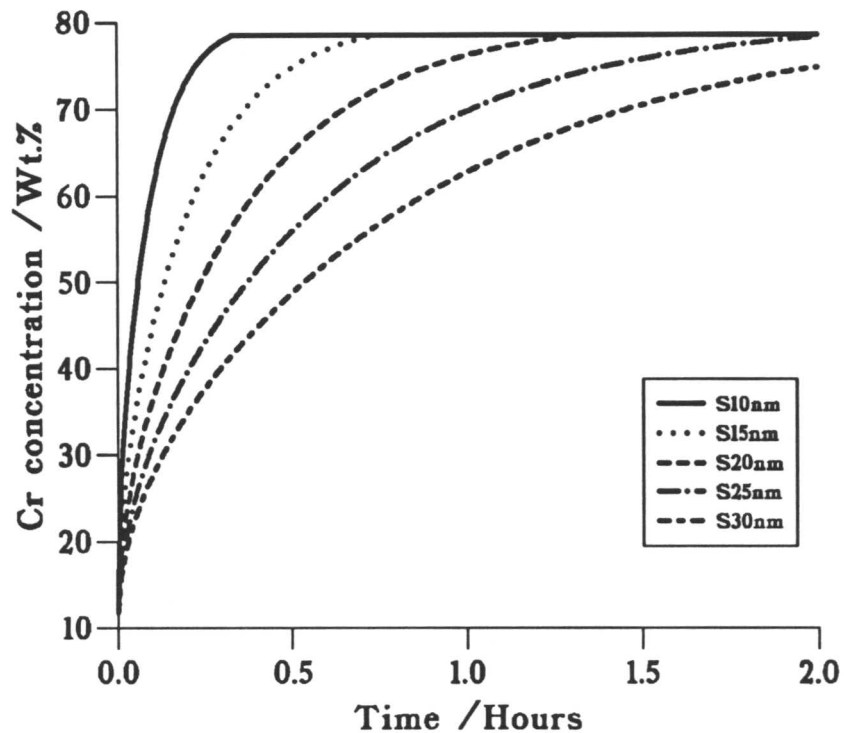


Figure 7.8: Calculated rate of cementite enrichment with respect to chromium concentration for particles of sizes 10–30 nm using a finite difference model.

75 wt.% Cr, 20 wt.% Fe and small amounts of molybdenum and manganese) is found to co-exist with $M_{23}C_6$ (with a composition of approximately 60 wt.% Cr, 30 wt.% Fe and 10 wt.% Mo). These compositions are in general agreement with those of Beech and Warrington (1966), the absolute values being dependent on the base composition of the steel. The average chromium concentration in $M_{23}C_6$ in all the specimens ranged from 60–63 wt.%. The transition from M_7C_3 to $M_{23}C_6$ is picked up in the 30 minute specimen. After 1 hour there is very little evidence of any M_7C_3 being present in the microstructure, and after the completion of the stress-relief heat treatment all the M_7C_3 has redissolved. Figure 7.9e) compares data from the ‘ex-service’ material and the specimen tempered for 1173 hours at 700°C. The chromium content in the carbides in the ‘ex-service’ material is larger than that in the isothermally tempered specimen, but this difference can be attributed to the the higher chromium content in the base composition of the steel and the longer tempering time. In both cases, however, the chromium content is constant.

7.3.5 X-ray diffraction analyses

X-ray diffraction analyses on particles extracted from the steel matrix using the method described in Chapter 4 for specimens tempered at 700°C for 10 minutes and 2 hours respectively

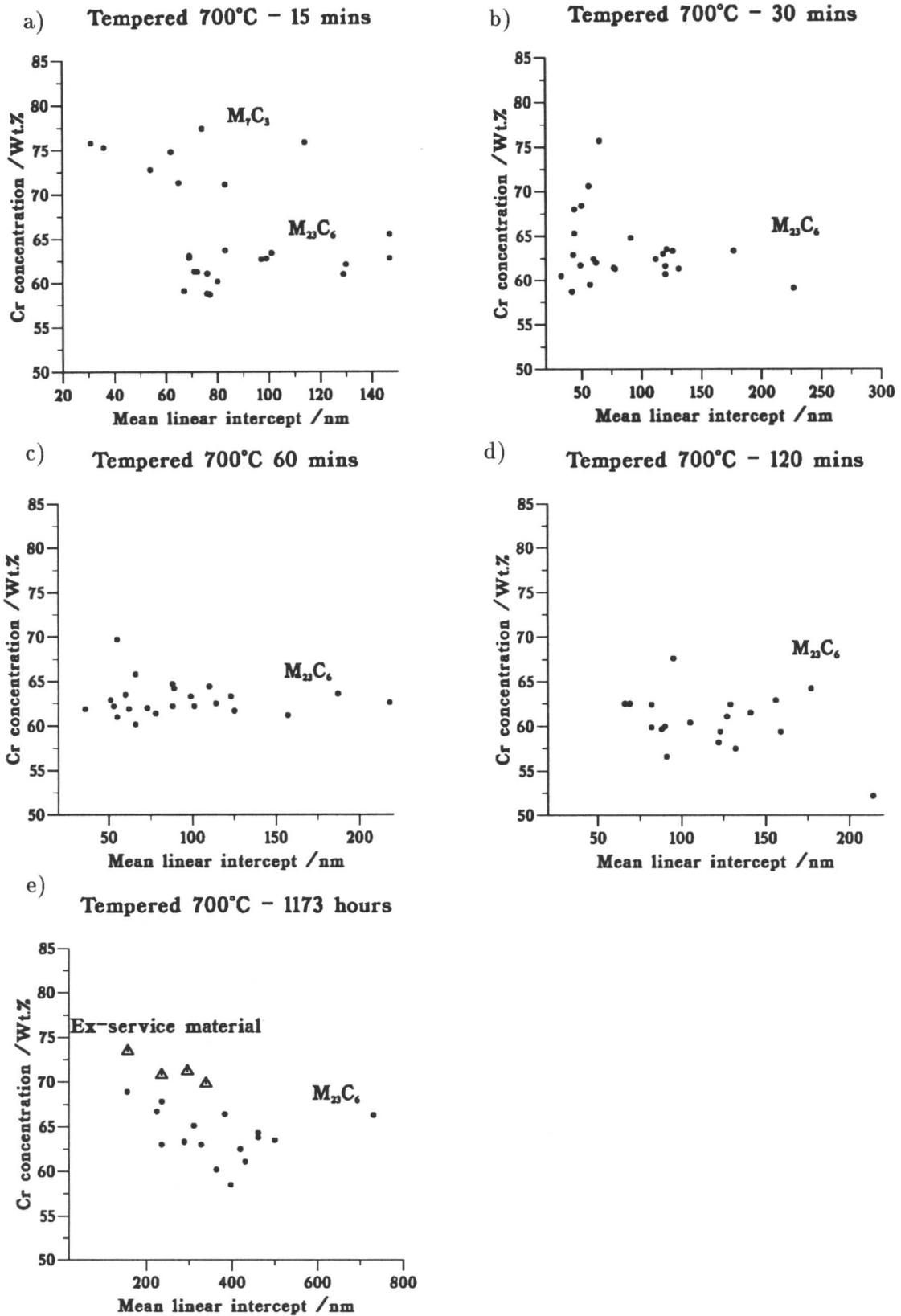


Figure 7.9: a)–e) Cr concentration versus particle size for specimens tempered at 700°C for varying times. In e) the results are compared with the composition of $M_{23}C_6$ in the ex-service material.

are presented in Figure 7.10a) and b). In the spectra for the specimen tempered for 10 minutes, the 420 and 202 peaks from M_7C_3 are clearly visible, whereas these have disappeared after tempering for 2 hours. The 420 and 202 peaks are the strongest visible peaks for M_7C_3 because the strong 421 peak overlaps with the strong 511 peak of $M_{23}C_6$. There was no further change in the diffraction pattern for specimens tempered up to 1200 hours at 700°C. The lattice parameters for $M_{23}C_6$ extracted from all the heat-treated specimens of the 12Cr1MoV steel were calculated using the measured values of d-spacings. Errors can arise in the measured values of the d-spacings factors such as the geometry of the diffractometer and absorption in the specimen. These were corrected for by fitting a polynomial function to the d-spacings of the internal standard, which are known to a high degree of accuracy. $M_{23}C_6$ is cubic and therefore the d-spacings and plane indices are related by the equation

$$d_{hkl}^2 = \frac{a^2}{h^2 + k^2 + l^2}.$$

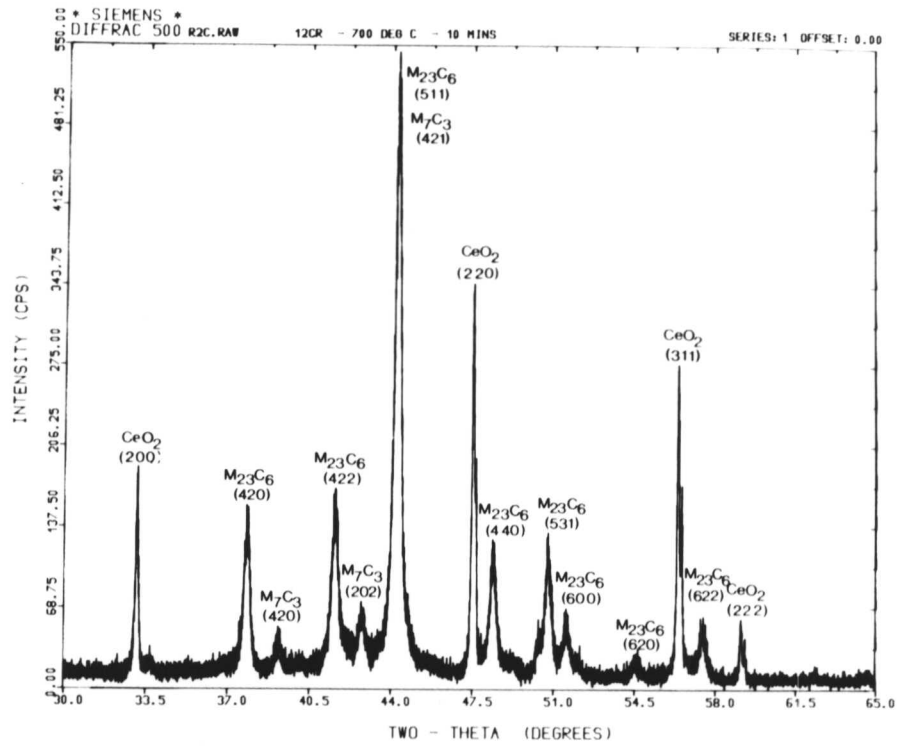
The adjusted d-spacings were fitted to this equation using a non-linear least-squares procedure. The calculated lattice parameters are presented in Table 7.4.

Table 7.4: Lattice parameters of $M_{23}C_6$ determined by X-ray diffraction.

Time at 700°C	Lattice parameter / Å
10 mins	10.64 ± 0.01
15 mins	10.65 ± 0.01
30 mins	10.66 ± 0.01
1 hour	10.65 ± 0.01
2 hours	10.65 ± 0.01
1173 hours	10.66 ± 0.01
2 hours + 16 hrs at 565°C	10.65 ± 0.01

The lattice parameter of $(Fe, Cr)_{23}C_6$ containing 60 wt.% Cr extracted from a commercial steel containing 14 wt.% Cr has previously been measured as 10.595 Å (Gullberg, 1971). In order to estimate the change in lattice parameter due to the molybdenum content in the $M_{23}C_6$ in this work the relative sizes of the atoms are considered. Molybdenum atoms are 10% larger than chromium and may replace up to 8 out of 92 of the metal atoms in the unit cell (Franck *et al*, 1982). The 10 wt.% Mo measured in the carbide corresponds to $Cr_{16}Fe_6Mo_1C_6$, and therefore an increase in lattice parameter to $10.59(1+0.1 \times \frac{1}{23}) = 10.64 \text{ Å}$ is predicted. This is

a)



b)

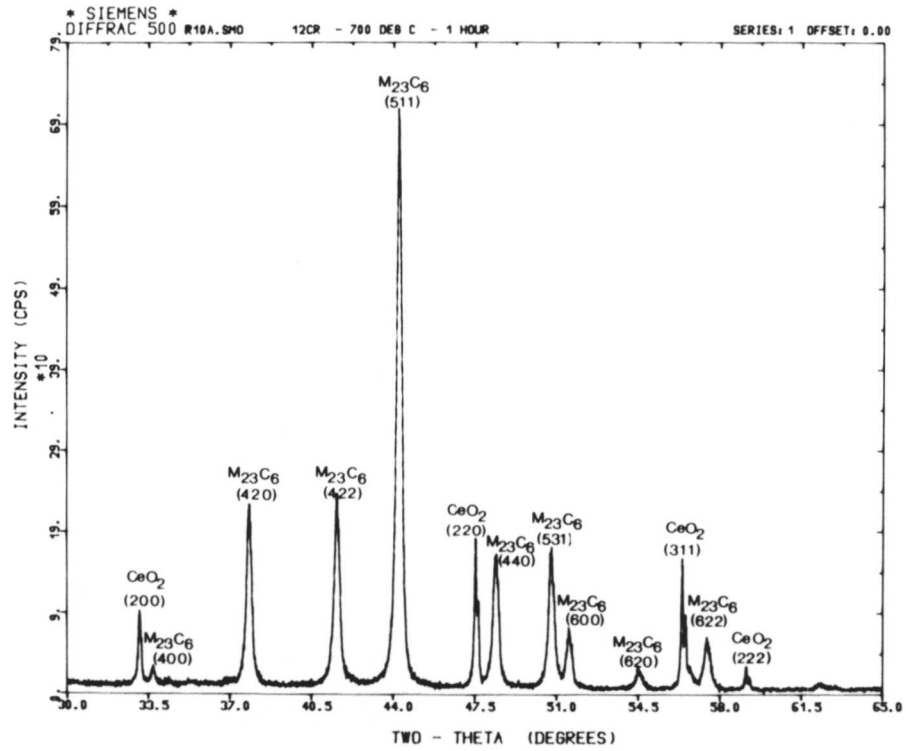


Figure 7.10: X-ray diffraction patterns for specimens tempered at 700°C for 10 mins a) and 1 hour b) respectively illustrating that M_7C_3 initially present along with $M_{23}C_6$ has dissolved after tempering for 1 hour.

in good agreement with the calculated value. The calculated lattice parameters differed by no more than 0.02\AA , indicating again no significant differences in the composition of the $M_{23}C_6$ after tempering.

7.4 Discussion

The carbides precipitating during the stress-relief heat treatment in 12Cr1MoV steel have been identified by X-ray diffraction and selected area electron diffraction as M_7C_3 and $M_{23}C_6$. Therefore, before entering service at approximately 565°C , the steel contains a distribution of $M_{23}C_6$ particles. The initial composition of the carbides is close to that predicted using equilibrium thermodynamics, and it has been established by EDX that there is no further change in the composition of the carbides with tempering. No significant dependence of chromium concentration on particle size was found. Lattice parameter measurements and comparison with ex-service material confirm that there is no change in composition of the $M_{23}C_6$ on tempering, especially with respect to molybdenum, which might have been expected from the thermodynamic calculations. The fact that there is no enrichment occurring on tempering in 12Cr1MoV steel is in contrast to the low alloy steels reported in the previous chapter. Du (1986) found that the chromium content in $M_{23}C_6$ precipitating in a $\frac{1}{2}\text{Cr}\frac{1}{2}\text{Mo}\frac{1}{4}\text{V}$ steel increased with time. Whether or not alloy carbides precipitate at their equilibrium composition is therefore dependent on the concentration of alloying elements available in the base composition of a steel. Recent work by Bjärbo (1991) (for an alloy with a higher chromium content than that used in this work) has shown that $M_{23}C_6$ which precipitates during the stress-relief heat treatment is enriched in chromium by less than 5 wt.% during a creep test for 20,000 hours at 600°C .

7.5 Conclusions

The kinetics of carbide precipitation in 12Cr1MoV steels are rapid when compared with other low-alloy steels of the type commonly used in power plant. This is attributed to the fact that the steel studied has relatively large concentrations of carbide-forming substitutional solutes. Thus, unlike the low-alloy steels, relatively stable alloy carbides have been found to dominate in the microstructure immediately after the stress-relief heat treatment. Since this heat treatment is always necessary before implementing the alloy in service, there seems little prospect of estimating the thermal history of a component from the chemical composition of its carbides. In fact, both the thermodynamic analysis and the experimental data show that the chromium concentration of the $M_{23}C_6$ carbide is very sensitive to the average chromium concentration of the steel. It is found that variations in the chromium concentration within

the accepted industrial specifications, can lead to larger corresponding variations in carbide compositions, than would be caused during service.

It has been established that there is no significant change in the carbide identity or composition during service after the stress-relief heat treatment. Therefore, the question arises as to which other microstructural changes could be fruitfully investigated. It seems from a comparison of figures 7.9d) and e), which show an increase in particle size from about 125–300 nm, that carbide coarsening could potentially be used as a microstructural parameter.

CHAPTER 8

ATOM PROBE AND STEM INVESTIGATIONS

The atom probe studies discussed in this chapter provide a link between the experimental measurements of mean concentration levels in cementite using energy dispersive X-ray analysis in a transmission electron microscope, and the theoretical modelling of the diffusion process discussed in Chapter 3. Consistent with theoretical predictions, the enrichment of substitutional solutes in the carbide at the carbide/matrix interface is not observed to reach the levels required for local equilibrium at the interface.

The material described in this chapter has been accepted for publication in Surface Science.

CHAPTER 8

ATOM PROBE AND STEM INVESTIGATIONS

8.1 Introduction

It was shown in Chapter 3 that the cementite associated with upper bainite forms with no redistribution of the substitutional alloying elements, by paraequilibrium transformation. The modelling of the subsequent approach towards equilibrium, involving the diffusion of substitutional elements is central to this work. It is often assumed in problems of diffusion that local equilibrium exists at an interface. † A calculation was performed using MTDATA (see Chapter 3) to determine the equilibrium concentration of chromium in cementite and ferrite for the $2\frac{1}{4}\text{Cr}1\text{Mo}$ steel at 565°C . Alloy carbide formation was suppressed; only the phases cementite and ferrite were allowed to exist. The results of the calculation are given in Table 8.1. The predicted volume fraction of cementite at this temperature was 0.022, which is consistent with mass balance considerations. The partitioning ratio indicated by the calculations is consistent with the values of $\simeq 50$ measured by Al-Salman *et al* (1979) at 600°C for pearlitic cementite in an Fe-Cr-Mn-C steel, although this comparison is not strictly valid because of the difference in steel chemistry. Local equilibrium therefore would require a very large increase in chromium concentration in cementite at the interface, compared with the 2.2 wt.% that exists in the bulk alloy.

Table 8.1: Calculated equilibrium concentration in cementite and ferrite at 565°C .

	Calculated equilibrium concentration of Cr /wt.%
Ferrite	1.05
Cementite	54.00

Modelling of the enrichment behaviour of cementite to date assumes only that local equilibrium exists in the *matrix* at the carbide/matrix interface. The concentration in cementite at the interface is determined by mass balance considerations in the diffusion equations. During the earlier stages of enrichment (*e.g.* 10 mins) the model predicts a small increase in the concentration of chromium at the edges of a cementite particle with respect to its core. At the

† Local equilibrium requires that the concentrations of the solute in both the carbide and the matrix at a carbide/matrix interface are given by the tie-line of the equilibrium phase diagram.

longer tempering times, after soft impingement of the diffusion fields from the extremities of the particle, the model predicts a more even distribution of chromium across the particle rising slowly to the equilibrium level. Measurements of cementite composition using energy-dispersive X-ray analysis (EDX) in a TEM are only able to determine the average particle concentration. The maximum measured Cr concentration in cementite by EDX in the specimens tempered at 565°C was $\simeq 35$ wt.%. It is not possible to measure the equilibrium Cr content in the cementite in this steel at this temperature because the alloy carbide M_7C_3 precipitates at the expense of the cementite before it has reached saturation.

The model assumes that the diffusion coefficients, D_α and D_θ , in the matrix and cementite respectively are the same; this assumption is justified to some extent by the good agreement between kinetic theory and experiment demonstrated in Chapters 5, 6 and 7. D_α is obtained as $1.65 \times 10^{-19} \text{m}^2 \text{s}^{-1}$ according to Fridberg *et al* (1969), whose assessed data are in good agreement with those of Bowen and Leak (1970). Barnard *et al* (1987) have used atom probe techniques to measure D_α and D_θ . The data for 486°C are presented in Table 8.2. The value of D_α measured by Barnard *et al* is an order of magnitude less than the other two values, and of D_θ approximately two orders of magnitude less than the measured value of D_α .

Table 8.2: Measurements of the diffusion of chromium in ferrite and cementite at 486°C.

	$D_\alpha/\text{m}^2\text{s}^{-1}$	$D_\theta/\text{m}^2\text{s}^{-1}$
Bowen and Leak (1970)	4.9×10^{-21}	–
Fridberg <i>et al</i> (1969)	4.6×10^{-21}	–
Barnard <i>et al</i> (1987)	(1) 2.6×10^{-22}	–
	(2) 4.9×10^{-22}	0.02×10^{-22}

The effect of varying the value of D_θ with respect to the value of D_α on the cementite enrichment rate was therefore investigated using the model described in Chapter 3. Three different values of D_θ were chosen and two different tempering times, 10 mins and 178 hours. The resulting composition profiles and predicted concentrations are presented in Figure 8.1 and Table 8.3. The most important result is that for $D_\theta = \frac{1}{50} D_\alpha$ the predicted average level of Cr in cementite is 16 wt.% for a 10 min ageing period, whereas if $D_\alpha = D_\theta$ this level is 2.5 wt.%. The average concentration of chromium in cementite after 10 mins tempering measured using EDX is $\simeq 6$ wt.%. This result is therefore inconsistent with the value of D_θ measured by Barnard *et al* (1987). It is possible that D_θ is slightly less than D_α , but not by a factor of 50.

The purpose of this work was therefore to investigate to what extent local equilibrium exists at the particle/matrix interface during the enrichment of cementite.

Table 8.3: Average Cr concentration and the interface concentration in cementite as a function of D_θ and tempering time. Concentrations are given in wt.%.

D_θ	10 mins		178 hours	
	Av. conc.	Interface conc.	Av. conc.	Interface conc.
$=D_\alpha$	2.48	3.14	13.09	13.11
$=0.3D_\alpha$	3.14	5.23	38.51	38.59
$=0.02D_\alpha$	16.06	47.74	53.99	53.99

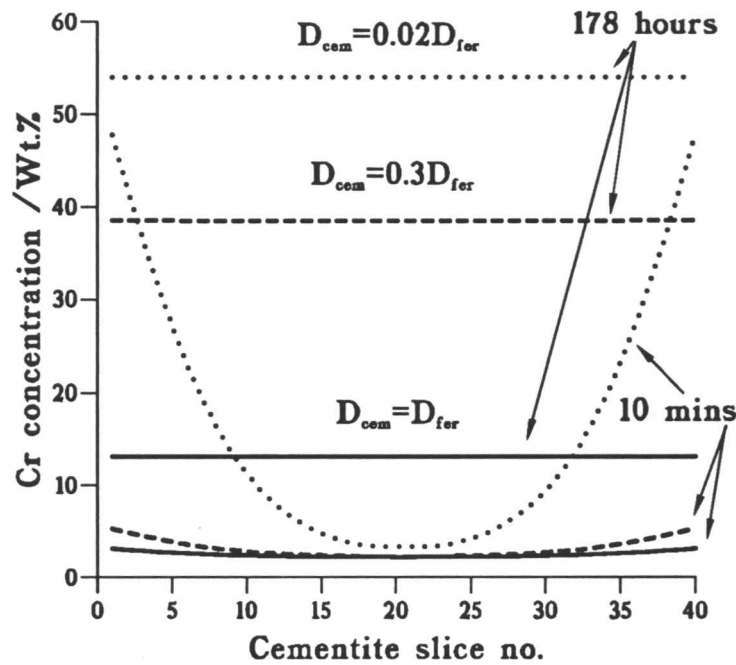


Figure 8.1: Predicted chromium concentration in a cementite particle of size 100 nm in a $2\frac{1}{4}\text{Cr1Mo}$ steel after 10 mins and 178 hrs tempering at 565°C as a function of the diffusion coefficient in cementite. Slices 1 and 40 represent the surfaces of a plate-shaped cementite particle in the finite difference model, the core being located at slice 20.

8.2 Atom probe field ion microscopy

8.2.1 Principle of operation of atom probe

An atom probe consists of a field ion microscope with an ultrahigh-resolution mass spectrometer attached. The field ion microscope produces images of the specimen in which there is one-to-one correspondence with atomic positions. The mass spectrometer is then used to

perform very accurate chemical analysis. A brief summary of the principle of operation of an atom probe is presented below. Extensive discussion concerning the operation of atom probes can be found in the book by Miller and Smith (1989), and details of the atom probe used in this work in the paper by Waugh *et al.* (1992).

A field ion specimen is a very sharp needle of tip radius approximately 100 nm. The specimen is cooled down to cryogenic temperatures using a closed-cycle helium refrigerator and held in a vacuum chamber with a background pressure of 10^{-11} mbar. For producing a field ion image (*field ionisation*), a background pressure of neon gas of 10^{-5} mbar is introduced into the chamber and a large positive voltage is applied to the specimen. The inert gas atoms become polarised in the high electric field near the tip and are attracted towards it. Ionisation of the polarised gas atom can then occur by quantum mechanical tunnelling of an electron to the tip. The remaining positively charged gas ion is then repelled from the tip towards the channel plate. On striking the channel plate, a cascade of electrons is produced which strike a phosphor screen resulting in a bright image spot. The number of ions will be greatest where the local field is highest, for example, above prominent surface atoms. A picture of the Cambridge atom probe is presented in Figure 8.2, and the corresponding schematic diagram in Figure 8.3.

Limited information can be obtained from the field ion image. The image is usually used to recognise features of interest such as second phases or boundaries. Phase contrast can arise where there are differences in the ionisation probabilities of the elements in the two phases. Ferrite is usually imaged as sets of concentric rings showing the b.c.c. symmetry of the phase, whereas austenite, martensite and carbides usually image darkly. The elements molybdenum and silicon, to a lesser extent, image brightly because the evaporation field for these elements from an iron-based matrix is higher than that for iron itself, and so they remain at prominent surface positions.

The second stage involves the removal of atoms from the surface of the specimen by the process of *field evaporation* as the voltage applied to the specimen is increased further. The background pressure of neon gas is reduced for atom probe analysis. The atoms are field-evaporated at a well-defined moment in time by the application of an additional voltage pulse. The mass to charge ratio of the atom can then be determined from the time taken to reach the detector, which can be measured to an accuracy of 1 ns. There is a hole in the channel plate which enables the selection of atoms from a specific area. The lateral resolution is the size of this hole projected onto the tip, which is approximately 5 nm. The accuracy with which small scale composition variations can be determined depends on their relative orientation to the axis of the analysis cylinder. Repeated pulsing of the sample is used to build up a layer by layer

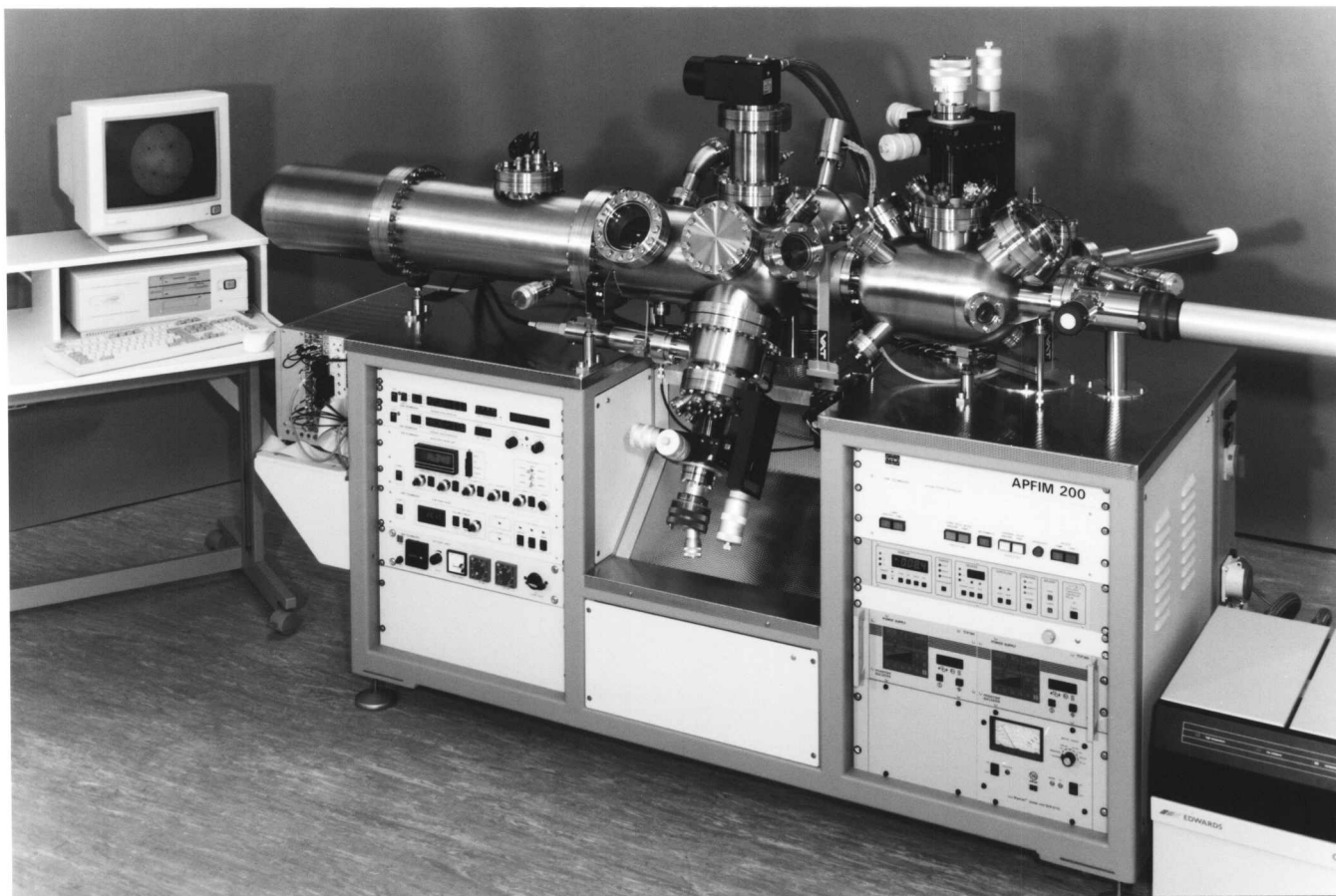


Figure 8.2: The atom probe field ion microscope (APFIM 200) used in this work.

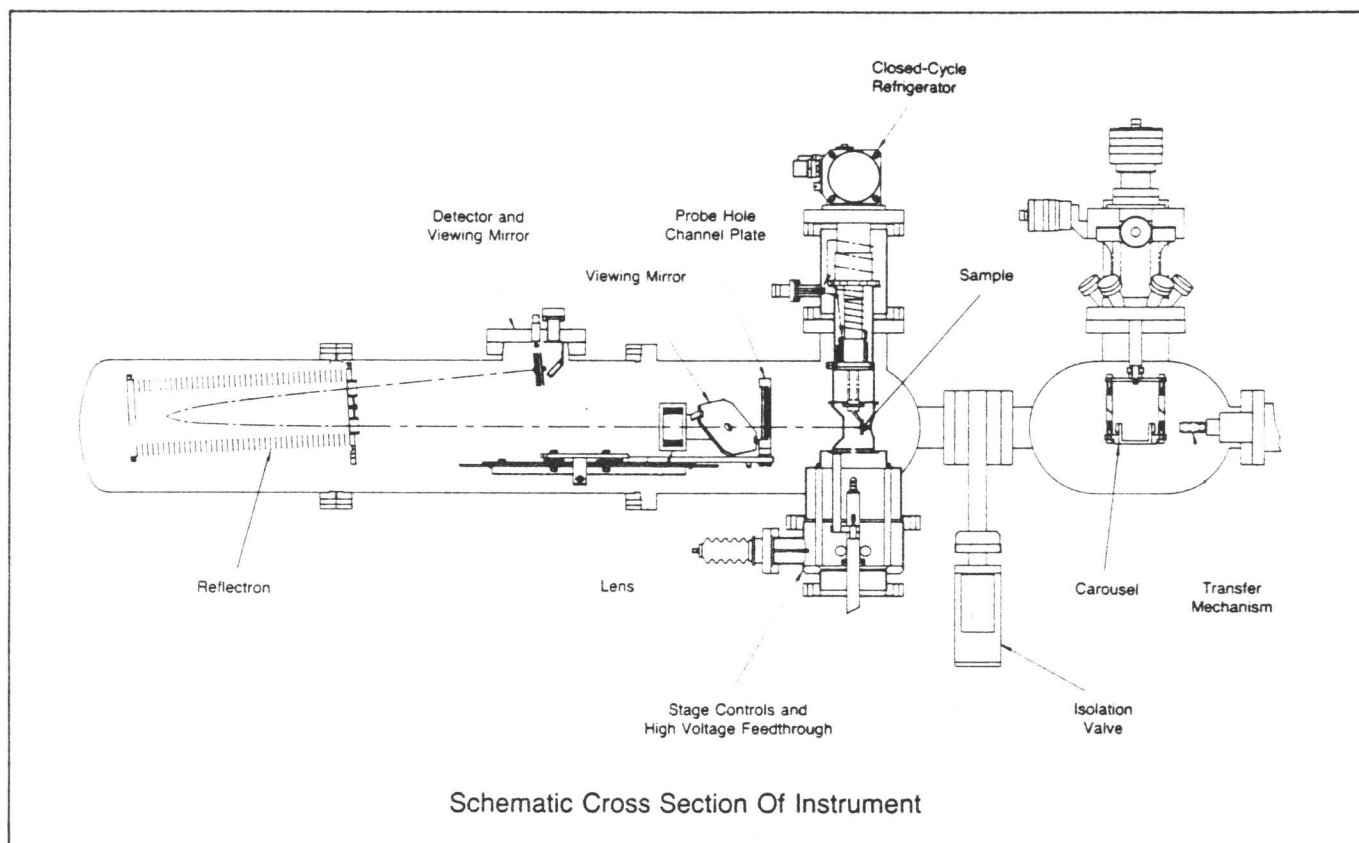


Figure 8.3: A schematic cross section of the APFIM 200.

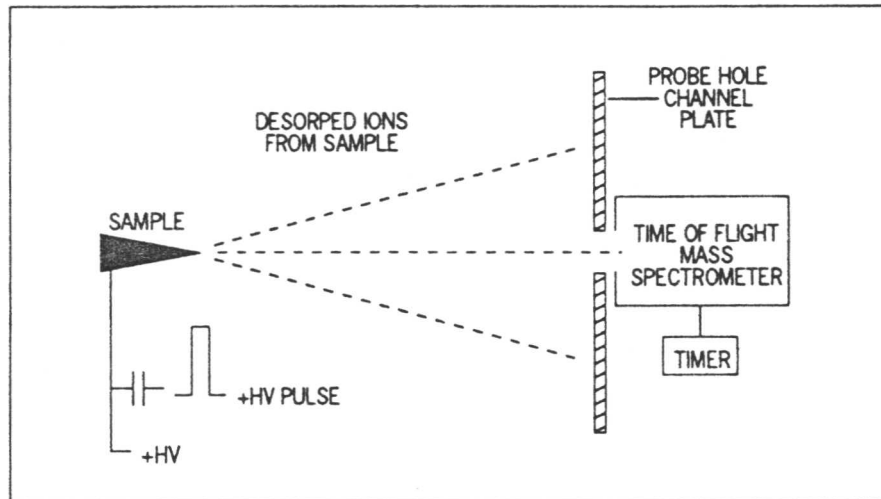


Figure 8.4: Schematic diagram illustrating the operation of the atom probe field ion microscope.

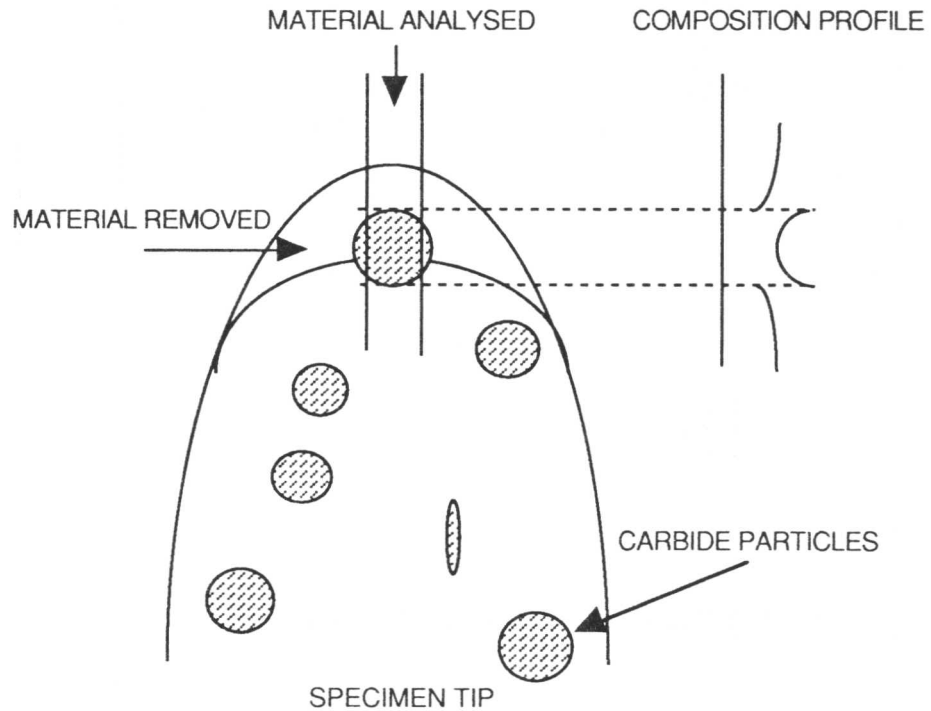


Figure 8.5: Diagram illustrating the ideal precipitate analysis geometry.

atomic composition profile from the specimen. A schematic diagram illustrating the operation of the atom probe field ion microscope is presented in Figure 8.4. A diagram illustrating the ideal precipitate analysis geometry is illustrated in Figure 8.5.

8.2.2 Experimental details

The $2\frac{1}{4}\text{Cr1Mo}$ steel discussed in chapter 5 was used for the atom probe studies. Blanks were cut from the heat treated specimens of size $0.5\times 0.5\times 20$ mm using a diamond saw. These were initially thinned electrochemically using the same conditions as for the preparation of the TEM foils of this material discussed in chapter 4. Needles for examination in the atom probe were then prepared using a two stage electropolishing technique; stage 1 producing a necked specimen profile using a thin layer of the electropolishing solution above floated on an inert solution at $\simeq 30$ V, and stage 2 producing a needle by electropolishing in a solution of 2% perchloric acid in butoxyethanol at $\simeq 25$ V. Both solutions were cooled to 0°C using liquid nitrogen. Specimens were resharpened by dipping the tips in a lacquer resist and electropolishing in the two solutions. Atom probe analyses were performed at 100 K with background pressures of neon gas of 1×10^{-5} mbar and 1×10^{-8} mbar for imaging and analysis respectively. The voltage pulse fraction used was 20%.

8.2.3 Results and discussion

The specimens tempered for relatively short times (up to 2 hrs) were examined in the atom probe, and those for longer times in the STEM, which was able to accommodate the larger particle sizes. A typical TEM micrograph from a thin foil tempered for 10 mins at 565°C is shown in Figure 8.6, showing plate-shaped carbides, identified as cementite using selected area electron diffraction. The cementite plates typically measured 125×30 nm. Analysis in the atom probe is easier if the particles are aligned with the long dimension parallel to the length of the needle. As observed by Wada *et al.* (1982), the cementite particles were found to be very unstable under the action of the applied electric field, leading to frequent specimen fracture. It was observed in the STEM that the cementite particles charged in the electron beam indicating poor conductivity.

Field ion micrographs from the matrix and cementite phases are presented in Figure 8.7. The image from the matrix was often found to contain small clusters of very bright atoms; subsequent atom probe analysis showed that these might be attributed to very small molybdenum carbides. The cementite phase is observed to have little structure in the image and to contain relatively large diffuse spots.

Mass spectra from specimens tempered for 10 mins and 2 hrs are presented in Figure 8.8.

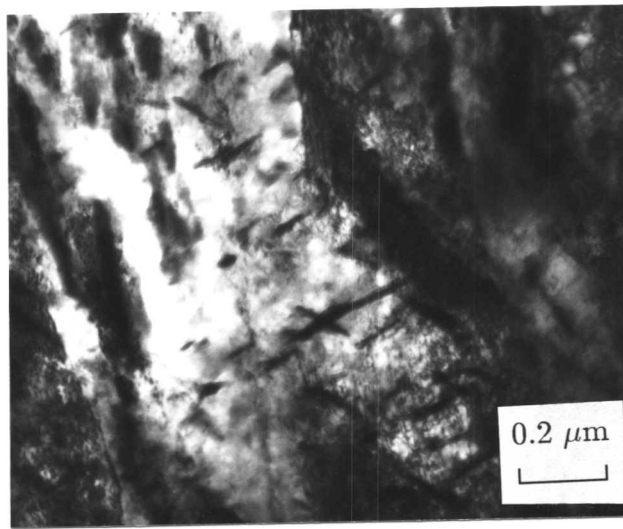


Figure 8.6: A transmission electron micrograph from a specimen tempered at 565°C for 10 mins illustrating plate-shaped cementite particles.

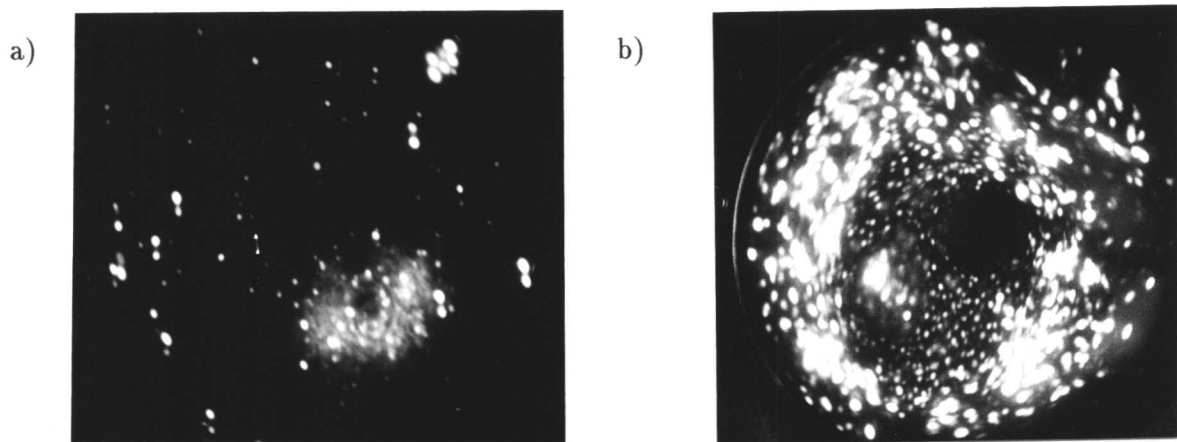


Figure 8.7: Field ion images from the matrix (a) and the cementite (b) phases.

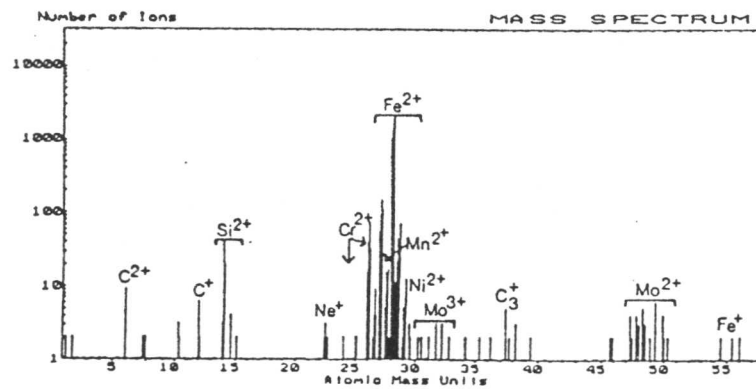
The calculated composition within the matrix, distant from the cementite particles, corresponding to each of these spectra is presented in Table 8.4. It can be seen that there is a reduction in the chromium level in the matrix after tempering for 2 hrs. This corresponds to the enrichment of cementite with respect to chromium, resulting in a drop in the chromium level in the matrix. After 2 hrs tempering, the concentration of chromium measured in cementite by energy-dispersive X-ray analysis on carbon extraction replicas in the TEM is approximately 11 wt.%.

It is interesting to note that the molybdenum and carbon contents in the matrix are a little higher than might be expected, particularly in the specimen tempered for 10 mins. Close examination of the composition profile corresponding to the mass spectrum in Figure 8.9a) reveals small clusters containing both molybdenum and carbon atoms. This is illustrated in Figure 8.9a). This suggests there are very small particles of molybdenum carbide in the early stages of formation within the matrix. A Markov chain analysis for the molybdenum atoms indicates that there are more Mo-Mo bonds than would be expected in a homogeneous solid

Table 8.4: Composition of the matrix measured in the atom probe for samples tempered for 10 mins and 2 hrs in wt. %.

Time	C	Si	Mn	P	S	Cr	Mo	V	Ni	Cu	Fe
10 mins	0.16 ±0.02	0.49 ±0.06	0.48 ±0.08	0.01 ±0.01	0.04 ±0.01	2.38 ±0.15	1.87 ±0.20	0.09 ±0.03	0.09 ±0.02	0.03 ±0.03	94.36 ±0.60
2 hrs	0.13 ±0.03	0.37 ±0.07	0.60 ±0.14	0.05 ±0.03	–	1.34 ±0.20	1.04 ±0.25	–	0.04 ±0.04	–	96.44 ±0.75

(a)



(b)

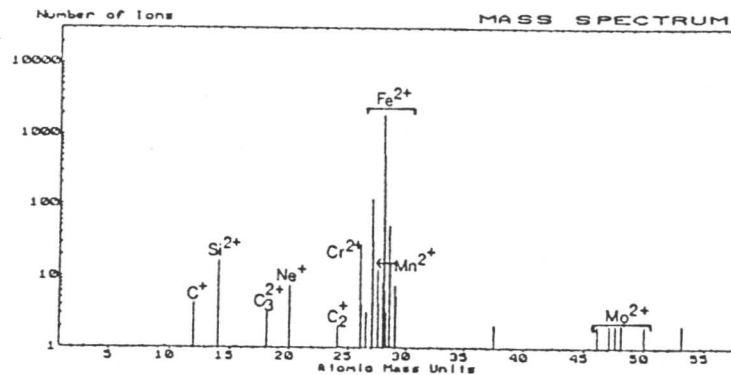


Figure 8.8: Mass spectra taken from the matrix in specimens tempered for 10 mins (a) and 2 hrs (b) containing 7,000 and 3,000 ions respectively.

solution, although many more ions are needed to establish the significance of this result. Further work is therefore needed to establish any correlation between the carbon and molybdenum concentrations, and to examine the development of clusters as a function of ageing time. Similar

observations have been made by Olson *et al.* (1991). Dark field imaging in the STEM at high magnification, which is especially good for showing high atomic number contrast, is able to resolve small particles which probably correspond to the molybdenum and carbon clusters observed in the atom probe. This is illustrated in Figure 8.9b). Mo_2C particles had not been observed in the atom probe. This is illustrated in Figure 8.9b). Mo_2C particles had not been observed in previous TEM investigations until the specimens had been tempered for 32 hrs.

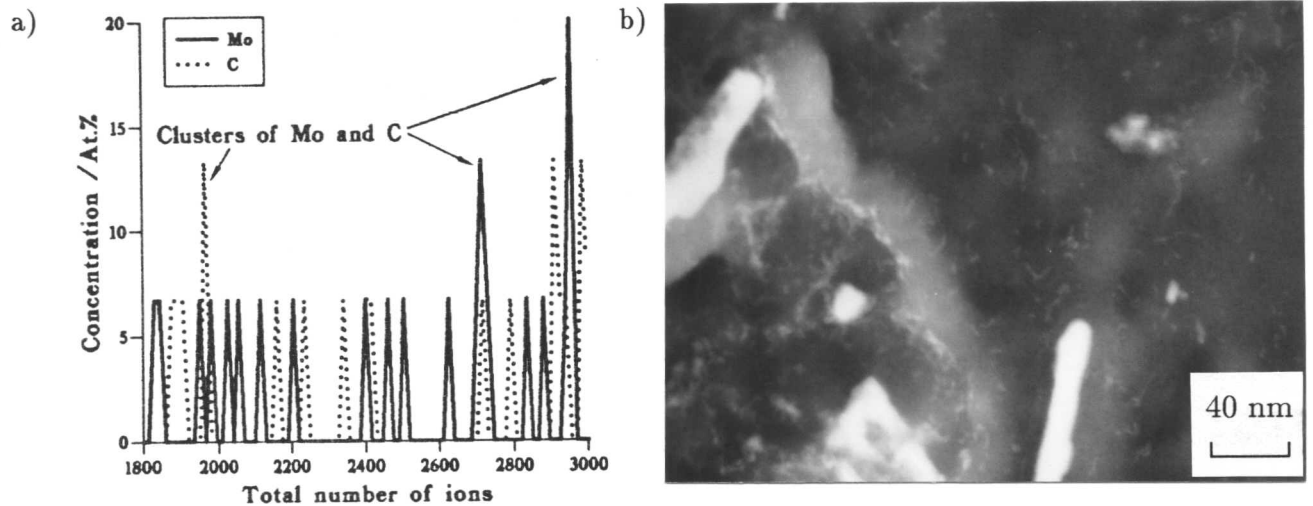


Figure 8.9: a) Composition profile (15 ions per block) corresponding to part of the mass spectrum in Figure 8.9a) for the specimen tempered for 10 mins showing small clusters of molybdenum and carbon atoms and b) dark field STEM micrograph from a carbon extraction replica taken from a specimen tempered for 10 mins illustrating very small particles exhibiting high atomic number contrast.

The measured content of silicon in the matrix is observed to be slightly higher than the composition of the steel as a whole. Silicon, usually observed as Si^{2+} , has a mass to charge ratio of 14, which is the same as that for N^+ . However, the concentration of nitrogen in the steel is expected to be less than 40 ppm. High levels of Si is a common observation, and is usually attributed to the preferential evaporation of the matrix because Si is refractory and hard to evaporate. Preferential evaporation occurs because the iron evaporates more easily, so that during the time when the specimen is not being pulsed (*i.e.* is at the set d.c. voltage) the iron continues to evaporate whereas the Si only evaporates during the pulsing. Therefore, the Si appears to have a larger concentration than expected.

A typical mass spectrum from a cementite particle after 10 mins tempering is illustrated in Figure 8.10. The corresponding concentration for the major alloying elements of interest is approximately 20 at.% C, 3 at.% Cr, 2 at.% Mo and the balance, Fe. The chromium and molybdenum levels are slightly lower than those measured by energy-dispersive X-ray analysis (≈ 5 at.% Cr), possibly because there is expected to be a variation with particle size. However,

the carbon content is clearly less than the 25 at% required by the stoichiometry of cementite, M_3C . It is possible that the probe hole did not completely overlap the cementite particle, but is more likely that the carbon detection efficiency has been reduced by the relatively high analysis temperature used to try to reduce the fracture rate of the samples. Carinci *et al.* (1988) found that a specimen temperature of 80 K reduced the observation of carbon clusters and led to a corresponding reduction in the overall carbon content. Sha *et al* (1992) have recently shown that there is an ambiguity in the assignment of the peaks due to carbon clusters C_2^+ and C_4^{++} and that careful reassignment of these peaks can increase the total amount of carbon in the atom probe analysis by as much as 10%.

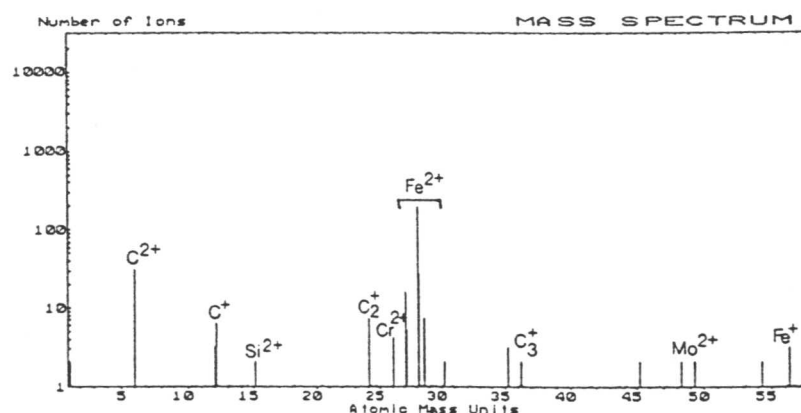


Figure 8.10: A typical mass spectrum from a cementite particle in a specimen tempered for 10 mins.

The composition profiles of carbon, chromium and silicon along a cementite/matrix interface for a specimen tempered for 5 mins are presented in Figure 8.11. The carbon concentration here is only 10 at.%, consistent with the probe hole being half way across the carbide and the matrix. The inclination of the probe hole to the interface was approximately $80^\circ C$. It is important to note that the concentration of chromium in the cementite at the interface is far less than the 54 wt.% expected from local equilibrium. This result therefore verifies the theoretical model in which local equilibrium does not exist in the cementite during the early stages of enrichment. There is also some evidence of an increase in the silicon content of the matrix outside the cementite particle. Silicon is known to partition from cementite.

8.3 Scanning transmission electron microscope studies

It has already been noted that atom probe analyses were difficult because of the size of the carbides relative to the size of the specimen tip. After the precipitation of the larger M_7C_3 carbides atom probe analyses proved nearly impossible. Therefore a scanning transmission

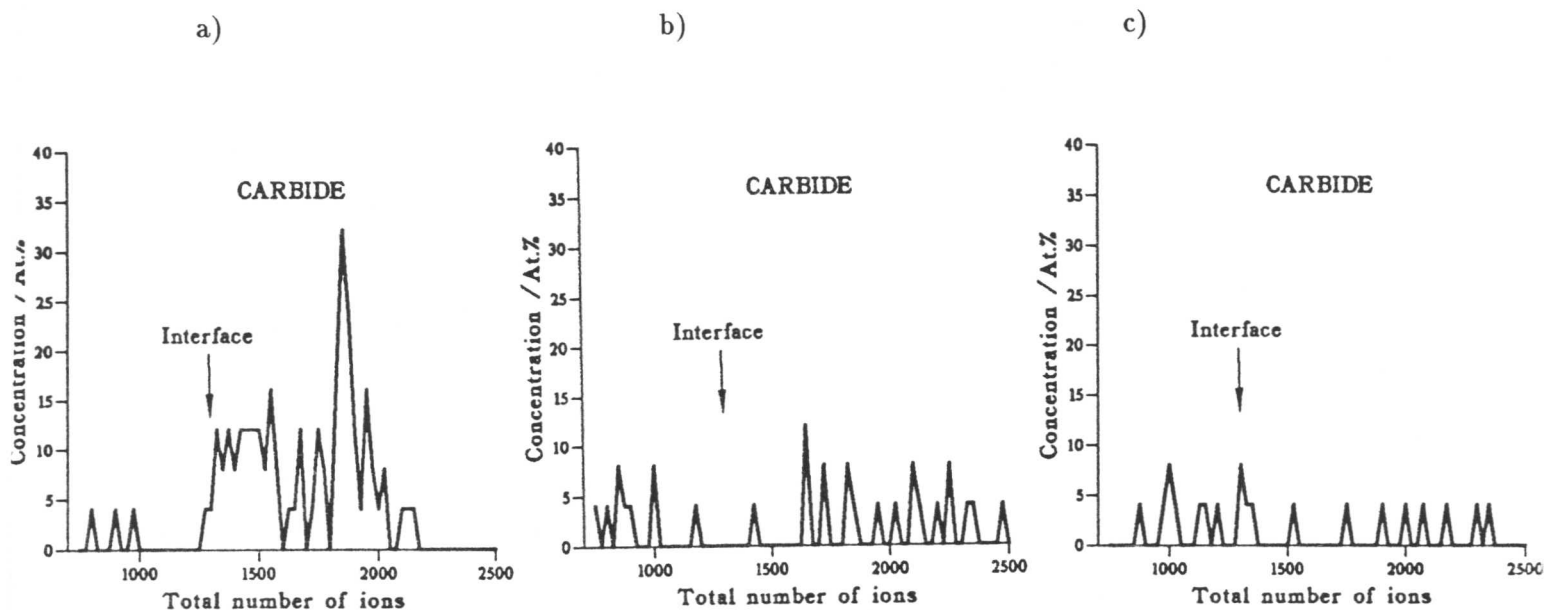


Figure 8.11: Composition profiles for carbon (a), chromium (b) and silicon (c) along a cementite/matrix interface in a specimen tempered for 5 mins.

electron microscope (STEM) was used to look at the composition profile through some of the larger cementite particles. Analyses were performed using a VGHB501 STEM operated at 100 kV on thin foils made from the specimens tempered for 178 hours. A little caution needs to be exercised in the interpretation of these results for two reasons. Firstly, the resolution of the STEM was at its poorest due to a strong astigmatism produced by the ferromagnetic specimen. (Attempts to use carbon extraction replicas proved unsuccessful because the specimen drifted within the time needed to perform accurate microanalysis.) In addition the particle is 3-dimensional; any surface enrichment will be averaged to some extent because the particle is probed by the electron beam in a 2-dimensional section.

8.3.1 Results and discussion

Figure 8.12 shows the chromium concentration profile across a cementite particle and into the matrix measured using energy-dispersive X-ray analysis in a STEM. This particle is contained in a specimen which has been tempered for 178 hours at 565°C. Care has been taken only to include the section of the particle having parallel sides in the analysis in order to remove any interference from the matrix at the ends of the particle. The analysis was performed in a direction exactly normal to the carbide/matrix interfaces. The absolute level of chromium measured in the matrix was lower than that measured on a carbon extraction replica (Chapter 5) due to interference from the predominantly iron-containing matrix. Thus, it is not possible

to determine an absolute level of chromium in the cementite. However, the relative difference between the chromium concentration at the centre and the edge of the particle was found to be approximately 3 wt.%. This result is significant because it would appear to preclude the possibility that the chromium concentration in the cementite at the carbide/matrix interface has reached the predicted equilibrium level, implying local equilibrium has not yet been attained at the interface.

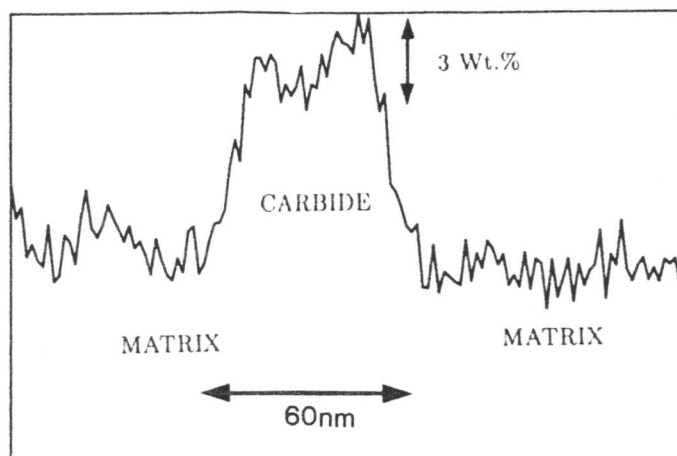


Figure 8.12: The concentration profile of chromium across a carbide and into the surrounding matrix measured using energy-dispersive X-ray analysis in a STEM from a specimen which has been tempered for 178 hours at 565°C.

8.4 Conclusions

The most important result is that, consistent with theoretical predictions the concentration of cementite at the cementite/ferrite interface is found to be far below that expected from equilibrium considerations. This is in samples which are annealed at elevated temperatures in order to permit the initially non-equilibrium cementite to enrich in chromium concentration. The apparent clusters of molybdenum and carbon atoms found in the ferrite matrix of specimens tempered for only 10 mins at 565°C using atom probe analysis, could indicate the early stages of Mo_2C formation, although much further work is needed to establish this quantitatively.

The diffusion coefficient of chromium in cementite needs to be established accurately, although this would be easier in a steel of slightly different composition in which the precipitates were more conducive to atom probe analysis.

STEM analyses have proved difficult for the magnetic specimens and the large interference from the predominantly iron containing matrix means that quantitative analyses are difficult, although used in conjunction with TEM on carbon extraction replicas they can provide useful information.

CHAPTER 9

FURTHER THEORETICAL STUDIES

In this chapter the question of whether simultaneous particle coarsening and enrichment can occur is addressed. It is shown quantitatively that the driving forces for the two processes are of opposite sign, and that the enrichment process appears to defeat coarsening until the bainitic carbides have reached their equilibrium compositions.

CHAPTER 9

FURTHER THEORETICAL STUDIES

9.1 Introduction

Particle coarsening is the dissolution of small precipitates and the simultaneous growth of larger particles at a fixed volume fraction. Ultimately a system will tend towards only one large particle. The driving force for the process is a decrease in the total interfacial energy. Factors which need to be considered in the development of a full theory of particle coarsening include the size and shape of the particles, the relationship between size and solubility, and whether the reaction is diffusion or interface controlled. A distribution of particle sizes within a matrix causes concentration gradients, and therefore, in order for these to be maintained, atoms have to transfer across the interface between the particle and the matrix. If diffusion of atoms within the matrix is the rate-controlling step then the growth is said to be *diffusion controlled*, whereas if it is more difficult for an atom to cross the interface into the matrix, then growth is said to be *interface controlled*.

Theoretical growth rate equations for individual particles for both diffusion and interface controlled reactions have been derived by Greenwood (1956) and (1969), and then these have been incorporated into analyses of the dispersion as a whole by Wagner (1961) and Lifshitz and Slyozov (1961). A brief review of experimental studies of particle coarsening is presented in the next section. The equations governing the coarsening process are then discussed in detail together with the necessary modifications to allow for the coarsening of particles in a solid matrix. The application of the theory to simultaneous particle coarsening and enrichment is then outlined.

9.2 Experimental studies of particle coarsening

Early experiments were performed under the conditions for which the Wagner, Lifshitz and Slyozov theories were developed, i.e. virtually pure particles in a liquid. This work has been reviewed by Greenwood (1969). Recent interest has, however, concentrated on extending the theory to account for precipitates in a solid matrix. In most cases, this has been studied successfully using thin foils and extraction replicas in a transmission electron microscope. The main area of interest in this work is the coarsening of carbide particles in steels, and so the previous work on the Fe-C system only will be reviewed here, although it should be noted that there have been considerable advances in studies on the Ni-Al system by Ardell (1969).

There have been many theories proposed in the literature for the mechanism of cementite coarsening. Hyam and Nutting (1956) measured the carbide particle size distribution during the tempering of four plain carbon steels in the temperature range 500–700°C. They then related the changes in the particle diameters on tempering to hardness measurements, from which they calculated the activation energy for the softening process, following the assumption that particle size and separation are directly responsible for changes in hardness. The value which they obtained led them to conclude that cementite coarsening is controlled by the self-diffusion of iron, rather than the diffusion of carbon. Mukherjee *et al.* (1969) have pointed out that these measurements are unreliable because changes in the matrix structure during tempering are not taken into consideration.

Oriani (1964) then considered that both the diffusion of carbon and the diffusion of iron should be taken into account. His argument was that the growth of a cementite precipitate requires a change in volume according to the equation



which must be accommodated at both the growing and dissolving precipitates which necessitates coupled diffusion of iron and carbon. There was limited agreement of this theory with the experimental data due to approximations having to be made for the values of various constants.

Oriani's theory of coupled diffusion was then challenged by Björkland *et al.* (1972) who studied the effect of alloying elements on the rate of Ostwald ripening of cementite. They used a sophisticated treatment of the thermodynamics of the problem, but a rather basic treatment of the diffusion. They suggested that the diffusion coefficient may be reduced by elements dissolved in the cementite which diffuse very slowly and are therefore rate-controlling. They predicted that a Mn content of 0.001 wt.% in an Fe–C alloy would decrease the growth rate by a factor of 10. This idea is supported by Mukherjee *et al.* (1969), who studied the effect of chromium on carbide coarsening. They found that increasing the chromium content retarded the growth of cementite particles, and that the coarsening rate of the various chromium-based alloy carbides decreased in the order Fe_3C , M_3C , M_{23}C_6 , M_7C_3 . It is interesting to note that they found that M_3C and M_7C_3 coarsened at a rate consistent with the diffusion of chromium being rate-controlling, whereas the coarsening of Fe_3C is too rapid for the equivalent diffusion of iron to be rate-controlling.

An alternative interface controlled coarsening mechanism was proposed by Heckel and De Gregorio (1965). They studied a spheroidised eutectoid steel containing 0.75 wt.% C, and with other elements, such as Si and Ni, being present at levels of less than 0.005 wt.%. They

concluded that interface controlled kinetics were applicable having obtained coarsening rates two or three times lower than those predicted by carbon diffusion being rate-controlling. One possible explanation, however, is that even the small amounts of impurities present are retarding the coarsening. Heckel and De Gregorio proposed that the coarsening rate is limited by the rate of formation of cementite at the growing interfaces where the interfacial reaction is proportional to the solute thermodynamic activity gradient across the interface.

Another important factor considered by Mukherjee *et al.* (1969) is the influence of the matrix structure on coarsening rates. They found that the fine grain size and dislocation substructure in a martensitic microstructure caused a significant increase in the coarsening rate. They also noted that irregularities in particle size distribution curves could be resolved by the superposition of two different distributions, one from particles within the matrix and one from particles situated on the grain boundaries, caused by a transfer of material from the matrix to grain boundaries during tempering.

9.3 Particle size and solubility

The starting point for a theory of coarsening must be to relate the size of a particle to its solubility. The simplest relationship is the Gibbs–Thomson or Thomson–Freundlich equation for spherical particles of radius r , with an interfacial energy per unit area γ . The complete theory is given in Christian (1975) from which the following synopsis is taken.

Consider an assembly in which θ (cementite) particles of surface area O and surface free energy per unit area γ are in equilibrium with the α (ferrite) matrix. It can be shown that the energy of the interfaces displaces the equilibrium condition, and may be considered to contribute an additional thermodynamic potential, resulting in the fact that the solubility limit, $c^{\alpha\theta}$, and the equilibrium composition, $c^{\theta\alpha}$, of the cementite may both vary with the radius of the particle. The quantities relating to interface curvature are denoted by c_r^α and c_r^θ , where r is the particle radius, and those referring to the equilibrium compositions for infinite planar interfaces by c_∞^α and c_∞^θ . (N.B. Concentrations are used here rather than atomic fractions which are valid only when there is a negligible volume change on transformation. However, this assumption is implicit here because no strain energy terms due to the transformation are included in the treatment.)

The effect can be illustrated as follows. If a virtual change is considered in which dn atoms are transferred from the α phase to the θ phase, there will be an increase in the surface area of the θ particles, and therefore a corresponding increase in energy of γdO . This may be

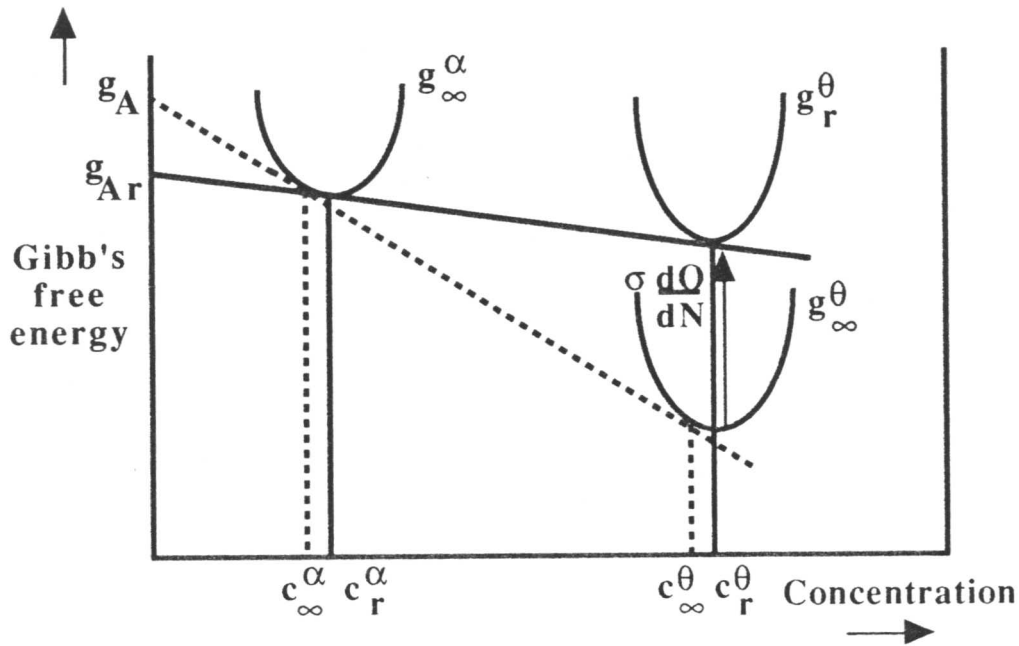


Figure 9.1: Free energy curves versus composition to illustrate the Gibbs–Thomson effect, (based on Christian, 1975).

represented as a displacement of the free energy per atom from g^θ to g_r^θ where

$$g_r^\theta = g^\theta + \gamma \frac{dO}{dn} . \quad (9.1)$$

The new equilibrium compositions are given by the common tangent construction to the free energy curves, as illustrated in Figure 9.1.

The effective chemical potentials per atom for curved interfaces are denoted by g_{Ar}^θ and g_{Br}^θ , and the new equilibrium conditions are $g_{Ar}^\theta = g_{Ar}^\alpha$ and $g_{Br}^\theta = g_{Br}^\alpha$. From the geometry of the diagram, it can be seen that

$$\Delta c_r^\alpha = c_r^\alpha - c_\infty^\alpha \quad (9.2)$$

which is of the same order of magnitude as

$$\Delta c_r^\theta = c_r^\theta - c_\infty^\theta , \quad (9.3)$$

and also that the approximation,

$$g_{Br}^\alpha - g_{B\infty}^\alpha = \frac{1 - c_\infty^\alpha}{c_\infty^\theta - c_\infty^\alpha} \gamma \frac{dO}{dn} , \quad (9.4)$$

can be made. The chemical potentials per atom of an ideal solution can be expressed as

$$g_A - g_A^0 = kT \ln(1 - x) \text{ and} \quad (9.5)$$

$$g_B - g_B^0 = kT \ln x , \quad (9.6)$$

where g^0 refers to the chemical potential of the pure substance. The absolute activity, λ , is defined in terms of the chemical potential as

$$g_A = kT \ln \lambda_A . \quad (9.7)$$

Equations 9.5 and 9.6 can then be written in terms of absolute activities as

$$\frac{\lambda_A}{\lambda_A^0} = \ln(1-x) \text{ and} \quad (9.8)$$

$$\frac{\lambda_B}{\lambda_B^0} = \ln x , \quad (9.9)$$

where λ^0 refers again to the pure substance. Equations 9.8 and 9.9 can then be modified to take into account non-ideal solutions by multiplying their right hand sides by the appropriate experimentally measured activity coefficients, such that

$$\frac{\lambda_A}{\lambda_A^0} = \Gamma_A \ln(1-x) \text{ and} \quad (9.10)$$

$$\frac{\lambda_B}{\lambda_B^0} = \Gamma_B \ln x . \quad (9.11)$$

Therefore, by substitution of the activity coefficients, Γ_{Br}^α and $\Gamma_{B\infty}^\alpha$, it can be shown that

$$g_{Br}^\alpha - g_{B\infty}^\alpha = kT \ln \left(\frac{\Gamma_{Br}^\alpha c_r^\alpha}{\Gamma_{B\infty}^\alpha c_\infty^\alpha} \right), \quad (9.12)$$

and then, using the dilute solution approximation that $\Gamma_B^\alpha = \text{constant}$ and equating equations 9.4 and 9.12 gives

$$\frac{\Delta c_r^\alpha}{c_\infty^\alpha} \simeq \ln \left(\frac{c_r^\alpha}{c_\infty^\alpha} \right) = \frac{\gamma}{kT} \left(\frac{dO}{dn} \right) \left(\frac{1 - c_\infty^\alpha}{c_\infty^\alpha - c_\infty^\alpha} \right) . \quad (9.13)$$

Using the approximation that the particles are spherical, for which

$$O = 4\pi r^2 \quad \text{and} \quad n = \frac{4\pi r^3}{3V_m}, \quad (9.14)$$

where V_m is the molar volume and n is the number of atoms per mole, and then using the properties of partial derivatives,

$$\frac{\partial O}{\partial n} = \frac{\partial O}{\partial r} \cdot \frac{\partial r}{\partial n} = \frac{2V_m}{r} , \quad (9.15)$$

equation 9.13 is simplified to the form usually used as the basis of coarsening theory,

$$\ln \left(\frac{c_r^\alpha}{c_\infty^\alpha} \right) = \frac{2\gamma V_m}{kTr} \left(\frac{1 - c_\infty^\alpha}{c_\infty^\alpha - c_\infty^\alpha} \right) , \quad (9.16)$$

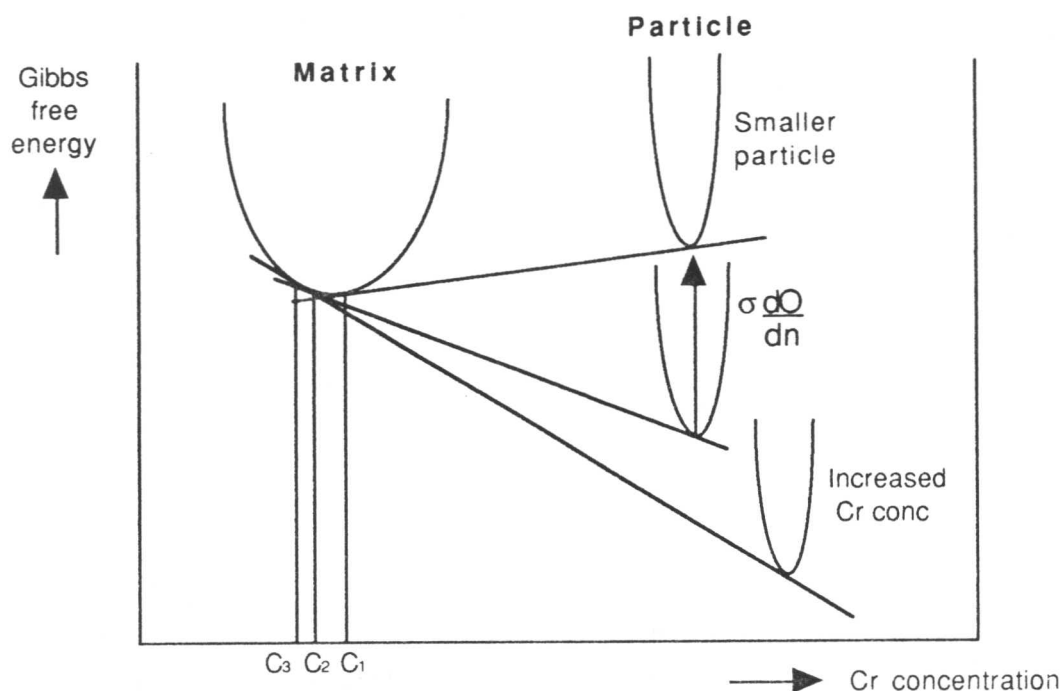


Figure 9.2: Schematic illustration of the increase in free energy due to particle curvature and the decrease in free energy due to increased thermodynamic stability.

equilibrium level, and that there is a constant volume fraction of precipitate. Oriani (1964) also points out that Wagner (1961) assumes that the atoms in the matrix offer no resistance to the motion of an interface, i.e. that the matrix atoms move at a much greater rate than the diffusion of the solute, and can therefore be neglected.

9.5 Application to simultaneous coarsening and enrichment of cementite

In order to address the question of whether or not particle coarsening (in the strictest sense) can occur whilst the process of enrichment is occurring the driving forces for the two reactions need to be investigated. It has been shown in the previous section that the driving force for coarsening originates from an increase in free energy due to particle curvature of a smaller particle. However, diffusion of chromium, for example, to cementite particles is driven by a reduction in free energy as thermodynamic equilibrium is approached. The driving forces for enrichment and coarsening will therefore tend to oppose each other. It has also been shown that smaller particles will enrich more quickly than larger particles and therefore the reduction in free energy due to an increased chromium content will be most marked for the smaller particles, thus cancelling out, to a certain extent, any increase in free energy due to an increased radius of curvature. This is illustrated schematically in Figure 9.2. These two opposing processes are quantified in the following sections.

9.5.1 Increase in free energy due to particle curvature

The increase in concentration of solute in the matrix surrounding a small particle has been discussed in section 9.3. An alternative approach is to consider the increase in free energy due to interface curvature. The expression for the increase in free energy due to interface curvature is given by the expression

$$\gamma \frac{\partial O}{\partial n} = \frac{2V_m \gamma}{r} . \quad (9.20)$$

For cementite, a value of γ given by Puls and Kirkaldy (1972) is 0.6 Jm^{-2} . The molar volume can be estimated from the unit cell dimensions and the number of atoms contain in one unit cell: cementite is orthorhombic with lattice parameters $a=4.523\text{\AA}$, $b=5.089\text{\AA}$ and $c=6.743\text{\AA}$, and there are 12 atoms contained in one unit cell. V_m is therefore given by

$$V_m = \frac{(4.523 \times 5.089 \times 6.743 \times 10^{-30})}{12} \times N_A , \quad (9.21)$$

where N_A is Avagadro's number. The increases in free energy for particle sizes of 10, 100 and 10000 nm are presented in Table 9.1. As expected the largest increase corresponds to the smallest particle size.

Table 9.1: Increase in free energy as a function of particle size.

Particle size /nm	Inc. in free energy /J mol ⁻¹
10	934
100	93.4
10000	0.934

9.5.2 Decrease in free energy due to increased thermodynamic stability

In order to quantify the decrease in free energy due to an increase in thermodynamic stability because of an increase in chromium content of the cementite, an expression for the free energy of cementite is required. Lundberg *et al.* (1977) state that the molar Gibbs free energy os cementite is given by

$$G_m = y_{Fe} G_{FeC_{\frac{1}{3}}}^o + y_{Cr} G_{CrC_{\frac{1}{3}}}^o + RT(y_{Fe} \ln y_{Fe} + y_{Cr} \ln y_{Cr}) + y_{Fe} y_{Cr} A_o , \quad (9.22)$$

where y_{Fe} and y_{Cr} are concentration parameters related to the ordinary mole fractions, x , by

$$y_{Cr} = 1 - y_{Fe} = \frac{x_{Cr}}{1 - x_C} . \quad (9.23)$$

Other data are $G_{FeC_{\frac{1}{3}}}^{\circ} = 74,113 \text{ J mol}^{-1}$, $G_{CrC_{\frac{1}{3}}}^{\circ} = -13,578 \text{ J mol}^{-1}$ and $A_o = 1,790 \text{ J mol}^{-1}$. Cementite is virtually stoichiometric with respect to carbon content and therefore it contains 0.0067 mole fraction carbon. Evaluating this expression for particles containing various proportions of chromium and iron indicates that addition of 1 at.% Cr lowers the free energy of the cementite by approximately 1 kJ mol^{-1} .

These results are summarised in Figure 9.3. It has been shown in previous chapters that chromium concentration varies linearly with reciprocal particle size. Calculations were performed using the finite difference model to determine the chromium concentration as a function of tempering time for typical sizes and concentrations of the cementite particles found in the $2\frac{1}{4}\text{Cr1Mo}$ steel. The predicted value of chromium concentration was then converted into a value of Gibbs free energy (using equation 9.22). An additional contribution to the free energy due to the capillarity effect was then added to give the total free energy. It can be seen from the plots of total free energy as a function of reciprocal size in Figure 9.3, for three different tempering times, that smaller particles become increasingly more stable than the larger ones. The contribution to the free energy from the capillarity term is also plotted for comparison. It is clear that capillarity is a very small effect compared with the fact that the larger particles enrich more slowly than the smaller ones.

9.6 Conclusions

The above results suggest that coarsening is defeated by the fact that in a distribution of particle sizes, the smaller particles will be richer in chromium and will not be able to give up chromium to the larger particles, as is the case in a true coarsening reaction, due to the opposite driving forces for the two reactions. Coarsening, in the true sense, will not therefore become important until the very late stages of ageing.

This argument explains why coarsening is not observed for the bainitic cementite discussed in Chapter 5. It has already been shown in Chapter 6 that pearlitic cementite particles are much larger than bainitic cementite and therefore the sensitivity to particle size effects is much reduced. However, for pearlitic cementite the lamellae are observed to spheroidise during the enrichment process (Figure 6.1). This can be thought of as a shape change from the initially coarse plate-shaped lamellae, rather than coarsening itself. In the absence of enrichment with respect to substitutional alloying elements, the spheroidisation rate would presumably be much faster.

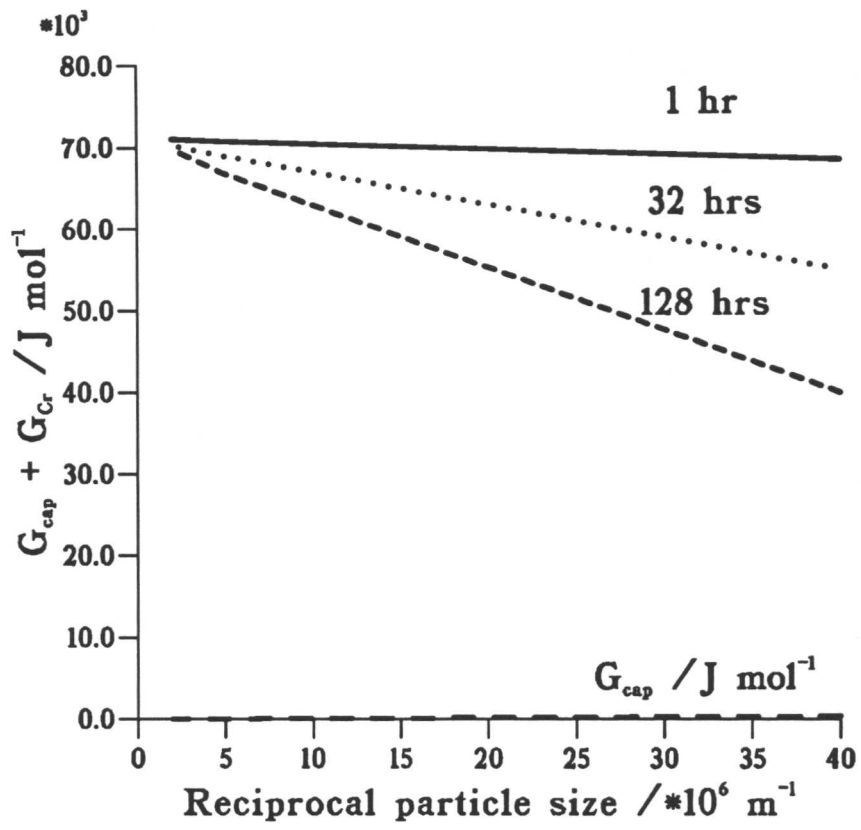


Figure 9.3: Total Gibbs free energy as a function of particle size after different enrichment times for cementite particles in $2\frac{1}{4}\text{Cr1Mo}$ steel.

CHAPTER 10

CONCLUSIONS AND SUGGESTIONS FOR FUTURE WORK

CHAPTER 10

CONCLUSIONS AND SUGGESTIONS FOR FUTURE WORK

It is now possible to interpret fundamentally carbide enrichment kinetics of the kind associated with remanent life prediction in power plant steels. Thus it is, in principle, possible to extrapolate carbide chemistries with confidence over the sort of time scales typical of elevated temperature applications. Specifically, the precipitation characteristics of three power plant steels containing different chromium concentrations, $\frac{1}{2}\text{Cr}\frac{1}{2}\text{Mo}\frac{1}{4}\text{V}$, $2\frac{1}{4}\text{Cr1Mo}$ and 12Cr1MoV , have been studied in detail.

$\frac{1}{2}\text{Cr}\frac{1}{2}\text{Mo}\frac{1}{4}\text{V}$ steel, being pearlitic, was found to contain relatively large cementite particles. As a consequence of this, the substitutional alloy content of the cementite is not particularly sensitive to particle size. The low chromium content in the steel means that the equilibrium concentration of chromium in the cementite is low. This results in a much smaller degree of enrichment during ageing, thereby reducing the sensitivity to the particle size. The agreement between the theoretical model and the experimentally measured enrichment data is found to be very good. For this steel, measurement of cementite composition change can prove a valuable indicator of the average thermal history, and therefore of the remanent creep life.

Power plant components are very large, and therefore the microstructure can vary considerably through the section of a given component. Studies of the precipitation characteristics in the $2\frac{1}{4}\text{Cr1Mo}$ steel have highlighted the importance of cementite composition being related to the position in the microstructure. Significantly different enrichment rates have been observed in fully bainitic and mixed ferritic/bainitic microstructures. The much larger equilibrium concentration of chromium in cementite and the smaller size of bainitic carbides in this steel result in the measured chromium concentration being very sensitive to particle size, the smaller particles enriching more quickly than the larger ones. It has also been shown that when alloy carbides co-exist in the microstructure with cementite, the cementite composition no longer changes in a simple manner. The precipitation of chromium-rich alloy carbides can substantially reduce the chromium level in the cementite.

The kinetics of precipitation have been found to be extremely rapid in the 12Cr1MoV steel. The equilibrium alloy carbide precipitates during the stress-relief heat treatment and subsequently does not change in composition. It is perhaps not surprising that changes in alloy carbide chemistries, induced by tempering, are found to be less striking than those observed for cementite. The growth of alloy carbides involves considerable long range diffusion and there is therefore greater opportunity for the carbide to be closer to equilibrium when it first forms.

The derivation of this approximation is given below. The Taylor expansions on the $(j + 1)^{th}$ time row are:-

$$c_{i+1,j+1} = c_{i,j+1} + \delta r \left(\frac{\partial c}{\partial r} \right)_{i,j+1} + \frac{1}{2}(\delta r)^2 \left(\frac{\partial^2 c}{\partial r^2} \right)_{i,j+1} + \dots \quad (I.7)$$

$$c_{i-1,j+1} = c_{i,j+1} - \delta r \left(\frac{\partial c}{\partial r} \right)_{i,j+1} + \frac{1}{2}(\delta r)^2 \left(\frac{\partial^2 c}{\partial r^2} \right)_{i,j+1} + \dots \quad (I.8)$$

Subtraction and addition of these two equations lead respectively to the following equations:-

$$\left(\frac{\partial c}{\partial r} \right)_{i,j+1} = \frac{c_{i+1,j+1} - c_{i-1,j+1}}{2\delta r} \quad (I.9)$$

$$\left(\frac{\partial^2 c}{\partial r^2} \right)_{i,j+1} = \frac{c_{i+1,j+1} - 2c_{i,j+1} + c_{i-1,j+1}}{\delta r^2} \quad (I.10)$$

Then, using the approximation that

$$\left(\frac{\partial c}{\partial r} \right) = \frac{1}{2} \left[\left(\frac{\partial c}{\partial r} \right)_{i,j+1} + \left(\frac{\partial c}{\partial r} \right)_{i,j} \right], \quad (I.11)$$

$$\left(\frac{\partial^2 c}{\partial r^2} \right) = \frac{1}{2} \left[\left(\frac{\partial^2 c}{\partial r^2} \right)_{i,j+1} + \left(\frac{\partial^2 c}{\partial r^2} \right)_{i,j} \right], \quad (I.12)$$

the following expressions can be obtained:-

$$\left(\frac{\partial c}{\partial r} \right) = \frac{1}{2} \left[\frac{c_{i+1,j+1} - c_{i-1,j+1}}{2(\delta r)} + \frac{c_{i+1,j} - c_{i-1,j}}{2(\delta r)} \right], \text{ and} \quad (I.13)$$

$$\left(\frac{\partial^2 c}{\partial r^2} \right) = \frac{1}{2} \left[\frac{c_{i+1,j+1} - 2c_{i,j+1} + c_{i-1,j+1}}{(\delta r)^2} + \frac{c_{i+1,j} - 2c_{i,j} + c_{i-1,j}}{(\delta r)^2} \right]. \quad (I.14)$$

This is termed the *implicit* finite difference method because unknowns on the time level $(j + 1)$ are expressed in terms of known values on the time level j . Therefore, N grid points result in N simultaneous equations to solve in order to obtain the unknown values. More computation is required at each step than with the explicit finite difference method, but this calculation remains stable for all values of δt , whereas the explicit method is only stable for $\delta t \leq 0.5\delta r^2$ and therefore it is possible to use larger and therefore fewer time steps.

APPENDIX II

FINITE.FOR

```
C Program using finite difference method for the solution of the problem
C of X enrichment of cementite during the ageing of bainitic steels
C
C EQFER = Equilibrium at.% of X in ferrite at ageing temperature
C EQCEM = Equilibrium at.% of X in cementite at ageing temperature
C EBAR = Average X at.% in alloy
C FERS = normalised concentration of X at ferrite surface
C CEMS = normalised concentration of X at cementite surface
C TIMH = time in hours
C KTEMP = Absolute temperature
C TCEM = Thickness of cementite in meters
C TFER = Half-thickness of ferrite in meters
C N.B. This is calculated from the volume fraction of chromium
C in the alloy in the program
C
C DFER = Diffusivity of X in ferrite
C DCEM = Diffusivity of X in cementite
C Q = Activation free energy for diffusion
C FREQ = Pre-exponential factor for diffusion
C The mean size of a cementite particle is usually taken to be 100nm
C (This is based on experimental experience)
C
C Concentrations normalized relative to average alloy concentration
C Dimension normalize relative to carbide particle thickness
C ICEM, IFER, J1 are the number of finite slices
C for dimension and time respectively
C (N.B. ICEM is read into this program but IFER is calculated: both
C values must be transferred to FINN via the dataset)
C TIM = Time, in seconds
C A3 controls the amount of information that is printed out
C SETIME controls the time in hours that the experiment runs.
C JTEST modifies the mass balance condition when the CEMS reaches
C the equilibrium concentration. Hence mass is conserved.
C
C Typical data
C 838.15 0.5D-03 39.0D+00 2.5D+00 1.0D-07 0.1 5
C 0.0003D+00 2.0D+00 1.0 1.0
C 2.53D-04 240580.0 (DIFFUSION DATA, JOULES ETC.)
C End of data
C
      IMPLICIT REAL*8(A-H,K-Z), INTEGER(I,J)
      DOUBLE PRECISION CFER(1500,2), CCEM(20,2)
      J4 = 0
      J5 = 0
      JTEST = 0
      READ(5,*) KTEMP,EQFER,EQCEM,EBAR,TCEM,VOLUME,ICEM
```

```

READ(5,*) CFER(1,1),CCEM(1,1),A3,SETIME
READ(5,*) FREQ,Q
RFER = 0.40D+00
RCEM = RFER
TFER = (TCEM*(1.0D+00-VOLUME))/(2*VOLUME)
DFER = DIFF(KTEMP,Q,FREQ)
DCEM = DIFF(KTEMP,Q,FREQ)
STCEM = 0.5D+00*TCEM/ICEM
IFER = DINT(TFER/STCEM)
STFER = TFER/IFER
TIME = RFER*STFER*STFER/DFER
J1 = DINT(3600*SETIME/TIME)
WRITE(6,100) DFER,DCEM,VOLUME,TFER,TCEM,EQFER,EQCEM,KTEMP,ICEM
+ ,IFER,STCEM,STFER
DO 1 I = 2,ICEM
    CCEM(I,1) = 1.0D+00
1 CONTINUE
DO 2 I = 2,IFER
    CFER(I,1) = 1.0D+00
2 CONTINUE
C
    FERS = EQFER/EBAR
    DR = DFER/DCEM
    WRITE(6,101) CCEM(1,1),CFER(1,1)
C
C Finite difference analysis
C
    TIM = 0.0D+00
    WRITE(6,102)
    DO 50 J = 2,J1
        TIM = TIM+TIME
        TIMH = TIM/3600.0D+00
        IF (TIMH .GT. SETIME) GOTO 51
        CEMM = 0.0D+00
        FERR = 0.0D+00
C
C          ***** Ferrite *****
C
        DO 10 II = 1,IFER
            IF (II .EQ. 1) THEN
C Note: surface concentration in ferrite is at equilibrium
C until CEMS reaches the equilibrium concentration
                IF (JTEST .EQ. 0) THEN
                    CFER(1,2) = CFER(1,1) + RFER*(FERS - 2.0D+00*CFER(1,1)
+                     + CFER(2,1))
                ELSE
                    FERS = ((CCEM(1,1)-CEMS)/DR) + CFER(1,1)
                ENDIF
            ELSEIF (II .EQ. IFER) THEN
                CFER(IFER,2) = CFER(IFER,1)+RFER*(CFER(IFER-1,1)

```

```

+           -2.0D+00*CFER(IFER,1)+CFER(IFER-1,1))
           CALL SOFT(CFER(IFER,2),1,J4,TIMH)
ELSE
           CFER(II,2) = CFER(II,1)+RFER*(CFER(II-1,1)
+           -2.0D+00*CFER(II,1)+CFER(II+1,1))
           ENDIF
           FER = CFER(II,2)*EBAR
           XTFER = STFER*I
           FERR = FER+FERR
           CFER(II,1) = CFER(II,2)
10          CONTINUE
C
C          ***** Cementite *****
C
           DO 20 I = 1,ICEM
C Calculate surface concentration in cementite
C appropriate for mass balance
           IF (I.EQ. 1) THEN
               CEMS = DR*(CFER(1,1)-FERS)+CCEM(1,1)
C Reflect at position of symmetry
               IF (CEMS.GT. (EQCEM/EBAR)) THEN
                   CEMS = EQCEM/EBAR
                   JTEST = 1
               ELSE
                   CCEM(1,2) = CCEM(1,1) + RCEM*(CEMS-2.0D+00*CCEM(1,1)
+                   + CCEM(2,1))
               ENDIF
           ELSEIF (I.EQ. ICEM) THEN
               CCEM(ICEM,2) = CCEM(ICEM,1)+RCEM*(CCEM(ICEM-1,1)
+               -2.0D+00*CCEM(ICEM,1)+CCEM(ICEM-1,1))
               CALL SOFT (CCEM(ICEM,2),2,J5,TIMH)
           ELSE
               CCEM(I,2) = CCEM(I,1)+RCEM*(CCEM(I-1,1)
+               -2.0D+00*CCEM(I,1)+CCEM(I+1,1))
           ENDIF
           CEM = CCEM(I,2)*EBAR
           XTCEM = I*STCEM
           CEMM = CEM+CEMM
           CCEM(I,1)=CCEM(I,2)
20          CONTINUE
C
           CEMM = CEMM/ICEM
           FERR = FERR/IFER
           DUMMY = J/A3
           DUMMY = DINT(DUMMY)-DUMMY
           IF (DUMMY.EQ. 0.0) THEN
               AVER = (FERR*TFER + CEMM*0.5D+00*TCEM)/(TFER+0.5D+00*TC
               WRITE(6,103) TIMH,CEMM,FERR,AVER,FERS*EBAR,CEMS*EBAR
           ENDIF
50          CONTINUE
51          WRITE(6,104)

```

```

DO 60 I = 1,ICEM
  IF (CCEM(I,2) .LT. 1.0001) GOTO 61
    WRITE(6,105) I,CCEM(I,2),CCEM(I,2)*EBAR
60  CONTINUE
61  WRITE(6,106)
    DO 70 J = 1,IFER
      IF (CFER(J,2) .GT. 0.999) GOTO 71
        WRITE(6,105) J,CFER(J,2),CFER(J,2)*EBAR
70  CONTINUE
71  CONTINUE
C
100  FORMAT(' Diffusion coefficient in ferrite, m**2/s = ',
+     D12.4/' Diffusion coefficient in cementite, m**2/s, = ',D12.4/
+     ' Volume fraction of cementite (MTDATA) = ',D12.4/
+     ' Half thickness of ferrite, m =',D12.4/
+     ' Thickness of cementite, m =',D12.4/
+     ' Eq. conc. of X at interface, in ferrite, at.% = ',D12.4/
+     ' Eq. conc. of X at interface, in cementite, at.% = ',D12.4/
+     ' Absolute Temperature = ', F8.2, ' ICEM, IFER = ',2I9/
+     ' STCEM (m) = ',D12.4, ' STFER (m) = ',D12.4//)
101  FORMAT(' Time 0, slice 1, cementite and ferrite norm conc ',
+     2F12.4/)
102  FORMAT(' HOURS CEM FERRITE AVERAGE X FERS CEMS')
103  FORMAT(D10.2,F9.4, F9.4,F9.4,F9.4,2F9.4)
104  FORMAT(' No Norm. Conc. at.%X in Cementite')
105  FORMAT(I8,D12.4,2F10.4)
106  FORMAT(' No Norm. Conc. at.%X in Ferrite')
    STOP
    END

```

```

.....
DOUBLE PRECISION FUNCTION DIFF(KTEMP,Q,FREQ)
DOUBLE PRECISION KTEMP, R, Q, FREQ
R = 8.3143
DIFF = FREQ*DEXP(-Q/(R*KTEMP))
C R = Universal Gas Constant, J/mol/K
C KTEMP = Absolute Temperature
C Data for X inter diffusion in alpha iron, from Fridberg (1969) paper
RETURN
END

```

```

.....
SUBROUTINE SOFT (A,I,J,TIMH)
DOUBLE PRECISION A,TIMH
IF (J .GT. 1) RETURN
IF (I .NE. 1) THEN
  IF (A .GT. 1.01D+00) THEN
    WRITE(6,11) TIMH
    J = 3
  ENDIF
ELSEIF (A .LT. 0.99) THEN
  WRITE(6,10) TIMH
  J = 3

```

```
ELSE
  RETURN
ENDIF
RETURN
10  FORMAT(' SOFT IMPINGEMENT IN FERRITE', F11.5,' hours')
11  FORMAT(' SOFT IMPINGEMENT IN CEMENTITE',F11.5,' hours')
END
```

APPENDIX III

INHOMOG.FOR

```
C Program using finite difference method for the solution of the problem
C of X enrichment of cementite during the ageing of bainitic steels
C for an inhomogeneous carbon distribution.
C
C TIMH time in hours
C KTEMP=Absolute temperature
C TCEM=Thickness of cementite in meters
C EQFER=Equilibrium wt.% of X in ferrite at ageing temperature
C EQCEM=Equilibrium wt.% of X in cementite at ageing temperature
C EBAR=Average X wt.% in alloy
C DFER=Diffusivity of X in ferrite
C DCEM=Diffusivity of X in cementite
C Q = ACTIVATION FREE ENERGY FOR DIFFUSION
C FREQ = PRE-EXPONENTIAL FACTOR FOR DIFFUSION COEFFICIENT
C Concentrations normalized relative to average alloy concentration
C Dimension normalize relative to carbide particle thickness
C TIM = Time, in seconds
C A3 controls the amount of information that is printed out
C SETIME controls the time in hours that the experiment runs.
C JTEST modifies the mass balance condition when the CEMS reaches
C the equilibrium concentration. Hence mass conserved
C RATIO is the ratio of TFERA to TFERB (the relative sizes of the
C inhomogeneous ferrite distribution)
C
C
      IMPLICIT DOUBLE PRECISION(A-H,K-Z)
      INTEGER I,J
      DOUBLE PRECISION CFERA(1500,2), CFERB(1500,2), CCEM(1500,2)
      READ(5,*) KTEMP,EQFER,EQCEM,EBAR,TCEM,VOLFRAC,ICEM,RATIO
      READ(5,*) A3,SETIME,FREQ,Q
      J4=0
      J5=0
      J6=0
      JTESTA=0
      JTESTB=0
C Set up the initial conditions
      TFERB=(TCEM*(1-VOLFRAC))/(VOLFRAC*(1+RATIO))
      TFERA=TFERB*RATIO
      DFER=DIFF(KTEMP,Q,FREQ)
      DCEM=DIFF(KTEMP,Q,FREQ)
      RFER=0.4D+00
      RCEM=RFER
      DR=DFER/DCEM
      STCEM=TCEM/(ICEM+1)
      IFERA=DINT(TFERA/STCEM)
      IFERB=DINT(TFERB/STCEM)
```

```

STFERA=TFERA/IFERA
STFERB=TFERB/IFERB
C Set up time loop
TIME=(RFER*STFERA*STFERA)/DFER
J1=DINT(3600D+00*SETIME/TIME)
C Write out the initial program parameters
WRITE(6,100) DFER,DCEM,VOLFRAC,TFERA,TFERB,TCEM,EQFER,EQCEM,
+ KTEMP,ICEM,IFERA,IFERB,STCEM,STFERA,STFERB
C Set up the initial conditions everywhere
DO 10 I=1,IFERA
    CFERA(I,1)=1.0D+00
10 CONTINUE
DO 20 I=1,ICEM
    CCEM(I,1)=1.0D+00
20 CONTINUE
DO 30 I=1,IFERB
    CFERB(I,1)=1.0D+00
30 CONTINUE
IMID=INT(ICEM-1)/2
FERSA=EQFER/EBAR
FERSB=EQFER/EBAR
TIM=0.0D+00
DO 40 J=2,J1
    TIM=TIM+TIME
    TIMH=TIM/3600D+00
C For the calculation of the average composition in the phases
CEMM=0.0D+00
FERRA=0.0D+00
FERRB=0.0D+00
C
C *****FerriteA*****
C
DO 50 II=1,IFERA
    IF (II .EQ. 1) THEN
        IF (JTESTA .EQ. 0) THEN
            CFERA(1,2)=CFERA(1,1)+RFER*
+            (FERSA-2.0D+00*CFERA(1,1)+CFERA(2,1))
        ELSE
            FERSA=((CCEM(1,1)-CEMSA)/DR)+CFERA(1,1)
        ENDIF
    ELSEIF (II .EQ. IFERA) THEN
        CFERA(IFERA,2)=CFERA(IFERA,1)+RFER*(CFERA(IFERA-1,1)
+        -2.0D+00*CFERA(IFERA,1)+CFERA(IFERA-1,1))
        CALL SOFT(CFERA(IFERA,2),1,J4,TIMH)
    ELSE
        CFERA(IFERA,2)=CFERA(IFERA,1)+RFER*(CFERA(IFERA-1,1)
+        -2.0D+00*CFERA(IFERA,1)+CFERA(IFERA-1,1))
    ENDIF
    FERA=CFERA(IFERA,2)*EBAR
    XTFERA=STFERA*II
    FERRA=FERA+FERRA

```

```

          CFERA(II,1)=CFERA(II,2)
50      CONTINUE
C
C *****FerriteB*****
C
      DO 60 II=1,IFERB
        IF (II .EQ. 1) THEN
          IF (JTESTB .EQ. 0) THEN
            CFERB(1,2)=CFERB(1,1)+RFER*(FERSB-2.0D+00*CFERB(1,1)
+           +CFERB(2,1))
          ELSE
            FERSB=((CCEM(1,1)-CEMSB)/DR)+CFERB(1,1)
          ENDIF
        ELSEIF (II .EQ. IFERB) THEN
            CFERB(IFERB,2)=CFERB(IFERB,1)+RFER*(CFERB(IFERB-1,1)
+           -2.0D+00*CFERB(IFERB,1)+CFERB(IFERB-1,1))
            CALL SOFT(CFERB(IFERB,2),2,J5,TIMH)
        ELSE
            CFERB(II,2)=CFERB(II,1)+RFER*(CFERB(II-1,1)
+           -2.0D+00*CFERB(II,1)+CFERB(II+1,1))
        ENDIF
        FERB=CFERB(II,2)*EBAR
        XTFERB=STFERB*II
        FERRB=FERB+FERRB
        CFERB(II,1)=CFERB(II,2)
60      CONTINUE
C
C *****Cementite*****
C
      DO 70 I=1,ICEM
C Calculate the surface concentration in cementite on border
C with ferrite A appropriate for mass balance
        IF (I .EQ. 1) THEN
          CEMSA=DR*(CFERA(1,1)-FERSA)+CCEM(1,1)
          IF (CEMSA .GT. (EQCEM/EBAR)) THEN
            CEMSA=EQCEM/EBAR
            JTESTA=1
          ELSE
            CCEM(1,2)=CCEM(1,1)+RCEM*(CEMSA-2.0D+00*CCEM(1,1)
+           +CCEM(2,1))
          ENDIF
        ELSEIF (I .EQ. ICEM) THEN
C Calculate the surface concentration in cementite on border
C with ferrite B appropriate for mass balance
          CEMSB=DR*(CFERB(1,1)-FERSB)+CCEM(ICEM,1)
          IF (CEMSB .GT. (EQCEM/EBAR)) THEN
            CEMSB=EQCEM/EBAR
            JTESTB=1
          ELSE
            CCEM(ICEM,2)=CCEM(ICEM,1)+RCEM*(CCEM(ICEM-1,1)
+           -2.0D+00*CCEM(ICEM,1)+CEMSB)
        ENDIF
      END DO

```

```

        ENDIF
    ELSE
        CCEM(I,2)=CCEM(I,1)+RCEM*(CCEM(I-1,1)-
+       2.0D+00*CCEM(I,1)+CCEM(I+1,1))
    ENDIF
    IF (I .EQ. IMID) THEN
        CALL SOFT(CCEM(IMID,2),3,J6,TIMH)
    ENDIF
    CEM=CCEM(I,2)*EBAR
    XTCEM=I*STCEM
    CEMM=CEM+CEMM
    CCEM(I,1)=CCEM(I,2)
70     CONTINUE
C Write out the results
    CEMM=CEMM/ICEM
    FERRA=FERRA/IFERA
    FERRB=FERRB/IFERB
    DUMMY=J/A3
    DUMMY=DINT(DUMMY)-DUMMY
    IF (DUMMY .EQ. 0) THEN
+       AVER=(FERRA*TFERA+CEMM*TCEM+FERRB*TFERB)/
+       (TFERA+TCEM+TFERB)
+       WRITE(6,101) TIMH, CEMM, FERRA, FERRB
+       ,AVER, FERSA*EBAR, CEMSA*EBAR, CEMSB*EBAR, FERSB*EBAR
    ENDIF
40     CONTINUE
    WRITE(6,*) ' No wt.%X in FerriteA'
    DO 80 I = IFERA,1,-1
        WRITE(6,102) ((I-(IFERA+1))*-1)*STFERA,CFERA(I,2)*EBAR
80     CONTINUE
    WRITE(6,*) ' No wt.%X in Cementite'
    DO 90 I = 1,ICEM
        WRITE(6,102) (I+IFERA-1)*STCEM,CCEM(I,2)*EBAR
90     CONTINUE
    WRITE(6,*) ' No wt.%X in FerriteB'
    DO 95 I = 1,IFERB
        WRITE(6,102) (I+IFERA+ICEM-2)*STFERB,CFERB(I,2)*EBAR
95     CONTINUE
100    FORMAT(' Diffusion coefficient in ferrite, m**2/s = ',D12.4/
+       ' Diffusion coefficient in cementite, m**2/s, = ',D12.4/
+       ' Volume fraction of cementite (MTDATA) = ',D12.4/
+       ' Thickness of ferriteA, m =',D12.4/
+       ' Thickness of ferriteB, m =',D12.4/
+       ' Thickness of cementite, m =',D12.4/
+       ' Eq. conc. of X at interface, in ferrite, wt.% = ',D12.4/
+       ' Eq. conc. of X at interface, in cementite, wt.% = ',D12.4/
+       ' Absolute Temperature = ', F8.2/
+       ' ICEM, IFERA, IFERB = ',3I9/
+       ' STCEM (m) = ',D12.4/
+       ' STFERA (m) = ',D12.4, ' STFERB (m) = ',D12.4//)
101    FORMAT(D10.4,3F8.3)

```

```

102          FORMAT(2D14.4)
            STOP
            END
.....
            DOUBLE PRECISION FUNCTION DIFF(KTEMP,Q,FREQ)
            DOUBLE PRECISION KTEMP, R, Q, FREQ
            R=8.3143
            DIFF=FREQ*DEXP(-Q/(R*KTEMP))
C R = Universal Gas Constant, J/mol/K
C KTEMP = Absolute Temperature
C Data for X tracer diffusion in alpha iron, from XC Handbook 57
            RETURN
            END
.....
SUBROUTINE SOFT(A,I,J,TIMH)
DOUBLE PRECISION A,TIMH
IF (J .GT. 1) GOTO 99
  IF (I .EQ. 1) THEN
    IF (A .LT. 0.99D+00) THEN
      WRITE(6,110) TIMH
      J=3
    ENDIF
  ELSEIF (I .EQ. 2) THEN
    IF (A .LT. 0.99D+00) THEN
      WRITE(6,111) TIMH
      J=3
    ENDIF
  ELSEIF (I .EQ. 3) THEN
    IF (A .GT. 1.01D+00) THEN
      WRITE(6,112) TIMH
      J=3
    ENDIF
  ENDIF
ENDIF
110          FORMAT(' SOFT IMPINGEMENT IN FERRITEA', F11.5,' hours')
111          FORMAT(' SOFT IMPINGEMENT IN FERRITEB', F11.5,' hours')
112          FORMAT(' SOFT IMPINGEMENT IN CEMENTITE', F11.5,' hours')
99          RETURN
            END

```

REFERENCES

- AARONSON, H. I., (1986)
'Bainite Reaction', Encyclopedia of Materials Science and Technology, Pergamon Press, Oxford.
p. 263-266.
- AFROUZ, A., COLLINS, M. J. and PILKINGTON, R., (1983)
'Microstructural Examination of 1Cr0.5Mo Steel during Creep', *Metals Technology*, **10**, p. 461-463.
- ALBERRY, P. J. and GOOCH, D. J., (1983)
'12CrMoV-A status review', Central Electricity Generating Board Report TRPD/L/2506/N83.
- AL-SALMAN, S. A., LORIMER, G. W. and RIDLEY, N., (1979)
'Pearlite Growth Kinetics and Partitioning in a Cr-Mn Eutectoid Steel', *Metallurgical Transactions A*, **10A**, p. 1703-1709.
- ANDREWS, K. W. and HUGHES, H., (1958)
'Micro-constituents in Steels; Their Electrolytic Isolation and X-ray Study', *Iron and Steel*, **30**, p. 43-50.
- ANDREWS, K. W., DYSON, D. J., and KEOWN, S. R., (1967)
'Interpretation of electron diffraction patterns', Publ. Hilger and Watts, London.
- ANDREWS, K. W., HUGHES, H. and DYSON, D. J., (1972)
'Constitution diagrams for Cr-Mo-V steels', *Journal of the Iron and Steel Institute*, **191**, p. 337-350.
- ARDELL, A. J., (1969)
'Experimental confirmation of the Lifshitz-Wagner theory of particle coarsening', in 'The mechanism of phase transformations in crystalline solids', *Institute of Metals Monograph No. 33*, p. 111-116.
- ARGENT, B. B., VAN NIEKERK, M. N. and REDFERN, G. A., (1970)
'Creep of ferritic steels', *Journal of the Iron and Steel Institute*, **208**, p. 830-843.
- AVRAMI, M., (1939)
'Kinetics of Phase Changes I', *Journal of Chemical Physics*, **7**, p. 1103.
- BAKER, R. G. and NUTTING, J., (1959)
'The tempering of 2.25Cr1Mo Steel after Quenching and Normalizing', *Journal of the Iron and Steel Institute*, **191**, p. 257-268.
- BARNARD, S. J., SMITH, G. D. W., GARRETT-REED, A. J. and VANDER SANDE, J., (1987)
'Atom Probe Studies (2) Low Temperature Chromium Diffusivity in Bainite', Proceedings of International Conference on Solid State Phase Transformations, Pittsburgh, USA.
- BARRACLOUGH, D. R. and GOOCH, D. J., (1985)
'Effect of inadequate heat treatment on creep strength of 12CrMoV steel', *Materials Science and Technology*, **1**, p. 961-967.
- BARRETT, C. S. and MASSALSKI, T. B., (1968)
'Structure of Metals and Alloys', McGraw-Hill, New York.

- BATTAINI, P., D'ANGELO, D., MARINO, G. and HALD, J., (1990)
 'Interparticle Distance Evolution on Steam Pipes of 12Cr1Mo1V Steel during Power Plant Service Times', in 'Proceedings of the 4th International Conference of the Creep and Fracture of Engineering Materials', Swansea, Eds. B. Wilshire and R. W. Evans.
- BEECH, J. and WARRINGTON, D. H., (1966)
 ' M_7C_3 to $M_{23}C_6$ transformation in chromium containing alloys', *Journal of the Iron and Steel Institute*, **204**, p. 460–468.
- BERRY, F. G. and HONEYCOMBE, R. W. K., (1970)
 'The Isothermal Decomposition of Austenite in Fe–Mo–C alloys', *Metallurgical Transactions*, **1**, p. 3279–3286.
- BHADESHIA, H. K. D. H., (1981)
 'Bainite: The Incomplete–Reaction phenomenon and the approach to equilibrium', Proceedings of the International Solid–Solid Phase Transformation Conference, Pittsburgh. p. 1041–1048.
- BHADESHIA, H. K. D. H., (1982)
 'A Thermodynamic Analysis of Isothermal Transformation Diagrams', *Metal Science*, **16**, p. 159–165.
- BHADESHIA, H. K. D. H., (1985)
 'Diffusional Formation of Ferrite in Iron and its Alloys', *Progress in Materials Science, Pergamon Press, Oxford*, **29**, p. 321–386.
- BHADESHIA, H. K. D. H., (1987)
 'Worked Examples in the Geometry of Crystals', The Institute of Metals, London.
- BHADESHIA, H. K. D. H., (1988)
 'Bainite in Steels', Phase Transformations '87, Institute of Metals, London, ed. G. W. Lorimer, p. 309–314.
- BHADESHIA, H. K. D. H., (1989)
 'Theoretical Analysis of Changes in Cementite Composition During Tempering of Bainite', *Materials Science and Technology*, **5**, p. 131–137.
- BHADESHIA, H. K. D. H., (1992)
 'Bainite in Steels', The Institute of Materials, London.
- BHADESHIA, H.K.D.B. and EDMONDS, D. V., (1979)
 'The Bainite Transformation in a Silicon Steel', *Metallurgical Transactions A*, **10A**, p. 895–907.
- BHADESHIA, H. K. D. H. and WAUGH, A. R., (1982)
 'Bainite: An atom probe study of the Incomplete–Reaction phenomenon', *Acta Metallurgica*, **30**, p. 775–784.
- BHADESHIA, H. K. D. H., SWENSSON, L.–E. and GRETOFT, B., (1987)
 'Theory for allotriomorphic ferrite formation in steel weld deposits', *Welding metallurgy of structural steels*, ed. J. Y. Koo, TMS–AIME, Warrendale, Penn., USA. p. 517–530.
- BHADESHIA, H. K. D. H. and CHRISTIAN, J. W., (1990)
 'Bainite in Steels', *Metallurgical Transactions A*, **21A**, p. 767–797.
- BJÄRBO, A., (1991)
 Ph.D. Thesis, Royal Institute of Technology, Sweden.
- BJÖRKLAND, S., DONAGHEY, L. F. and HILLERT, M., (1972)
 'The effect of alloying elements on the rate of Ostwald ripening of cementite in steel', *Acta Metallurgica*, **20**, p.867–874.

- BOWEN, A. W. and LEAK, G. M., (1970)
 'Diffusion in Bcc Iron Base Alloys', *Metallurgical Transactions*, **1**, p. 2767-2773.
- BRIGGS, J. Z. and PARKER, T. D., (1965)
 'The Super 12%Cr Steels', Climax Molybdenum Company.
- CAHN, J. W., (1956)
 'Transformation kinetics during continuous cooling', *Acta Metallurgica*, **4**, p. 572.
- CANE, B. J., (1986)
 'Present Status of Predictive Methods for Remanent Life Assessment and Future Developments', *Materials Forum*, **9**, p. 5-33.
- CANE, B. J. and TOWNSEND, R. D., (1984)
 'Prediction of Remaining Life in Low Alloy Steels', Central Electricity Generating Board Report TPRD/L/2674/N84.
- CANE, B. J. and WILLIAMS, J. A., (1987)
 'Remaining Life Prediction of High Temperature Materials', *International Metals Reviews*, **32** (5), p. 241-262.
- CARINCI, G. M., HETHERINGTON, M. G. and OLSON, G. B., (1988)
 'M₂C precipitation in AP1410 steel', *Journal de Physique (Paris) C6*, **49**, p. 311-316.
- CARRUTHERS, R. B. and DAY, R. V., (1968)
 'The Spheroidization of Some Ferritic Superheater Steels', Central Electricity Generating Board Report SSD/NE/R 138.
- CARRUTHERS, R. B. and COLLINS, M. J., (1980)
 Central Electricity Generating Board Report, NER/SSD/M/80/327.
- CARRUTHERS, R. B. and COLLINS, M. J., (1981)
 'Quantitative Microanalysis with High Spatial Resolution,' (Conf. Proc.), London, The Metals Society. p. 108-111.
- CHANCE, J. and RIDLEY, N., (1981)
 'Chromium Partitioning During Isothermal Transformation of a Eutectoid Steel', *Metallurgical Transactions*, **12A**, p. 1205-1213.
- CHRISTIAN, J. W., (1975)
 'Theory of transformations in metals and alloys', Part I, 2nd Edition, Oxford, Pergamon Press.
- CHRISTIAN, J. W. and KNOWLES, K. M., (1981)
 'Solid-solid phase Transformations', Eds. H.I.Aaronson et al., TMS-AIME, Warrendale, Pennsylvania. p. 1175.
- CHRISTIAN, J. W. and EDMONDS, D. V., (1984)
 'The Bainite Transformation', Phase Transformations in Ferrous Alloys, ASM, Metals Park, Ohio. p. 293-326.
- CRANK, J., (1975)
 'The mathematics of Diffusion', 2nd Edition, Oxford, Clarendon Press.
- DAVISON, J. K. and YELDHAM, D. E., (1975)
 'Boiler Tube Failures and their Causes', *Materials in Power Plant*, Series 3, Number 3.
- DU, X., (1986)
 Ph.D. Thesis, Sheffield University, England.

- DUNLOP, G. L. and HONEYCOMBE, R. W. K., (1976)
 'Ferrite morphologies and carbide precipitation in a Cr-Mo-V creep-resisting steel', *Metal Science*, **10**, p. 124-132.
- EDMONDS, D. V. and HONEYCOMBE, R. W. K., (1973)
 'Structure and properties of an isothermally transformed Fe-4Mo-0.2C alloy', *Journal of the Iron and Steel Institute*, **211**, p. 209-216.
- FRANCK, F. J., TAMBUYSER, P. and ZUBANI, I., (1982)
 'X-ray powder diffraction evidence for the incorporation of W and Mo into $M_{23}C_6$ extracted from high temperature alloys', *Journal of Materials Science*, **17**, p. 3057-3065.
- FRIDBERG, J., TORNDAHL, L-E, and HILLERT, M., (1969)
 'Diffusion in Iron', *Jernkont. Ann*, **153**, p. 263-276.
- GOLDSCHMIDT, H. J., (1948)
 'The Structure of Carbides in Alloy Steels', *Journal of the Iron and Steel Institute*, **160**, p. 345-362.
- GOLDSTEIN, J. I., WILLIAMS, D. B. and CLIFF, G., (1986)
 'Quantitative X-ray analysis' in 'Principles of Analytical Electron Microscopy', Ed. Joy *et al.* p. 155-183.
- GOOCH, D. J., (1982)
 'Creep Fracture of 12CrMoV steel', *Metal Science*, **16**, p. 79-88.
- GOOCH, D. J., (1988)
 'How much longer? - Remanent life assessment of high temperature components', in 'Central Electricity Generating Board Research', Special Issue, **21**, p. 60-67.
- GREENWOOD, G. W., (1956)
 'The growth of dispersed precipitates in solutions', *Acta metallurgica*, **4**, p. 243-248.
- GREENWOOD, G. W., (1969)
 'Particle Coarsening', in 'The mechanism of phase transformations in crystalline solids', *Institute of Metals Monograph No. 33* p. 103-110.
- GULLBERG, R., (1971)
 'Comparison of chromium content in $(Fe, Cr)_{23}C_6$ carbides by electron microprobe and X-ray diffraction', *Journal of the Iron and Steel Institute*, **209**, p. 71-72.
- HALE, K. F., (1975)
 'Creep Failure Prediction from Observation of Microstructure in 2.25Cr1Mo Steel', in 'Physical Metallurgy of Reactor Fuel Elements', The Metals Society, London. p. 193-201.
- HART, R. V., (1976)
 'Assessment of Remaining Creep Life Using Accelerated Stress-Rupture Tests', *Metals Technology*, **3**, p. 1-7.
- HECKEL, R. W. and DE GREGORIO, R. L., (1965)
 'The growth and shrinkage rates of second-phase particles of various size distributions', *Transactions of the Metallurgical Society of the A.I.M.E.*, **233**, p. 2001-2011.
- HEHEMANN, R. F., (1970)
 'The bainite transformation', Phase Transformations in Ferrous Alloys, ASM, Metals Park, Ohio. p. 293-326.

- HILLERT, M., (1962)
 'The formation of pearlite', in 'The Decomposition of austenite by diffusional processes', Eds. V. F. Zackay and H. Aaronson, Interscience, New York, NY.
- HIPPSLEY, C. A., (1981)
 'Precipitation sequences in the Heat-Affected-Zone of 2.25Cr1Mo steel during stress-relief heat treatment', *Metal Science*, **15**, p. 137-147.
- HODSON, S. M., (1989)
 MTDATA-Metallurgical and Thermochemical Databank, National Physical Laboratory, Teddington, Middlesex, U.K.
- HONEYCOMBE, R. W. K., (1976)
 'Transformation from Austenite in Alloy Steels', *Metallurgical Transactions A*, **7A**, p. 915-936.
- HULTGREN, A., (1947)
Transactions of the American Society of Metals, **39**, p. 415.
- HULTGREN, A., (1951)
Kungl. Svenska Vetenskapsakademius Handlingar, **135**, p. 403.
- HYAM, E. D. and NUTTING, J., (1956)
 'The tempering of plain carbon steels', *Journal of the Iron and Steel Institute*, **184**, p. 148-184.
- IRVINE, K. J., CROWE, D. J. and PICKERING, F. B., (1960)
 'The physical metallurgy of 12% chromium steels', *Journal of the Iron and Steel Institute*, **195**, p. 386-405.
- JACK, D. H. and JACK, K. H., (1973)
 'Carbides and Nitrides in Steel', *Materials Science and Engineering*, **11**, p. 1-27.
- KINSMAN, K. R., EICHEN, E. and AARONSON, H. I., (1975)
 'Thickening Kinetics of proeutectoid ferrite plates in Fe-C alloys', *Metallurgical Transactions A*, **6A**, p. 303-317.
- KLUEH, R. L., (1978)
 'Interaction solid solution hardening in 2.25Cr1Mo steel', *Materials Science and Engineering*, **35**, p. 239-253.
- KO, T. and COTTRELL, S. A., (1952)
 'The formation of bainite', *Journal of the Iron and Steel Institute*, **175**, p. 307-313.
- KUO, K., (1953)
 'Carbides in Chromium, Molybdenum and Tungsten Steels', *Journal of the Iron and Steel Institute*, **173**, p. 363-375.
- LAI, J. K. L., CHAN, S. T. and DUGGAN, B. J., (1990)
 'The development of a novel temperature indicator', *High Temperature Technology*, **8**, p. 18.
- LARSON, F. R. and MILLER, J., (1952)
Trans. ASME, **74**, p. 765.
- LEE, Y. J., (1989)
 Ph.D. Thesis, Monash University, Australia.
- LEITNAKER, J. M., KLUEH, R. L., and LAING, W. R., (1975)
 'The composition of eta carbide phase in $2\frac{1}{4}$ Cr1Mo steel', *Metallurgical Transactions*, **6A**, p. 1949-1955.

- LIFSHITZ, J. M. and SLYOZOV, V. V., (1961)
 'The kinetics of precipitation from supersaturated solid solutions', *Journal of Physics and Chemistry of Solids*, **19**, p. 35–50.
- LUNDBERG, R., WALDENSTRÖM, M. and UHRENIUS, B., (1977)
 'Isothermal Sections of the Fe–Cr–C system in the Temperature Range of 873–1373K', *CALPHAD*, **1**, p. 159–199.
- M^cLELLAN, R. B., RUDEE, M. L. and ISCHIBACHI, T., (1965)
 'Thermodynamics of dilute interstitial solid solutions with dual site occupancy and its applications to the diffusion of carbon in α -iron', *Trans. Met. Soc. A.I.M.E.*, **233**, p.1938–1948.
- MIDDLETON, C. J., (1986)
 Central Electricity Generating Board Report TPRD/L/MT0380/M86.
- MILLER, M. K. and SMITH, G. D. W., (1989)
 'Atom probe microanalysis; Principles and applications to materials problems', Materials Research Society.
- MUKHERJEE, T., STUMPF, W. E., and SELLARS, C. M., (1968)
 'Quantitative assessment of extraction replicas for particle analysis', *Journal of Materials Science*, **3**, p. 127–135.
- MUKHERJEE, T., STUMPF, W. E., SELLARS, C. M. and TEGART, W. J. MCG., (1969)
 'Kinetics of coarsening of carbides in chromium steels at 700°C ', *Journal of the Iron and Steel Institute*, p. 621–631
- OHMORI, Y. and HONEYCOMBE, R. W. K., (1971)
 'The isothermal transformation of plain carbon steels', Proceedings ICSTIS *Supplementary transactions of the Iron and Steel Institute of Japan*, **11**, p. 1160–1164.
- OKA, M. and OKAMOTO, H., (1986)
 'Isothermal transformations in hypereutectoid steels', in Proceedings of International Conference on martensitic transformations, ICOMAT '86, Japan Institute of Metals, p. 271–275.
- OLSON, G. B., KINKUS, T. J. and MONTGOMERY, J. S., (1991)
 'APFIM study of multicomponent M₂C carbide precipitation in AF1410 steel', *Surface Science*, **246**, p. 238–245.
- ORIANI, R. A., (1964)
 'Ostwald ripening of precipitates in solid matrices', *Acta Metallurgica*, **12**, p. 1399–1409.
- PILLING, J. and RIDLEY, N., (1982)
 'Tempering of 2.25 Pct Cr–1 Pct Mo Low Carbon Steels', *Metallurgical Transactions*, **13A**, p. 557–563.
- PITSCH, W. and SCHRADER, A., (1958)
Arch. Eisenhuettenw., **29**, p. 715
- PULS, M. P. and KIRKALDY, J. S., (1972)
 'The Pearlite Reaction', *Metallurgical Transactions A*, **3A**, p.2777–2796.
- ROBINSON, E. L., (1938)
Trans. ASME, **60**, p. 253.
- SELLARS, C. M., (1974)
 'Creep Strength in Steel and High Temperature Alloys', The Metals Society, London. p. 20–30.

- SHA, W., CHANG, L., SMITH, G. D. W., LUI CHENG and MITTEMEIJER, E. J., (1992)
 'Some aspects of atom probe analysis of Fe-C and Fe-N systems', *Surface Science*, **266**, p. 416-423.
- SHAMMAS, M. S., (1987)
 'Remanent Life Assessment of the Ferritic Weld Heat Affected Zones by a Metallographic Measurement of Cavitation Damage-The 'A' Parameter', Central Electricity Generating Board Report, TPRD/L/3200/R87.
- SHAW, S. W. K. and QUARRELL, A. G., (1957)
 'The Formation of Carbides in Low-Carbon Chromium-Vanadium Steels at 700°C ', *Journal of the Iron and Steel Institute*, **185**, p. 10-22.
- SMITH, R. and NUTTING, J., (1957)
British Journal of Applied Physics, **7**, p. 214-217.
- SMITH, R. and NUTTING, J., (1957)
 'The Tempering of Low-Alloy Creep-Resistant Steels containing Chromium, Molybdenum, and Vanadium', *Journal of the Iron and Steel Institute*, **187**, p. 314-329.
- STARK, I., SMITH, G. D. W., and BHADESHIA, H. K. D. B., (1987)
 'The element redistribution associated with the Incomplete-Reaction Phenomenon in Bainitic Steels: An atom probe investigation', Proceedings of an International Conference, 'Phase transformations 1987', Institute of Metals, London, Edited by G.W. Lorimer. p. 211-215.
- STEVENS, R. A. and LONSDALE, D., (1987)
 'Electrolytic Extraction of Carbide Precipitates from Low Alloy Ferritic Steel Power Plant Components', Central Electricity Generating Board Report OED/STB(S)/87/0028/R.
- STRANGWOOD, M. and BHADESHIA, H. K. D. H., (1987)
 'Solute segregation, oxygen content, and the transformation start temperature of steel welds', Proceedings of International Conference on Welding Metallurgy of Structural Steels, AIME, Warrendale, Pennsylvania, Edited by J.Y. Koo p. 495-504.
- STUART, H. and RIDLEY, N., (1966)
 'Thermal Expansion of Cementite and Other Phases', *Journal of the Iron and Steel Institute*, **204**, p. 711-717.
- TILLMAN, C. J. and EDMONDS, D. V., (1974)
 'Alloy carbide precipitation and aging during high-temperature isothermal decomposition of an Fe-4Mo-0.2C alloy steel', *Metals Technology*, **1**, p. 456-461.
- TITCHMARSH, J. M., (1978)
 'The Identification of Second-Phase Particles in Steels using an Analytical Transmission Electron Microscope', in Proc. 9th Inst. Congress on Electron Microscopy, J.M. Sturgess, ed., Microscopical Society of Canada, Toronto. 1 p. 618-619.
- TOFT, L. H. and MARSDEN, R. A., (1961)
 'The Structure and Properties of 1Cr0.5Mo Steel After Service in Central Electricity Generating Board Power Stations', *Journal of the Iron and Steel Institute, Special Report 70*, p. 276-294.
- VENGOPULAN, D. and KIRKALDY, J. S., (1978)
 'Hardenability Concepts with Applications to Steels', Conference Proceedings, 249, New York, AIME.
- WADA, M., HOSOI, K. and NISHIKAWA, O., (1982)
 'FIM observation of 2.25Cr1Mo steel', *Acta Metallurgica*, **30**, p. 1013-1018.

- WAGNER, C., (1961)
'Theorie der Alterung von Niederschlägen durch Umlösen', *Z. Elektrochem*, **65**, p. 581–591.
- WAUGH, A. R., RICHARDSON, C. H. and JENKINS, R., (1992)
'APFIM 200 – A reflectron-based atom probe', *Surface Science*, **266**, p. 501–505.
- WESTGREN, A., PHRAGMÉN G. and NEGRESCO, T. R., (1928)
'On the structure of the iron–chromium–carbon system', *Journal of the Iron and Steel Institute*, **117(1)**, p. 383–400.
- WILLIAMS, P. R., MILLER, M. K., BEAVEN, P. A. and SMITH, G. D. W., (1979)
'Fine scale analysis of partitioning in pearlitic steels,' in Proceedings of the York phase transformations meeting, **2**, p. 11–98.
- WILSON, M., (1986)
'The Assessment of the Remaining Creep Life of Carbon and Low Alloy Steel Power Plant Components', *Materials Forum*, **9**, p. 53–66.
- WOODFORD, D. A., (1974)
Proc. International conference on Creep and Fatigue in Elevated Temperature Applications, Philadelphia, 1973. Sheffield 1974.
- WOODHEAD, J. H. and QUARRELL, A. G., (1965)
'Role of Carbides in Low-alloy creep Resisting Steels', *Journal of the Iron and Steel Institute*, **203**, p. 605–620.
- YAKEL, H. L., (1985)
'Crystal structures of stable and metastable iron-containing carbides', *International Metals Reviews*, **30(1)**, p. 17–40.
- YU, J., (1989)
'Carbide stability diagrams in 2.25Cr1Mo steels', *Metallurgical Transactions A*, **20A**, p. 1561–1564.